HAL
open science

Enhanced Raman signatures on copper based-materials

Deniz Cakir

To cite this version:

Deniz Cakir. Enhanced Raman signatures on copper based-materials. Other [cond-mat.other]. Université Montpellier, 2017. English. NNT : 2017MONTS066 . tel-01944233

HAL Id: tel-01944233

https://theses.hal.science/tel-01944233

Submitted on 4 Dec 2018

HAL is a multi-disciplinary open access archive for the deposit and dissemination of scientific research documents, whether they are published or not. The documents may come from teaching and research institutions in France or abroad, or from public or private research centers.

L'archive ouverte pluridisciplinaire **HAL**, est destinée au dépôt et à la diffusion de documents scientifiques de niveau recherche, publiés ou non, émanant des établissements d'enseignement et de recherche français ou étrangers, des laboratoires publics ou privés.

THÈSE POUR OBTENIR LE GRADE DE DOCTEUR
DE L'UNIVERSITÉ DE MONTPELLIER

En : Physique

École doctorale : Information Structure et Systèmes (I2S)

Unité de recherche : Laboratoire Charles Coulomb

ENHANCED RAMAN SIGNATURES ON COPPER BASED-MATERIAL

Présentée par Deniz CAKIR
Le 20 décembre 2017

Sous la direction d'Éric Anglaret
et de Nicole Fréty

Devant le jury composé de

Marc LAMY de la CHAPELLE, Professeur des Universités, Le Mans Université	Rapporteur
Pascal PUECH, Maître de conférences, Université Toulouse III	Rapporteur
Dominique BARCHIESI, Professeur des universités, Université de Technologie de Troyes	Examinateur
Matthias DAMMASCH, Ingénieur, Atotech Deutschland GmbH	Examinateur
Loïc FAVERGEON, Maitre de conférences, École Nationale Supérieure des Mines de Saint-Étienne	Examinateur
Nicole FRETY, Professeur des universités, Université de Montpellier	Co-directrice
Éric ANGLARET, Professeur des universités, Université de Montpellier	Directeur
Lucyna FIRLEJ, Professeur des universités, Université de Montpellier	Présidente du jury

UNIVERSITÉ DE MONTPELLIER

Table of contents

Remerciements 1
Introduction 3
Chapter I: Literature 5
1. Copper and its oxides 5
1.1. Structural properties 5
1.1.1. Crystalline structure of copper 5
1.1.2. Crystalline structures of most common copper oxides 5
1.2. Major structural defects in Cu_2O 7
1.3. Electronic and optical properties 8
1.3.1. Electronic properties 8
1.3.2. Optical properties 9
2. Copper oxidation mechanisms and kinetics 13
2.1. Thermodynamic approach 13
2.2. Kinetic approach 14
2.2.1. Copper oxidation kinetics at high temperature (>600°C) 14
2.2.2. Copper oxidation kinetics at low temperature (<600°C) 15
2.3. Influence of experimental parameters on oxidation kinetics 17
2.3.1. Influence of the crystalline orientation 17
2.3.2. Influence of the temperature 18
2.3.3. Influence of oxygen partial pressure 18
2.4. Cuprous oxide film growth 19
2.5. Cu_2O/ CuO predominance 21
3. Generalities on light- matter interaction 21
3.1. Light 21
3.2. Light-mater interactions 22
3.1. Transmittance of a thick layer with parallel faces 23
4. Raman spectroscopy 25
4.1. Theory 25
4.2. Scattering in a wave perspective 25
4.2.1. Scattering in a quantum perspective 26
4.2.2. Selection rule for first and second order Raman 26
4.3. Raman intensities 27
4.3.1. General equation 27

4.3.2. Resonance Raman scattering 28
4.3.3. Vibrational properties of copper oxide 29
4.3.4. Vibrational properties of Raman probes 32
4.3.5. Interference enhanced Raman Scattering (IERS) 36
5. Surface enhanced Raman spectroscopy (SERS) 40
5.1. Physical background on light – metal interactions 41
5.1.1. Polarizability, and relative permittivity 41
5.1.2. Plasmon definitions 41
5.1.3. Optical properties of metals 42
5.2. Localized surface plasmon resonance and local fields 44
5.2.1. Influence of the size and shape 44
5.2.2. Coupling of nanoparticles 47
5.3. Effective metals for SERS 48
5.4. Probe for SERS 49
5.5. Enhancement factor 50
5.6. SERS on copper 51
Chapter II: Materials and methods 55
1. Copper and copper oxide reference samples 55
2. Copper and copper oxide calibration thin films 56
2.1. Calibration of copper thin films 56
2.2. Calibration of copper oxide thin film 57
3. SERS substrates 59
3.1. Electroless copper substrates 59
3.2. Etched copper substrates 60
3.3. Gold based substrates 61
4. Raman probes 62
4.1. Graphene probe 62
4.2. Organic molecules probes 62
5. Characterization techniques 63
5.1. SEM / AFM observations 63
5.2. XPS chemical analyses 65
5.2.1. XPS principle 65
5.2.2. XPS experiments 66
5.3. Ellipsometry 68
5.3.1. Multiple angle of incidence (MAI) ellipsometry 70
5.3.2. Spectroscopic ellipsometry 71

5.4. UV-vis 72
5.5. Raman spectroscopy 73
Chapter III: Coupled microscopic/ spectroscopic characterization of ultra-thin copper/ copper oxide films 75
1. Thin films microstructure 76
1.1. Microstructure observation of the raw Cu thin films 76
1.2. Microstructural observation of the oxidized thin films 78
2. Determination of the copper oxidation state of thin films 81
2.1. Study of the Cu LMM Auger transition 81
2.2. Study of the Cu 2p3/2 XPS transition 82
3. Determination of the copper and the oxidized thin films thicknesses 84
3.1. Thickness determination from microscopy 84
3.2. Thickness determination from ellipsometry 86
3.2.1. Multiple-angle incident (MAI) ellipsometry 86
3.2.2. Spectroscopic Ellipsometry (SE) 87
3.3. UV-vis spectroscopy (UVS) 88
3.3.1. Raw and fully oxidized surfaces 88
3.3.2. Partially oxidized samples 89
3.3.3. Fitting procedure description. 91
3.3.1. Refractive indices 99
3.3.2. Summary of UVS fit 100
4. Discussion 101
4.1. Raw samples 101
4.2. Partly and fully oxidized surfaces 103
4.3. Estimation of the thickness of a cuprous oxide layer on a ‘‘bulk’’ copper substrate 104
Chapter IV: Raman signature enhancement 107
1. Raman signatures of copper oxide 107
1.1. Pure powders 107
1.2. Calibrated thin films 110
1.2.1. Series S50 110
1.2.2. Influence of the initial thickness of the undercoating of copper 112
1.2.3. Discussion on the IERS enhancement 117
1.3. Expected IERS on copper substrates 120
1.3.1. Series S180 120
1.3.2. Correlated Raman / PL signatures of various series of samples 123

2. Expected IERS enhancement for molecules deposited on the copper / copper oxide surface 130
2.1. IERS study on a copper single crystal 130
2.2. Influence of the nanostructuration on IERS of SLG 132
2.2.1. Electroless copper samples 132
2.2.2. Copper etching sample 134
Chapter V: Comparative SERS studies of gold and copper 135
1. Optimization of the SERS measurements on raw Au-SERStrate 135
1.1. Raman spectra of bare substrate 135
1.2. Wavelength dependence of the SERS enhancement 136
1.3. Effect of the pillar leaning 138
1.4. Estimation of the enhancement factor in optimal conditions 139
2. Comparison of Au- and Cu- plated SERStrates 140
2.1. Microstructure evolution on a copper covered SERStrate 141
2.2. In situ Raman monitoring of the surface of the SERStrate 142
2.3. Influence of BPE concentration 147
2.4. Detection of another organic molecule: MBT 148
Conclusion and perspectives 151
Appendix 153
Appendix 1: Ratio of transformation 153
Appendix 2: Fitting procedure 154
Appendix 3: Quantification of the copper species by XPS 159
Bibliography 163

Remerciements

Cette partie essentiellement adressée à des francophones est rédigée en français.

J'exprime ici toute ma reconnaissance envers mon directeur de thèse, Eric Anglaret et ma co-directrice de thèse Nicole Fréty.

Ce travail n'aurait pas été possible sans le soutien de d'Atotech GmbH, qui m'a permis, grâce à une allocation de recherches et diverses aides financières, de me consacrer sereinement à l'élaboration de ma thèse. Je remercie en particulier Hans Jürgen Schreier, et son successeur à la tête du département de R&D Gerd Linka qui m'ont fait confiance et ont permis le financement de 3 ans et demi de recherche.

J'exprime tous mes remerciements à l'ensemble des membres de mon jury : Mesdames Lucyna Firlej et Nicole Fréty ainsi que messieurs Matthias Dammasch, Loïc Favergeon, Dominique Barchiesi, Pascal Puech, Marc Lamy de la Chapelle et Eric Anglaret. Je tiens à remercier Dominique Barchiesi pour avoir non seulement participé à mon jury de thèse mais également pour sa participation scientifique ainsi que le temps qu'il a consacré à ma recherche. Je tiens à le remercier tout particulièrement pour son enthousiasme sur les propriétés optiques du cuivre et de ses oxydes. Je remercie également Pascal Puech et Marc Lamy de la Chapelle qui ont rapporté la thèse.

Ce travail n'aurait pu être mené à bien sans la disponibilité et l'accueil chaleureux que m'ont témoignés les différents membres de l'équipe nanomatériaux à Montpellier, et celle de Stéphanie Reich, à Berlin qui m'a initié à la spectroscopie Raman. Je tiens à remercier en particulier Benjamin Hatting, Donal Flanagan et Maximilian Ries qui ont participé aux débuts du projet. Un grand merci à Max, qui m'a aidé avec les arcanes de l'administration allemande, et ouvert sa porte autant de fois que nécessaire. Toujours à Berlin je remercie les chercheurs d'Atotech des différents départements STT, PTH et R&D EL qui m'ont invité dans leur salles de manip pour m'apprendre à utiliser les différentes techniques de dépôt de cuivre et différentes stratégies de structurations, ainsi que les personnes qui m'ont aidé à la caractérisation des surfaces. En particulier je tiens à remercier Yoshiko Nishihara, ma tutrice en entreprise qui a su quand rediriger les recherches et suggérer un déménagement à Montpellier pour profiter de l'entourage universitaire. Originaire du Japon, elle non plus n'a pas su s'adapter ni au repas à terminer en moins de vingt minutes, ni aux quantités et aux goûts et consistances des plats.

Je remercie Pierre Lefebvre pour m'avoir accueillie au laboratoire Charles Coulomb. Je salue en particulier son équipe administrative pour leur diligence et la qualité de leur travail. Je salue également la qualité du travail réalisé par Didier Cot, passionné de photographie qui a permis d'avoir des clichés MEB de grande qualité, ainsi que Michel Ramonda pour sa bonne humeur constante lors de l'acquisition des clichés AFM. Je n'oublie pas de remercier l'ensemble des collègues doctorants, qui en oubliant de passer plus de temps chez eux qu'au laboratoire, en ont fait un lieu de vie convivial. Je tiens en particulier à remercier Khadija Yazda qui a été un exemple de résilience et de persévérance pour moi. Je n'oublie pas ni Lérys Granado ni Paul-Augustin Wasner, grâce à qui le doctorat a été moins solitaire. Finalement ma gratitude va vers Laurent Alvarez et Nicolas Izard qui par leur écoute et leur compassion ont empêché l'arrêt prématuré de mon doctorat. Un grand merci à Nicolas qui

en m'initiant à python m'a permis de traiter l'ensemble de mes résultats, et d'illustrer mes résultats de la façon la plus efficace, tu m'as fait gagner un temps précieux.

Au terme de ce parcours, je remercie enfin celles et ceux qui me sont chers et que j'ai quelque peu délaissés ces derniers mois pour achever cette thèse. Merci à Huong Huynh pour les multiples encouragements répétés. Merci à Claire Hugonnard et Pauline Burner qui m'ont hébergé lors de mes multiples aller-retour à Berlin. Merci aux pratiquants du kendo qui m'ont permis de me concentrer sur autre chose que la thèse. Merci à Caroline Tarquini, Mathieu Debernardi et leur chat, compagnon de ma rédaction. Vos attentions et encouragements m'ont accompagnée tout au long de ces années. Je suis redevable à mes parents, pour leur soutien moral et matériel et pour avoir cru en moi.

Introduction

The field of ‘‘plasmonic’’, which designates the study of optical phenomena related to the electromagnetic response of metals, is a domain of growing interest. Indeed with the recent development of nanotechnologies, it is possible to create, manipulate and characterize nano-objects. Plasmonic properties can be applied in many domains such as sensing or photonics. In particular, resonant coupling between an electromagnetic field and localized surface plasmons of metal nanostructures leads to huge local fields which can be used to enhance the spectroscopic (*e.g.* fluorescence or Raman) signals of molecules deposited on the surface. Resonance and enhancement are governed by the size, and shape of the metal nanostructures, as well as their dielectric properties and those of their environment.

Surface Enhanced Raman Spectroscopy (SERS) is the technique that uses this enhancement, and allows the detection of very low concentration of molecules (ppm / ppb). The metal chosen to support SERS are often gold or silver, due to their particular optical properties in the visible range. Gold is widely studied due its stability. Copper is often cited as a cheaper alternative to gold, with plasmon resonances in the same spectral ranges, but its spontaneous oxidation in air hinders its development as an alternative to gold for SERS applications.

Atotech is a leading company in metal plating chemicals and equipment. One of their domain of expertise is copper plating for printed circuit boards. The company developed many processes to prepare and characterize the microstructure and oxide state of copper-based materials, and is interested in developing new applications in synergy with their current knowhow. In this context, the goal of my PhD thesis is to study how SERS can be achieved on copper-based materials and how it can help understanding the interactions between organic additives and copper surfaces during metal plating.

A first part of the PhD thesis is devoted to the preparation and microstructural study of various copper-based materials. A special focus is made on the measurements of the thickness and dielectric properties of copper and its superficial layer of copper oxide.

A series of thin copper films are prepared by thermal evaporation and oxidized by thermal oxidation in air at temperatures below 170°C. Their microstructure is characterized by SEM and AFM. Thicknesses are characterized by those techniques, and compared to spectroscopic studies by ellipsometry and UV-visible absorption spectroscopy (UVS). A modeling of the UVS spectra based on interference calculations from Fresnel equations is proposed, in collaboration with Dominique Barchiesi at Université Technologique de Troyes (UTT), allowing the determination of both the layers thicknesses and their refractive indices.

When a thin layer of dielectric material is deposited on a metal, the Raman signal is modulated by multiple reflection interferences. In order to discuss and quantify this so-called IERS phenomenon, a coupled Raman / photoluminescence study of the copper oxide signatures is performed on the series of thin films, and on other copper-based materials as well. On the other hand, the IERS enhancement of the signal of molecules deposited on the surface of copper / copper oxide materials is investigated by transferring single layer graphene (SLG) on the surface of the samples. Here, SLG is used as a model probe able to quantify the IERS phenomenon, but also to passivate the surface thanks to its gas barrier properties.

The last part of this manuscript is dedicated to the SERS study of organic molecules deposited on a nanostructured gold commercial substrate and to the evolution of this signal after the coverage by a thin copper layer. Both dyes and molecules of interest for Atotech are studied. The SERS enhancement factor is estimated and the possibility of developing a SERS method to detect the adsorption of additives during copper plating is discussed.

The manuscript is structured as follows: the first chapter presents the state of the art. It starts with a description of the structure of copper and its oxides, the oxidation mechanisms phase diagrams and kinetic laws. Then the basics of Raman, IERS and SERS are described, followed by a review on the particular case of copper and copper oxide. Chapter II describes the materials and methods used in the thesis. The third chapter focus on the characterization of thin copper films before and after oxidation, and proposes a method of fit based on Fresnel equations to determine the thickness and dielectric properties of the films. In chapter IV, we report coupled Raman / photoluminescence study of copper-based materials, focusing on the signatures of cuprous oxide, and we discuss the IERS enhancement for copper oxide and for SLG deposited on the surface of the samples. Finally, in the last chapter, we compare the SERS signature of dyes and organic additives of interest for Atotech, using a nanostructured gold commercial substrate before and after deposition of a thin copper layer.

Chapter I: Literature

In this chapter the structural, electronic and optical properties of copper and copper oxides are presented. The possible light matter interactions and the Raman spectroscopy theory are presented. Vibrational properties of copper and copper oxides are presented as the graphene as the 2-Bis(4-pyridyl)ethylene (BPE). Finally we give the background of the physical phenomena that can lead to enhanced intensities of the Raman signal: Interference enhanced Raman Scattering (IERS) and Surface Enhanced Raman Spectroscopy (SERS).

1. Copper and its oxides

1.1. Structural properties

1.1.1. Crystalline structure of copper

Copper is the 29th element of the periodic table of the element. It forms a metallic face centered cubic (fcc) crystalline structure with a lattice parameter of 4.61 Å and a density of 8.96. Together with silver (Ag) and gold (Au), it was used for centuries as a coinage metal due to its high malleability and rarity. Nowadays copper is largely used in electrical wiring and in electronic devices due to its high electrical conductivity (6. 10^7 S/m). Copper spontaneously oxidizes in air at room temperature with the formation of a non-protective oxide layer.

1.1.2. Crystalline structures of most common copper oxides

In a dry atmosphere, copper oxidizes mainly into Cu_2O (referred as cuprite or cuprous oxide) and CuO (referred as tenorite or cupric oxide). Hereafter we present the structure, electronic and optical properties of theses oxide forms.

Note that we will not address other rarer copper oxide forms, such as Cu_2O_3 which has been reported by some groups as a metastable oxide forming at low temperature [1, 2], or Cu_4O_3 (paramelaconite) which is formed in particular conditions as well. On the other hand, we will also ignore the oxide formed in presence of water, like copper hydroxide $Cu(OH)_2$, or in the presence of salts such as copper acetate $Cu(C_2H_3O_2)_2.H_2O$, copper sulfate (Cu_2SO_4) or copper carbonate $Cu(OH)_2.CO_3$, this latter form being the chemical form of the natural patina of copper statues, known as verdigris.

Cuprous oxide, Cu_2O, crystallizes in a cubic structure of the space group $Pn3m$ (Figure I-1, Table I-1). The primitive cell contains 2 Cu_2O units, with a lattice parameter of 4.18 Å and a density of 6 g.cm^{-3}. Cu^+ ions are in D_{3d} symmetry forming a fcc sub-lattice, with two O^{2+} ions as first neighbors in tetrahedral position, while oxygens are in T_d symmetry with 4 copper as first neighbors, forming a bcc sub-lattice. Oxygen atoms form a bcc lattice, while copper atoms are described by a fcc lattice. Oxygen is in tetrahedral position of interstitial sites of copper. The primitive cell contains 2 Cu_2O units, with lattice parameters given in Table I-1.

Cupric oxide, CuO, crystallizes in a monoclinic structure of space group C2/c. The primitive cell contains 2 CuO units with lattice parameters reported in Table I-1. Copper ions are on sites with C_i symmetry, while oxygen ions are in C_2 symmetry (Figure I-1).

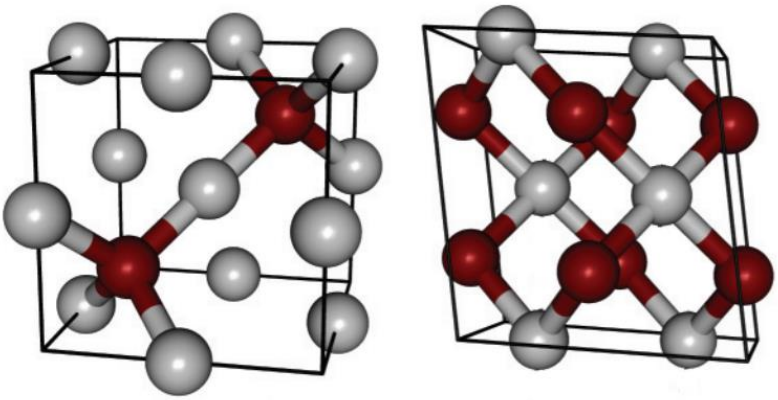

Figure I-1: Primitive cell for Cu_2O (left) and CuO (right) [3] Red spheres represent the O^{2-} ions while the grey spheres symbolize the copper ions.

	Cu_2O	CuO
System	Cubic ($Pn\bar{3}m$)	Monoclinic ($C\ 2/c$)
Lattice parameters	a = 4.18 Å	a = 4.6837 Å b = 3.4226 Å β= 99.54° c = 5.1288 Å
Shortest distances		
$d_{Cu\text{-}O}$	1.84 Å	1.95 Å
$d_{O\text{-}O}$	3.68 Å	2.62 Å
$d_{Cu\text{-}Cu}$	3.02 Å	2.90 Å
Density	6.0 g/cm³	6.31 g/cm³

Table I-1: Structural characteristics of Cu_2O and CuO

The reciprocal lattices in the first Brillouin zone for the two phases are represented together with the highest symmetry points in Figure I-2.

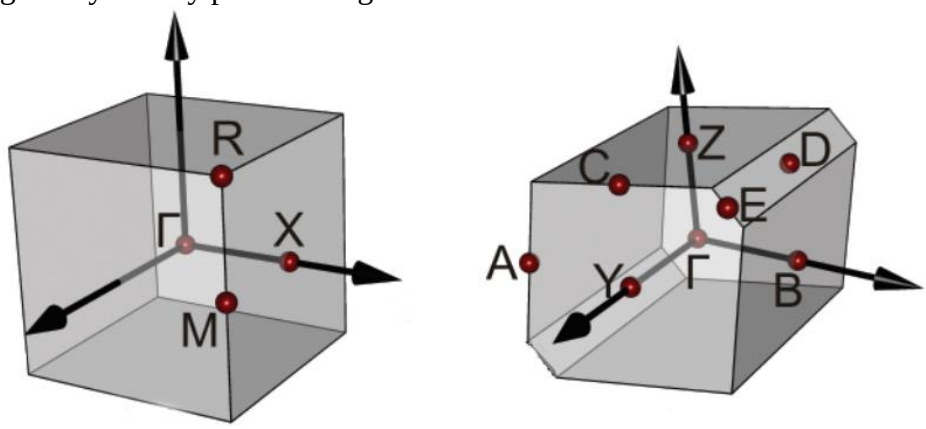

Figure I-2: 1st Brillouin zone of the reciprocal lattices for Cu_2O (left) and CuO (right). Γ refers to the center zone and the letters to other points of high symmetry (adapted from [3])

1.2. Major structural defects in Cu_2O

After a description of the perfect structure, we briefly focus on the possible defects present in the Cu_2O oxide lattice, which is essential to understand why Cu_2O is an intrinsic p-type semi-conductor.

Crystalline non-stoichiometry arises from Schottky defects which correspond to anion or cation vacancies. The electro-neutrality can be maintained if the number of cation and anion vacancies is equal. On the other hand, Frenkel defects correspond to interstitial ions (generally cations, due to their smaller size) and don't change the crystal stoichiometry. Kröger *et al*. [4] introduced the creation / annihilation of electrons and holes to complete the description of possible defects in a structure. The notation of Kröger – Vink used to describe the different defects is reported in Table I-2.

The energy of defect formation is given by Scanlon *et al*. for Cu-rich /-poor and O-poor /-rich conditions (Figure I-3) [5]. Dominant defects under normal conditions (P_{atm} and RT) are V_{Cu} or split vacancy V_{Cu}^{split} which have the lowest formation energies (see their representation in in Figure I-4) [6].

The copper vacancy (left of the Figure I-4) is symbolized by a missing Cu light grey ball. The split vacancy (right of the Figure I-4) occurs when a copper atom moves from its initial position toward the vacancy. It becomes then coordinate to 4 oxygen atoms, which is very stable, since it is the normal coordination in CuO crystal. Interstitial oxygens in tetra- or orthogonal sites are other possible defects, but their energy of creation is higher than the copper vacancies (Figure I-3). Studies at higher temperature (977 < T < 1053 °C) and in various pressures of oxygen (10^{-8} < P < 1 atm) confirm the presence of these defects: a majority of copper vacancies with holes formation, with oxygen interstitial atoms as minor defects [7-11].

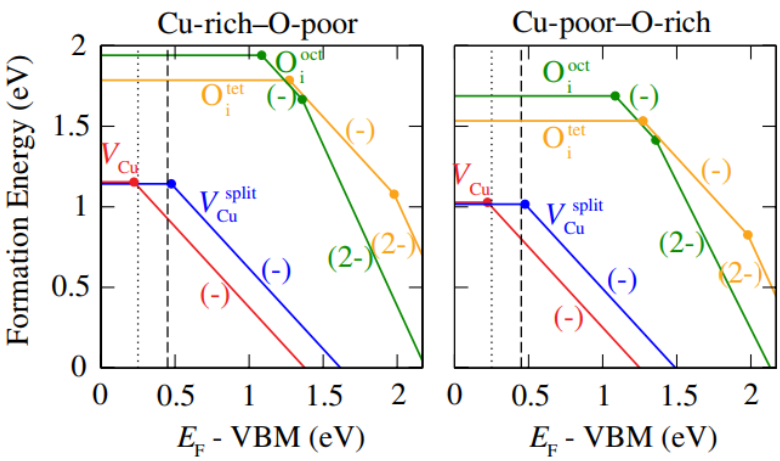

Figure I-3: Formation energies for intrinsic p-type defects in Cu2O in Cu-rich O-poor conditions (left) and Cu-poor O-rich conditions [5]

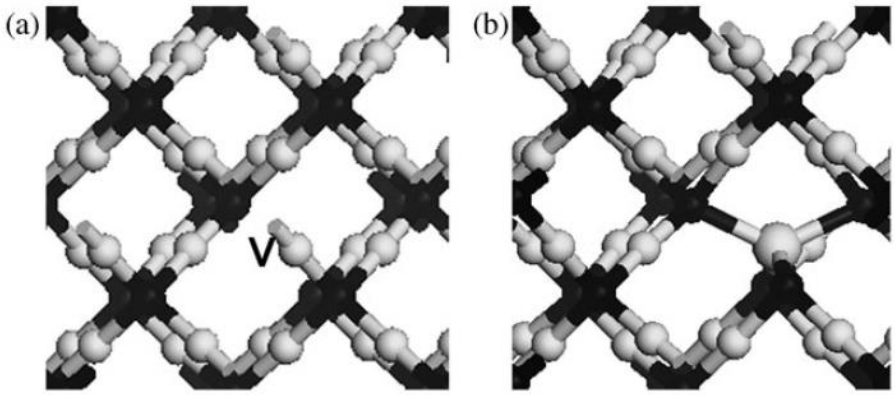

Figure I-4: Representation of the vacancy (left) and the split vacancy (right) in a Cu_2O crystal. Copper and oxygen ions are represented respectively in light grey and black, from [6]

Notation	Signification
V_{Cu}	Vacancy in the copper lattice
V_O	Vacancy in the oxygen lattice
Cu_i	Copper atom in interstitial site
O_i	Oxygen atom in interstitial site
Superscripts	Charge state
$[\ \ ]^{\times}$	Neutral
$[\ \ ]^{\bullet}$	Positively
$[\ \ ]'$	Negatively
Notation used in the manuscript	
$V_{Cu}^{\times}$ or V_{Cu}	Neutral vacancy of copper
$V_{Cu}^{\bullet}$, V_{Cu}^{+} or V_{Cu^+}	Positively charge copper vacancy
V_O'' , V_O^{2-} or $V_{O^{2-}}$	Vacancy of oxygen doubly charged

Table I-2: Notation of Kröger – Vink to describe the different defects.

1.3. Electronic and optical properties

1.3.1. Electronic properties

The dispersion curves and electronic density of states (DOS) calculated from hybrid functional DFT are represented in Figure I-5 for Cu_2O and CuO. Cuprous and cupric oxides are semiconductors with a direct band gap of about 2.17 eV for Cu_2O, and an indirect band gap of CuO of about 1.35 eV, respectively (arrows in Figure I-5).

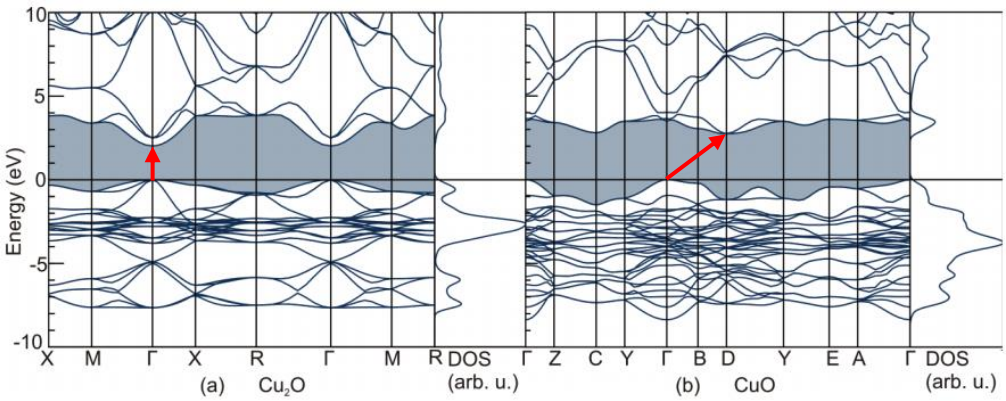

Figure I-5: Dispersion curves and electronic density of states for Cu_2O (left) and CuO (right) from hybrid functional DFT calculations [3]. Direct and indirect band gaps are represented by the red arrows [3]

1.3.2. Optical properties

1.3.2.1. Absorption

The refractive indices (n, κ) of cuprous and cupric oxide are represented in Figure I-6. The imaginary part κ, related to the absorption coefficient α (see 3.1) decreases with the wavelength. For Cu_2O and CuO, κ is negligible for wavelengths above 510 and 850 nm respectively.

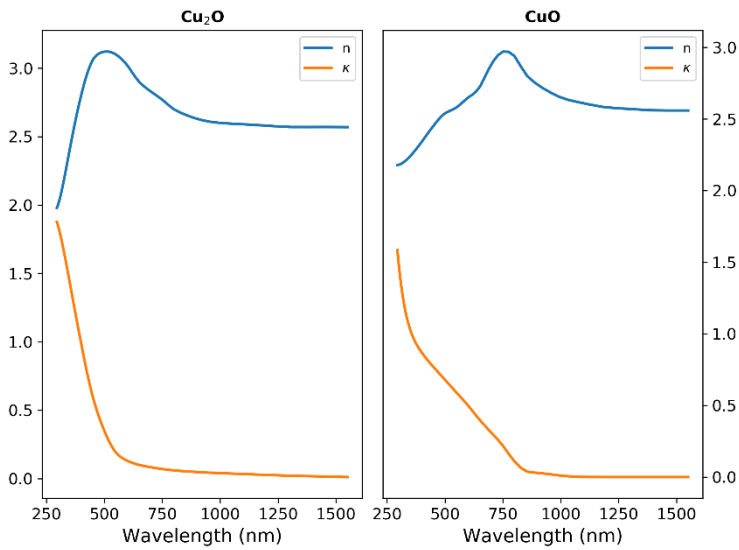

Figure I-6: Refractive indices of Cu_2O and CuO from Sopra [12]

The absorption coefficient differs considerably as a function of photon energy for cuprous and cupric oxides (Figure I-7). The photon energy shifts from 2.7 to 2.1 eV from cuprous to cupric oxide for an absorption coefficient of 1.10^5 cm^{-1}. In the visible range (1.55 - 3.10 eV), cupric oxide absorb all the light which explains its black color. Cuprous oxide absorbs energies higher than its gap about 2.17 eV so all colors except the red, which explains its observed color (red).

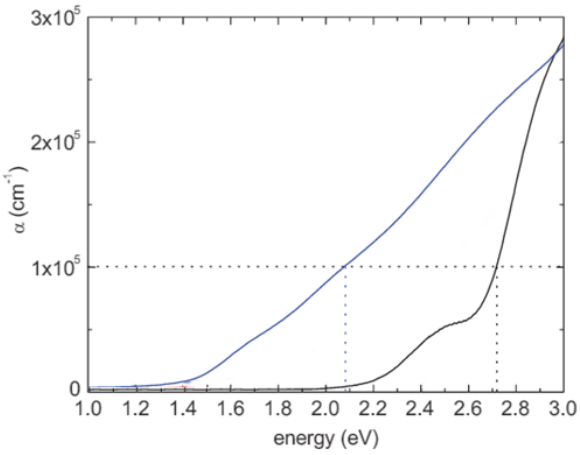

Figure I-7: Absorption spectra of cuprous (black) and cupric (blue). The horizontal and vertical dotted lines indicates the energies where the absorption coefficient reaches 1.10^5 cm^{-1} in the spectra, from Meyer et al [13].

1.3.2.2. Photoluminescence properties of Cu_2O

In spite of the large amount of studies, the photoluminescence (PL) properties of Cu_2O are still controversial. Different studies are particularly difficult to compare since different growing and post-processing methods are used. The position, width and intensity of the PL bands are very sensitive to the quality of the samples and notably to the vacancy concentration.

The band structure of a perfect crystal is represented at the gamma point (left of Figure I-8), with the corresponding energy levels and the different allowed optical transitions (AOT). The first AOT is the yellow 1s, occurring between the maximum of the valence band (VBM) and the minimum of the conduction band (CBM). In defective structures the presence of vacancies and interstitials creates additional levels within the band gap (right of Figure I-8) [5], which can be used as dexcitation channel.

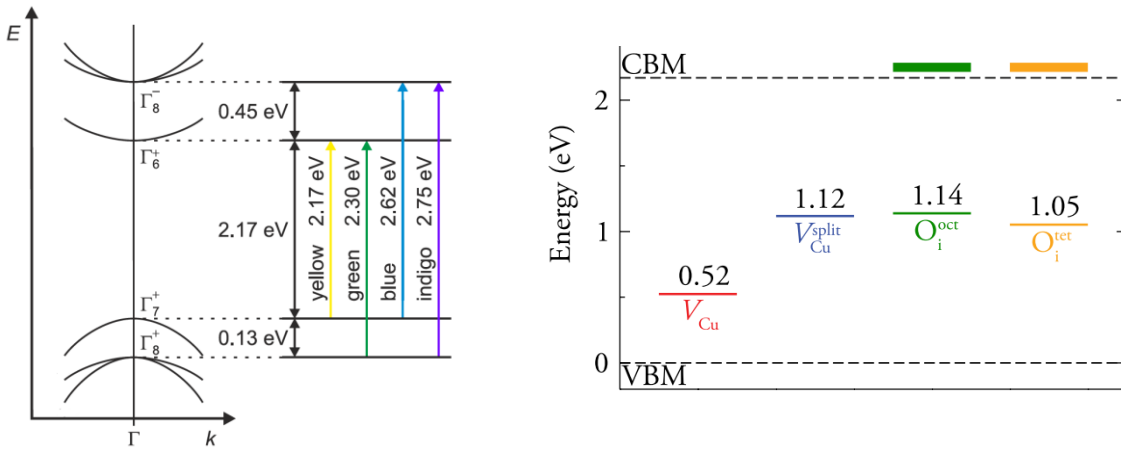

Figure I-8: Band structure of Cu_2O at the gamma point (left) Additional levels within the band gap due to vacancy or interstitial defects in Cu_2O [5] (right)

The PL spectra measured for different samples can be separated in two main groups, one group related to the yellow 1s transition (Y1s) with a band centered between 560 and 660 nm, and a second group involving vacancy states with a band centered between 650 and 1000 nm (Figure I-9). Note the weak contribution of the green (G2) transition at 540 nm for thermally oxidized Cu on sapphire and ZnO [14].

Li *et al.* [14] reported a strong signature for the usually forbidden Y1s direct dipole transition. The lift of the parity conservation rule is assigned to assisted phonon recombination: Γ_{15}^{-} and Γ_{12}^{-} phonon absorption at 609 and 627 nm, followed by Γ_{12}^{-} phonon emission at 636 nm allow a good fit of the Y1s signature.

By contrast with Li *et al.* [14], Meyer *et al.* [13] observed that the PL is dominated at room temperature by contribution of V_{Cu} centered at 920 nm (Figure I-10), with respect to those of simple charged and double charged oxygen vacancies (V_O^{+}, V_O^{2+}) around 810 and 720 nm, respectively. They studied, the PL according to the temperature, with the broadening of all contribution to the PL with increasing temperatures.

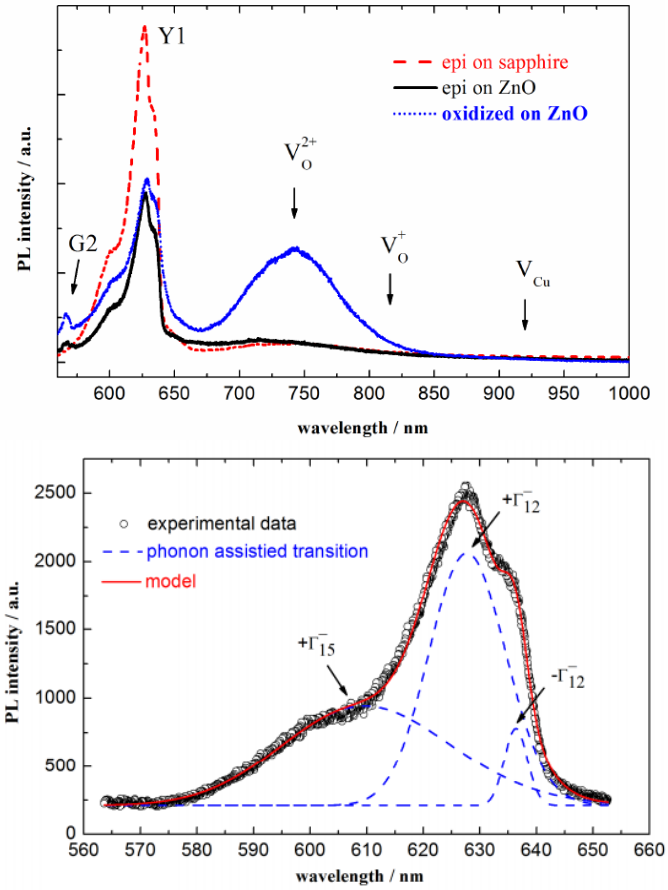

Figure I-9: Luminescence spectra of Cu_2O at room temperature [14] on various substrates (top) and a zoom on the yellow 1s (Y1) signatures of Cu_2O on sapphire (bottom)

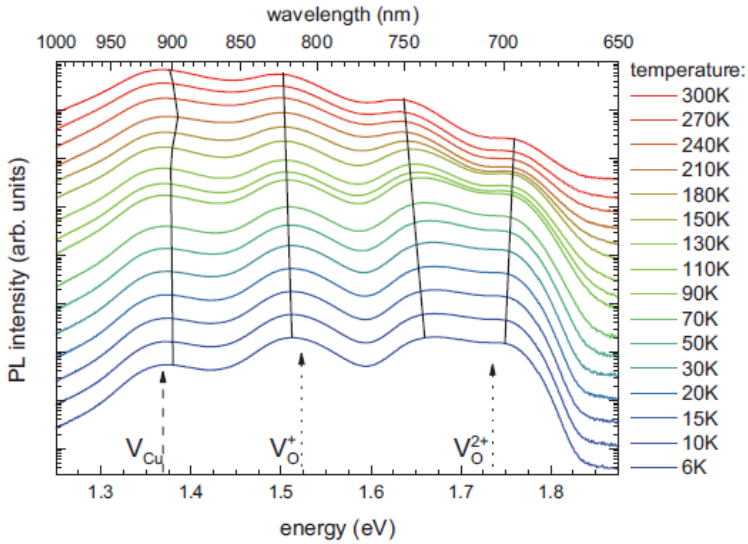

Figure I-10: Luminescence spectra of Cu_2O as a function of the temperature [13]

1.3.2.3. Photoluminescence properties of CuO

Only a few studies of the optical properties of CuO have been published. To our best knowledge no PL observation was reported from bulk CuO. By contrast, CuO nanoparticles display a weak PL signal in the blue region at room temperature (RT) [15, 16].

Son *et al*. reported a dominant PL peak for CuO nanocrystals of size in the range 3-5 nm around 379 nm, with a full width at half maximum (FWHM) as small as 30 nm, indicative of the high crystalline quality [16] Erdoğan and Güllü [15] observed a broader PL emission band, red shifted to 467 nm as compared to Son's study (Figure I-11) The PL is attributed to a near band edge emission and not to quantum confinement as in Son's study, which can explain the red-shift and the broadening.

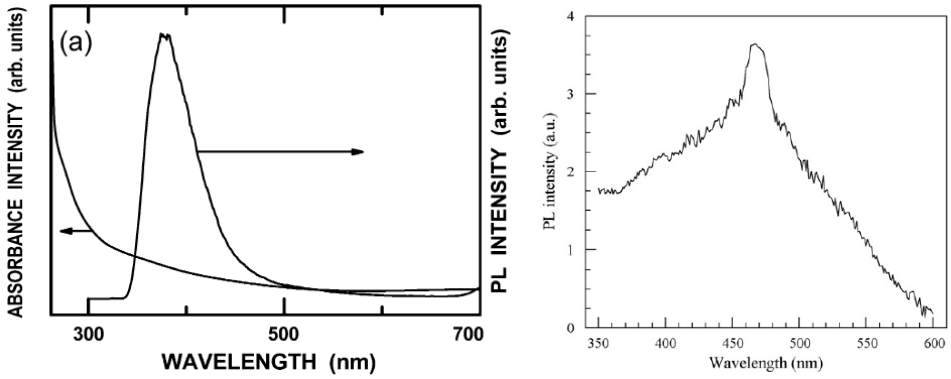

Figure I-11: PL spectrum of CuO (left) [16] and (right) [15]

2. Copper oxidation mechanisms and kinetics

Despite extensive studies, as recently reviewed by Gattinoni and Michaelides [17] copper oxidation mechanisms are still not completely understood. In particular, the suggested oxidation kinetics are still controversial especially at low temperature (<600°C). This can be explained by the large number of factors which can influence the oxidation mechanisms and kinetics such as the temperature the oxygen partial pressure, the type of sample (thin film, polycrystalline or single bulk materials), the crystalline orientation, the microstructure (grain size, impurities), the initial surface state (roughness) and the lattice defects. Therefore the ranges of preferential formation of Cu_2O, CuO or of coexistence of these two phases are controversial as well. Moreover, thickness measurements are inaccurate for small thicknesses, which makes the results even more controversial at low temperature.

2.1. Thermodynamic approach

As previously stated, Cu_2O and CuO are the two stable copper oxide phases in dry atmospheres. The P, T phase diagram is shown in (Figure I-12).

Rakhshani *et al.* [18] calculated the oxygen partial pressure vs the temperature phase diagram (Figure I-12). CuO is observed to be the stable phase at atmospheric pressure below 1000°C. For higher temperature (> 1000°C), Cu_2O becomes the stable oxide form.

It can be noted that the Rakshani diagram is in good agreement with the experimental data obtained by Wright [19] and Coughlin [20] in the range 10^{-15} – 1 atm and 280 – 1200 °C. O'Keeffe [21] observed a good agreement as well for pressures ranging from 10^{-9} to 1 atm and temperatures from 400 to 1200°C.

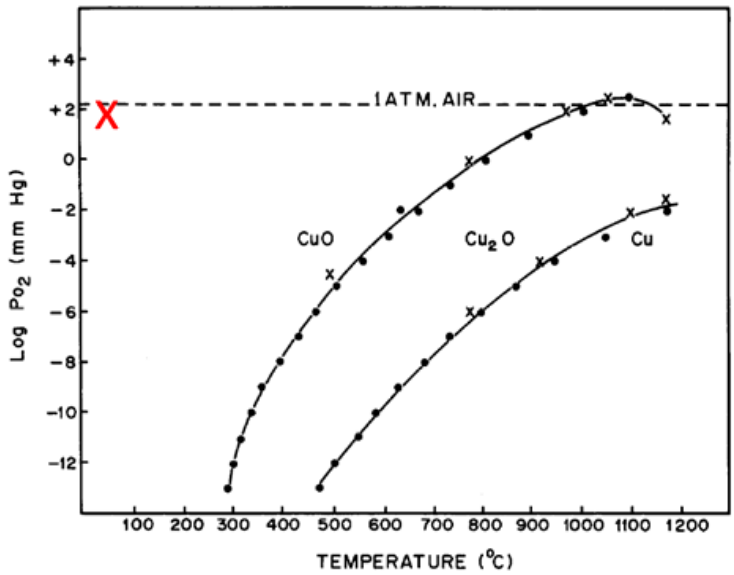

Figure I-12: Cu-O common pressure temperature phase diagram. X: standard conditions (from [18])

The stability domains of copper and its oxides phases have been determined from the Gibbs free energy (ΔG) expressed at atmospheric pressure in Table I-3 [22]

General equation	Thermodynamic law	Constant of the reaction	
$Cu + \frac{1}{4}\ O_{2(g)} \rightarrow \frac{1}{2}\ Cu_2O$	$\Delta G_2 = -164 + 67.10^{-3}T$	$K_2 = \frac{1}{[P(O_2)]_{eq}^{1/4}}$	(1)
$Cu_2O\ + \frac{1}{2}O_2 \rightarrow 2\ CuO$	$\Delta G_3 = -156 + 267.10^{-3}T$	$K_3 = \frac{1}{[P(O_2)]_{eq}^{1/2}}$	(2)

Table I-3: Gibbs free energy for copper oxide formation from Dubois [22]

As shown in Figure I-13, under atmospheric pressure the Cu phase is in equilibrium with the Cu_2O phase and cannot co-exists with the CuO phase. Therefore the CuO phase can only be formed from the Cu_2O oxidation.

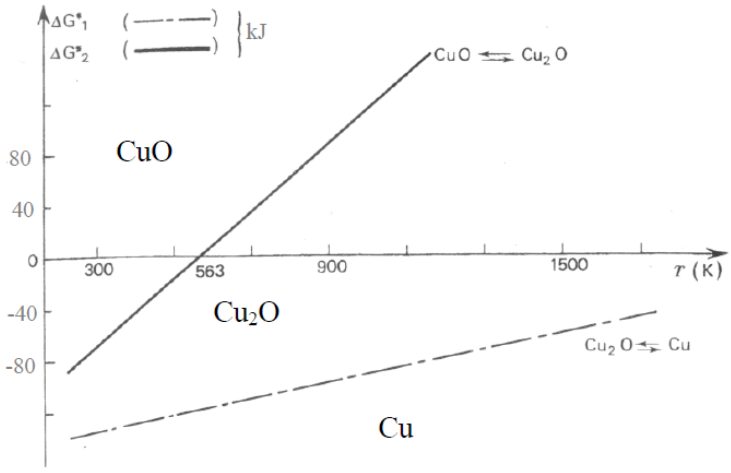

Figure I-13: Ellingham diagram for copper [22]

2.2. Kinetic approach

2.2.1. Copper oxidation kinetics at high temperature (>600°C)

In the early 1930's, Wagner proposed a model for the description of metal oxidation [23], valid at high temperature (> 600°C) and for an oxide thickness higher than 20 nm. The oxidation is driven by the decrease of free energy changes associated to the formation of the oxide, which established a gradient of species concentrations across the oxide layer. In Wagner's model the oxide growth is limited by the diffusion of charged species (ions, holes) through the oxide layer. The oxidation through the diffusion of species at grain boundaries is considered to be negligible.

The Wagner's model describes the oxidation kinetic based on a diffusion process, where the volume diffusion is the limiting step, following a parabolic law:

$$x^2 = K_{11}\ (T)t + K_{12}(T) \qquad (3)$$

where x is the thickness of the oxide layer formed at a time, t ; K_{11} and K_{12} are constant, following Arrhenius law for K_{11}.

For temperature above 600°C the parabolic law well describes the oxidation kinetics. The assumption from Wagner that the oxidation process is limited by the diffusion of charged species through the oxide layer was corroborated by many authors such as Park and Natesan on polycrystalline Cu (99.995%) under air or pure O_2 at T = 750-1040°C [10]. More recently Mimura *et al.* in 2006 [24] and Liang *et al.* in 2010 [25] confirmed this parabolic law for the oxidation of copper of various purities (99.99 to 99.9999%) at temperatures above 550°C in pure O_2 and air, with the formation of single Cu_2O phase and duplex Cu_2O / CuO phases, respectively. However, the authors suggested the model, proposing that not only charged species $V_{Cu}^{\bullet}$ but also neutral species $V_{Cu}^{\times}$ could participate to the diffusion.

Even though most of the authors observed a copper oxidation kinetics following the parabolic law, a large dispersion is reported for the calculated kinetic constant values. Park and Natesan [10] and Zhu *et al.* [24] showed that this dispersion is due to different sample purities. They also showed that the grain boundaries don't contribute significantly to the oxidation process, in good agreement with the Wagner's theory.

2.2.2. Copper oxidation kinetics at low temperature (<600°C)

The wagner's theory is based on thermal activation and this model fails at low temperatures (< 600°C). Various other models have then been proposed. Most of them are based on the Cabrera-Mott theory which considers first the rapid growth of a thin oxide layer, followed by a remarkable growth slowing down [26, 27].

According to the Cabrera-Mott theory, the metal oxidation is due to an electrical field setting up through the oxide layer between the adsorbed oxygen at the surface and the metal and induces the diffusion of ions. For very thin films (< 5-10 nm), the field is very strong and enables the copper cations Cu^{+} to move through the oxide layer to the reaction zone at the oxide-air interface [26]. The oxidation rate is observed to follow the inverse logarithmic law.

For larger oxide thickness (> 10 nm), the effect of the electrical field is small and the diffusion of cations through the oxide film is limited. This leads to an oxidation rate following a cubic law.

Regarding copper oxidation, the Cabrera-Mott theory predicts that the growth of the cuprous oxide layer growth follows an inverse logarithmic law up to 7.3 nm and then a cubic law up to 1.5 µm for T< 50°C [26]. These predictions describe well the experimental results from Rhodin, except the fact that the logarithmic law was observed up to 5 nm [28]. By contrast Raugh *et al.* [29] and Derin *et al.* [30] observed that the copper oxide growth follows a linear oxidation kinetic.

2.2.2.1. Linear kinetic law

The linear rate law was first suggested by Evans in 1947 for defect oxide films [31]. In the case of copper oxidation, Bouillon *et al* [32] evidenced this linear oxidation kinetic for a single crystal oxidized during 1 h under oxygen ($P(O_2)$ = 1 atm) and T < 225°C. Note that these authors took care of reducing the crystal before oxidation to describe the whole oxidation process. Even though the substrate has a (111) orientation, the oxide grows without any particular crystalline orientation. The possible formation of CuO on this Cu_2O layer follows the initial non-specific orientation, then a reorganization forces the grain to adopt a

specific direction while it continues its growth [32]. O'Reilly *et al* also observed this linear oxidation rate at a temperature of about 150°C for sputtered copper films (500 nm thick) and electroless films (80 nm thick) under dry air at atmospheric pressure for less than 2 h of oxidation. It can be noted that they measured the native Cu_2O oxide layer which was only 2 - 5 nm thick before the oxidation starts [33]. More recently, this linear law was also observed by Gao *et al*. in 2001 [34] for a film (500 nm thick) sputtered onto a $Si/SiO_2/TaN$ multilayer structure.

2.2.2.2. Logarithmic kinetic law

The logarithmic law describes an adsorption limited process (oxygen adsorption in the case of copper) and takes into account the steric hindrance of adsorbed molecules. It was first proposed by Cabrera and Mott [26] for copper oxide thicknesses below 7.6 nm grown on an evaporated copper film ($P(O_2) = 1 - 3 .10^{-3}$ atm, T < 140°C).

The logarithmic law was also found to well describe the oxidation kinetics for bulk copper and films by Iijima *et al.* [35] at room temperature and long time (up to 800 h). Boggio *et al* [36] showed that the oxidation rate of copper single crystal also follows the logarithmic law during the first hour of oxidation ($P= 10^{-2}$-1 atm, T = 20-180°C). Rhodin [28] also confirmed this kinetic law with copper crystal platelets (0.254 mm of mean diameter) for the first hour of oxidation ($P=10^{-6} - 10^{-1}$ atm, T < 80°C).

2.2.2.3. Inverse logarithmic kinetic law

The inverse logarithmic law is expected for various limiting phenomena, such as ion transport under an electrical field, chemisorption of a molecule, or even pores formation inside an oxide layer.

This law was observed by O'Reilly *et al* [33] for sputtered copper films (500 nm) and electroless deposited films (80 nm) during the first 300 min of oxidation (air, P_{atm}, T < 150°C).

2.2.2.4. Cubic kinetic law

The cubic law is expected for cation diffusion under an electric field, and once again Cabrera and Mott were the first to observe this law for the formation of a Cu_2O film of thickness varying between 7.3 nm and 1.5 µm.

O'Reilly *et al* [33] observed this cubic law for T > 250°C on the previously described sputtered copper films. The cubic law for the growth of Cu_2O was observed together with CuO formation. Fujita *et al* [27] underlined poor characterizations of the surface state (in terms of native oxidation and morphology) in previous studies. In order to get more reliable results they studied the oxidation of a copper single crystal after reducing it, and evidenced a cubic oxidation law for thickness ranging from 5 to 25 nm.

2.2.2.5. Parabolic kinetic law

The parabolic oxidation law corresponds to a process limited by the diffusion through the oxide layer volume and through the grain boundaries. This kinetic law was observed by Fujita *et al* [27] for a single crystal in orientation (111) even for time as short as 20 min (air, P_{atm}, T>140°C). Cabrera and Mott [26] suggested that copper oxide films above 1.5 µm are growing according to this parabolic law. Both Gao *et al.* for thin film [34] and Bouillon *et al.* for a single crystal [32] confirmed this kinetic, for temperatures higher than 275 °C and 317°C respectively.

2.3. Influence of experimental parameters on oxidation kinetics

As previously described, the oxidation limiting process depends on various parameters, but we will focus on the influence of the crystalline orientation, the temperature and the oxygen partial pressure, since these parameters are the most commonly tuned.

2.3.1. Influence of the crystalline orientation

Copper single crystals are interesting samples to study the initial oxide growth. Studies of the early stage of oxidation on different faces of Cu single crystal evidence the variation of the kinetics with the crystalline orientation.

Homma correlated the faster oxidation of the Cu (111) face to the easy diffusion of V_{Cu} through the oxide layer [37]. Young *et al.* compared the oxide growth on copper single crystal with (100), (111), (110) and (311) orientation. Under the same condition the thicker film is obtained for the (100) face and then Cu (111). The faces Cu (110) and (311) are giving similar results. The (100) face has four energetically equivalent orientation where the (111) has only one. The nuclei formation is very easy, the activation barrier is the lowest. The numerous oxide grain boundaries are enabling a faster oxide growth on this direction. The slow oxidizing (110) and (311) faces have a unidirectional oxide growth with a small amount of oxide grain boundaries. These microstructural difference may partially account for the large rate difference for all faces [38]. The kinetic of growth at 178°C for different crystalline orientations are compared in Figure I-14.

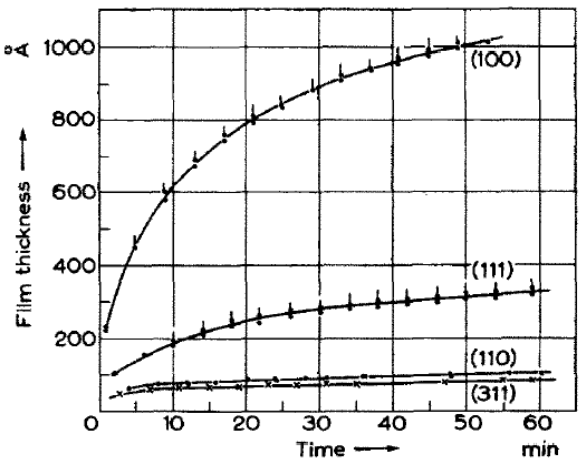

Figure I-14: Cu_2O growth on Cu single crystal faces (100), (111), (110) and (311) with time under air heated at 178°C from [39]

2.3.2. Influence of the temperature

Most of the studies are focusing at temperatures above 600°C, where the oxide growth follows the parabolic law, due to a diffusion limited process. The oxidation is a thermally activated process, with K_{11} the oxidation constant following Arrhenius law. However, a large dispersion for the values of the kinetic constant is reported according to the authors [10, 41-43]. That fact can be explained by the nature of the process, i.e. the diffusion is mostly supported by grain boundaries or by bulk diffusion of Cu^{+}. In the case of duplex Cu_2O / CuO structure, the diffusion can be limited only by CuO or Cu_2O , or by both oxide layer. Park and Natesan [10] and by Zhu and Isshiki [43] showed that the dispersion in the values of the activation energy arise from the sample purity.

2.3.3. Influence of oxygen partial pressure

During the initial oxidation stage, where the oxygen adsorption is the limiting phenomenon, the oxide growth kinetic is strongly dependent on the oxygen partial pressure $P(O_2)$ [44]. For low oxygen pressure, Wagner [23] reported that the growth is proportional to $P(O_2)^{1/7}$ when $P_{O_2} < 10^{-2}$ atm and T > 900°C. Hausgrud and Kofstad [40] observed the same evolution for P_{O_2} varying in the (10^{-4} - 10^{-2} atm) range. Mansour *et al* [45] reported that the oxide growth rate for copper nanoparticles (mean diameter of 122 nm) is limited by the adsorption of oxygen at the surface of the oxide for P_{O_2} under 10^{-1} atm.

For high oxygen pressure and when the diffusion is the limiting process, the growth is proportional to $P(O_2)^{1/4}$ [40]. Roy *et al* [42] also observed the good agreement ($\propto P(O_2)^{1/4}$) for $P(O_2)$ in the range (10^{-3} - 10^{-1} atm) and temperatures between 110 and 125°C. The kinetic difference between lower and higher oxygen pressures is explained by a change of carriers: V_{Cu^+} for low P_{O_2} and V_{Cu} for P_{O_2} in the [10^{-2} - 1] atm range [40].

For duplex Cu_2O / CuO structure, the thermodynamic equilibrium at Cu_2O / CuO rules the Cu_2O growth. No matter the external $P(O_2)$ the local $P(O_2)$ at Cu_2O interface is fixed by the thermodynamic equilibrium.

To summarize, different oxidation kinetic laws are observed for similar ranges of oxide thickness / temperature as shown in Figure I-15. These variations can be explained by a deviation from the Cabrera-Mott theory which assumes the formation of a uniform oxide film at the metal surface. Also the crystalline orientation, the microstructure, the impurities greatly influence the oxidation mechanisms [46].

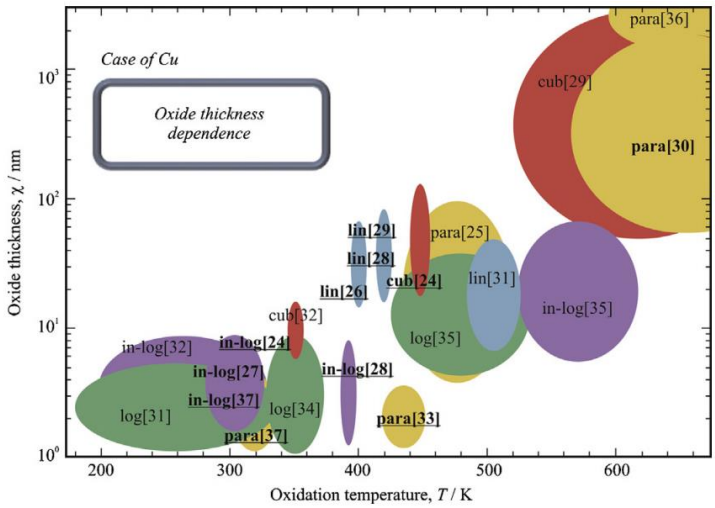

In Fig.:	Ref.
24	[39]
25	[47]
26	[29]
27	[48]
28	[30]
29	[33]
30	[49]
31	[34]
32	[28]
33	[50]
34	[51]
35	[52]
36	[43]
37	[53]

Figure I-15: Experimental kinetic laws reported by different authors, as a function of temperature and oxide thickness (from [27]). "lin," "para," "cub," "log," and "in-log" indicate linear law, parabolic law, cubic law, logarithmic law, and inverse-logarithmic law, respectively. Underlined results use ellipsometry as characterization technic, others method often consider the sample weight gain.

The different rate laws previously reported for Cu oxidation are reported in Table I-4:

Kinetic law	Equation
Linear	$x = K_1 t + K_2$
Logarithmic	$x = K_3 \log(K_4 t + K_5)$
Invers logarithmic	$\frac{1}{x} = K_6\, log(K_7 t + K_8)$
Cubic	$x^3 = K_9 t + K_{10}$
Parabolic	$x^2 = K_{11} t + K_{12}$

Table I-4: Oxidation kinetic laws

This short review on copper oxidation at low temperature shows that it is very difficult to predict the kinetic law, due to the influence of various parameters such as the oxidizing conditions (pressure, temperature, environment), the crystalline orientation, the microstructure (grain size), the initial surface state (roughness), the impurities. Moreover, especially at low temperature, this prediction is made more complicated due to the difficulty to measure precisely the thickness of ultrathin oxide films as will be discussed in chapters II and III.

2.4. Cuprous oxide film growth

Even if there is no consensus on the kinetic of oxidation at low temperature, at least the oxidation mechanism leading to Cu_2O formation is understood and accepted.

The oxidation of a metallic copper surface occurs in two steps: nucleation and growth. The generally accepted reaction sequence starts by the oxygen chemisorption, followed by nucleation of Cu_2O and then oxide growth and coalescence [17] (Figure I-16). During the first step, the oxygen from the environment is chemisorbed before diffusing through the

copper lattice. In a second step the nucleation proceeds through the formation of Cu_2O nano-islands. Nucleation occurs preferentially at the vicinity of dislocations and grain boundaries where the nucleation energy is lower. In the third step a continuous oxide layer is formed through growth and coalescence of the Cu_2O nano-islands.

The different steps of Cu_2O formation on the metallic surface is sketched, Figure I-16:

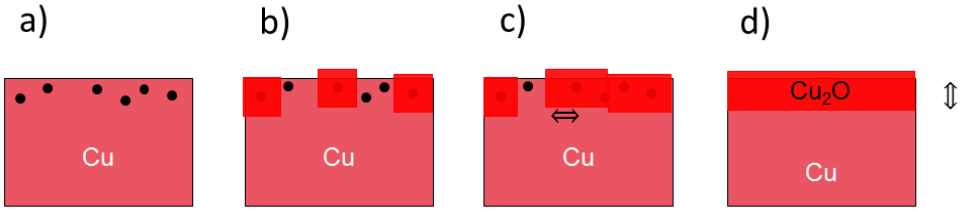

Figure I-16: Sketch of the nucleation of cuprous oxide: a) oxygen chemisorption b) nucleation c&d) Growth and coalescence

The Cu_2O formation is described by the following chemical reaction (4) which can be subdivided into 2 half reactions (5)(6):

$$2\,Cu + O_2 \rightarrow Cu_2O \tag{4}$$

$$Cu \rightarrow Cu^+ + e^- \tag{5}$$

$$\frac{1}{4}\,O_2 + 2e^- \rightarrow \frac{1}{2}\,O^{2-} \tag{6}$$

The diffusion of the moving species, Cu^+ and e^- occurs through the oxide grain boundaries and through the oxide bulk. This displacement is allowed by the presence of V_{Cu}, a naturally present defect, moving in the opposite direction. The activation energy for oxidation is weaker at grain boundaries due to the larger presence of defects. The dissociation of chemisorbed oxygen is very rapid at the copper surface, and combined with e^- produces oxygen ion O^{2-} [54]. The diffusion of Cu^+ is a thermally activated phenomenon assumed to follow the Arrhenius law. The generally admitted limiting oxidation process for copper is the diffusion of copper vacancies (V_{Cu}) allowing (4) the oxygen ions to recombines with Cu^+ [55].

This oxidation process is sketched in Figure I-17 with details of the species creation and recombination.

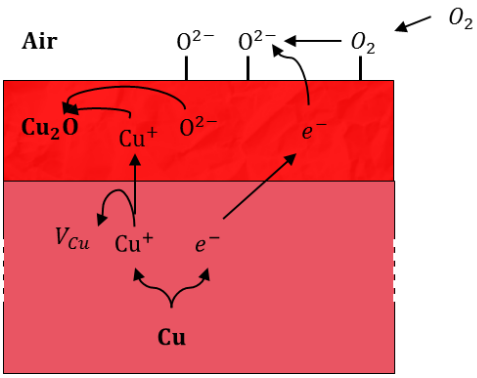

Figure I-17: Sketch of the Cu_2O oxidation process showing the creation of copper cations and copper vacancies and the oxygen dissolution

Depending on the temperature and the oxygen partial pressure, CuO may be formed at the Cu_2O surface, forming a duplex oxide structure.

2.5. Cu_2O/ CuO predominance

Figure I-18 represents the copper oxide phases formed for copper thin films as a function of the oxidation time and temperature. Most of the studies were carried out at atmospheric pressure (P_{atm}) on copper thin films [33-35, 56-58]. For comparison the results of the study of Yabuki *et al* [41] for powders particles (20 nm in mean diameter) and of Bouillon *et al* [32] for polished copper bulk surface are reported.

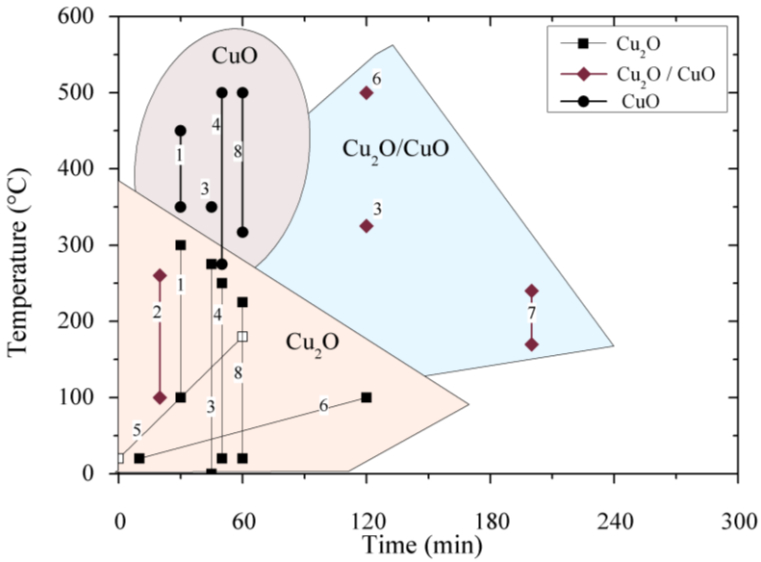

thin films:
1 [57]
2 [58]
3 [56]
4 [34]
5 [35]
6 [33]
Powder:
7 [41]
Bulk:
8 [32]

Figure I-18: Predominant oxide depending on the temperature for short oxidation time. Full symbol: P_{atm}, hollow symbol: $P<P_{atm}$

Although results somehow vary in these different studies, there is a general agreement on the dominant phase formed for short oxidation times:

- Below 200°C, Cu_2O is preferentially formed
- Above 300°C CuO formation is always observed.
- Longer oxidation times lead to a duplex oxide formation, Cu_2O / CuO

3. Generalities on light- matter interaction

3.1. Light

The current definition of light is given in classical and quantum physics. In classical physics, light is an electromagnetic wave propagating in the direction given by a wave vector $\vec{k}$. A sketch of the electromagnetic wave is given in Figure I-19, where $\vec{E}$ and $\vec{B}$ represents the electric and the magnetic field, respectively. $\vec{E}$ and $\vec{B}$ are in phase, and oscillate at the same frequency (7). They are always perpendicular to each other and both perpendicular to $\vec{k}$. The wavelength λ is defined as the spatial periodicity (Figure I-19).

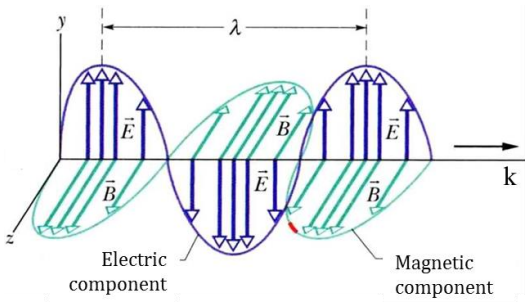

Figure I-19: Sketch of an electromagnetic wave propagating among k

$$\vec{E}(x,t) = \overrightarrow{E_0}\cos(\phi) \tag{7}$$

3.2. Light-mater interactions

In general, light propagation in a medium is described by Maxwell's equation. Reflection, absorption, and scattering are the possible interaction of an incoming light with matter, as sketched in Figure I-20. Regarding the scattering processes, light can be scattered elastically (described by Mie and Rayleigh theories), or inelastically (measured in Brillouin and Raman spectroscopies).

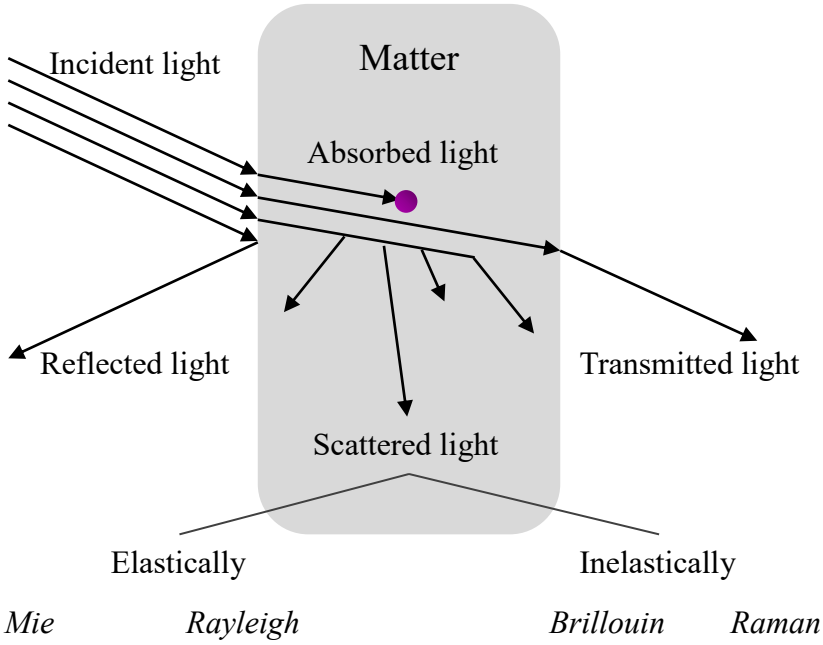

Figure I-20: Sketch of possible light interaction with a plane surface

Each class of material have specific interactions with light. For instance bulk metals are very good reflectors (> 90% of the incident light is reflected in the visible range, and the remaining part is absorbed). Glasses transmit almost all the incident light, while only a very small (<5%) part being reflected, and absorption being negligible. Semi-conductors transmit photons of energy smaller than their gap but absorb energies above.

3.1. Transmittance of a thick layer with parallel faces

Here we briefly describe the transmittance of a thick layer (much larger than the wavelength) with parallel faces, with details on the absorbed and reflected beams, scattering being neglected due to the low surface roughness.

The transmittance is defined as the ratio between the transmitted intensity I_T and the incident intensity I_0:

$$T = \frac{I_T}{I_0} \tag{8}$$

For a multilayer system transmission is limited by reflection at each interface and by absorption of each layer.

Absorption

For an absorbing medium, the absorbance, A depends on the thickness of the material and of its absorption coefficient α (related to the imaginary part of the refractive index κ, see equation (10)) as stated by Beer's law (9). Absorbance is the natural logarithm of the ratio of incident to transmitted intensity.

$$A = -\,log\frac{I}{I_0} = \exp(-\alpha \cdot x) \tag{9}$$

$$\alpha = \frac{4\pi\kappa}{\lambda} \tag{10}$$

Reflection

At the interface between two media, Maxwell equation at the limits are leading to the expression of the reflectance, the so-called Fresnel equation, defined as the ratio between the incident and the reflected intensities. The reflectance depends on the direction of the polarization with respect to the interface:

$$R_{\perp} = \frac{\tan^2(\theta_1 - \theta_2)}{\tan^2(\theta_1 + \theta_2)} \tag{11}$$

$$R_{//} = \frac{\sin^2(\theta_1 - \theta_2)}{\sin^2(\theta_1 + \theta_2)} \tag{12}$$

Where $R_{\perp}$ and $R_{//}$ refer to polarizations in the plane perpendicular to the interface (also called s-polarization) or parallel (p-polarization) to the interface, with θ_1 and θ_2 are the incident and transmitted angle, and $\tilde{n}_1$ and $\tilde{n}_2$ are the complex refractive index of two media (Figure I-21).

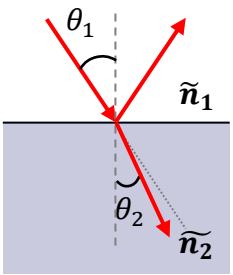

Figure I-21: Sketch of the incident and reflective angle at the interface between two media of complex refractive index $\widetilde{n_1}$ and $\widetilde{n_2}$.

For a normal incidence at the interface between a dielectric and a metal, the expression of the reflectance simplifies (13) and can be even more simplified at the interface between two dielectrics (14), where n_i is the real part and κ_i, the imaginary part of the refractive index.

$$R = \frac{(n_1 - n_2)^2 + k_1^2}{(n_1 + n_2)^2 + k_1^2} \tag{13}$$

$$R = \left(\frac{n_1 - n_2}{n_1 + n_2}\right)^2 \tag{14}$$

Therefore for an air / cuprous oxide / air system, with a strong absorption through the layer, the transmission expression is close to::

$$T \sim (1 - R_{12})(1 - R_{21}) \cdot 10^{-\alpha_2 * x} \tag{15}$$

where R_{12} and R_{21} are the reflection at air / copper and copper / air interface, respectively, α_2 the absorption coefficient of cuprous oxide, and x the layer thickness.

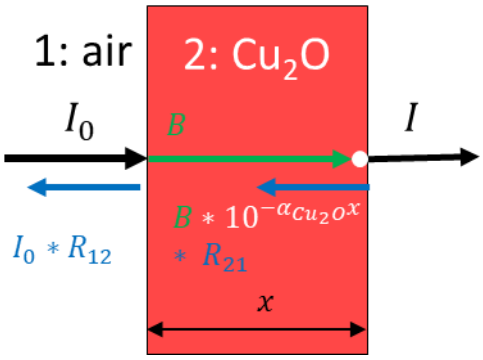

Figure I-22: Transmittance of a thick layer of a dielectric in air

4. Raman spectroscopy

4.1. Theory

This section provides the background of Raman scattering process and describe the principle of Raman spectroscopy, one of the possible process induced by an interaction of light with matter. The selection rules are recalled for first and second order Raman scattering. The Raman intensity in discussed in a semi-quantum approach, to explain the resonance phenomenon. Finally we discuss important phenomena to increase the Raman signal, Interference Enhanced Raman Scattering (IERS) and Surface Enhanced Raman Scattering (SERS).

Raman scattering was observed for the first time in 1921, by Chandrasekhara Venkata Raman, using the sun light as the excitation source and his eyes as the detector. Nowadays the instrumentation has evolved: the excitation comes from lasers, with the advantages of being monochromatic and intense, which is required to observe the Raman signals which are only ~10^{-6}-10^{-7} of the incoming signal [59, 60].

4.2. Scattering in a wave perspective

This section was written with the help of [61]. The electron displacement under the electric field is small, $\tilde{\alpha}$ can be developed using Taylor's expansion at first order as:

$$\tilde{\alpha} = \tilde{\alpha}_i + \frac{\partial \tilde{\alpha}}{\partial Q_m} \tag{16}$$

- Q_m is a normal coordinate

For an electric field oscillating periodically with time:

$$\vec{E} = \vec{E_\iota} \cos(\omega_i\, t) \tag{17}$$

The equation of a quantum vibration motion gives:

$$Q_m = (Q_m)_i \cos(\omega_m t + \varphi_m) \tag{18}$$

The induced polarization can be written for a first order Raman scattering process as:

$$\vec{P} = \alpha_i \vec{E_\iota} \cos(\omega_i\, t) + \alpha (Q_m)_0 \cos(\omega_m t + \varphi_m) \vec{E_\iota} \cos(\omega_i\, t) \tag{19}$$

Using the trigonometric identity:

$$\cos(a)\cos(b) = \frac{1}{2}(\cos(a+b) + \cos(a-b))$$

Equation (19) can be written as:

$$P(\omega_i) = \underbrace{\alpha_i \vec{E_\iota} \cos(\omega_i t)}_{Rayleigh} + \frac{\partial \alpha}{\partial Q} \frac{(Q_m)_0 E_i}{2} \left[\underbrace{cos\left((\omega_i - \omega_{\mathrm{ph}})t - \varphi_m\right)}_{Stokes} + \underbrace{cos\left((\omega_i + \omega_{\mathrm{ph}})t - \varphi_m\right)}_{Anti-Stokes} \right] \tag{20}$$

In this equation, the first term corresponds to the Rayleigh scattering, while the second and third terms respectively corresponds to the Stokes and anti-Stokes Raman scattering processes.

4.2.1. Scattering in a quantum perspective

The quantum perspective of the scattering process is sketched in Figure I-23 both for elastic Rayleigh scattering and the two possible Raman scattering processes, namely the Stokes and anti-Stokes processes. In the general case of non-resonant scattering, E_0 is the ground state and E_i , $E_i \pm E_{phonon}$ are intermediates virtual states. The scattered photon at $\hbar\omega_i$ corresponds to Rayleigh scattering, while $\hbar\omega_i - \hbar\omega_{\mathrm{ph}}$ and $\hbar\omega_i + \hbar\omega_{\mathrm{ph}}$ correspond to a phonon creation and annihilation (with Ω the phonon frequency), respectively.

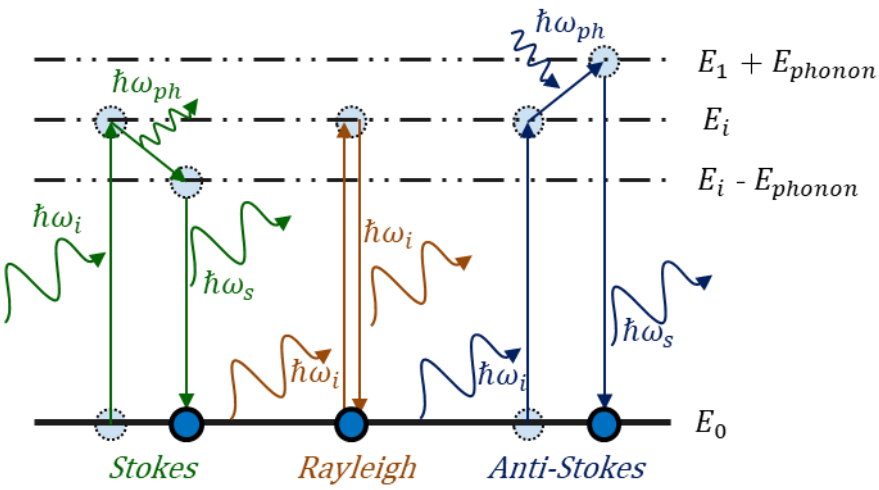

Figure I-23: Quantum description of the Rayleigh, Raman Stokes and anti-Stokes scattering process ω_q the eigenfrequency of the phonon

Note that in the case of resonant Raman scattering the intermediate states are not virtual but real, as will be discussed below.

4.2.2. Selection rule for first and second order Raman

For any scattering process, both the energy and the momentum must be conserved. For first order Raman scattering, these selection rules express:

$$\hbar\omega_i = \hbar\omega_s + \hbar\omega_{\mathrm{ph}} \tag{21}$$

$$\vec{k_i} = \vec{k_s} \pm \vec{q} \tag{22}$$

Raman excitations are in the visible-near infrared domain. The wavevector of the incident wave is $\vec{k}_i = \frac{2\pi}{\lambda}$ and the phonon wavevector in the first Brillouin zone lies in the range $0 \leq \vec{q} \leq \frac{2\pi}{a}$. Since $\lambda \gg a$, only the phonons at the center zone satisfy equation (22).

On the other hand, second order Raman scattering process involve two phonons, or one phonon together with an elastic scattering process involving a defect. In this case, non-center-of-zone phonons Raman modes can be activated.

On the other hand, Raman process have to fulfill selection rules related to molecular/crystal symmetry. The point group symmetry is defined by all the invariant possible point operations (translation, rotation, inversion, reflection). The Raman active modes are given in the point group tables [59, 60].

4.3. Raman intensities

In this part we discuss the Raman intensities. We first define the Raman cross section, and then discuss the influence of other parameters on the Raman intensity.

4.3.1. General equation

The Raman intensity is given by the general equation:

$$I_s(\vec{q},\omega,R) = K(\omega) * \frac{dR_s}{d\omega_{\mathrm{ph}}} \tag{23}$$

- K is a constant depending on the Raman set-up: the lenses, the gratings, the slits, the objectives
- $\frac{dR_S}{d\omega_{\mathrm{ph}}}$ the scattering Raman cross section of the active mode

For an active mode, the equation for Raman scattering cross-section is [62]

$$\frac{dR_S}{d\Omega} = \frac{I_L}{\hbar\omega_L}\frac{d\sigma}{d\omega_{\mathrm{ph}}} \tag{24}$$

- $\frac{I_L}{\hbar\omega_L}$ is the flux of incident photons per unit area inside the scattering medium
- $\frac{d\sigma}{d\omega_{\mathrm{ph}}}$ the differential scattering cross section of the active mode

Equation (25) can be developed as follow [62]:

$$\frac{dR_S}{d\omega_{\mathrm{ph}}} = \frac{\omega_S^3 P_L \tilde{n}_S}{(\alpha_L+\alpha_S)\tilde{n}_L}\frac{n(\omega_{\mathrm{ph}})+1}{32\pi^2 c^4 \omega_{\mathrm{ph}}}\left|\overrightarrow{\epsilon_{\vec{S}}}\,\chi_S''\overrightarrow{\epsilon_L}\right|^2 \tag{25}$$

- ω_S and ω_L the frequencies of the incident (laser) and scatter waves
- P_L is the laser power, $\frac{P_L}{(\alpha_L+\alpha_S)}$ is appropriate for a backscattering configuration, for strongly absorbing media (α_L and α_S the absorptions)
- $\tilde{n}_S$ and $\tilde{n}_L$ are the complex refractive index
- $\overrightarrow{\epsilon_S}$ and $\overrightarrow{\epsilon_L}$ are the light polarization unit vector
- χ_S'' is the Raman susceptibility tensor
- $n(\omega_{\mathrm{ph}})$ phonon-occupation factor for the Raman mode of frequency ω_{ph} which express:

$$n(\omega_{\mathrm{ph}}) = \frac{1}{\exp\left(\frac{\hbar\omega_{\mathrm{ph}}}{k_B T}\right)-1} \tag{26}$$

$where\ k_B$ is the Boltzman constant

The phonon creation is called Stokes process, and is more likely than the anti-Stokes process (phonon annihilation). This can be explained by the population of states. At room temperature, the population of the phonons ground state is much larger than those of the excited states (26) therefore the Stokes process is much more probable and the Stokes spectra are more intense.

4.3.2. Resonance Raman scattering

Resonance Raman scattering occurs when the incident laser energy is close to the energy of an allowed optical transition. A quantum description of the first order Raman susceptibility tensor is given in [63]. $\chi_S'' \cong K_{2f,10}$ $K_{2f,10}$ is the Raman matrix element used to explain the resonance

$$K_{2f,10} = \sum_{a,b} \frac{< \omega_S, f, i|H_{eR}|0, f, b >< 0, f, b|H_{ep}|0,0, a >< 0,0, i|H_{eR}|\omega_L, 0, i >}{\underbrace{\left[\hbar\omega_L - \left(E_a^e - E_i^e\right) + i\gamma\right]}_{resonance\ on\ the\ incident\ photon} \underbrace{\left[\hbar\omega_L - \hbar\omega_{\mathrm{ph}} - \left(E_b^e - E_i^e\right) + i\gamma\right]}_{resonance\ on\ the\ scattered\ photon}} \quad (27)$$

Where $|\underbrace{\omega}_{Photon}, \underbrace{f}_{Phonon}, \underbrace{a}_{Electron}>$ denote the state with an incoming photon of energy $E_L = \hbar\omega_L$, the ground state of the phonon and the ground electronic state a, respectively.

The first Hamiltonian represents a photon ω_L, absorbed by an electron excited from an initial state E_i to a higher energy level E_a. The second Hamiltonian represents the energy loss of an electron to a phonon f ($E_{ph} = \hbar\Omega$.) The electron goes from E_a to an energy level E_b. The last Hamiltonian describes the relaxation to the initial state: the electron goes from the energy level E_b to E_i. These processes are described in the sketch in Figure I-24:

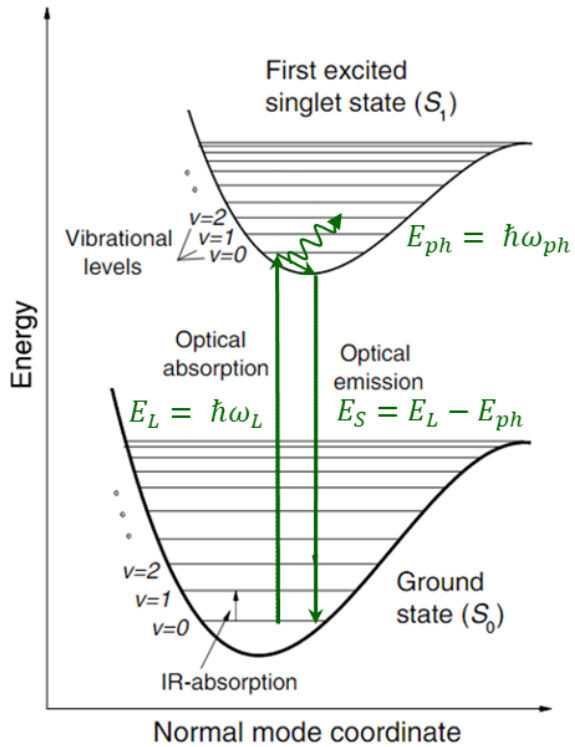

Figure I-24: Sketch of resonant Raman stokes scattering represented on the energy level of a molecule using the Jablonski diagram

The Raman intensity is given by the magnitude squared of $K_{2f,10}$, leading to strong signature enhancement when the incoming or outcoming photon energy matches an allowed optical transition. Indeed in (27) the energy match implies a denominator who approaches zero, which means an overall high ratio.

4.3.3. Vibrational properties of copper oxide

The Raman spectra of Cu_2O and CuO and the attribution of their Raman active modes are discussed below. Figure I-25 compares the experimental spectra of CuO and Cu_2O [64].

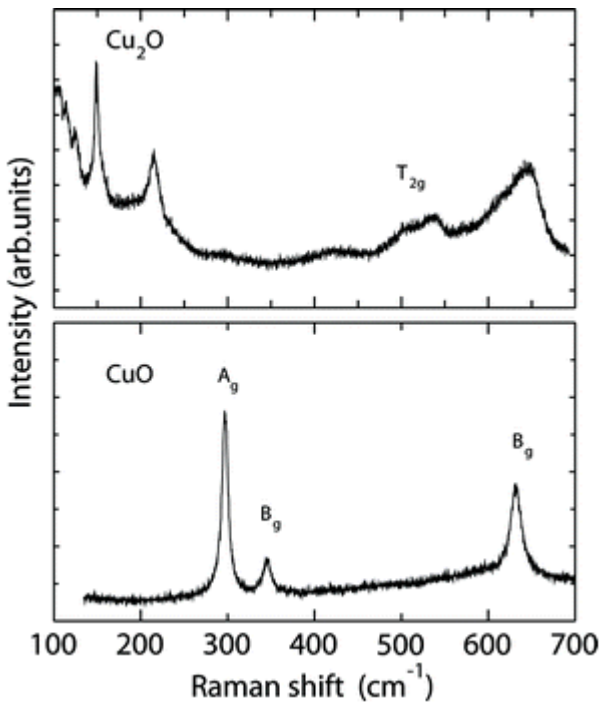

Figure I-25: Experimental Raman spectra of Cu_2O (top) and CuO (bottom) measured at 514 nm, with a power low enough to avoid heating of sample, with the attributed Raman actives modes (adapted from Debbichi et al [64])

4.3.3.1. CuO

For CuO, there are 6 atoms in the unit cell, and therefore 12 phonon branches (see the dispersion curves in the 1st Brillouin zone in the Figure I-26) of symmetry in the center zone [56, 64-65]:

$$\Gamma = 4\,A_u \oplus 5\,B_u \oplus A_g \oplus 2\,B_g$$

A representation in the 1st Brillouin zone with the points of high symmetry is sketched in Figure I-2. The phonon dispersion is represented in Figure I-26.

The symmetries of the 3 acoustic phonons are A_u, 2 B_u those of the 6 IR-active modes 3 A_u, 3 B_u, and those of the 3 Raman active modes A_g and 2 B_g (since CuO possesses an inversion center, the IR active modes are Raman-inactive and vice-versa). These three Raman first-order modes are observed experimentally at ~296-300 cm^{-1} (A_g) and ~346-350 with ~6Ram-638 cm^{-1}(B_g) (Figure I-25, see also [66] and [64]), and the corresponding atom motions are represented in Figure I-27.

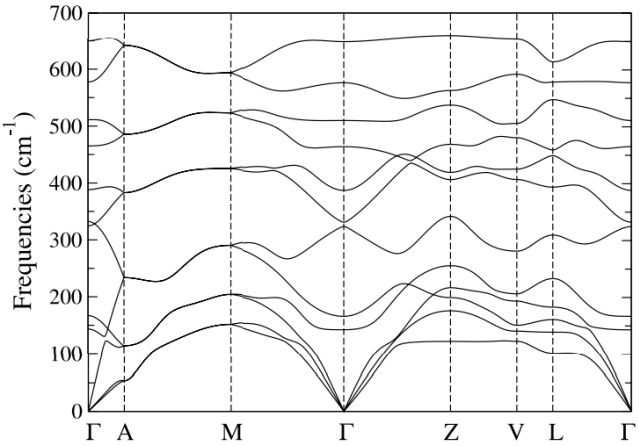

Figure I-26: Phonon dispersion curves of cupric oxide along the main symmetry directions in the 1st Brillouin zone (from [67])

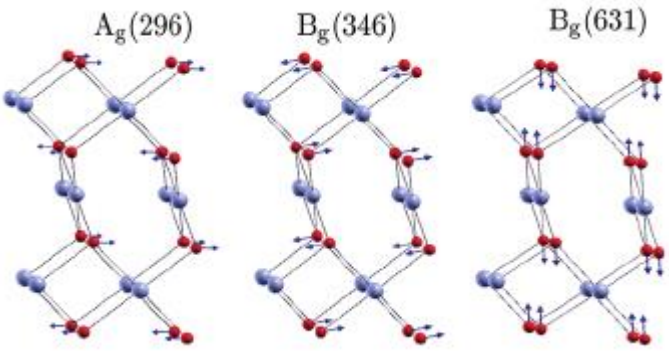

Figure I-27: Sketch of the Raman active mods of CuO, $Cu^{2+}$and O^{2-} ions are in blue and red, respectively (inspired from [64])

4.3.3.2. Cu_2O

There are 6 atoms in the unit cell of Cu_2O, and therefore 18 phonon branches [64].

$$\Gamma = A_{2u} \oplus E_u \oplus 3T_{1u} \oplus T_{2u} \oplus T_{2g}$$

where A, E, and T symmetry are one-, two-, and three-fold degenerated, respectively. The phonon dispersion curves and the corresponding density of states are shown in (Figure I-28).

The 3 acoustic modes are described by T_{1u} symmetry. Among the optical active modes, 2 IR-active modes have a T_{2u} symmetry, and the only Raman active mode is T_{2g}. The other modes are optically-silent. The symmetries and frequencies of each mode at the zone center are reported in the following Table I-5 and the modes are sketched in Figure I-29.

Symmetry	Calculated frequencies (cm^{-1}) [64, 65]	Experimental values (cm^{-1}) [64, 65]
T_{2u} / Γ_{25}^{-}	60 - 98.6	86 – 88
E_u / Γ_{12}^{-}	72 - 110	109 – 110
T_{1u} / $\Gamma_{15}^{-(1)}$	144 - 143 (TO) – 159 (LO)	146 – 153
A_{2u} / Γ_{2}^{-}	338 - 307	350
T_{2g} / Γ_{25}^{+}	503 - 549	515
T_{1u} / $\Gamma_{15}^{-(2)}$	616 - 608 (TO) – 639 (LO)	638 – 665

Table I-5: Symmetry calculated and experimental frequencies of the vibrational modes of Cu_2O at the center zone.

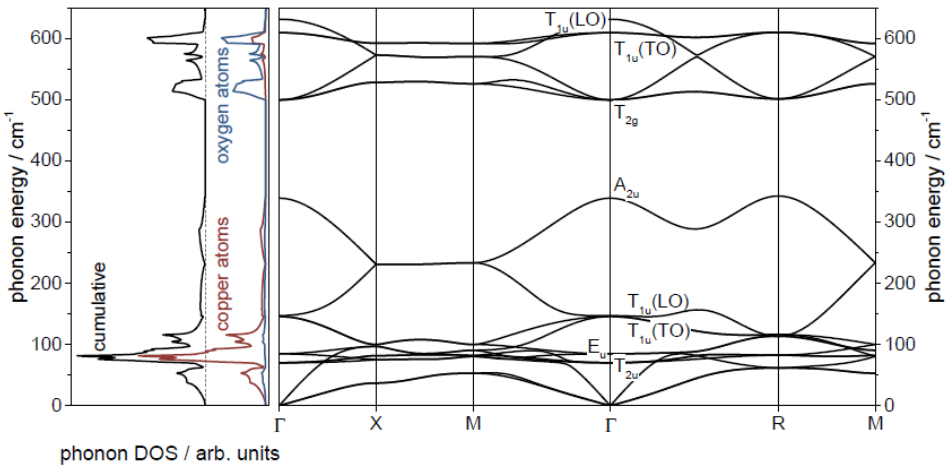

Figure I-28: Phonon density of states (DOS) and dispersion curves along the main symmetry directions in the 1st Brillouin zone for cuprous oxide from [68]. For clarity, the cumulative phonon DOS (black line) is shifted horizontally with respect to those involving copper (red line) or oxygen atoms (blue line).

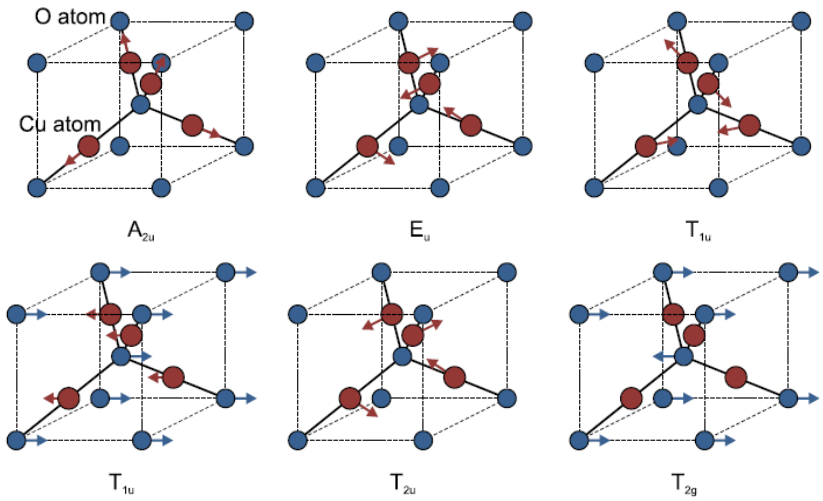

Figure I-29: Schematic representation of zone-center phonon modes in Cu_2O, (copper atoms are in red, oxygen atoms in blue) [68]

The E_u, T_{2u}, and one of the T_{1u} mode corresponds to rotations of the Cu tetrahedra around their centers. The second mode of T_{1u} symmetry corresponds to out-of-phase motions of the Cu- and O- sublattices. Phonons of A_{2u} symmetry correspond to oscillations of the copper atoms along the diagonal axes of the cubic structure, *ie* to a ‘‘breathing’’ mode of the Cu tetrahedron. Finally the only Raman-active mode, of T_{2g} symmetry, consist of the out-of-phase motion of the two oxygen sublattices with respect to each other, with the copper sublattice remaining fixed. In opposition with group theory predictions, this T_{2g} mode, at 515 cm^{-1}, is not the only Raman peak observed on the experimental spectrum (Figure I-25). Other modes are actually reported at 94, 149, 245 and 645 cm^{-1}, independently from the sample quality and preparation method, and their observation has been discussed by several groups in the past 50 years [21,69-85].

- the T_{1u} modes measured around 150 and 645 cm^{-1} correspond to phonons not at the zone center: they are activated by defects [77, 78], and resonantly enhanced by a Fröhlich interaction involving an intra-band transition and electron-phonon coupling [69-70, 77]
- the Raman peak measured around 220 cm^{-1} is the second order of the E_u mode [69, 70]
- The intensity ratio of the Raman peaks at 150 and 220 cm^{-1} was reported to be very sensitive to surface damages [78].

4.3.4. Vibrational properties of Raman probes

4.3.4.1. BPE

The Raman spectrum and the peak attribution for 2-Bis(4-pyridyl)ethylene (BPE) are presented in Figure I-30 according to the work from Kim *et al* [86]. The main bands of BPE are assigned to $\nu(C-C)$ and $\delta(C-N)$ of the pyridyl at 1200 and 1600 cm^{-1}, and to the $\nu(C=C)$ of the vinyl group about 1635 cm^{-1}. This group compared the Raman spectra of a powder to the SERS signal on flexible gold pillars with two configurations (raw substrates and pre-leaned pillars. They reported a blue-shift of the peak at 994 cm^{-1}, assigned to pyridyl ring breathing and a shift of the peak at 1596 cm^{-1} assigned to $\delta(C-N)_{py}$; $\nu(C-C)$. These blue shifts are an indication that the BPE molecule interact with gold via the pyridyl nitrogen atoms. On the other hand the band at 880 and 1635 cm^{-1} assigned to $\delta(C=C)$ and $\nu(C=C)$, respectively remain unshifted, which suggests by an absence of bond by the conjugated π electrons of the vinyl group, between the pyridine rings.

Chen *et al* [87] remarked a peak intensity variation between the bands at 1588 and 1618 cm^{-1}, respectively assigned to $\delta(C-N)_{py}$; $\nu(C-C)$ and $\nu(C=C)$.

The DFT calculation show that BPE can adsorb on metallic surface in two configurations: vertical or horizontal. The adsorption occurs either via the π electrons from the vinyl group between the pyridyl rings (horizontal bond) or the nitrogen bond (vertical bond). Both bonds are stable at low concentration, but as the BPE concentration increases, the BPE molecules in horizontal configuration reorient into the vertical configuration to accommodate additional adsorbed molecules, by making more surface available for adsorption. After reaching the full surface coverage no change is observed.

The intensity of the peak at 1618 cm^{-1} in vertical configuration is larger, and explains the higher ratio R_{BPE}= I (1618 cm^{-1}) / I(1583 cm^{-1}) around 1.2 for BPE concentration above 10^{-3} g/l (Figure I-31). A similar simulation on Ag and oxidized Ag surfaces also gives the same intensity ratio change for a BPE concentration of 10^{-3} g/l. The simulation on oxidized Ag surfaces predicts that the horizontal configuration is more stable compared to the metallic Ag surface.

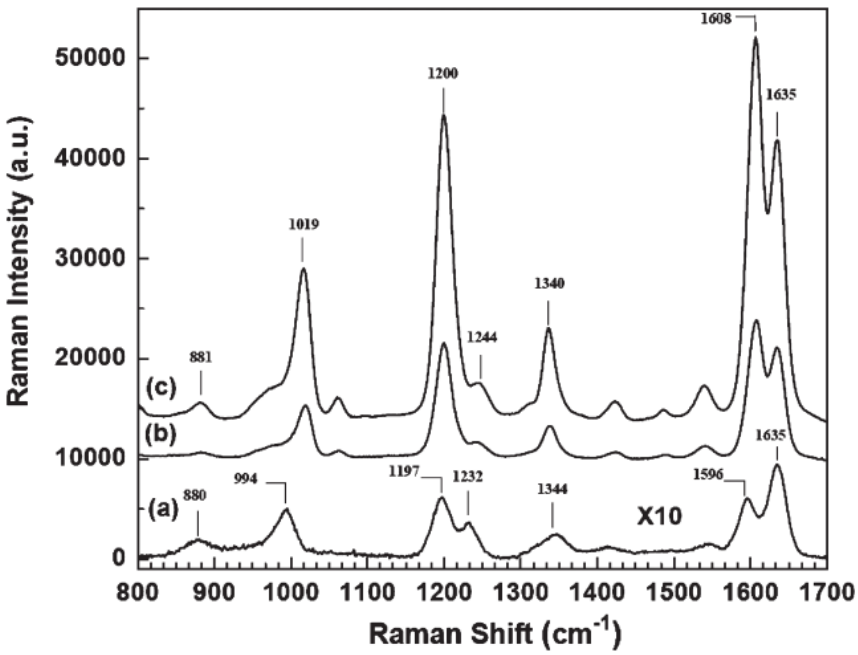

frequency (cm^{-1})			
powder	preclosed finger	BPE-trapped finger	assignments
880	881	881	δ(C=C)
994	1016	1019	ring breathing
1197	1200	1200	ν $(C-C)_{py}$, $\delta(C-N)_{py}$
1232	1246	1244	$\delta(C-H)_{py}$
1344	1339	1340	δ(C−H), δ(C=C)
1413	1422	1424	$\delta(C-H)_{py}$
1546	1542	1542	$\nu(C-C)_{py}$, $\delta(C-H)_{py}$, $\delta(C-N)_{py}$
1596	1607	1608	$\delta(C-N)_{py}$, ν $(C-C)_{py}$
1635	1635	1635	ν (C=C)

Figure I-30: Raman /SERS spectra (top) and assignments of the main peaks (bottom) for a powder BPE (a) and BPE molecule on raw (b) and pre-closed (c) pillars (from [86])

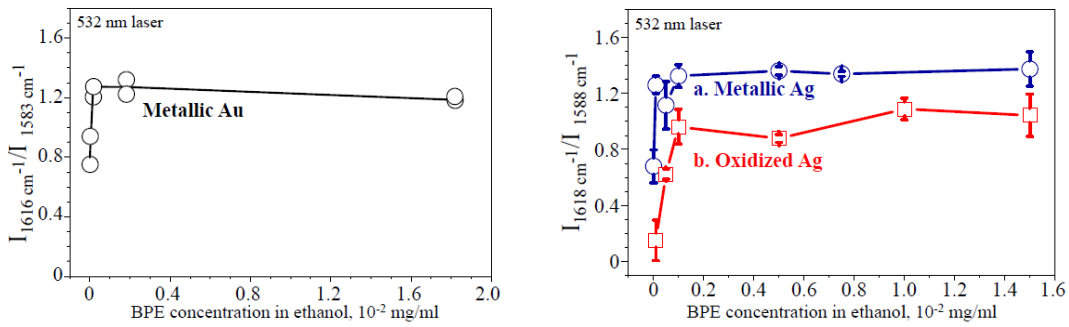

Figure I-31: Comparison of the intensity ratio between BPE bands at 1588 and 1618 cm^{-1}, for a gold (left), and silver and oxidized silver (right) surfaces, as function of the BPE concentration.

4.3.4.2. Graphene

Graphene is a two-dimensional allotrope of carbon, with atoms arranged in a sp^2-bonded hexagonal lattice. The direct and reciprocal lattices are presented in Figure I-32:

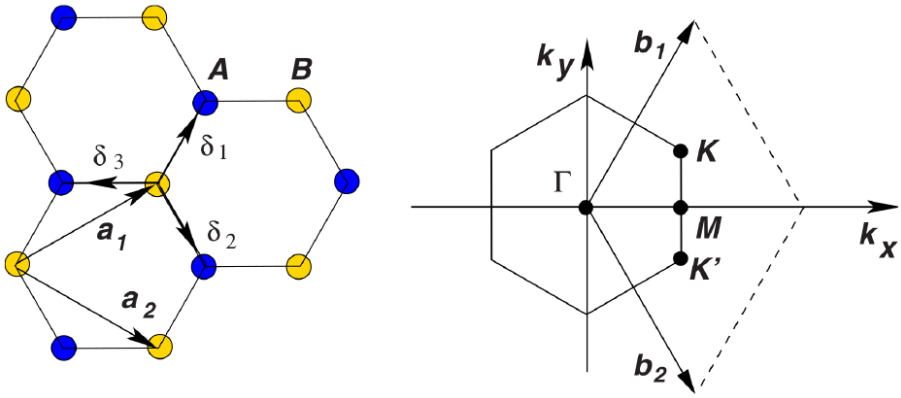

Figure I-32: Left: representation of the direct lattice of graphene, δ_i are the nearest-neighbor vectors and a_i are the lattice unit vectors. Right: representation of the reciprocal lattice,b_i are the unit vectors, K, M and K' the point of high symmetry [88]

One of the most interesting properties of graphene is the Dirac cones around K and K' points. The intensity and position of the G and 2D Raman bands are directly related to the resonant scattering pathways on these cones (Figure I-33)

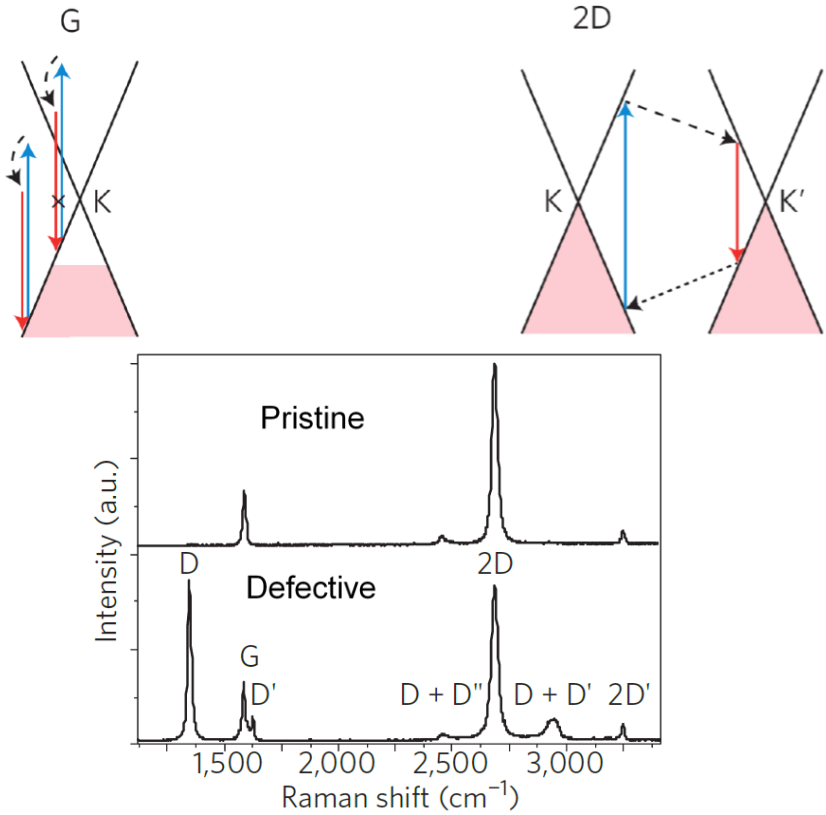

Figure I-33: Raman scattering pathways for the G mode (left) and the 2D mode (right). The top of the pink areas corresponds to the Fermi level. Raman spectrum excited at 532 nm for pristine graphene and defective graphene (bottom) [89]

Graphene is a good probe for SERS measurements on copper for several reasons. The deposition of a Single Layer Graphene (SLG) is possible even for large surfaces (~1 cm²). The Raman signal of SLG, *i.e.* the ratio of 2D and G area and the shape and width of 2D band (A_{2D}/A_G and Γ_{2D}) is informative on the number of layers for the most general case with Bernal (ABA) stacking. On the other hand, the best parameter to discriminate monolayers from multilayers is the intensity ratio of the G peak of graphene with respect to that of highly pyrolitique graphene (HOPG) A_G/A_{HOPG} [90]. The Raman characterization also gives indications on strain and doping notably with the position of 2D and G bands [89, 91-94]. Table I-6 gives the positions and width of the G and 2D band for suspended and supported graphene excited at 514.5 nm. The positions are sensitive to stress and doping [93-94]. The position of the G band is independent of the wavelength, but not for the 2D band, shifting about 110 $cm^{-1}.eV^{-1}$ [93]. According to Frank *et al*, the graphene grown on copper is under compressive stress and can be n- or p-doped (yellow square in Figure I-34).

λ = 514.5 nm	Suspended Graphene		Graphene on SiO_2	
	G	2D	G	2D
Position (cm^{-1})	1580-1582	2672-2678	1586-1593	2678-2685
FWHM (cm^{-1})	12-15	23-26	4-8	26-29
λ = 633 nm [1]	Graphene on Cu (111)		Graphene on Cu (all orientations)	
	G	2D	G	2D
Position (cm^{-1})	1591-1598	2655-2684	1584-1598	2650-2684
FWHM (cm^{-1})	7-12	20-32	7-17	17-34

Table I-6: Position and width of the G and 2D band for suspended and supported graphene measured at 514.5 nm [95] and on Cu single crystal (111) and all orientations [96]

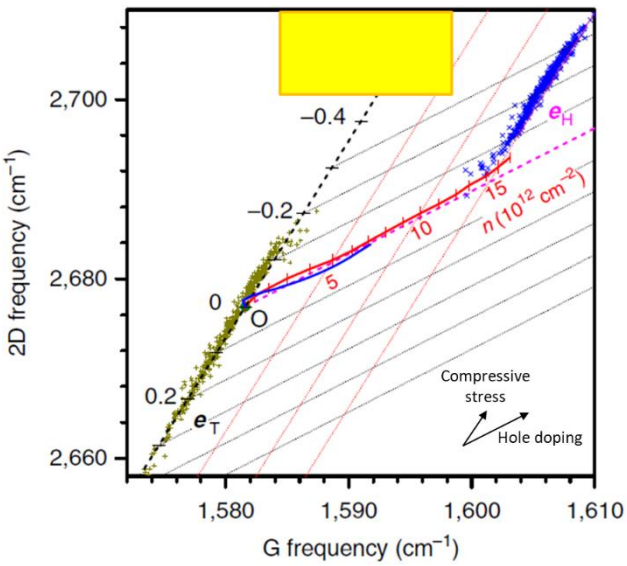

Figure I-34: Comparison of the G and 2D band position from pristine graphene and for graphene under stress and doping from [93] with the position of G and 2D on copper reported in the yellow square from [96]

[1] To compare the 2D position at 633 and 488 nm to the results at 514.5 nm, $\Delta\Gamma_{2D,633}$ = 49 cm^{-1} ; $\Delta\Gamma_{2D,488}$= -14.3 cm^{-1}

4.3.5. Interference enhanced Raman Scattering (IERS)

Interferences occur when spatial, temporal and polarization coherence exist. This means that the interfering waves should come from the same source or from a coherent source. The path length should be much smaller than the wave train (which represents a certain amount of temporal periods).

This interference phenomenon leads to a variety of signal amplification, from a maximal amplification with pure amplitude addition to destructive interferences, when the two waves are completely out of phase.

Multi-reflection of light on the interfaces of a thin homogeneous layer leads to interferences. Therefore, the Raman signal of a molecule or a crystal lying on a thin layer is modulated by these interferences, which leads to the so-called Interference Enhanced Raman Scattering (IERS) phenomenon.

The beam reflected on the top interface of a thin layer interferes with that refracted and then reflected on the bottom interface. The phase mismatch Δϕ between these two beams is directly related to the difference of path δ, *i.e*: $\delta_{54} = 2\,nd \cdot \cos\theta_r$ where n is the refractive index and θ_r the refraction angle (Figure I-35). Finally, the reflected field is expressed $E_R = E_4 + E_5$, with $\Delta\phi = \phi_5 - \phi_4 = \frac{2\pi}{\lambda_0}\delta_{54} = 2k_z d$ for a normal incidence where $\overrightarrow{k_z}$ is the wave-vector of the beam in the dielectric, so that constructive interferences are expected for $d = m\lambda_0/2n$d were m is an integer.

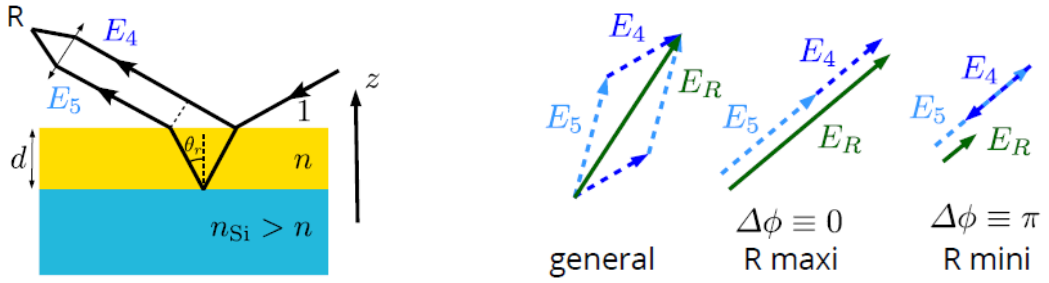

Figure I-35: Modulation by interferences of the field reflected by a dielectric thin layer (left), and details on the reflected field for the general case, and for the maxima and minima intensities (right)

In a similar way, the incident field on the top of a thin layer is modulated by interference with that refracted and then reflected on the bottom inter-face, with a difference of path of: $\delta_{10} = 2ndcos\,\theta_r$ and a corresponding difference of phase: $\phi_1 - \phi_0 = 2k_z d + \pi$, so that constructive interferences are expected for $d = [(2m-1)\lambda_0]/(4n)$ where m is an integer.

It is worth noting that the differences of phase are opposite for reflection and absorption, *i.e.* when constructive interferences occur for the reflected beam, destructive ones occur for the incident beam, and reciprocally. Furthermore, for ultrathin dielectric layers, the difference of phase is close to 0 and Pi for the reflected and incident beam at the top interface, respectively and therefore, one expects an intense reflection but a weak local field, respectively (Figure I-36).

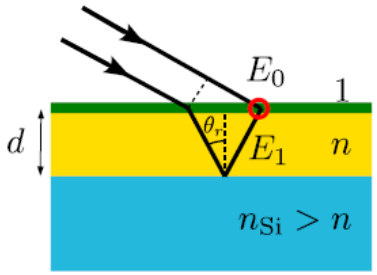

Figure I-36: Modulation by interferences of the incident field on the top of a thin layer

The effect of interferences on the Raman intensity of thin films of amorphous carbon on Si-substrate was studied by Ramsteiner in 1989 [97].They showed that the intensity of C-C peak from a-CH film deposed on a silicon substrate are oscillating with the film thickness (Figure I-37).

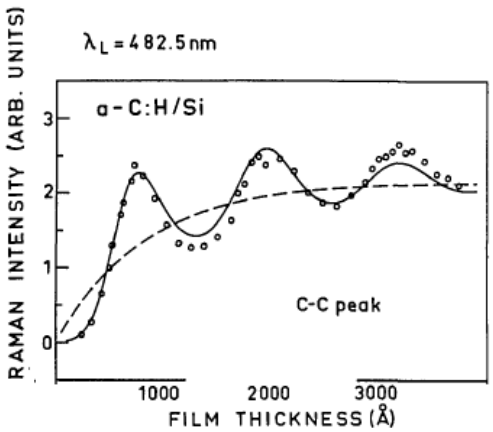

Figure I-37: Raman scattering intensities of C-C peak from a-CH film deposed on a silicon substrate versus a-CH film thickness.

The example of a single graphene layer deposited on a Si/SiO_2 substrate, which is widely used to image by optical microscopy or detect by Raman some 2D materials at the surface, is developed below in the framework of the multi-reflection model, as developed by Yoon *et al* in reference [98]. Here, the extinction of the beam going through the graphene sheet is neglected, so that the previous expression of the reflection is valid.

$$E_R = \frac{r_{12}+r_{23}e^{i\phi}}{1+r_{12}r_{23}e^{i\phi}}; \quad \text{with} \quad \phi = 2\,k_z d \tag{28}$$

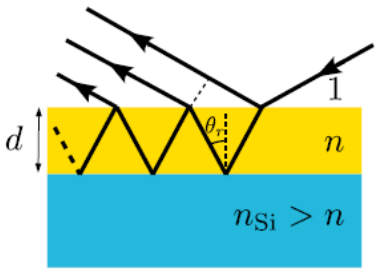

Figure I-38: Multiple refraction on a duplex system

When one considers multiple reflections, the reflected field is expressed as (28). On the other hand, the first step for Raman scattering by graphene is ab-sorption of the effective incident beam on top of the thin layer. Considering multiple reflections, the amplitude of the effective incident beam E_{ab} is the sum of the red dots in Figure I-39 and the enhancement factor is related to the absorption step:

$$F_{ab} = t_1 \frac{[1 + r_2 r_3 e^{-2i\beta_2}]e^{-i\beta_x} + [r_2 + r_3 e^{-2i\beta_2}]e^{-i(2\beta_1 - \beta_x)}}{1 + r_2 r_3 e^{-2i\beta_2} + (r_2 + r_3 e^{-2i\beta_2}) r_1 e^{-2i\beta_1}} \quad (29)$$

where $t_1 = 2n_0 / (\widetilde{n_1} + n_0)$, $r_1 = (n_0 - \widetilde{n_1}) / (n_0 + \widetilde{n_1})$, $r_2 = (\widetilde{n_1} - \widetilde{n_2}) / (\widetilde{n_1} + \widetilde{n_2})$, and $r_3 = (\widetilde{n_2} - \widetilde{n_3}) / (\widetilde{n_2} + \widetilde{n_3})$ are the Fresnel transmittance and reflection coefficients for the interfaces involving Air: 0, graphene: 1, SiO_2: 2, and Si: 3. n_0=1 is the refractive index of air, and $\widetilde{n_1}$, $\widetilde{n_2}$, and $\widetilde{n_3}$ are the refractive indices for graphene, SiO_2, and Si, respectively. $\beta_x = 2(\pi\, x\, \widetilde{n_1})/\lambda$, $\beta_1 = 2(\pi\, d_1\, \widetilde{n_1})/\lambda$, $\beta_2 = 2(\pi\, d_2\, \widetilde{n_1})/\lambda$

On the other hand, the scattering field E_{sc} is modulated by interferences as well (Figure I-39), and the corresponding enhancement factor F_{sc}:

$$F_{sc} = t_1' \frac{[1 + r_2 r_3 e^{-2i\beta_2}]e^{-i\beta_x} + [r_2 + r_3 e^{-2i\beta_2}]e^{-i(2\beta_1 - \beta_x)}}{1 + r_2 r_3 e^{-2i\beta_2} + (r_2 + r_3 e^{-2i\beta_2}) r_1 e^{-2i\beta_1}} \quad (30)$$

where $t_1' = 2\widetilde{n_1} / (\widetilde{n_1} + n_0)$

Note that the enhancement factors, as well as the positions of the maxima/minima depend on the incident angle of the beam and therefore on the numerical aperture (NA) of the objective. The expressions above rigorously correspond to NA=0. The changes are relatively small up to NA=0.5 [99] (typical of long working distance 50x objectives), but are significant for a numerical aperture NA=0.9 (typical of short working distance 50x objectives).

Finally, the total enhancement factor F is:

$$F = N \int_0^{d_1} |F_{ab} F_{sc}|^2 \, dx \quad (31)$$

The total enhancement factor for a single layer of graphene deposited on a Si/SiO_2 substrate is plotted in Figure I-39 as a function of the silica thickness in the interval (0-500) nm for a laser excitation at λ=532 nm.

The thickness of silicon dioxide leading to the largest enhancement is about 90, 270 and 450 nm in the approximation that the incident and scattered waves have the same frequency. The position of these interference maxima shift to larger thicknesses when the mode frequency increases (G band and 2D band) and the corresponding enhancement factors decrease accordingly.

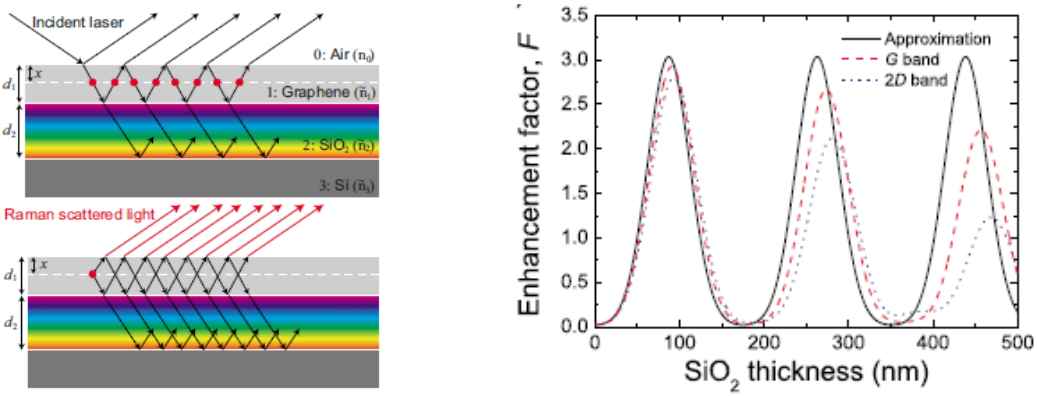

Figure I-39: Schematic diagrams of multiple reflection interference in the absorption and scattering processes (left). Calculated IERS enhancement factor as a function of the thickness of the SiO_2 layer in the approximation that the incident and scattered frequencies are the same (solid line), for the G band (dashed line) and for the 2D band (dotted line) (right).

The IERS phenomenon has been addressed recently for the Copper / Cu_2O / Graphene system [100, 101]. An IERS enhancement factor of about 10 is predicted, and supported by experimental measurements, even though no precise measurement of the thickness of the copper oxide layer was achieved in these works. Ramirez-Jimenez *et al* reported recently much larger IERS enhancements (up to 55 experimentally, and 70 theoretically) for CVD single layer graphene grown on copper after one year aging [102] They assigned this enhancement to the growth of air bubbles at the graphene/copper oxide interface, leading to an additional dielectric layer of smaller refractive index and a concomitant increase of the effective incident and scattered field on the graphene sheet (Figure I-40). They also discussed the relation between the dielectric permittivities of the layers and the IERS enhancement: the smallest the real part of the refractive index, the largest the enhancement factor, and the larger the corresponding thickness of the dielectric layer (Figure I-41). On the other hand, the IERS enhancement increases when the imaginary part of the refractive index of the metal increases.

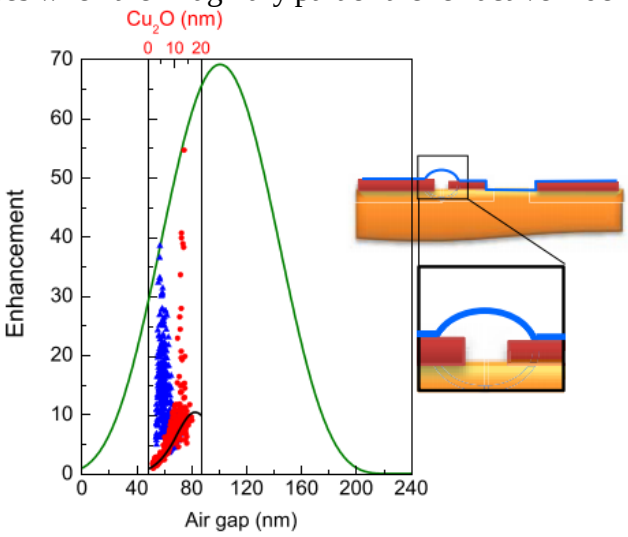

Figure I-40: Measured (symbols) IERS enhancement factor for the G peak of CVD single layer graphene grown on copper as a function of aging (red and blue symbols for 8 and 12 months, respectively) as a function of Cu_2O and air thicknesses, compared to calculations (solid lines) for graphene/Cu_2O/Cu (black line) and graphene/air/Cu (green line and corresponding sketch on the right), from [102]

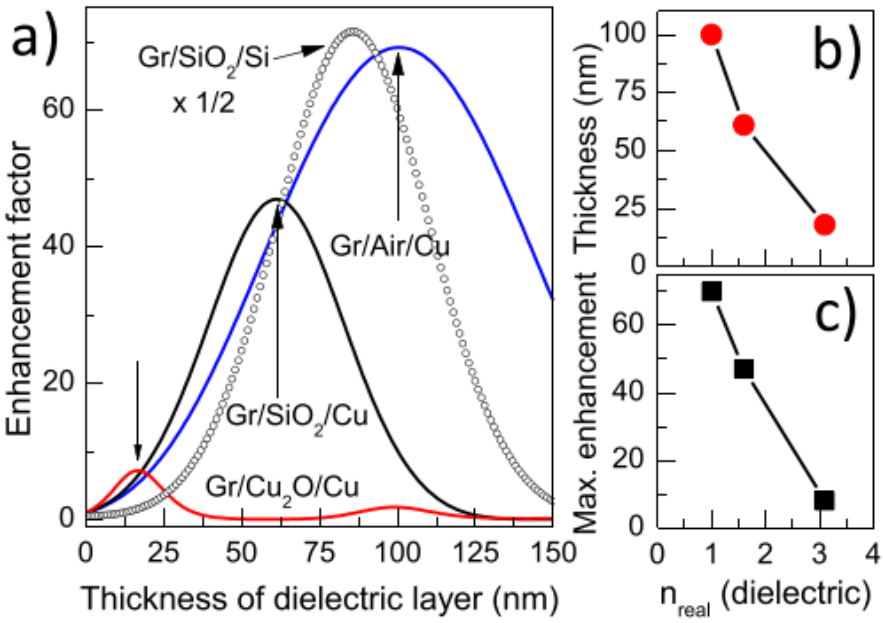

Figure I-41: Compared calculated IERS enhancement factor (for a 488 nm excitation) for the G peak for various dielectric layers in an Al/dielectric/Graphene trilayer system, as a function of the dielectric thicknesses (a) Optimal thickness of the dielectric layer (b) and corresponding maximum enhancement (c) as a function of the real part of the dielectric layer refractive index, from [102]

5. Surface enhanced Raman spectroscopy (SERS)

A way to overcome the low Raman cross-sections is to take advantage of the enhanced local fields at the surface of metallic nanostructures. Here we consider only the electromagnetic enhancement, and ignore any chemical enhancement.

This section focuses on the description of the physical mechanisms leading to SERS enhancement. First the electronic and optical properties of metals will be described in the framework of the Drude model. Metallic nanostructures present localized surface plasmon modes which can couple with electromagnetic waves and lead to huge local fields responsible of the SERS enhancement. We will discuss LSP resonance signatures measured in extinction spectroscopy, in far field. Then, we will discuss the main parameters which influence local field enhancement, namely the nature, size and shape of nanostructures, as well as gap between two nanostructures. Finally, we will review the molecular probes used in the literature to measure SERS and the literature addressing the SERS properties of copper, which has been so far only scarcely used for SERS. This part was mainly written with the help of [103].

5.1. Physical background on light – metal interactions

5.1.1. Polarizability, and relative permittivity

The polarizability $\tilde{\alpha}$ is the ability of an electron cloud to be distorted by an external electric field. It is defined as the ratio of the induced dipole moment and the incident electric field (32). The matrix description is given in (33).

$$\vec{P} = \tilde{\alpha}\vec{E} \tag{32}$$

$$\begin{bmatrix} P_x \\ P_y \\ P_z \end{bmatrix} = \begin{bmatrix} \alpha_{xx} & \alpha_{xy} & \alpha_{xz} \\ \alpha_{yx} & \alpha_{yy} & \alpha_{yz} \\ \alpha_{zx} & \alpha_{zy} & \alpha_{zz} \end{bmatrix} \cdot \begin{bmatrix} E_x \\ E_y \\ E_z \end{bmatrix} \tag{33}$$

In case of crystals, the long periodicity allowed by the crystal's invariance in some direction requires a new description. The polarizability is the product of the susceptibility, the vacuum permittivity and the electric field:

$$\vec{P} = \epsilon \cdot \chi \cdot \vec{E} \tag{34}$$

The permittivity is defined as the square of the complex dielectric function, with n the real part and κ the imaginary part of the complex refractive index, respectively (35). The permittivity is related to the susceptibility as equation (36) gives.

$$\epsilon(\omega) = \tilde{n}^2 = (n + i\,\kappa)^2 \tag{35}$$

$$\epsilon = 1 + \chi \tag{36}$$

5.1.2. Plasmon definitions

Plasmons are quantum quasi-particles associated with the elementary collective oscillations of free electrons in the metal (the plasma). A simple analogy: plasmons are to the electron plasma what photons are to the electromagnetic field.

The properties of bulk plasmons are not sensitive to the surrounding medium. However, as the characteristic size of the metal diminishes plasmons get confined to the surface and may interact strongly with some incoming light at a metal / dielectric interface.

They are two type of Surface Plasmon Polaritons (SPP) depending on the geometry of the surface. On continuous and homogeneous thin films, surface plasmons are propagating following a dispersion relation sketched in Figure I-42. Such Propagating Surface Plasmon-Polariton (PSPP) are evanescent waves of wavevector $k_x > \omega/c$ (Figure I-43) which therefore can never be in phase and couple with photons of wavevector $k = \omega/c$. Coupling can only occur in special conditions, including the case of nanostructured surfaces. When surface plasmons get spatially confined at the nanometric scale, they become radiative and can then couple with light. The coupling of a photon with a localized surface plasmon gives rise to mixed photon-plasmon modes called Localized Surface Plasmon Polaritons (LSPP). When the frequency of light gets close to that of localized surface plasmons, the resonance of LSPP gives rise to strong local electric fields which are involved in SERS.

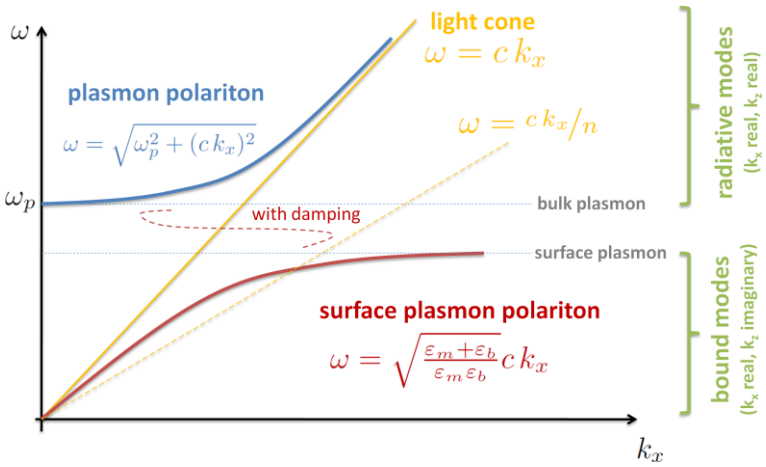

Figure I-42: Sketch of the plasmon dispersion relation at a metal interface with air.

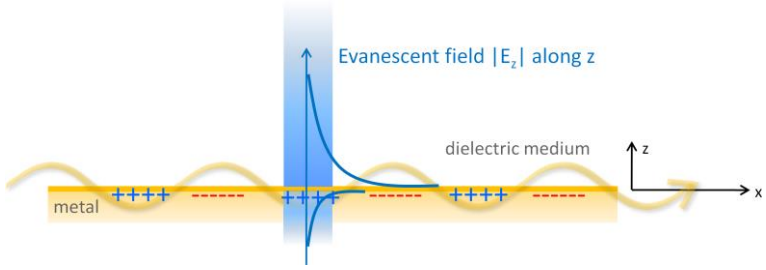

Figure I-43: An evanescent wave corresponds to a transversal magnetic-mode that propagates along the interface of a metal and a dielectric, where the z-component of the electric field decays exponentially

5.1.3. Optical properties of metals

Metals are a class of material for which conduction electrons are weakly bounded to the nuclei. Under an electromagnetic (EM) field these so-called "free electrons" can therefore easily move.

We start by considering the optical response of a dipole, formed by an electron and an ion, interacting with an EM wave. Both the electrons and ions are submitted to the Coulomb force ($\vec{F}_{coulomb} = -e\vec{E}$). But given their respective masses, one can neglect the motion of the ion, and consider only the electron motion, submitted to a local field E_{loc}. This local field is the sum of the incident field and the depolarization field created by the surrounding charges. By solving the equation of motion (37), one can define the polarizability as the factor relating the local electric field and the induced dipolar moment (38).

$$m\frac{d^2\vec{r}}{dt^2} = \sum \vec{F}_{applied} = -e\vec{E} \quad - m\,\omega_0^2\,\vec{r} \quad -\frac{m}{\tau}\frac{d\vec{r}}{dt} \tag{37}$$

The solution to this equation is:

$$\vec{r} = \frac{-e}{m\left[(\omega_0^2 - \omega^2) + i\frac{\omega}{\tau}\right]}\overrightarrow{E_0}e^{i\omega t}$$

$$\vec{P} = \frac{-n_e e^2}{m\left[(\omega_0^2 - \omega^2) + i\frac{\omega}{\tau}\right]}\overrightarrow{E_0}e^{i\omega t} \tag{38}$$

- n_e the number of electron per volume unit

The Drude model was proposed to explain the transport properties of electrons in material, applying the classical kinetic theory of gases to the conduction electrons. One way to introduce the Drude model is by using the Lorentz model for the atomic polarizability. The model describes the optical response of an electron bounded to a nucleus with a restauration force ($\vec{F}_r = -m\,\omega_0^2\,\vec{r}$) and the damping force ($\vec{F}_d = -\frac{m}{\tau}\frac{d\vec{r}}{dt}$). In a metal the conduction electrons are not bound, therefore the restoration force is considered to be zero.

Extending this approach to the macroscopic scale, one can define the relative permittivity as a key parameter to describe the optical properties of a solid. Identifying (38) with (34), the permittivity is:

$$\epsilon\,(\omega) = 1 - \frac{n\,e^2}{m\,e_0} \cdot \frac{1}{\omega^2 + i\,\gamma_0\,\omega} \tag{39}$$

- n, the number of free electrons per unit of volume
- m, the mass of electrons
- γ_0, is a damping term, which is related to the collision rate of free electrons.

In absence of perturbation the charge density is uniform. The electron cloud will oscillate around its equilibrium position at its eigen plasma frequency: ω_{plasma}, the plasma frequency defined as:

$$\omega_{plasma} = \sqrt{\frac{n\,e^2}{m\,e_0\epsilon_\infty}} \tag{40}$$

At small frequencies $\omega \ll \omega_{plasma}$

$$\epsilon\,(\omega) = \epsilon_\infty\left(1 - \frac{\omega_{plasma}^2}{\omega^2 + i\,\gamma_0\,\omega}\right) \tag{41}$$

And the separation of the real and the imaginary part of the dielectric function leads to:

$$\epsilon(\omega) = \epsilon_\infty\left(1 - \frac{{\omega_{plasma}}^2}{\omega^2 + {\gamma_0}^2}\right) + i\left(\frac{\epsilon_\infty {\omega_{plasma}}^2\,\gamma_0}{\omega\,(\omega^2 + {\gamma_0}^2)}\right) \tag{42}$$

The Drude model only considers the contribution of free electrons to the permittivity, which correspond to intra-band transitions (in the conduction band). On the other hand, at sufficiently high frequencies, some bound electrons may be excited to a higher band. The contribution of such inter-band electronic transitions to the dielectric function is taken into account by an additional term $\epsilon_b\,(\omega)$:

$$\epsilon\,(\omega) = \epsilon_b\,(\omega) + \epsilon_\infty\left(1 - \frac{\omega_{plasma}^2}{\omega^2 + i\,\gamma_0\,\omega}\right) \tag{43}$$

Inter-band transitions occur in the UV for silver (which explains its bright grey color). By contrast for gold and copper they occur in a frequency range closed to or below the plasma frequency, in the visible range.

5.2. Localized surface plasmon resonance and local fields

The physical phenomena such as localized surface plasmon-polariton resonance (LSPR) is to take the case of a spherical metal nanoparticle (NP).We first describe the polarizability and the resonance conditions, then we stress the parameters influencing the resonance and the associated local fields, namely the geometrical aspect (shape, size of the NP), the dielectric properties of the metal and the environment, and the coupling of two nanoparticles.

In the simplest case of an isolated metallic sphere of radius D and permittivity $\epsilon(\omega)$ standing in a medium of permittivity ϵ_0, the optical interactions between light and the particle are described by the Mie theory, which allows to calculate accurately the absorption, scattering and extinction cross-sections, and therefore to evidence the resonance of the LSPP. For particles with different geometries, no exact analytic solution of Maxwell equations can be derived. The electrostatic approximation (ESA, also called the quasi-static approximation [103, p. 279]) is widely used to calculate the optical responses of nanoparticles and provides good results as long as their size remains small with respect to the wavelength. The basic assumption of the ESA is that the electric field is homogeneous in any point of the particle. In particular, the ESA neglects any retardation effect and therefore any interference effect. Therefore, the ESA is strictly valid only for small particles (D $\leq \lambda/20$) but is actually widely used for larger ones, as an easy tool to capture the evolution of the optical properties for various geometries.

The local field intensity enhancement for $LFIEF(\lambda_1)$ defined as (44), by le Ru as the ratio of the local electric field and the incident electric field, squared.

$$LFIEF(\lambda_1) = \frac{|E(\lambda_1)|^2}{|E_0(\lambda_1)|^2} \tag{44}$$

5.2.1. Influence of the size and shape

First, we consider the polarizability of a sphere, considering the simple case of a spherical NP, given by Maxwell theory (45). Under an EM field, the polarized electron cloud will move periodically Figure I-44.

In the ESA [104] the phase of the wave is assumed constant through the nanoparticle. Under this approximation, the polarizability of a metallic sphere of radius R and relative permittivity ϵ_m, surrounded by a medium of permittivity ϵ_1 is expressed as:

$$\alpha = 4\,\pi\,\epsilon_0 R^3 \left(\frac{\epsilon_m - \epsilon_1}{\epsilon_m + 2\epsilon_1}\right) \tag{45}$$

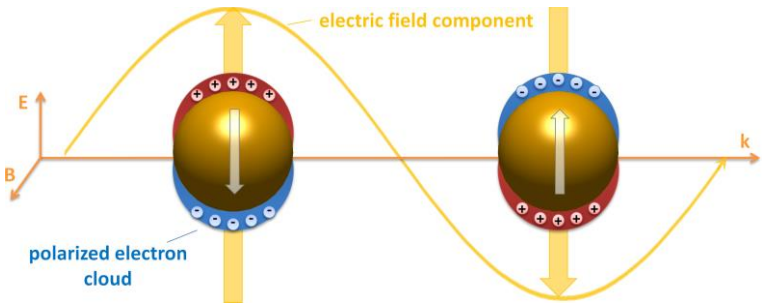

Figure I-44: Representation of the polarized electron cloud excited by an EM wave

From the polarizability is expected to be maximum for $(\epsilon_m) = -2\,\epsilon_1$, which is referred as the Fröhlich condition. Resonance is achieved when the frequency of the incident EM wave matches the eigen frequency of the LSP, *ie* when the Fröhlich condition is fulfilled.

This following paragraphs are stressing the influence of the size and the shape from a far field point of view, *i.e.* on the absorption and scattering cross-sections and related LSPP resonance.

Scattering cross section C_{sca}, is calculated as a difference between the extinction cross section (C_{ext}) is the sum of the absorption C_{abs} and scattering cross-sections.

$$C_{ext} = \frac{4\pi k}{|E_o|^2} \sum_i \Im(E_{0,i}^* \cdot P_i) \tag{46}$$

$$C_{abs} = \frac{4\pi k}{|E_o|^2} \sum_i \{\Im[P_i \cdot (\alpha_i^{-1})^* * P_i^*] \cdot P_i^*\} \tag{47}$$

$$C_{sca} = C_{ext} - C_{abs} \tag{48}$$

The resonance frequency depends on the size and shape of the particles. Figure I-45 gives the scattering cross section calculated in the ESA (more details on the calculation are given in [105]), as shown in Figure I-45. The maxima for a gold particle in air is given for an excitation in the red, for particles with a diameter of 80-100 nm. The aspect ratio giving the highest scattering cross section is L=0.3-0.5.

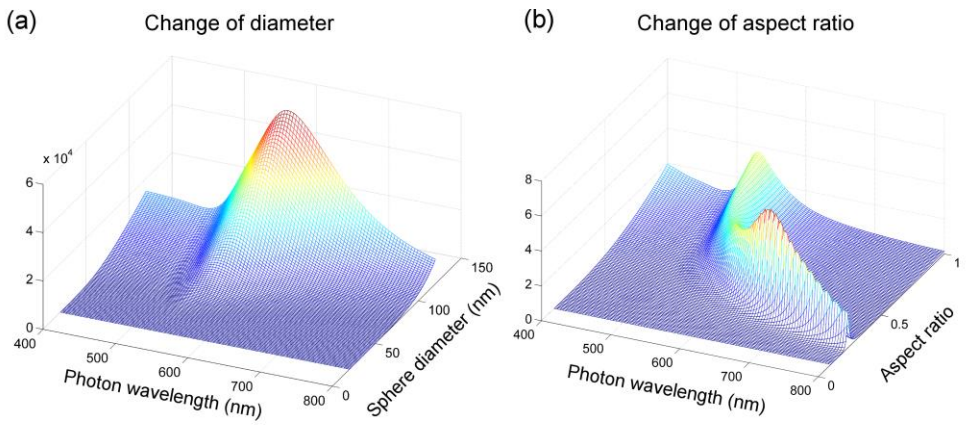

Figure I-45: Scattering cross section for varying diameter of a gold nanosphere (a) or by tuning its aspect ratio (b) [105]

The best size for the SERS platform, leading to the higher SERS cross section, can be determined for a given metal in a fixed medium. Pointed shapes should be preferred, since they lead to the larger local field enhancements.

Now we focus on the influence of the dielectric background. For a gold nanorod of fixed size and aspect ratio, the resonant scattering cross section vary as a function of the dielectric constant of the environment, as shown in Figure I-46.

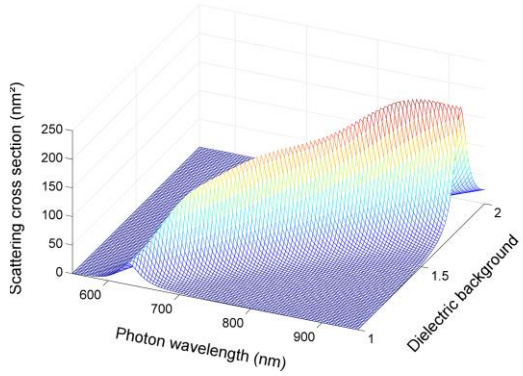

Figure I-46: Scattering cross section of a gold nanorod with diameter 10 nm and an arm length of 35 nm. The dielectric constant ϵ of the embedding medium varies from 1.0 to 2.0 [105]

The expression of the polarizability depends on the shape of the nanoparticle. For an ellipsoid, the polarizability along the $i^{th} - axis$ is expressed as:

$$\alpha = \frac{V}{L_i}\,\epsilon_0 \left(\frac{1 - \epsilon_m}{\left(\frac{1}{L_i} - 1\right) + \epsilon_m} \right) \tag{49}$$

- V: the volume of the elliptical particle $V = \frac{4}{3}\pi abc$, with a, b, c the elliptical radii of the ellipsoid, and L_i the geometrical factor related to the shape of the particle: $L_i = \left(1 + \frac{a}{b}\right)^{-1.6}$

Remark that equation (45) for a sphere can be recovered from (49), with $L_i = \frac{1}{3}$

An example illustrating all the parameters influencing the LSPP resonance and related local field enhancement maximum scattering cross-section (size, shape, permittivity of particle and surrounding medium) is given Figure I-47.

The resonance wavelength is found to redshift for increasing aspect ratio, and the maximum enhancement at resonance is found to increase accordingly.

Like Raman cross section the SERS cross section will also depend of the excitation wavelength the refractive index of the environment and the vibrational mode considered.

On the other hand, the nature of the metal has only a little influence with small blue shift from Au to Ag, but the change of dielectric medium leads to a much larger blue when Au NP are dispersed air rather than in water.

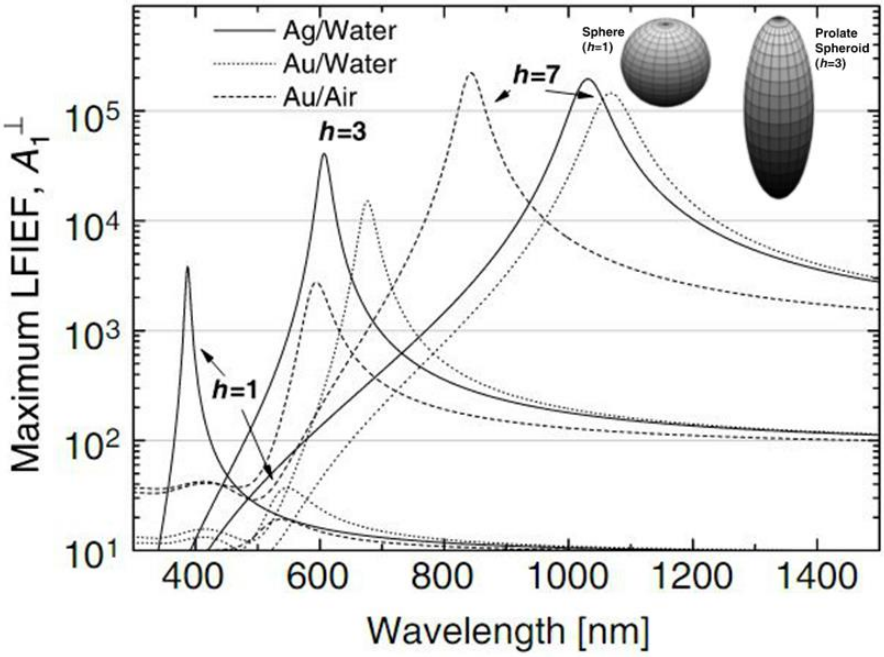

Figure I-47: Local field enhancement for $LFIEF, A_1^{\perp}(\lambda_1)$ defined in (44) and L_i the geometric factor characterizing the curvature of the ellipsoid along $i - axis$. $LFIEF, A_1^{\perp}(\lambda_1)$ is given for a prolate spheroid, sketch with an aspect ratio of 3. Straight lines are for Ag NP in water, dotted line for Au in water and the dashed lines are for Au in air, in the extended visible range [103, pp. 326-351]

5.2.2. Coupling of nanoparticles

The last parameter discussed in the following paragraph is the coupling of two metal NP. Figure I-48 shows the evolution of the calculated enhancement factors (50) [103, pp. 274-275] for gold dimers formed of two spherical NP (ϕ= 25 nm) in water, as a function of the inter particle distance. Decreasing this distance leads to an amplification of the local field, and to a concomitant red shift of the resonance. From Figure I-49, the quality factor is good (higher than 2) for wavelength above 600 nm. This explains the damping of the enhanced field, depicted Figure I-48 for the larger gaps, which are blue-shifted below 600 nm.

$$F_{E4}^{0} = M_{Loc}(\omega_L, \vec{r})^2 = \frac{|E_{Loc}\,(\omega_L, \vec{r})|}{|E_{Inc}|^2} \tag{50}$$

We can also remark that all considered gaps (1-20 nm) between the NP are leading to a higher enhancement than that of a single sphere.

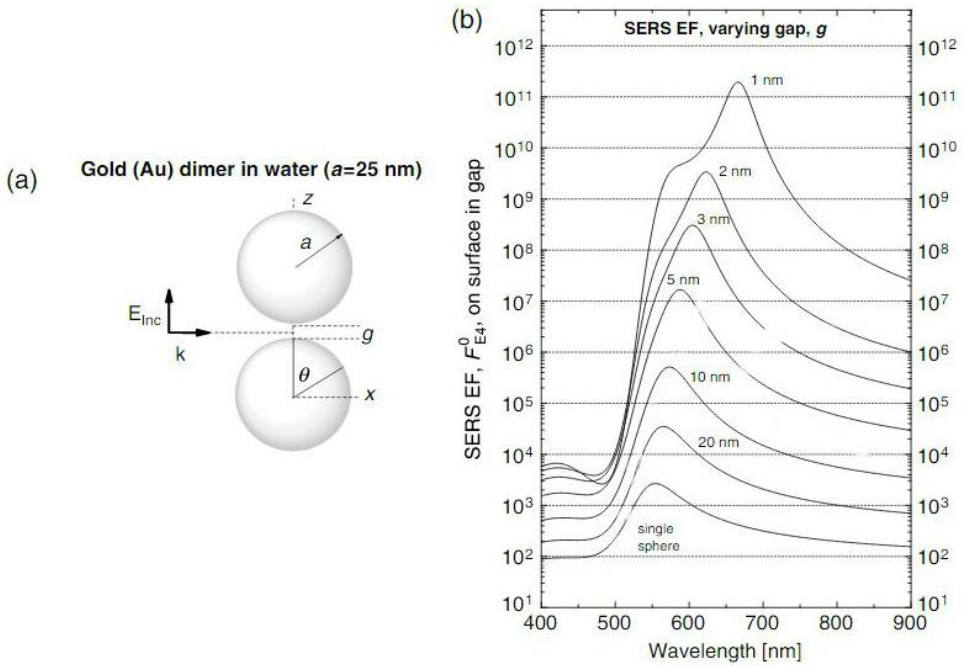

Figure I-48: Local field enhancement of a gold dimer in water from [103, p. 357]

5.3. Effective metals for SERS

The quality factor is a key parameter to evaluate if a metal can be used as an effective substrate for SERS. The higher the Q, the better the enhancement.

$$Q = \frac{\omega(dRe(\epsilon)/d\omega)}{2\left(Im(\epsilon)\right)^2} \tag{51}$$

The relative permittivities and the corresponding quality factors of different metals are compared in Figure I-49. Good quality factor (>2) are achieved for metals with a small imaginary part and a large negative real part, as expected from (51). Therefore, in the visible range, the more effective metals for SERS are Ag, Au and Cu. Pd presents a good quality factor, but the large imaginary part of its dielectric function leads to a huge absorption which hinders him to be a good SERS platform.

In summary the more promising platforms for SERS are metals with:

- a negative $Re(\epsilon)$: $-20 \leq Re(\epsilon) \leq -1$
- a small enough $Im(\epsilon)$
- a quality factor (51) larger than 2, and preferably to 10

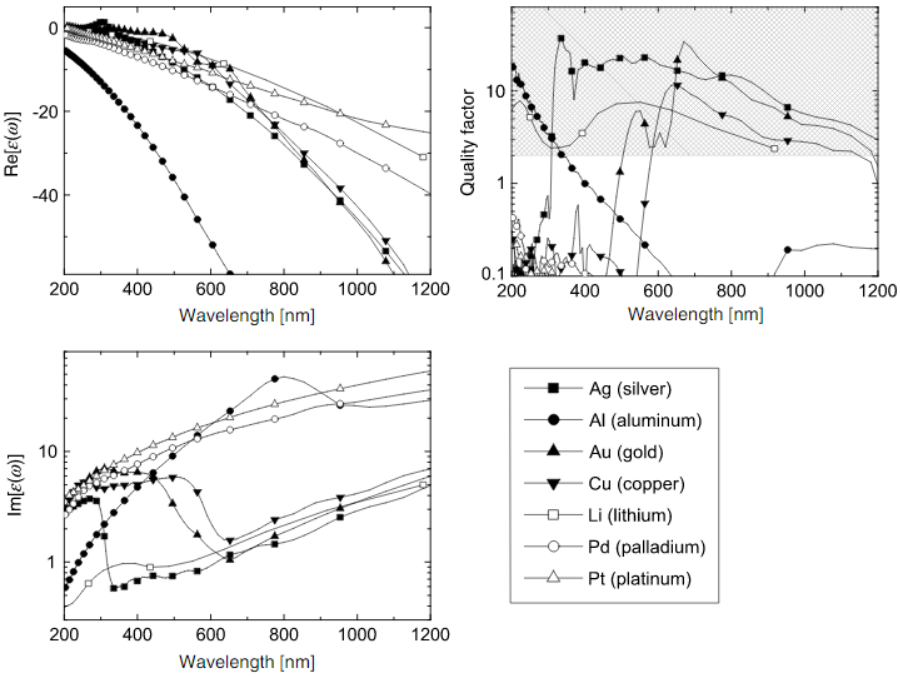

Figure I-49: Optical properties of a selection of metals in the UV-vis-NIR range. Real (top) and imaginary (bottom) parts of the relative permittivity (left). Quality factor as defined in equation (51) [103](right)

5.4. Probe for SERS

We now discuss what molecule/system can be used for probing the SERS signal at the surface of relevant nanostructured metallic platforms. An effective SERS probe should have a large Raman cross sections. This especially occurs when the laser energy matches an optical transition of the probe, *ie* when the probe is studied in Raman resonant conditions, and this leads to a so-called SERRS phenomenon, where the second R states for resonance. As recalled in section 4.3.2, resonant Raman scattering (RRS) intensities can be up to 10^6 times larger than non-resonant ones [103].

Among the variable parameters in a SERS experiment, the probe – substrate interaction is the most important one. Adsorption/stacking of the probe onto the substrate is requested to benefit from a significant enhancement. Some molecules/functional groups have a strong chemical affinity with metallic surfaces such as Au. In particular thiols groups are known to form covalent bond on gold surfaces [106]. Amino group are also known to bonds to the metallic atoms, which promote bonding partially electrostatic and partially covalent [107, 108]. Another mechanism for probe adsorption is through physical bounding, with electrostatic interactions. Another mechanism for the probe adsorption is through physical bonding, with electrostatic interactions such as π −stacking or Van der Waals [87].

Often, dyes are used as reference molecules for SERS studies, since they present both large intrinsic Raman cross sections and chemical affinities with noble metal surfaces. Among others, Rhodamine 6G (R6G) and crystal violet (CV) are widely used (see their skeleton formula in Figure I-50). 1,2-Bis(4-pyridyl)ethylene (BPE) is a dye in the UV domain, widely used in SERS due to its large Raman cross section and its two amino groups and the vinyl group that may form bonds to the metallic surface [87].

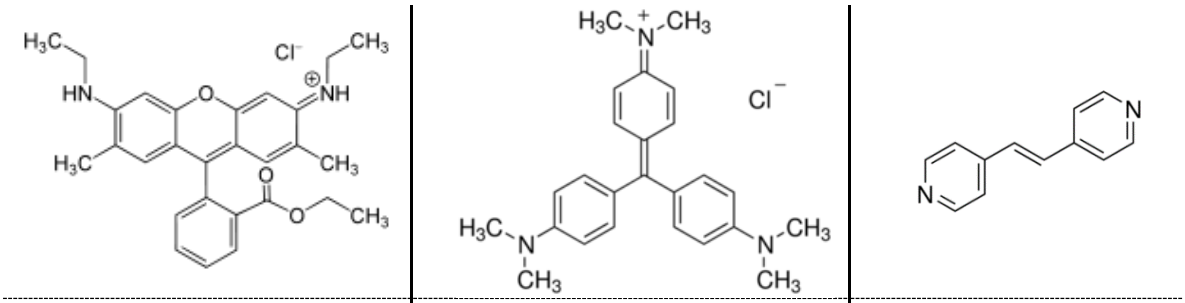

R6G | CV | BPE

Figure I-50: Skeletal formula of some dyes widely used in SERS studies Rhodamine 6G (R6G), crystal violet (CV) and 1,2-bis(4-pyridyl)ethylene (BPE)

5.5. Enhancement factor

The enhancement factor can be theoretically defined at the level of the single molecule as the ratio of the local field E_{Loc} and the incoming electric field at the power 4 divided by the incoming electric field E_0 also at the power 4, as le Ru defines [103, p. 217], the so-called SMEF:

$$SMEF = \frac{|E_{Loc}|^4}{|E_0|^4} \tag{52}$$

Experimentally, the measurement of the enhancement factor is not straightforward. The main issue is that the number of molecules actually participating to the enhancement is generally unknown. The way of estimating the enhancement factor as proposed by le Ru is the average surface enhancement factor:

$$E_{f\,;\,A} = \frac{I_{SERS}/N_{surface}}{I_{RS}/N_{volume}} \tag{53}$$

- $N_{volume} = c_{RS}V$ where c_{RS} is the concentration of the molecule and V the Raman scattering volume
- $N_{surface}$ the average adsorbed molecules

According to Le Ru [103], Sharma [109] or Kneipp [110], experimental values as high as 10^5-10^6 for the average Ef and 10^{10}-10^{11} for the maximum Ef can be reached. SERS enhancement is not uniform, therefore the $E_{f\,;\,A}$ is giving a good estimation on the substrate quality. $E_{f\,;\,max}$ is the maximum enhancement measured, at places with a high density of hotspots (a spatial area where the local field is huge), and is much more complicated to estimate in a correct way.

5.6. SERS on copper

Many papers and reviews on are mentioning copper nanomaterials as possible platforms for SERS. Van Duyne's underlines the spectral ranges where Cu, Au or Ag are expected to support SERS [109] (Figure I-51). However, literature reporting SERS effective copper-based materials remains scarce. The main reason for this absence of papers on copper is likely its spontaneous oxidation in air, hindering the coupling of LSP with the incident EM excitation. The main papers regarding this issue are from Van Duyne's group [111] and Ghodselahi and Vesaghi [112]. Van Duyne's group measured *in situ* the extinction of a lattice of copper nanopyramids during reduction by glacial acetic acid (Figure I-52). The extinction peak broadens and redshifts with oxidation, which corresponds to a redshift and damping of the LSPP resonance. On the other hand, Ghodselahi and Vesaghi calculated the influence of the thickness of a copper oxide shell on the LSPP resonance, and found a damping of the resonance with increasing thickness, and a redshift with decreasing relative permittivity (Figure I-53) in qualitative agreement with the experimental result from [111].

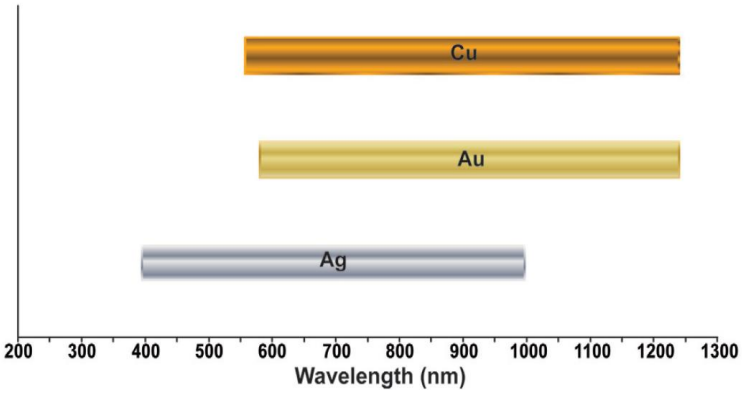

Figure I-51: Compared expected spectral ranges for SERS activity of Ag, Au, and Cu nanomaterials [109]

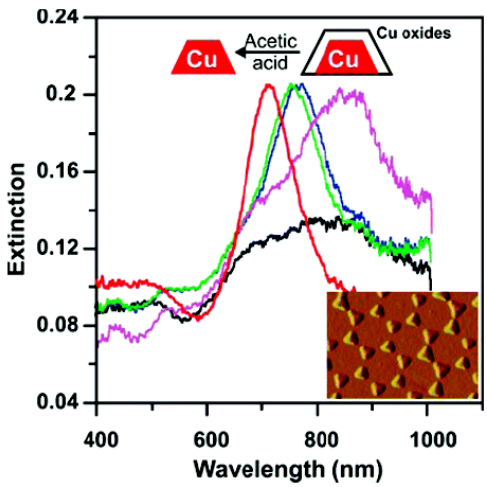

Figure I-52: Evolution of the experimental extinction spectra during reduction of triangular copper nanopyramids [111]

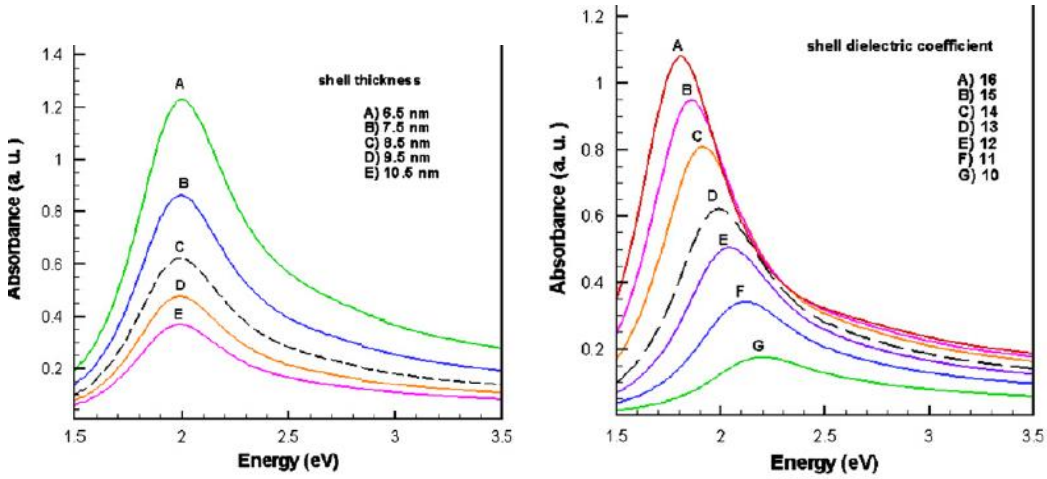

Figure I-53: Calculated absorbance of core/shell spherical nanoparticles with a copper core of diameter 4 nm as a function of (left) the thickness of the copper oxide shell , (right) the real relative permittivity of the shell [112]

Some groups reported SERS experimental studies on various molecular probes on various copper-based nanomaterials, like 4-aminobenzenethiol (10^{-5} M) on copper colloids [113] phenolic capping molecule (1,10-phenanthroline) on laser ablated substrates [114]. R6G and CV dyes (at concentrations down to 10^{-5} M) on porous copper structures formed by dealloying $Cu_{30}Mn_{70}$ [115]. Lastly the electrolytic deposition of copper has given interesting surfaces [116].

Typical SEM / AFM / TEM pictures of those surfaces are presented in Figure I-54.

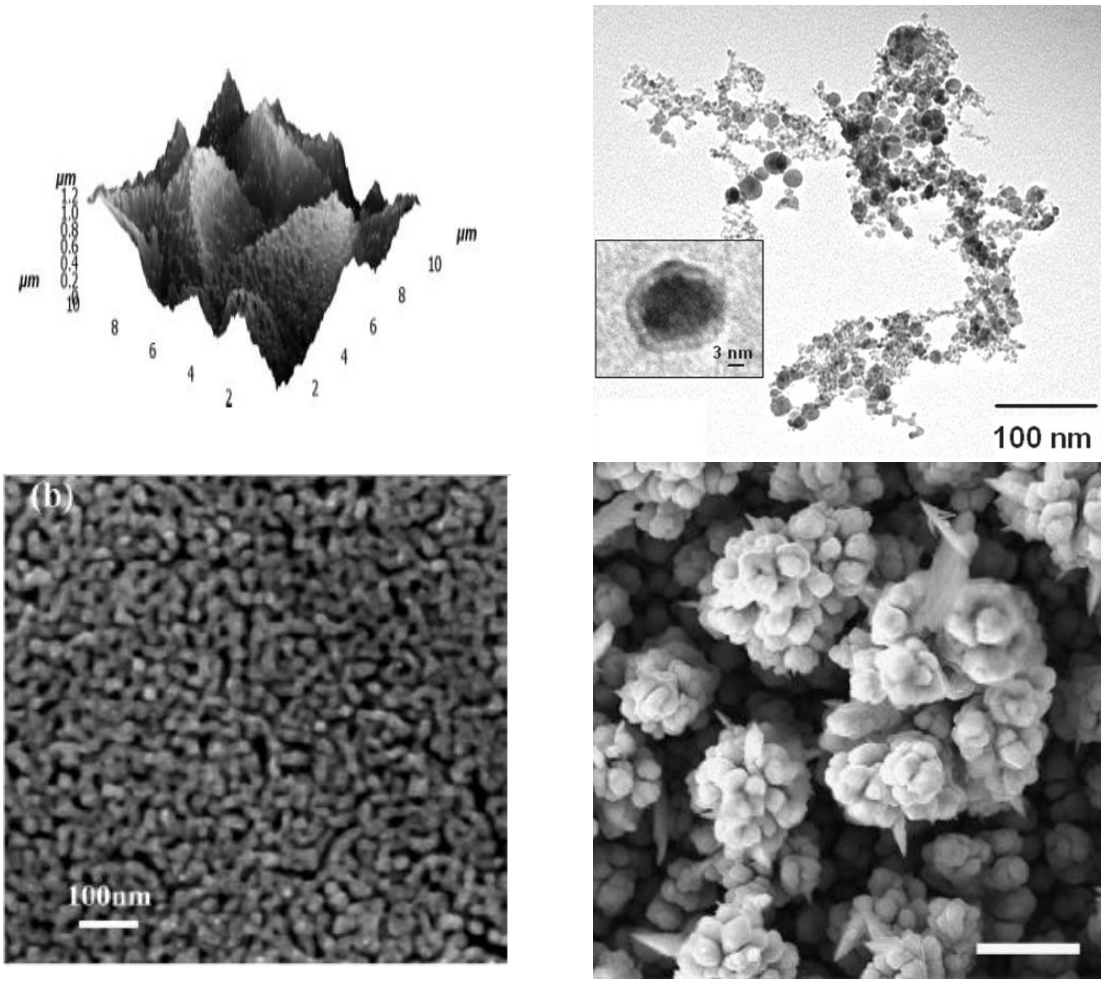

Figure I-54: SEM, AFM or TEM pictures of efficient copper based SERS platform: copper colloids deposited on a copper foil surface [113] (upper left), laser ablation (upper right) [114], dealloyed surface from [115] (lower left) and electrolict deposition [116]

Chapter II: Materials and methods

Using copper as a SERS substrate requires to study of the effect of the copper oxide native layer on the Raman signal, in a first step, and on the enhanced signal, in a second step.

In this chapter the different samples used as Raman references for oxide thickness calibration samples and SERS substrates are described as well as the related characterization techniques.

1. Copper and copper oxide reference samples

In a first step the Raman signals of copper and copper oxides have to be determined for reference sample. Raman experiments were carried out using a T64000 equipment with a Linkam cell (Figure II-1).

A (111) oriented copper single crystal (MTI supplier) was selected to get the Raman signal of pure copper. The sample was heated during 10 min at 400°C under H_2 flow (400 sccm) to reduce the native copper oxide before analysis.

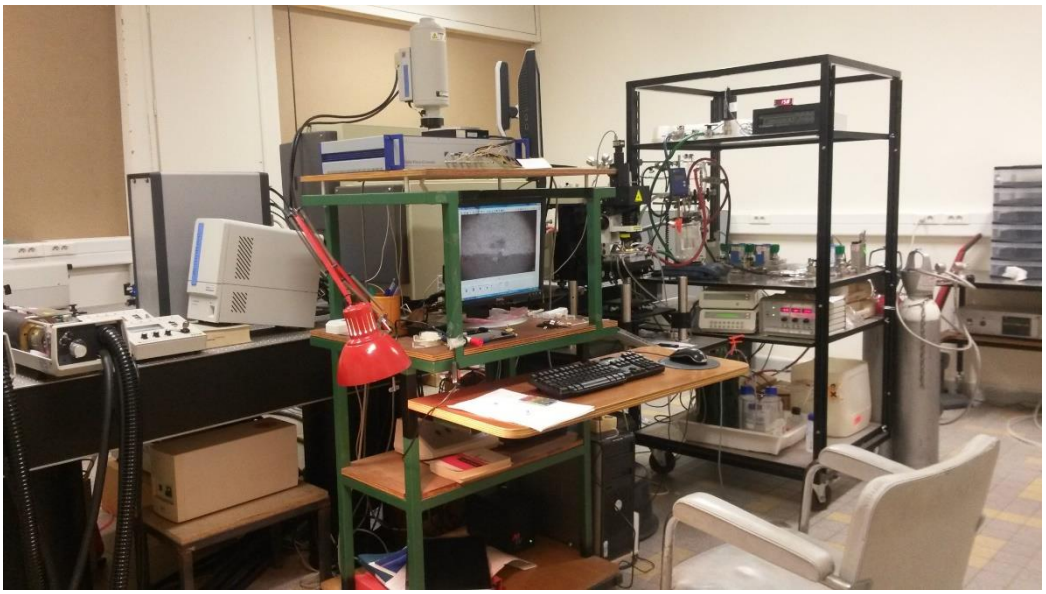

Figure II-1: Raman T64000 with a Linkam cell, equipped with H_2, O_2 and Ar.

Copper oxide powders, from Alfa Aesar, were chosen as references. Cu_2O cuprous oxide powder (Alfa Aesar 40188) shows a purity of 99 % and a granulometry of 200 mesh whereas cupric oxide powder (Alfa Aesar 10700) shows a purity of 99.995 % for a granulometry of 350 mesh (Figure II-2).

Figure II-2: Cuprous and cupric oxide powders

2. Copper and copper oxide calibration thin films

In order to determine the effect of copper oxide, and more precisely the copper oxide thickness, on the Raman signal, copper and copper oxide thin films with calibrated thicknesses were prepared.

2.1. Calibration of copper thin films

Copper thin films were deposited onto fused silica substrates using thermal evaporation. Experiments were carried out by F. Pichot and J. Lyonnet from the Centrale de Technologie en Micro et Nanotechnologie (CTM) of the Université de Montpellier using a home-made equipment. Thin films were deposited from the evaporation of a copper wire, 99,999% pure (Alfa Aesar), under secondary vacuum of 10^{-5} mbar and an applied intensity of 120 A. The thickness calibration was performed onto glass substrates using quartz crystal micro-balance (QCM) and atomic force microscopy (AFM) measurements.

Prior to deposition, fused silica substrates were ultrasonically cleaned in an acetone bath for 5 min and plasma treated in a 70 % O_2 / 30 % N_2 atmosphere for 6 min. A silicon piece was used to create a double step in the middle of the substrate for the AFM thickness measurements (Figure II-3).

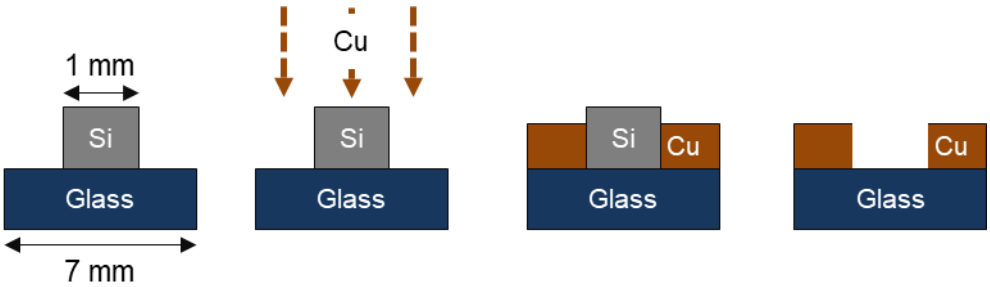

Figure II-3: Preparation of the Cu calibration thin films

Copper calibration samples with a thickness varying from 10 to 180 nm were prepared, *i.e.* 10, 15, 20, 30, 50 and 180 nm. The cross-sectional SEM (Scanning electron Microscopy) image of the 180 nm thick film is shown in Figure II-4.

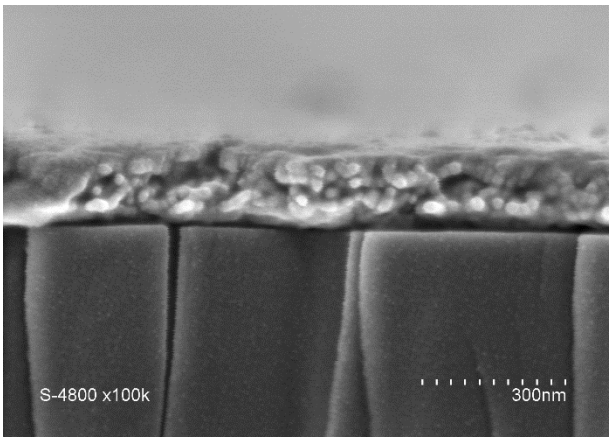

Figure II-4: SEM cross-section image of the Cu thin layer (180 nm)

2.2. Calibration of copper oxide thin film

Copper oxide thin films were obtained from the oxidation of copper thin films prepared by thermal evaporation as previously described. Cu thin films, of thickness varying from 10 to 180 nm, deposited onto fused silica substrates were annealed under air at atmospheric pressure.

The annealing temperatures were chosen to be low enough to preferentially form Cu_2O. Based on literature [34-35, 56-58], thin films were annealed in the range of 120 to 170°C. Annealing was performed progressively, for increasing time and temperature following the thermal treatment described in Figure II-5. Annealing times are reported in Table II-1. The evolution of the oxidation was studied by UV-vis absorbance analyses for each annealing condition from the Cu signal evolution. The time required to achieve full oxidation of the copper thin film for the different thicknesses is reported in Table II-2. However, even though the fully oxidized state of the thinnest Cu layers was achieved for lower annealing times, all the samples were submitted to the complete annealing treatment whatever the initial Cu thickness was.

The samples will be referred as "S 'thickness' - 'annealing time' ". As an example, S180-t600 means the series of samples with an initial thickness of 180 nm annealed during 600 min (according to the thermal treatment of Table II-1).

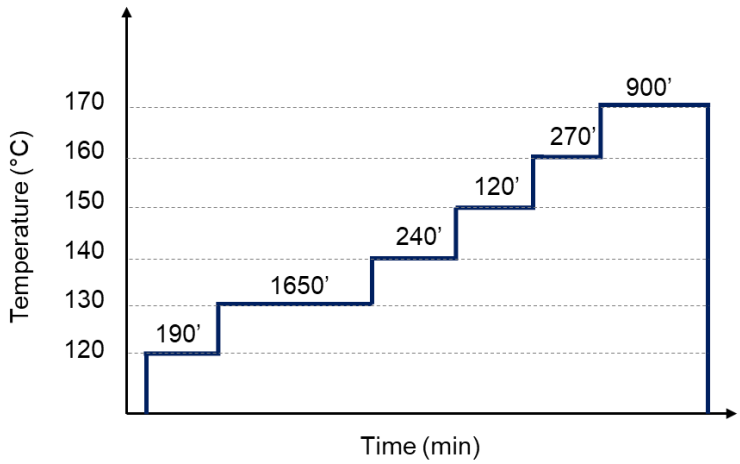

Figure II-5: Oxidation steps for increasing temperature, with indication of the time at each temperature plateau.

Temperature (°C)	Time (min)	Sample name
25	0	S‘thickness’-‘t0’
120	11	
	22	
	72	
	102	S‘thickness’-t102
	160	
	190	S‘thickness’-‘t190’
130	+ 130	
	+ 240	S‘thickness’-‘t240’
	+ 330	
	+ 450	
	+ 600	S‘thickness’-‘t600’
	+ 900	
	+ 1650	
140	+ 240	
150	+ 120	
160	+ 150	
	+ 270	
170	+ 60	
	+ 190	
	+ 900	S‘thickness’-‘t900’

Table II-1: Annealing conditions of Cu thin films.

Sample	Oxidation time
S10	t600
S30	t900
S50	t900
S180	Not reached

Table II-2: Oxidation step to reach full oxidation

SEM cross-section images of the 50 and 180 nm oxidized layers are shown in Figure II-6. Note that the thermal cycle was not long enough to fully oxidize the thickest Cu layer of 180 nm as it will be discussed in chapter III.

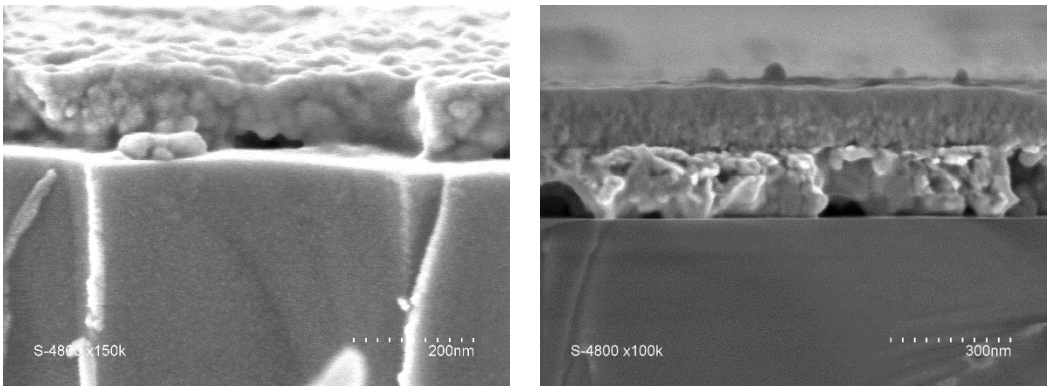

Figure II-6: SEM cross-section images of the oxidized copper thin layer 50 nm (left) and 180 nm (right) for -t900

3. SERS substrates

As the SERS signal is very sensitive to the surface morphology and roughness, three different substrates were prepared: silicon substrates coated with electroless plated copper, chemically etched copper foils and commercial substrates made of Au pillars coated with a 50 nm thick copper layer.

3.1. Electroless copper substrates

Copper coated silicon wafers were used as SERS substrates. The copper layer was deposited using the electroless plating process.

The electroless plating process is a metallization method based on chemical oxidation and reduction reactions without application of an external current, unlike electrodeposition. The main advantage of electroless deposition is that nonconductive substrates of complex shapes can be uniformly plated, at a relative slow deposition rate, which enables the control of thin deposits [117]. The process requires the use of a reducing agent (formaldehyde [118] or glycolic acid [119, 120]) and copper ions as the metal source. A complexing agent is added to build a ligand system (CuL) with the metal ions and prevent the formation of copper hydroxide in the alkaline electrolyte. To provide OH^- ions, the pH is set to 13. Furthermore, commercial plating baths contain additives to stabilize the electrolyte against uncontrolled plate out and to control the plating rate and the morphological properties of the deposited Cu film. For formaldehyde and glycolic acid the general copper electroless deposition equation are respectively:

$$CuL + 2\,HCHO + 4\,OH^- \rightarrow Cu + 2\,HCOO^- + 2H_2O + H_2 + L^{2-} \quad (54)$$

$$CuL + 2\,HOOCCHO + 4\,OH^- \rightarrow Cu + 2\,\mathrm{HOOCCO}O^- + 2H_2O + H_2 + L^{2-} \quad (55)$$

The SERS substrates were prepared from silicon wafers coated with a SiO_2 layer (~300 nm) and a TaN (35 nm) / Ta (30 nm) bi-layer to prevent copper diffusion (*i.e.* electro-migration) into the silicon substrate. Prior to electroless deposition a thin Ru layer, 2-5 nm thick, is deposited to catalyse the Cu electroless process. The electrolyte solutions used for copper plating were the Atotech "PRINTOGANTH PV" or "*EXPT SEEDPLATE bath"* ones [121, 122]

Electroless copper layers with a thickness of about 300 nm are deposited. The surface microstructure is represented in Figure II-7 and Figure II-8. The substrates are homogenous at a large scale with a fine microstructure, as observed from the Scanning Electron Microscopy (SEM) images. The roughness was determined from Atomic Force Microscopy (AFM) images (59) with a mean square roughness R_{ms} of 15 nm (average value of 5 zones in the 10x10 µm² images).

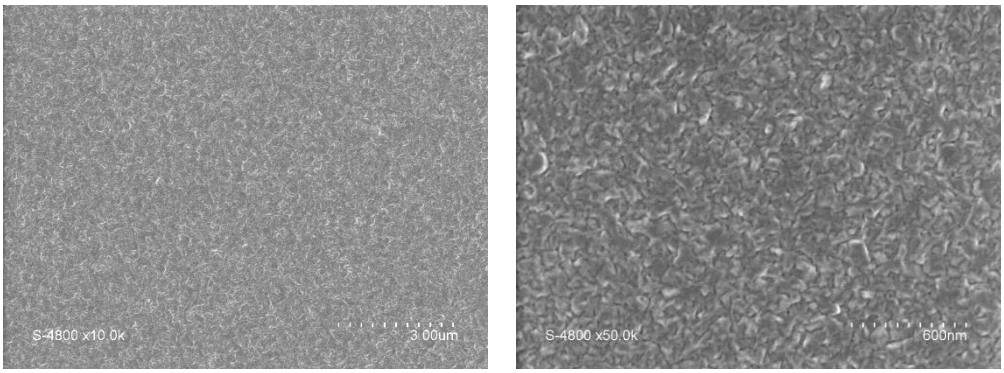

Figure II-7: SEM images of the surface of the 300 nm thick electroless Cu layer

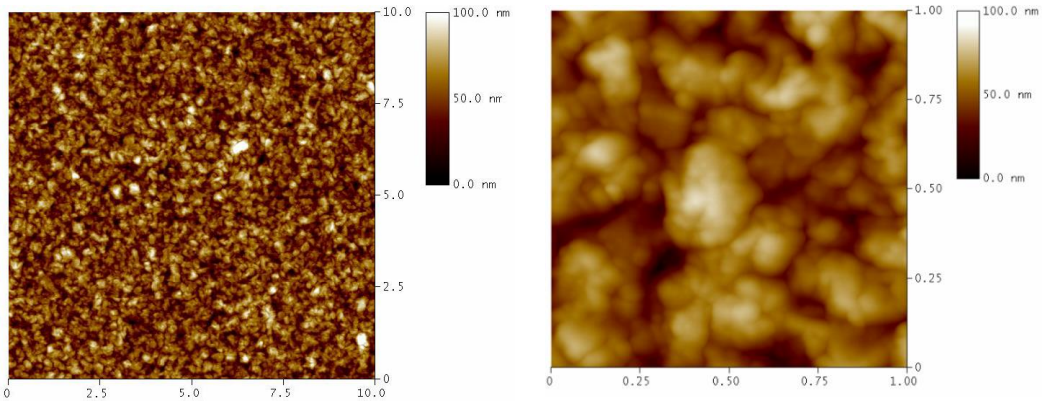

Figure II-8: AFM images of the surface of the 300 nm thick electroless Cu layer (10x10 µm² (left) and 1x1 µm² (right))

3.2. Etched copper substrates

Etched copper substrates were prepared from bare copper foils. Copper foils, 30 µm thick, were chemically etched for 30s, at 35°C in a solution of sodium persulfate ($S_2O_8^{2-}$) at a concentration of 0.1 M. The etching is based on the oxidation reactions of metallic copper and cuprous oxide by sodium persulfate ((56) and (57)). Cupric oxide remains at the same oxidation state but oxygen is replaced by sulfur by a double replacement with the sodium sulfate (SO_4^{2-})(58).

$$Cu + S_2O_8^{2-} \rightarrow Cu^{2+} + 2\,SO_4^{2-} \quad (56)$$

$$Cu_2O + S_2O_8^{2-} + H_2O \rightarrow 2\,Cu^{2+} + 2\,SO_4^{2-} + 2\,OH^- \quad (57)$$

$$CuO + SO_4^{2-} + H_2O \rightarrow CuSO_4 + 2\,OH^- \quad (58)$$

SEM images of the copper foil surface after etching are represented in Figure II-9. A quite different microstructure is observed in comparison to the previous electroless copper substrate with a rougher surface. Topography at two different scales is observed, one at the micron scale and the other one at the nano-scale.

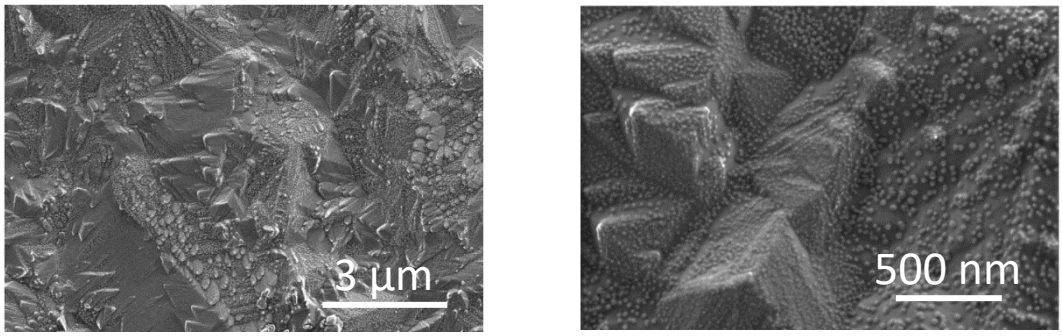

Figure II-9: SEM typical surfaces for etched copper foil Cu.

3.3. Gold based substrates

As previously described, gold is the material usually used as SERS substrate. For this reason, commercial gold substrates have been used in this study for preliminary SERS experiments. These substrates, supplied by Silmeco with "SERStrate" commercial reference, are prepared from a silicon substrate. Pillars structures are formed by maskless reactive ion etching of the silicon substrate and gold is deposited on the Si pillars structures by thermal evaporation (Figure II-10). This process leads to the formation of pillars with a height of around 1 µm, a diameter of about 100 nm and a distance between the pillars of about 100 nm . To study the Raman signal enhancement, "flat" Au samples, with a mean square roughness, Rms, of 5 nm, were additionally prepared from thermal evaporation of a gold wire (99.9999 % pure) onto a glass substrate. Au layers with a thickness of 500 nm were prepared.

In a second step the SERS enhancement from a copper pillar structure has been studied. A copper layer, about 50 nm thick, has been deposited by thermal evaporation onto the Au SERStrate previously described. This thickness is low enough so that the pillar structure is still observed (Figure II-10). This makes these substrates suitable to study the SERS behavior of a copper pillar structure.

a) Au SERStrate

b) Au SERStrate + Cu

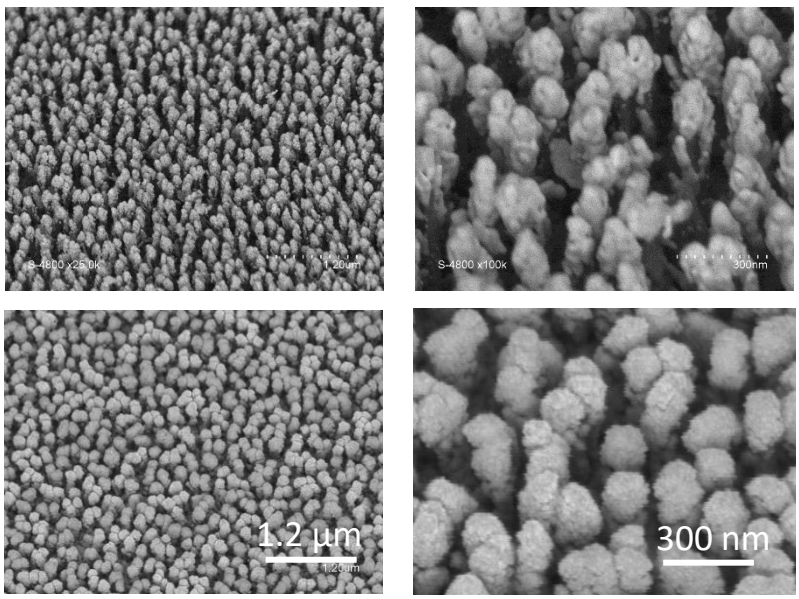

Figure II-10: SEM observation of the Au SERStrate a) as received and b) after deposition of a Cu layer (50 nm thick)

4. Raman probes

Raman experiments were carried out using either graphene or organic molecules probes.

4.1. Graphene probe

Graphene samples were synthesized by F. Otakar and M. Kalbac [96, 123] from the J. Heyrovsky Institute of Physical Chemistry in Prag, using chemical vapor deposition (CVD) as reported by Li *et al* [124] and Reina *et al* [125]. A copper foil is heated at 1000°C, and annealed 20 min under flowing H_2 (50 standard cubic centimeter per minute (sccm)). Then the foil is exposed to 1 sccm $12CH_4$ for 1 min, leaving hydrogen gas on with the same flow rate of 50 sccm. Finally the substrate was cooled down under H_2 by opening the furnace and removing the reaction tube from the heated zone. The cool down time from 1000 to 500°C was of 5 min. The pressure was kept at 0.35 Torr during the whole process. The as-grown graphene was subsequently transferred to the target copper substrate using polymethylmethacrylate (PMMA) (MicroChem, 950,000 MW, 9-6 wt. % in anisole), according to procedures reported previously [8].

Figure II-11 gives an example of transferred graphene on a (111) orientated copper single crystal using this method.

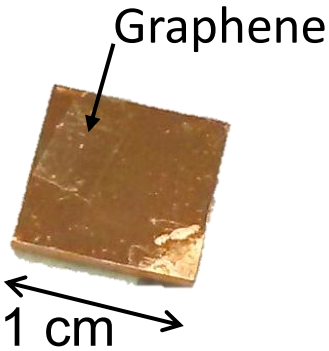

Figure II-11: Picture of the (111) copper single surface after graphene transfer using PMMA

The graphene transferred is essentially a single layer. This is checked by the ratio of A_{2D}/A_G ~2-5 [126], the 2D profile [127], and the A_G/A_{HOPG} [128, 129]. The quality of SLG is proved by the absence of the D peak. The position and width of the G and 2D peaks are an indication of the good adhesion of graphene to the copper substrate.

4.2. Organic molecules probes

The organic molecules chosen as Raman probes are the 1,2-Bis(4-pyridyl)ethylene (BPE) and 2-Mercaptobenzothiazole (MBT) ones supplied from Sigma Aldrich. The skeletal formula of these molecules are reported in Figure II-12. The interest of these two molecules is related to the presence of the – N and – S bonds which promote bonding with metallic surfaces [107, 108] and show strong intrinsic Raman signatures [86-87, 130].

1,2-Bis(4-pyridyl)ethylene (BPE)	Mercaptobenzothiazole (MBT)
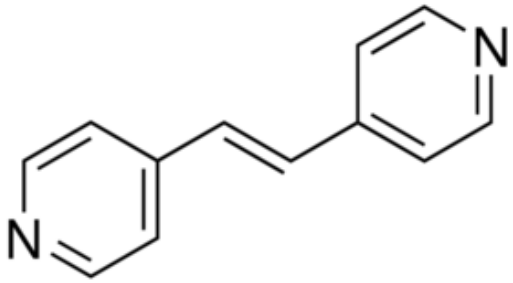	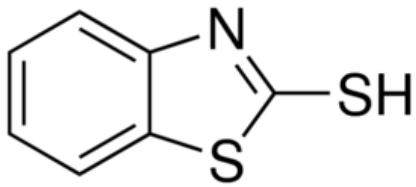

Figure II-12: Skeletal formula of 1,2-Bis(4-pyridyl)ethylene (BPE) (left) and 2-Mercapto-benzothiazole (MBT) (right)

Solution of BPE were prepared at various concentration (10^{-1}, 10^{-6} and 10^{-8} M) in Ethanol, or MilliQ water, or in acidic solution (c(H_2SO_4) = 0.1 M).

Due to its poor solubility in water, MBT was prepared in ethanoic solution at 10^{-6} M.

Raman spectra on SERStrates (Au and Cu coated ones) acquired in two conditions: the first one with the SERStrate immersed in those solutions and the second one with the dried SERStrate after thorough rinsing in the solvent (MilliQ water or ethanol) to remove unattached molecules, and drying at room temperature.

5. Characterization techniques

Various experimental techniques were selected to characterize the substrates (surface morphology and roughness) and the copper / copper oxide films (thickness, microstructure).

5.1. SEM / AFM observations

The sample microstructure was observed using Scanning Electron Microscopy (SEM). High resolution Hitachi S4800 and Helios NanoLab 660 FEI microscopes were a to observe the sample surfaces and cross-sections.

Additionally, Atomic Force Microscopy (AFM) was performed to determine the copper substrate and oxide roughness and the lateral auto-correlation length. An AXS Brücker equipment was used in the tapping mode using silicon nitride cantilevers with sharpened pyramidal tips. 2 x 2 µm^2, 5 x 5 µm^2 and 10 x 10 µm^2 scans were recorded with a resolution of 512 x 512 pixels and a residual noise of ± 0.5 Å. Data were computed using *Gwyddion* and *NanoScope Analysis* softwares.

The layer roughness was determined considering the R_{ms} mean square roughness defined as:

$$R_{ms} = \sqrt{\frac{1}{n}\sum_{i=1}^{n}(z_i - \bar{z})^2} \qquad (59)$$

where z_i is the height of the profile and $\bar{z}$ the average 2D plane height. If the R_{ms} roughness is widely used to characterize the surface morphology with reliability, this statistical description makes no distinction between peaks and valleys and does not account for the lateral distribution of surface features. A more complete description is provided by the power spectral density (PSD) of the surface topography, which performs a decomposition

of the surface into its spatial wavelengths and allows comparison of roughness measurements over different spatial frequency ranges [131].

The PSD analysis requires the transformation of the spatial domain into the frequency domain using the Fourier transform [132]. It consists in the Fourier transform (FT) of the height distribution $FT\left(z(\vec{r})\right)$ of a topographic image:

$$PSD\left(\vec{k}\right) = \frac{4\pi}{L^2}\left|FT\left(z(\vec{r})\right)\right|^2 \quad (60)$$

where $z(\vec{r})$ is the height distribution of the surface, centered on a mean medium plane and L the topographic picture length (µm).

Considering any waveform line in the topographic image, it can be deconvoluted using a sum of sine and cosine waves of different wavelengths. The PSD representation plots the pondering coefficient in front of each sinus (the PSD) as a function of spatial frequencies (inverse of the spatial period). Figure II-13 displays an example of a PSD profile obtained for an evaporated Cu layer after the final oxidation process (S50-t900).

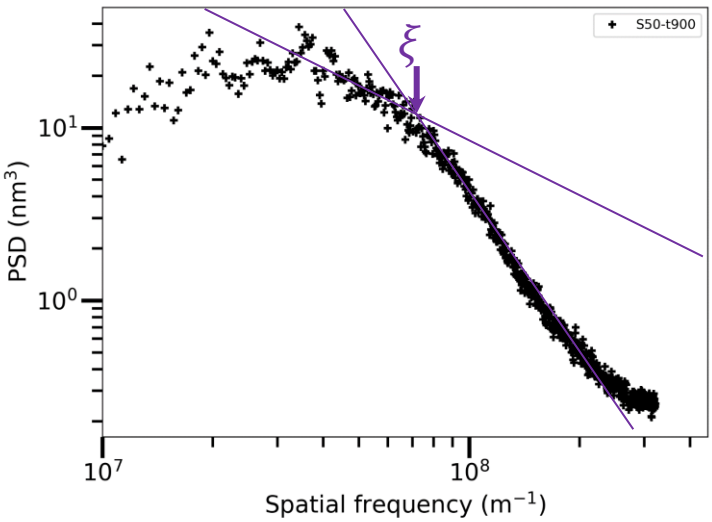

Figure II-13: PSD profile as a function of the spatial frequency for S50-t900.

The PSD profile reported in Figure II-13 is characteristic of all the Cu deposits studied. Two distinct regimes can be observed a low and high-frequencies. The transition between these two regimes allows determining a lateral auto-correlation length ξ, calculated as $2\pi/\xi$. This lateral auto-correlation length allows the characterization of the in-plane copper and copper oxide microstructure. Additionally AFM was used to determine the thickness of copper and copper oxide thin layers of the calibration reference samples.

5.2. XPS chemical analyses

The chemical composition and degree of oxidation of the copper oxide were studied using X-Ray Photoelectron Spectroscopy (XPS).

5.2.1. XPS principle

XPS is a chemical surface analysis technique which gives information on the chemical nature and state of the detected elements [133].

XPS is based on the energy analysis of the electrons emitted from a surface illuminated by X-rays and exhibiting the photoelectric effect. Photoelectrons are emitted with a specific kinetic energy, E_{KE} which is measured by an electron energy analyzer. The electron kinetic energy depends on the energy, hν, of the primary X-ray source and on the electron binding energy, E_{BE}:

$$E_{BE} = h\nu - E_{KE} - \phi_S \quad (61)$$

Where ϕ_S is the spectrometer work function

The XPS spectrum is obtained as a plot of the number of detected electrons per energy interval versus their kinetic energy. Since the mean free path of the electrons in solids is very small, most of the detected electrons originate from the top few atomic layers, typically from a depth of 10 nm at the most (Figure II-14).

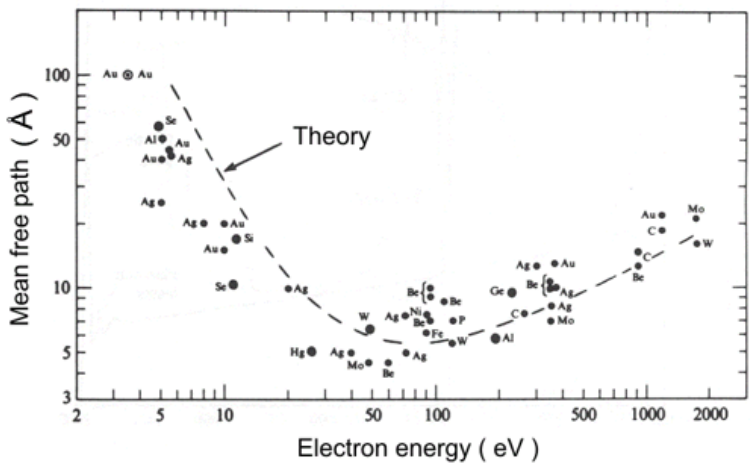

Figure II-14: Mean free path of electrons for different elements, as a function of the excitation source Kα in eV [134]

Also the XPS spectrum contains Auger peaks arising from relaxation processes (Figure II-15). These peaks are useful to identify element chemical states when XPS peaks include the contribution of elements with very close binding energy values.

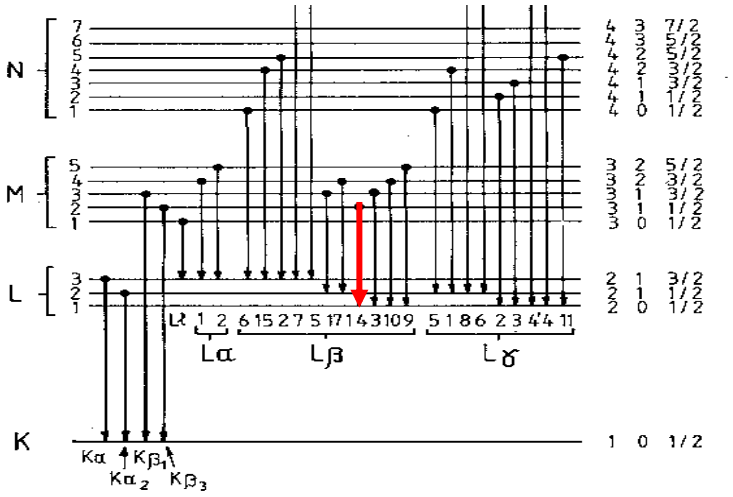

Figure II-15: LMM Auger transition

5.2.2. XPS experiments

XPS experiments are performed using an ESCALAB 250 spectrometer (Thermo Electron) with a monochromatized X-ray Al K_α radiation (1486.6 eV). The pressure in the analysis chamber is maintained at approximately $4x10^{-9}$ Torr. The analyzed core-level lines are calibrated against the C 1s binding energy set at 284.6 eV**.** The signals are deconvoluted using mixed Gaussian-Lorentzian curves where the Gaussian character was set to 80 %. The spatial resolution is limited by the X-ray beam with a diameter of about 400 µm. The elemental detection limit is of 0.1 % atomic and the chemical quantification is calculated with a standard deviation of ± 10 – 20 at. %.

Reference XPS spectra were performed for copper and copper oxides. The reference for metallic copper is obtained from a copper foil after acid etching ("NAPS" etching) and copper oxide powders, previously described, were used as Cu_2O and CuO references. Prior to analysis, the native oxide thin layer formed at the surface of the copper foil is removed through in situ erosion using Ar ions bombardment. The oxide removal is controlled from the evolution of the O1s spectrum as metallic copper doesn't show any peak in the O1s kinetic energy region.

The chemical composition of the reference samples, and more specifically of the Cu oxidation states, was studied from the XPS Cu 2p peak. This Cu 2p peak is usually used to determine the relative amount of each species [135].

The reference spectra of the etched copper foil and of the copper oxide powders are reported in Figure II-16 for the Cu 2p transition. Metallic copper, Cu(0), shows two peaks: Cu $2p_{1/2}$ at 952.4 eV and Cu $2p_{3/2}$ at 932.6 eV. For Cu(II) oxide, there are five large peaks: the two main peaks Cu $2p_{1/2}$ and Cu $2p_{3/2}$ at 953.5 and 933.9 eV respectively and their satellites at 941.0, 943.9 and 962.4 eV respectively.

The relative intensity of the satellites over the main peaks is 1.92 ± 0.1. Shake-up peaks occur when the outgoing photoelectron simultaneously interacts with a valence electron which is excited to a higher-energy level. The kinetic energy of the shaken-up core electron is then slightly reduced giving a satellite structure a few eV below the core level position [136].

Hence, these electrons are part of the total Cu 2p emission. For Cu(I) oxide, the two main peaks are at the same position as for Cu(0). In addition, one can observe a shoulder at the bottom of the Cu $2p_{3/2}$ peak at 934.4 eV, attributed to Cu(II) oxide. Moreover, one observes an additional peak at 946.9 eV, of low intensity, assigned to Cu(I) satellite. In the region from 939.4 to 945.9 eV, it is difficult to distinguish the presence of Cu(II) oxide satellites from the noise.

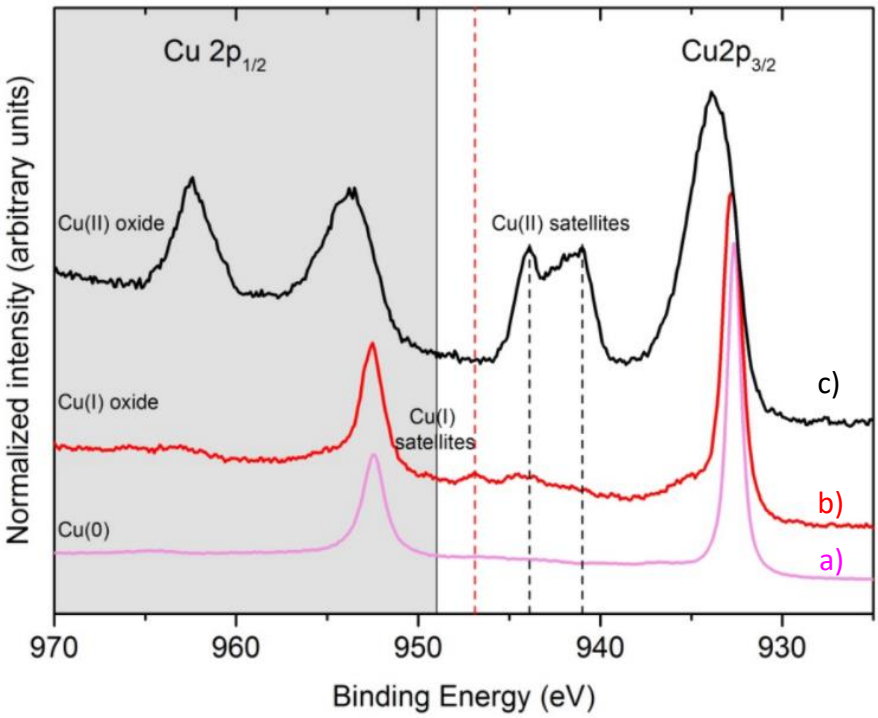

Figure II-16: Cu 2p transitions for etched copper surface (a) and reference powders of Cu_2O (b) and CuO (c)

The experimental values of the binding energy for the reference samples are reported in Table II-3 and are observed to be in good agreement with literature.

	Cu $2p_{3/2}$ peak (eV)		Satellites (eV)	
Reference samples	Exp.	Lit. [135]	Exp.	Lit. [135]
CuO powder	933.9	941 - 945	941 - 944	941 - 945
Cu_2O powder	932.8	932.2		
Etched copper	932.3	932.6		

Table II-3: Binding energies of Cu $2p_{3/2}$ and satellite peaks for etched copper foil and Cu_2O and CuO reference powders.

It is possible to confirm the assignments done on Cu $2p_{3/2}$ with the Auger spectrum. The Auger transitions for Cu(0), Cu(I) and Cu(II) are well defied in the (912.2 - 920.4) eV kinetic energies ranges [137]. The Auger spectra of the reference samples are shown in Figure II-17. The Cu(I) and Cu(II) peaks are broad. The experimental values of the Auger binding energy are reported in Table II-4 and are observed to be in good agreement with literature.

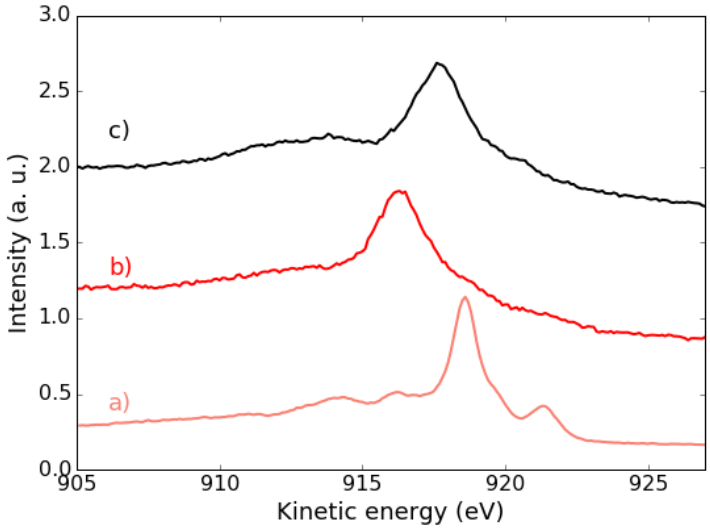

Figure II-17: Cu LMM transitions for etched copper surface (a) and reference powders of Cu_2O (b) and CuO (c)

	Cu LMM peak (eV)		
Reference sample	Experimental		Literature [135, 137]
CuO powder	917.4		917.7
Cu_2O powder	916.6		916.3
Etched Cu foil with	918.5		918.7
secondary maxima	913.8	916.5	920.9

Table II-4: Binding energy of Auger peaks for reference samples

5.3. Ellipsometry

Ellipsometry is a non-destructive method used to characterize materials with respect to their optical properties. If thin films are considered their thickness can be determined using this technique.

The ellipsometer principle is sketched in Figure II-18, with also shows the ellipsometric angle Ψ and Δ. Incident light is emitted by a laser beam or by a monochromatized light from a broad band source. The incident beam is linearly polarized and hits the sample surface with an incident angle ϕ. Depending on the optical properties and on the composition of the sample (complex refractive index and thickness of the film under investigation), the parallel and perpendicular components of the electric field in the reflection plane respectively E_p and E_s are modified according to Fresnel's equations. In most cases, the reflected light is elliptically polarized, which is the origin of the name of the instrument and the technique (Ellipsometer, ellipsometry).

Knowing the polarization of the incident beam, it is possible to determine to what extent the polarization has change after interaction with the sample. A portion of light is reflected under the same angle as ϕ, while the other portion enters the material and is refracted according to Snell's law under a refraction angle ϕ_2. Fresnel's equations determine the

complex reflection coefficients $\widetilde{r_p}$ and $\widetilde{r_s}$ for the parallel (p subscript) and for the perpendicular (s subscript) component to the reflection plane.

$$\widetilde{r_p} = \frac{\widetilde{N_2}\cos\phi_1 - \widetilde{N_1}\cos\phi_2}{\widetilde{N_2}\cos\phi_1 + \widetilde{N_1}\cos\phi_2} \tag{62}$$

$$\widetilde{r_s} = \frac{\widetilde{N_1}\cos\phi_1 - \widetilde{N_2}\cos\phi_2}{\widetilde{N_1}\cos\phi_1 + \widetilde{N_2}\cos\phi_2} \tag{63}$$

The complex ellipsometric parameter $\tilde{\rho}$ is defined as the ratio of $\widetilde{r_p}$ and $\widetilde{r_s}$. $\tilde{\rho}$ is determined by ellipsometry, with tanΨ being the ratio of the amplitude ($\tan\Psi = \left|\frac{\widetilde{r_p}}{\widetilde{r_s}}\right|$) and Δ is the phase shift ($\Delta = \delta_p - \delta_s$):

$$\tilde{\rho} = \tan\Psi \; e^{i\Delta} \tag{64}$$

Δ and Ψ are the ellipsometric angles measured experimentally from which the complex refractive index of an unknown material, or the thickness of a known thin film can be determined.

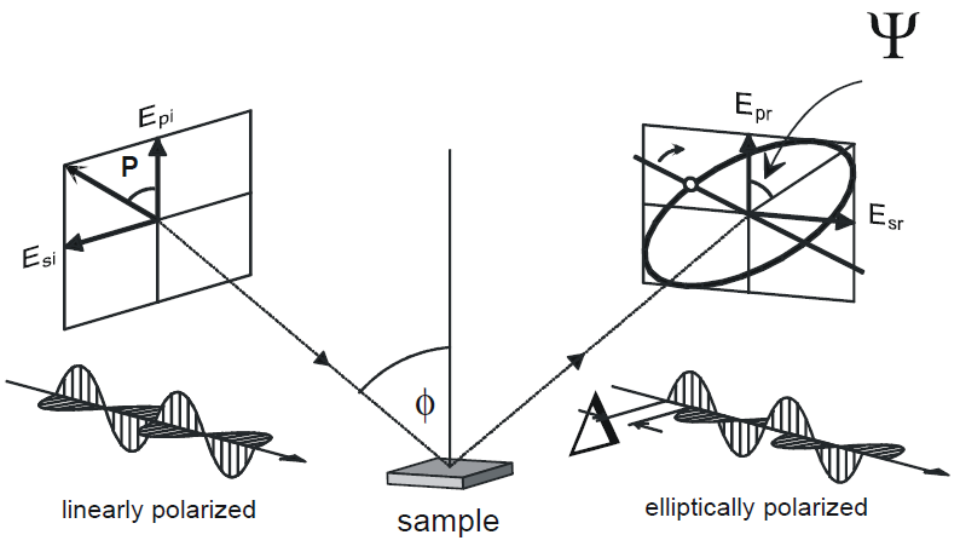

Figure II-18: Representation of the ellipsometer principle. ϕ is the incident angle and P the initial polarization angle. E_{pi} and E_{si} are the incident parallel and perpendicular components of the electric field in the reflection plane and E_{pr} and E_{sr} are the reflected components [138]

The ellipsometric angles are particularly sensitive around Brewster's angle (θ_B) which is a particular angle of incidence where the reflection of linearly polarized light with parallel orientation has a minimum (for metals, in case of dielectric at Brewster angle there is no reflection at all).

Brewster's angle θ_B is defined as:

$$\tan\theta_B = \frac{\widetilde{n_1}}{\widetilde{n_2}} \tag{65}$$

Where $\widetilde{n_1}$ and $\widetilde{n_2}$ are the complex refractive angles of the incident and studied media respectively.

In modelling fixing some parameters is essential for the determination of others. In case of multiple stacked layers, fixing the refractive index of the known layers allows the determination of their thicknesses.

By numerical routines, the modeled parameters are varied to find the best possible match between the measured and the calculated Δ and Ψ. The fit return the chosen fitted parameter, $i.e\ n, \kappa$, or the layer thicknesses. Two different ellipsometer setups were considered for the ellipsometric measurements, multiple angle of incidence (MAI) ellipsometry and spectroscopic ellipsometry.

5.3.1. Multiple angle of incidence (MAI) ellipsometry

Multiple angle of incidence (MAI) measurements were performed using an ellipsometer (Optrel, Germany) working with green laser light (λ = 532 nm) closed to the Brewster's angle. Brewster's angle is estimated by a simulation of the modelled layer stack for each sample using the 'Ellipsometry: Simulation and Data-evaluation' software from Nanofilm before the measurement. Typical value for optical glass is 56°, while for samples modelled by: substrate=fused silica / Cu / Cu_2O its value is closer to 70°. Ten experimental points are chosen around θ_B with a step from 2 - 5°. The laser power was set to P = 50 mW, for an illuminated surface area about 1 mm². The polarizer step and analyzer step for measurement to determine the ellipsometric parameters (ρ, Ψ, Δ) are respectively fixed to 15 and 3° for the best estimation. Thickness of Cu and Cu_2O is searched using the model: substrate= optical grade SiO_2 / Cu / Cu_2O.

A typical fit of ellipsometric angles Ψ, Δ is represented in Figure II-19 with data points for S15-t0.

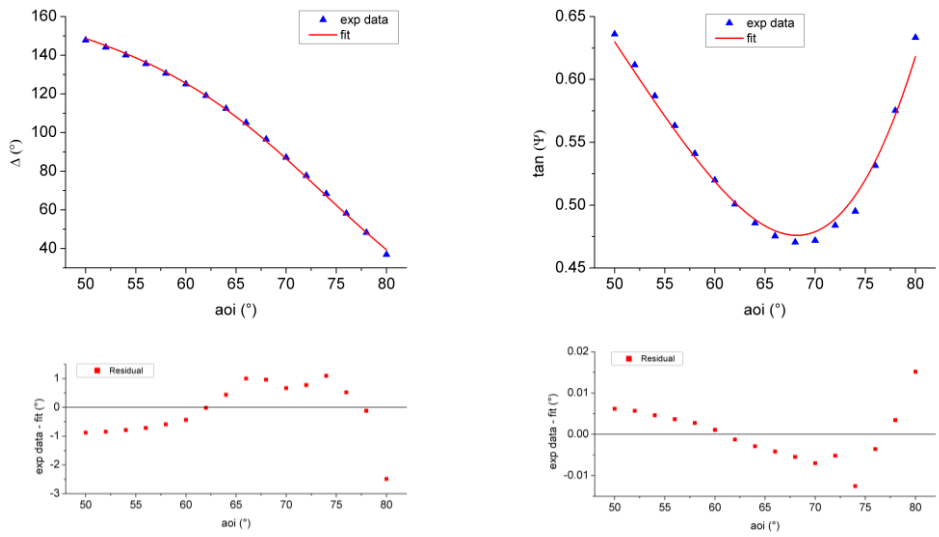

Figure II-19: Experimental and fitted Δ (left) and tan(Ψ) (right) evolution as a function of the incidence angle (aoi (°)) for S15-t0 (top), with residuals (bottom)

5.3.2. Spectroscopic ellipsometry

Spectroscopic ellipsometry was performed with monochromatized light at 560, 660, 760, 860 and 960 nm. Additional data points at 360 and 460 nm were analyzed for the thickness determination of the Cu and Cu_2O thin films, S10 and S30 (10 and 30 nm thick respectively), after annealing, to confirm the result obtained with smaller spectral range. The incidence angle is fixed at 50° for a model: substrate = optical grad SiO_2 / Cu / Cu_2O. For S50 and S180, the thickness of copper is too high for a quantification with ellipsometry, because Cu films become opaque at a thickness of 40-50 nm. Only Cu_2O thickness is fitted using copper as a substrate for the model: substrate = Cu / Cu_2O.

A typical fit of experimental ellipsometric angles Ψ, Δ for S30-t0 gives very good fitting results (Figure II-20).

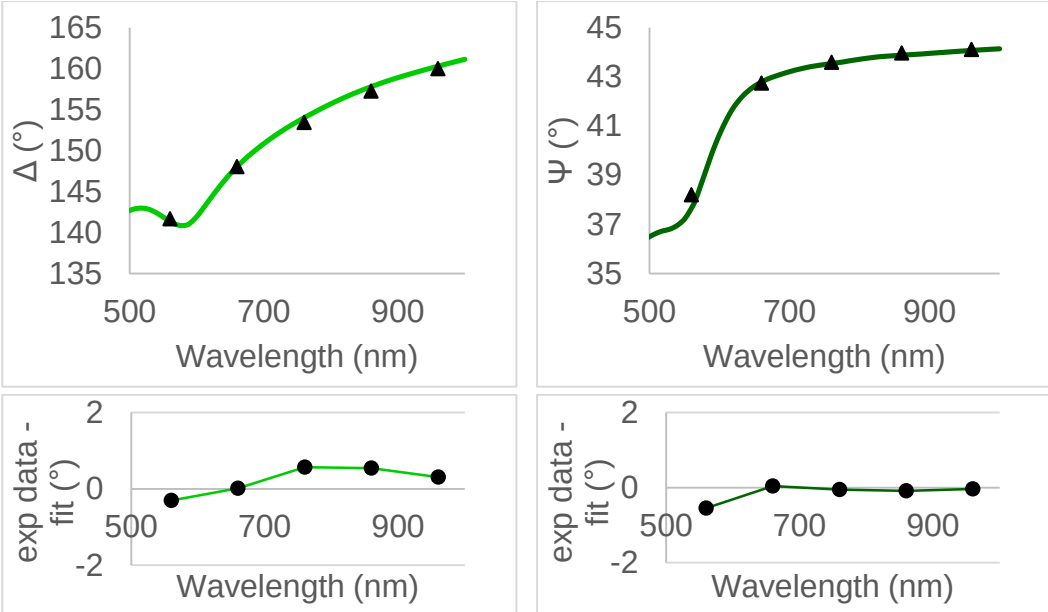

Figure II-20: Experimental and fitted Δ (left) and tan(Ψ) (right) evolution as a function of the wavelength for S30-t0 (top), with residuals (bottom)

5.4. UV-vis

The absorbance of the thin layers of copper/copper oxide was measured on a UV-Visible-NIR CARY 5000 in the spectral range 350-800 nm. The beam diameter was fixed to 1 mm

Refractive indices of Cu and of Cu_2O are represented in Figure II-21. The imaginary part of the refractive index is increasing with the wavelength from 2 at 380 nm to a value as high as 10 for $\lambda > 1450$ nm. The imaginary part of Cu_2O is decreasing with the wavelength and can be neglected for $\lambda > 600$ nm. Cu_2O imaginary part of the refraction index cannot be neglected from copper's for $\lambda < 600$ nm. At $\lambda = 380$ nm its value is 1.2 while copper's is of 2.

In summary for shorter wavelengths, the absorbance of Cu_2O is at maximum. While for wavelength above 600 nm, the contribution of Cu_2O to the sample absorption can be neglected because Cu is largely dominant.

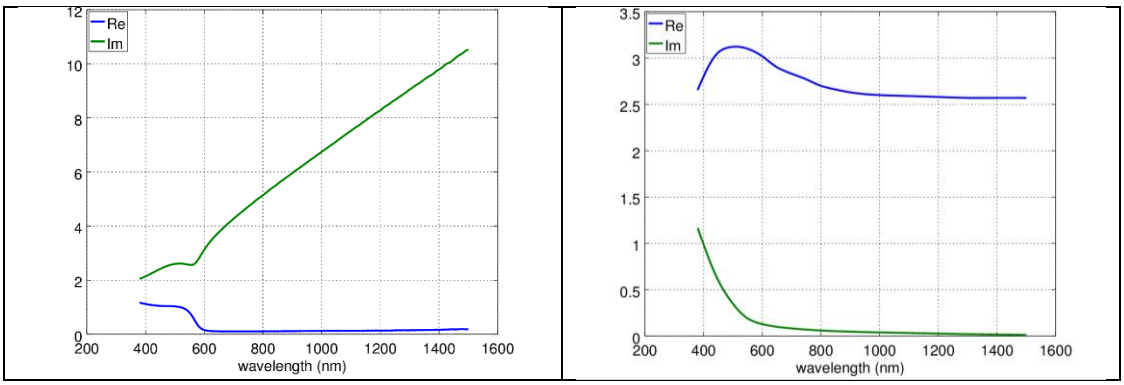

Figure II-21: Real and imaginary part of the refractive index plotted as a function of the wavelength The data are taken from Mc Peak [139] for Cu (left) and from Sopra [12] for Cu_2O (right)

5.5. Raman spectroscopy

Raman measurements were carried out on two spectrometers of Laboratoire Charles Coulomb:

- a Renishaw Invia spectrometer, using three laser lines (532, 633 and 785 nm and associated edge filters), two gratings (2400 l/mm at 532 nm and 1200 l/mm at 633 and 785 nm) and a CCD camera detector. Measurements in air and in a liquid cell are achieved in a microscopic configuration using a 50xlwd objective with a numerical aperture of 0.5
- a Raman Horiba T64000 spectrometer using a laser line at 488 nm (and an associated edge filter), a grating with 600 l/mm and a CCD camera detector

Raman maps were measured:

- on the Invia spectrometer with 2 µm steps for typical maps of 20*10 spectra
- on a Horiba XploRA™ spectrometer in the lab of Pr Stephanie Reich at FU Berlin, using a laser line at 638 nm with 1 µm steps for a typical map of 20*20 spectra.

For calibration, we used the silicon peak at 521 cm^{-1}, varying as a function of the wavelength. 488 nm spectra are acquired on the Horiba T64000, while the Renishaw Invia spectrometer is used for excitation at 532, 633 and 785 nm. Figure II-22 compares the Raman spectra of silicon acquired at those wavelengths.

The typical Raman spectra of HOPG, from SPI (grade SPI-1) acquired at 488 nm, for 30 s and a power ~500 µW is given in Figure II-23 with its band G at 1582 cm^{-1} and 2D lorentzian contributions at respectively 2700 and 2740 cm^{-1}.

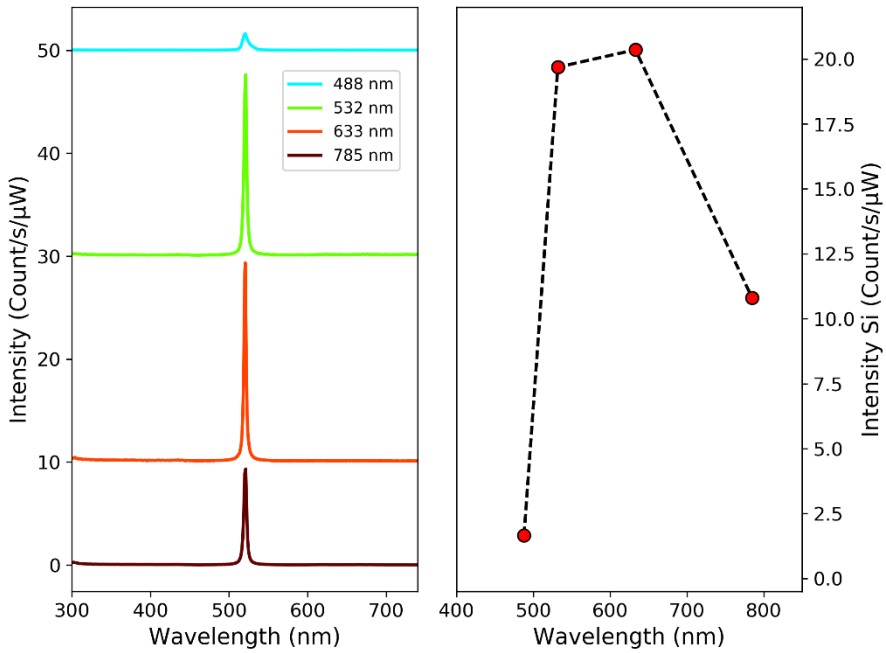

Figure II-22: Raman spectra on Si / 100 nm SiO_2 acquired at 488, 532, 633 and 785 nm (left) the fitted peak at 521 cm^{-1} gives the intensities (right).

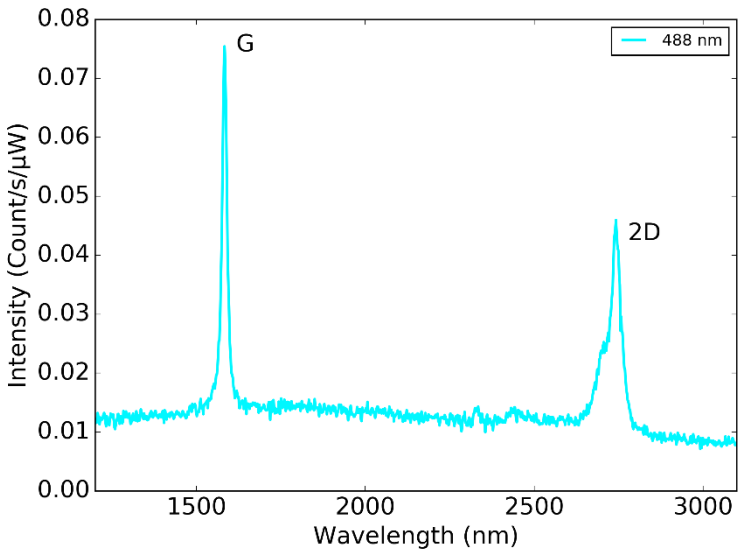

Figure II-23: Raman spectra of HOPG acquired at 488 nm for 30 s and a power ~500 µW

Chapter III: Coupled microscopic/ spectroscopic characterization of ultra-thin copper/ copper oxide films

One of the main goals of this thesis is to study the influence of the copper oxide layer on the Raman / SERS signal. The accurate measurement of the nature and thickness of thin (< 100 nm) and ultra-thin (< 10 nm) layers of copper oxide is not straightforward. In this chapter, we propose a coupled microscopic / spectroscopic study of series of thin and ultra-thin copper films (10-180 nm) deposited by thermal evaporation on fused silica substrates, and a monitoring of copper oxide growth during thermal oxidation.

We first characterize the microstructure and the thickness of raw and fully-oxidized samples by SEM and AFM. We then study the nature of the superficial oxide by XPS. Finally, we use ellipsometry and UV-visible absorption spectroscopies to accurately determine the thicknesses and optical properties of both the copper and the copper oxide layers. One of the main originality of this approach is the use of UV-vis spectroscopy in transmission which allows to couple simple measurements and thorough calculations.

Samples described in this chapter will be referred to with their initial target thickness, and with the subsequent oxidation time (Table III-1). Four series of samples are studied, hereafter called S10, S30, S50 and S180. Thermal oxidation was achieved at various temperatures and times as summarized in chapter II.

Temperature (°C)	Time (min)	Sample names
RT	-	S10-t0 S15-t0 S20- t0 S30-t0 S50-t0 S180-t0
120	102	S10-t102 S30-t102 S50-t102 S180-t102
	190	S10-t190 S30-t190 S50-t190 S180-t190
130	240	S10-t240 S30-t240 S50-t240 S180-t240
	600	S10-t600 S30-t600 S50-t600 S180-t600
170	900	S10-t900 S30-t900 S50-t900 S180-t900

Table III-1: Studied samples names, with oxidation step, temperature and time

1. Thin films microstructure

The microstructure of as-deposited copper thin films and oxidized ones has been observed using SEM and AFM in order to determine the roughness, porosity and grain size.

1.1. Microstructure observation of the raw Cu thin films

SEM cross-section and surface of the as-deposited 180 nm thick Cu layer (S180-t0) are reported in Figure III-1. Films are observed to be formed with a very fine grain size of about 30 nm. A non-columnar growth seems to be formed.

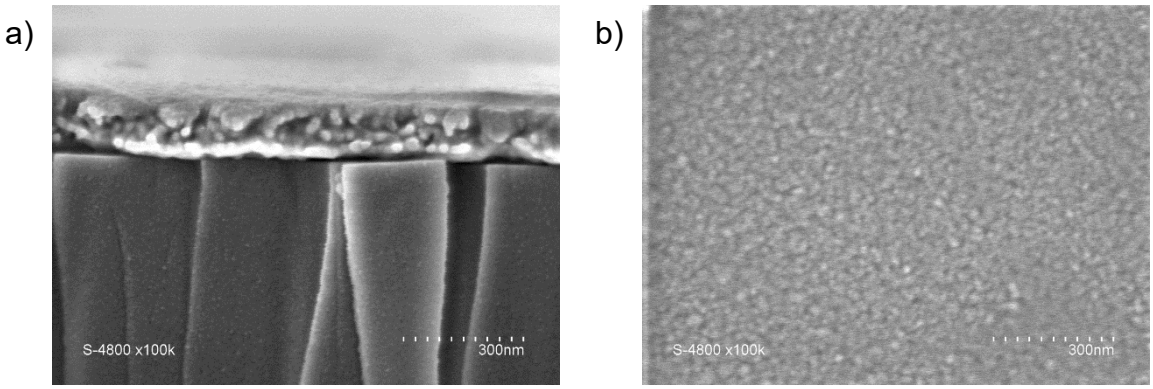

Figure III-1: SEM observation of as-deposited 180 nm thick Cu film cross-section (a) and surface (b)

The roughness of the film surface, R_{ms}, is observed to be low with a mean value of 1.2 nm determined from the 5 x 5 µm^2 image (Figure III-2). A lateral correlation length, ξ of 79 nm is determined which is higher but in the same range than the grain size evaluated from SEM image (~ 30 nm). The lateral correlation length is therefore assumed to be more representative of agglomerates of very fine grains than of the film grain size itself.

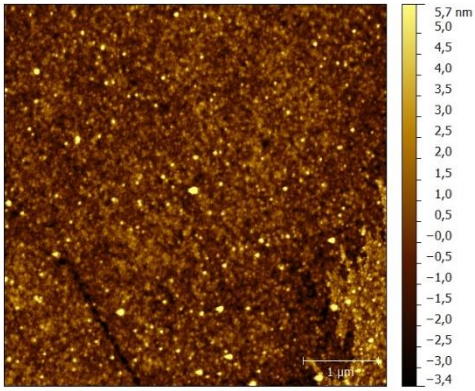

Figure III-2: AFM image of raw 180 nm thick Cu film

Regarding the 10 nm thick as-deposited layer, a R_{ms} roughness of 0.8 nm is measured, which is even slightly lower than the 180 nm thick film (1.2 nm) (Figure III-3). A finer grain size of 24 nm is also determined from the auto-correlation length which is in good agreement with the germination / growth mechanisms.

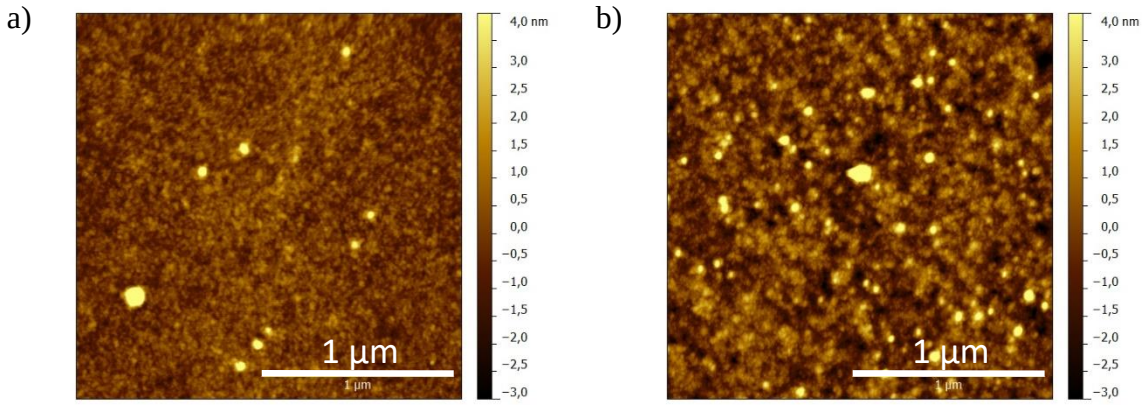

Figure III-3: 2x2 µm² AFM image of raw Cu films 10 nm (a) and 180 nm (b) thick

1.2. Microstructural observation of the oxidized thin films

SEM images of the oxidized Cu thin films are shown in Figure III-4 for samples exposed to the higher oxidation time (t900). The 10 nm surface could not be observed due to difficulties in the sample preparation.

From cross-section observation, it appears that the film microstructure is similar for all the samples except for the 180 nm one (Figure III-4a). In this last case, one can observe a bi-layer structure which suggests that the Cu layer is not fully oxidized as confirmed from UV-vis experiments (§3.3.1). The oxide growth is related to a significant increase of the grain size when the initial thickness increases (Figure III-4b).

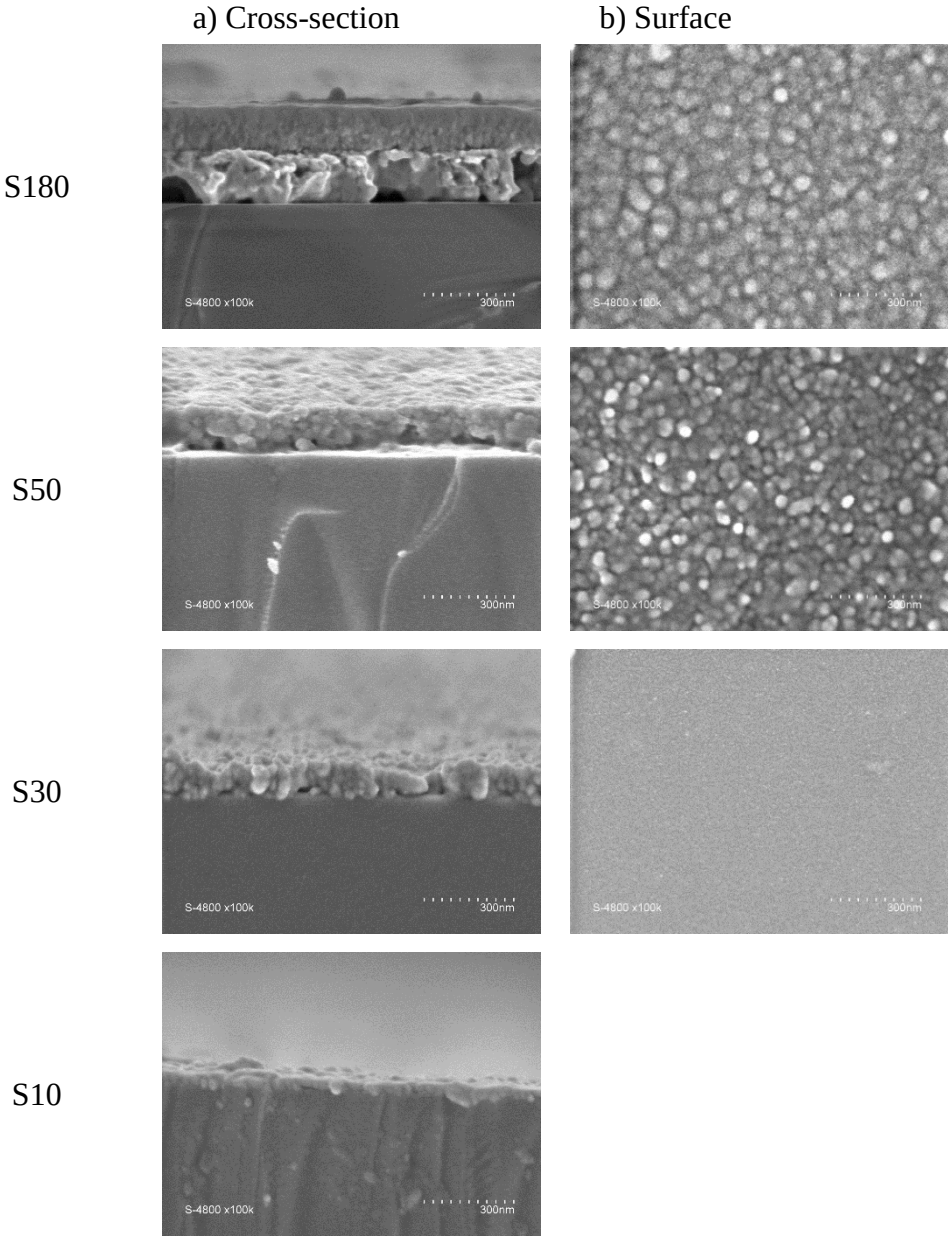

Figure III-4: SEM images of the cross-section (a) and surface (b) of the oxidized Cu layers (t900)

The increase of the grain size with the oxide thickness evolution is related to a decrease of the R_{ms} roughness (Figure III-5).

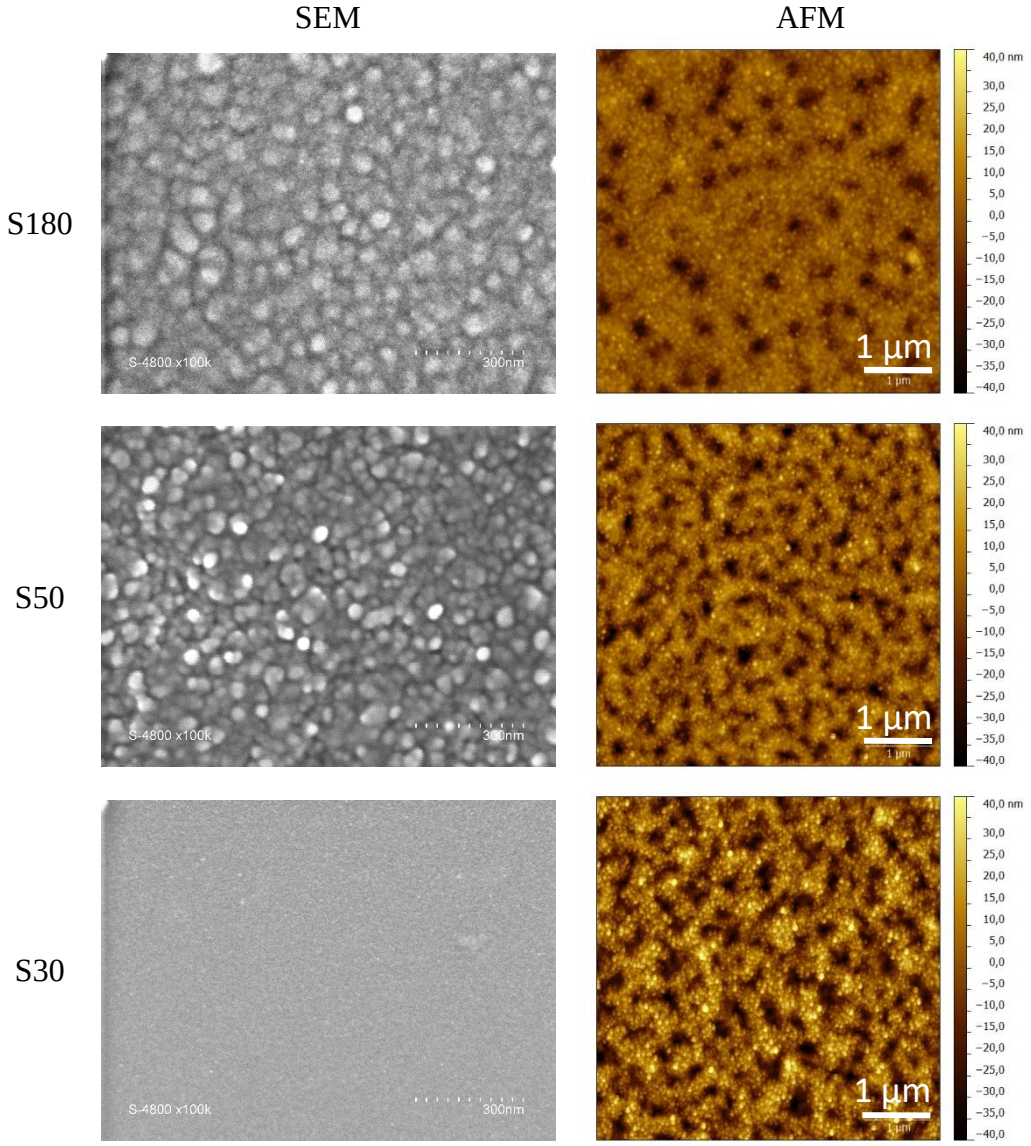

Figure III-5: SEM and AFM for the fully-oxidized films (t900)

The R_{ms} values for the as-deposited and oxidized films are reported in Table III-2. The roughness decreases from 13.6 to 6.6 nm when the initial thickness increases from 30 to 180 nm, respectively. This may be explained by the decrease of the oxide porosity with the oxide growth as observed from the cross-section SEM images. Additionally, it can be noted that oxidation induces an increase of the roughness for both S10 and S180 series even though the S10 sample shows a very low roughness.

	S10	S30	S50	S180
Raw samples				
R_{ms} (nm)	0.8			1.2
Fully oxidized samples				
R_{ms} (nm)	2.2	13.6	10.2	6.6*

*Table III-2: R_{ms} roughness of the raw and fully-oxidized samples (t900) * the S180 is not fully oxidized*

The evolution of the power spectral density (PSD) as a function of the spatial frequency is reported in Figure III-6 and Figure III-7 for the raw and fully-oxidized film respectively. The values of the lateral auto-correlation length ξ determined from the slope change are reported in Table III-3. For raw samples, the lateral correlation length is in the range of 24 - 79 nm for S10-t0 and S180-t0 respectively, and is increasing after oxidation for samples S10 to reach 35 nm. For S30, S50 and S180 fully-oxidized (t900), ξ is about 70-79 nm. The oxidation seems to form larger oxide grain compared to the initial copper grains. The fully-oxidized S10 has a smaller ξ than the other oxidized samples, which can be understood by the thinner layer, preventing a larger grain growth.

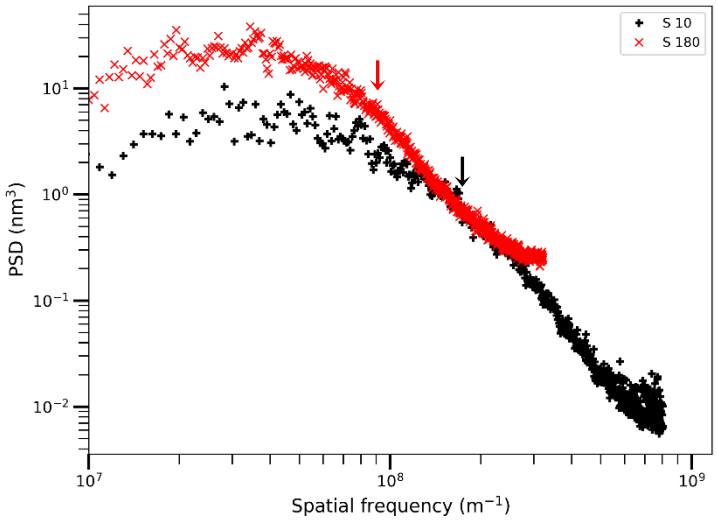

Figure III-6: Evolution of the PSD as a function of the spatial frequency for the raw copper films (S10-t0 and S180-t0)

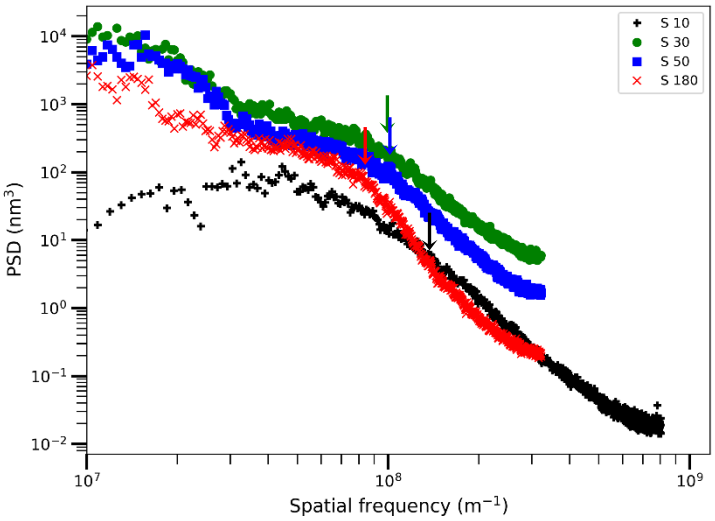

Figure III-7: Evolution of the PSD as a function of the spatial frequency for the oxidized films (S10 to S180, t900)

		S10	S30	S50	S180
Raw sample	ξ (nm)	24			79
	Grain size (nm)				30
Fully oxidized samples	ξ (nm)	35	70	70	79*
	Grain size (nm)		10	40	60*

Table III-3: Lateral auto-correlation length ξ and the grain size from of raw and fully-oxidized samples the S180 is not fully oxidized*

As previously detailed, the values of the auto-correlation length is higher than the grain size evaluated from SEM images and are therefore more representative of agglomerates of very fine grains. We also note a low roughness from about 1 nm to 14 nm for raw and fully oxidized surfaces, two order lower than the visible light scale.

2. Determination of the copper oxidation state of thin films

The nature of the oxidized copper films has been investigated from high resolution Cu LMM and $Cu2p_{3/2}$ XPS spectra.

2.1. Study of the Cu LMM Auger transition

The Cu LMM Auger spectra for as-deposited S10, S15 and S180 series are shown in Figure III-8 (left) with the peak positions reported Table III-4. The raw spectra show similar profiles with however a shift to lower kinetic energies for the S180-t0. This shift is attributed to calibration.

The main peak centered at 916.5 eV is assigned to Cu_2O (916.3 eV [140]) whereas the peak at 918.5 eV is assigned to Cu (918.7 eV [140]). It seems that CuO (917.7 eV [140]) is not detected for these samples (assuming that the S180 spectrum is shifted due to calibration effect).

The Auger Cu LMM spectra for t900 oxidized films are shown in Figure III-8 (right), with the position reported in Table III-4. A change in the spectra is observed in comparison with raw Cu films with one large peak only for each series (S10 to S180). This large peak may be attributed to the contribution of both Cu_2O (916.3 eV) and CuO (917.7 eV). Contrarily to raw films, Cu is not detected which let assume that the copper oxide thickness is higher than 5-10 nm.

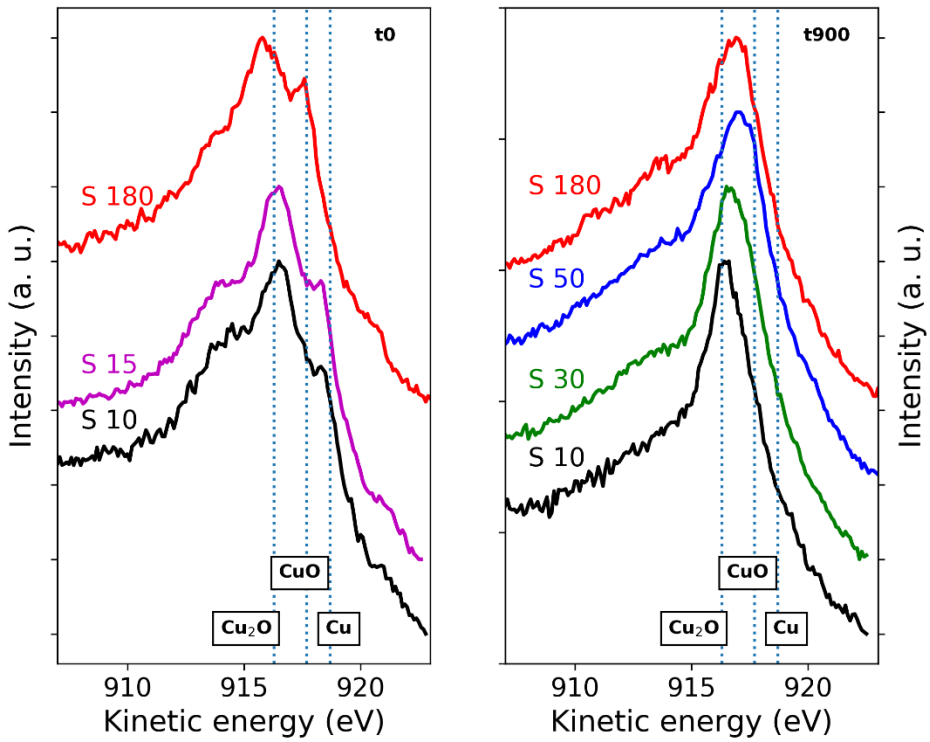

Figure III-8: Cu LMM Auger transition for S10, S15, S30, S50, S180 for raw (left) and fully oxidized (right) samples.

Sample	Cu LMM maxima position (eV)			
S10-t0	913.5	916.5	918.4	921.0
S15-t0	913.9	916.5	918.3	920.8
S180-t0	913.7	915.8	917.6	920.8
S10-t900		916.5		
S30-t900		916.7		
S50-t900		917.1		
S180-t900		916.9		

Table III-4: Positions of the major peaks for the Auger Cu LMM transition for initial and final surfaces.

2.2. Study of the Cu 2p3/2 XPS transition

The CuO contribution to the copper oxide film cannot be precisely determined from the Cu LMM Auger transition. Therefore the Cu $2p_{3/2}$ transition is used for a better characterization of the CuO contribution.

Figure III-9 shows the Cu $2p_{3/2}$ spectra of the raw S10, S15 and S180 samples and fully oxidized S10, S30, S50 and S180 samples. The deconvolution of these spectra evidences the presence of the following peaks: one peak related to both metallic Cu and Cu_2O (932.7 - 933.0 eV), one peak due to CuO (934.5 - 934.8 eV) and a shake-up satellite peak related to. CuO (940.8 - 944.3 eV). The peak positions determined from the deconvolution are reported in Table III-5. The intensity of the CuO peak relatively to the Cu/Cu_2O one is higher after oxidation.

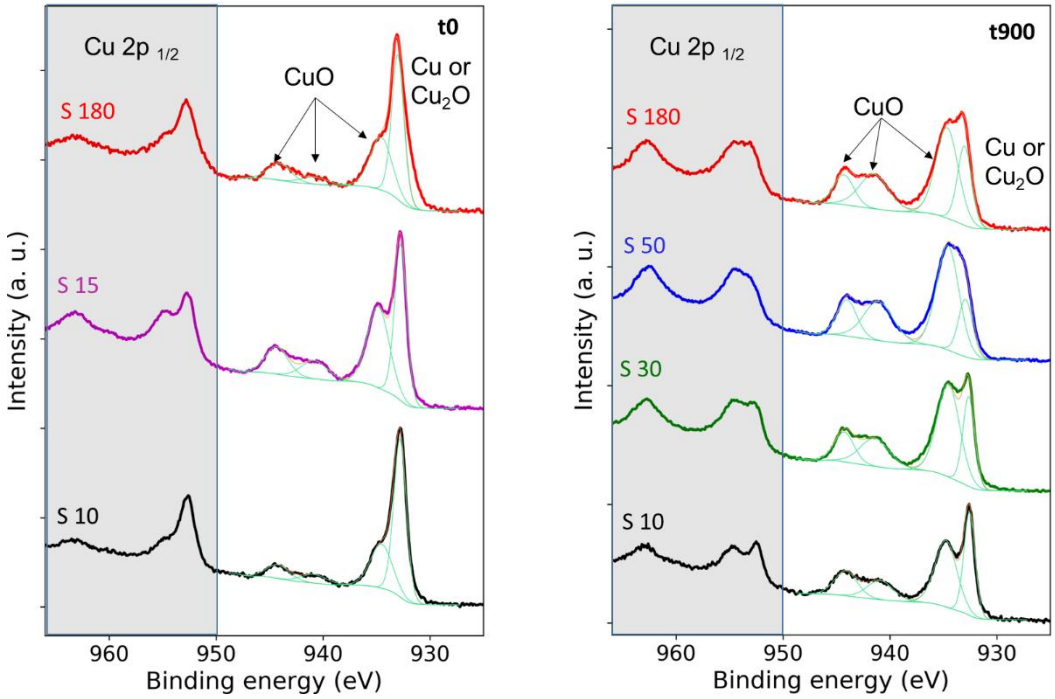

Figure III-9: Cu $2p_{3/2}$ XPS transition for S10, S15, S30, S50 and S180 raw films (left) and fully-oxidized surfaces (right).

Sample	Cu $2p_{3/2}$ maxima position (eV)				%CuO
	Cu or Cu_2O	CuO	CuO satellite		
S10-t0	932.8	934.5	940.83	944.2	43 %
S15-t0	932.7	934.8	940.8	944.3	60 %
S180-t0	933.0	934.6	940.8	944.0	49 %
S10-t900	932.6	934.8	940.9	944.1	69 %
S30-t900	932.6	934.5	941.4	944.3	77 %
S50-t900	932.9	934.6	941.0	944.0	84 %
S180-t900	933.0	934.7	941.5	944.3	77 %

Table III-5: Binding energy value of the major peak for the XPS Cu $2p_{3/2}$ transition for raw and fully-oxidized films.

As a conclusion, as-deposited copper films show a very fine microstructure, with a grain size of a few nm, and a very low roughness with a R_{ms} value of about 1 nm. This microstructure remains thin after full oxidation with a grain size varying from a few nm to 80 nm according to the oxide thickness and a roughness varying from 2 to 14 nm. The oxide layer is observed to be essentially composed of Cu_2O, with the presence of CuO. Even if the semi-quantification shows a non-negligible CuO presence, we will assume in a first approach

that this CuO layer remains thin enough to be ignored in the modeling described in Chapter IV.

3. Determination of the copper and the oxidized thin films thicknesses

The thickness of raw and fully-oxidized thin films has been determined coupling microscopy and spectroscopic techniques, as thicknesses in the ten nanometers range are difficult to access.

3.1. Thickness determination from microscopy

The film thickness has been determined from cross-section SEM images. About 10 measurements in different regions of the sample (1 µm length) have been performed with an accuracy of ± 10 %.

Values are reported in Table III-6. For the 180 nm raw sample the thickness is lower than expected which may be attributed to the thickness inhomogeneity. Additional measurements would be necessary to conclude. For the oxidized samples, an increase of the thickness by a factor of about 1.5 in comparison with the initial targeted Cu thickness is observed. This is related to the volume increase arising from the copper to copper oxide transformation. The Cu to Cu_2O volume variation is theoretically of 1.68 (α_{th} see Appendix 1).

Sample	Thickness (nm)	
	Raw (t0)	Fully oxidized (t900)
S10		34 ± 7
S30		104 ± 29
S50		136 ± 15
S180	137 ± 14	285 ± 35*
* with e_{Cu}: 164 ± 30 and e_{Cu_2O}: 133 ± 20		

Table III-6: Thickness determination from SEM cross section measurement

Additionally to SEM the film thickness has been determined using AFM. The mean thickness of the layers is estimated by the average height of the deposit on the substrate / film steps.

AFM profiles of the raw samples are shown in Figure III-10. Except for the lowest thickness (S10), the steps are well-defined which suggests an accurate determination of the thickness. The AFM thickness values are summarized in Table III-7. These values are close to the targeted ones for raw samples, with standard deviations of the order of the R_{ms} (~ 5 nm).

The AFM profiles for the oxidized samples are reported in Figure III-11. After oxidation, the thickness significantly increases as expected from the Cu to Cu_2O volume increase. The thickness increases by a factor of 2.6, 3.2 and 2.8 for S10, S30 and S50 respectively (Table

III-7). These values are higher than the theoretical volume expansion ($\alpha_{th} = 1.68$). This is assigned to the porous structure of the copper oxide layer.

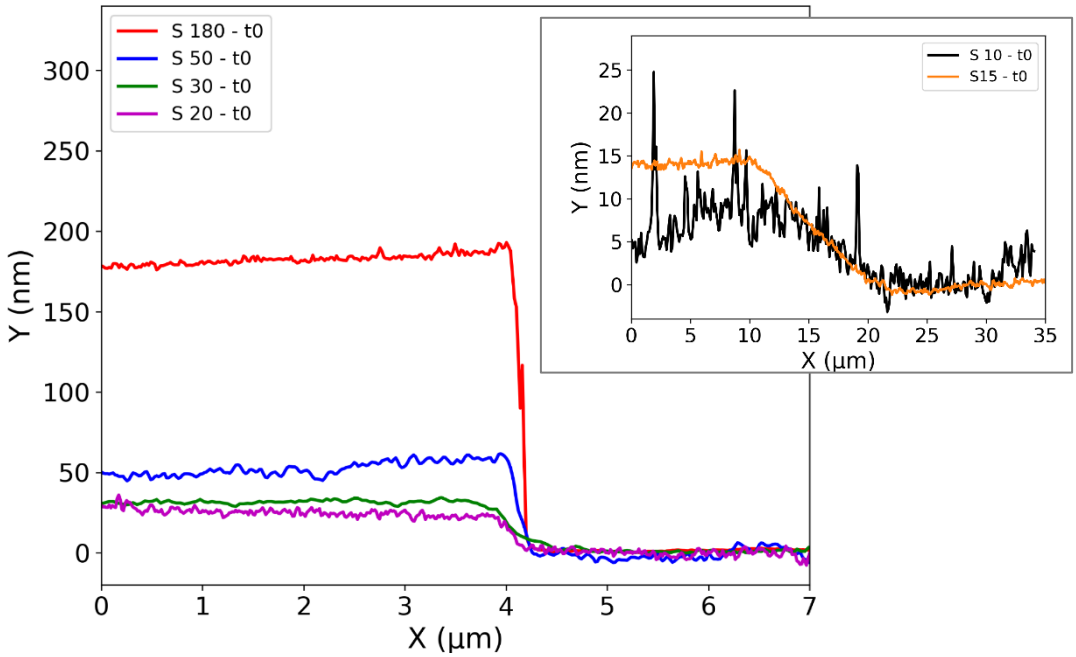

Figure III-10: AFM profiles for raw samples (S10 to S180, t0)

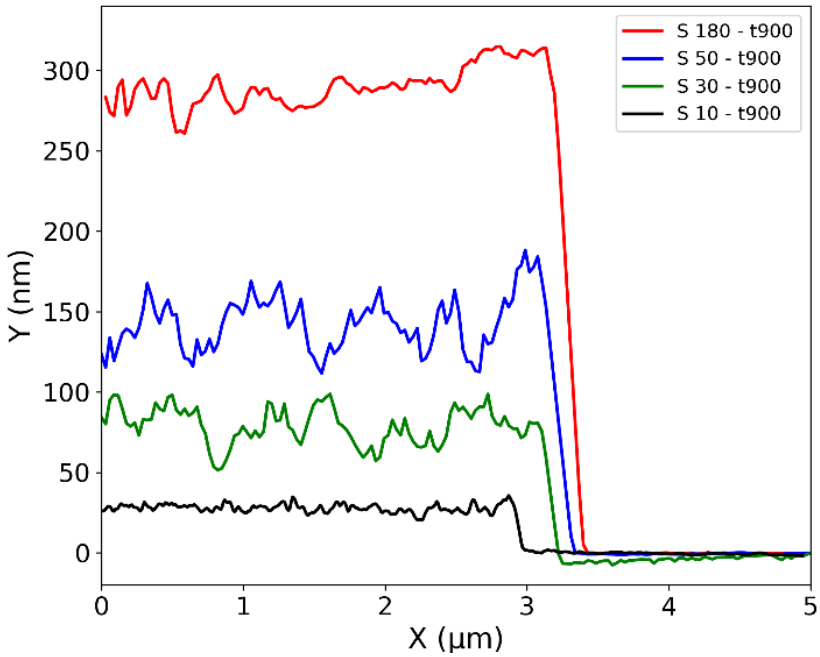

Figure III-11: AFM profiles for oxidized samples (S10 to S180, t900)

Samples	Thickness (nm)		α_{t900}
	Raw	Fully oxidized	
S10	11 ± 3	26 ± 3	2.4 ± 1.2
S15	15 ± 3		
S20	22 ± 5		
S30	31 ± 5	98 ± 23	3.2 ± 1.4
S50	51 ± 8	142 ± 30	2.8 ± 1.2
S180	180 ± 5	288 ± 10*	1.6 ± 0.1

*Table III-7: Thicknesses of raw and fully oxidized sample determined from AFM. * S180-t900 is not fully oxidized*

As a conclusion AFM is a technique allowing the measurement of thin film thickness with a good accuracy.

3.2. Thickness determination from ellipsometry

Multiple angle-dependent (MAI) ellipsometry and spectroscopic ellipsometry (SE) have been used to determine the mean film thickness. A bi-layer Cu/Cu_2O model was chosen with refractive index of n = 0.94530 and κ = 2.5997 and n = 3.1137 and κ = 0.2323 respectively for Cu [141] and Cu_2O [12] for MAI and from Sopra [12] for SE.

3.2.1. Multiple-angle incident (MAI) ellipsometry

The thickness values determined from MAI ellipsometry are reported in Table III-8. The result accuracy is very high, but it is important to note that absolute thickness values are extracted from a model. In our case, the refractive indices are chosen from the literature (Cu: [141] and Cu_2O: [12]). Note also that surface roughness is not accounted in our model. The refractive index of fused silica used as a substrate is measured, and the value obtained perfectly matches that of literature [142]. For the samples with additional copper deposition the model layer stack: substrate / Cu / Cu_2O is considered.

The total thicknesses determined from MAI ellipsometry are close to the AFM values for S15, S20 and S30 Table III-8. The mismatch between AFM and MAI ellipsometry for S10 copper thicknesses is attributed to the assumption on the bulk refractive indices, which poorly describe the optical states of thin sample films. For S50-t0, S180-t0, S50-t900 and S180-t900, the copper films and cuprous films respectively are too thick for a good thickness estimation of cuprous oxide (t0 and t900) and of copper (t0) by ellipsometry. From the ellipsometric measurements, the Cu_2O thickness is close to 2-5 nm. According to the fits, a non-negligible Cu thickness is always present on the ‘fully-oxidized’ samples, which is unexpected. This could be also due to the literature refractive indices used in our models. In fact, for fully oxidized samples a microstructure showing porous layers could affect the refractive index of the layer. Another source of refractive indices change is the increased presence of CuO, manifested by its increased XPS signature. To conclude on this technique, additional error bars should be calculated as the accurate refractive indices of the medium, in particular for the S10 series, and the t900 oxidation step.

Sample	Thickness (nm) from MAI			Thickness (nm) from AFM
	e_{Cu}	e_{Cu_2O}	e_{tot}	e_{tot}
S10-t0	7.2	0.2	7.4	11 ± 3
S15-t0	15	1.8	16.8	15 ± 3
S20-t0	19.7	1.9	21.6	22 ± 5
S30-t0	28.2	2.9	31.1	31 ± 5
S50-t0		3.6		51 ± 8
S180-t0		5.1		180 ± 5
S10-t900	5.6	19.6	25.2	26 ± 3
S30-t900	4.9	84.6	89.5	98 ± 23
S50-t900*	17.1*	102.6*	119.7*	142 ± 30
S180-t900*	114.3*	103.5*	217.8*	288 ± 10

*Table III-8: Cu and Cu_2O thicknesses as determined from MAI ellipsometry. *bad fit: $R^2<0.9$*

As a conclusion MAD ellipsometry is a suitable technique to determine the thickness of raw copper films with a thickness ranging from 15 to 30 nm and allows the determination of the native copper oxide thickness.

3.2.2. Spectroscopic Ellipsometry (SE)

Spectroscopic Ellipsometry (SE) is used in addition to MAI Ellipsometry, to take advantage of the absence of absorbance of Cu_2O at wavelength higher than 600 nm, in the modelling.

The thicknesses determined from SE are reported in Table III-9. The thickness of copper oxide, e_{Cu_2O}, is around 3-5 nm for all the samples, and in general the total thicknesses are comparable to the AFM (within the error bars).

Again the copper thickness for S50-t0 and S180-t0 as the cuprous oxide thickness for S50-t900 and S180-t900 cannot be correctly determined, since the films absorbance are too high. For S10 and S30, the ratio α_{t900} (~1.7) calculated as (66) is very close to the one expected for a dense layer (1.68), which support the hypothesis of a dense layer of uniaxial growth.

$$\alpha_{t900} = \frac{e_{Cu_2O,t900} - e_{Cu_2O,t0}}{e_{Cu,t0} - e_{Cu,t900}} \quad (66)$$

Samples	Thickness (nm) from SE			Thickness (nm) from AFM
	e_{Cu}	e_{tot}	e_{tot}	e_{tot}
S10-t0	11.0 ± 0.2	3.4 ± 0.2	14.4 ± 0.4	11 ± 3
S15-t0	18.2 ± 0.3	3.7 ± 0.2	21.9 ± 0.5	15 ± 3
S20-t0	24.5 ± 0.5	4 ± 0.2	28.5 ± 0.7	22 ± 5
S30-t0	38.7 ± 1.3	3.7 ± 0.2	42.4 ± 1.5	31 ± 5
S50-t0		5 ± 0.9		51 ± 8
S180-t0		4.2 ± 0.7		180 ± 5
S10-t900	0.9 ± 0.4	20.3 ± 3.1	21.2 ± 3.5	26 ± 3
S30-t900	0.3 ± 1.4	65.1 ± 7.4	65.4 ± 8.8	98 ± 23
S50-t900	0 ± 7.9	87.5 ± 3.7		142 ± 30
S180-t900*		107.7 ± 1.7*		288 ± 10
		α_{t900}		
S10		1.67 ± 0.46		
S30		1.60 ± 0.33		

*Table III-9: Cu and Cu_2O thickness determination from SE, *bad fit: $R^2<0.9$*

To summarize, the thicknesses values determined from SE are comparable to AFM ones. Compared to MAI, SE is wavelength dependent which for Cu/Cu_2O sample may be more sensitive in particular for fully oxidized samples for $\lambda > 600$ nm, where only copper absorbs. The technique returns expected thicknesses of Cu_2O for the raw surface (3 - 5 nm), and no Cu presence for the fully oxidized samples. In addition the results support the complete transformation of copper into copper oxide, with a ratio α_{t900} close to that of a uniaxial volume expansion of dense copper to cupric oxide layers.

3.3. UV-vis spectroscopy (UVS)

SE measurements can be considered as UV-visible absorption measurements in a reflection and polarized configuration. On the other hand, transmission mode is generally not used to study metallic layers because of their strong absorption, but thin and ultra-thin copper layers deposited on fused silica substrates are eligible for such a study. Experimental measurements are compared and fitted by calculations based on Fresnel equations, in collaboration with Dominique Barchiesi at Université Technologique de Troyes. The main objectives are to estimate the thickness of the copper and oxide layers but also to discuss the evolution of the optical properties as a function of the thickness.

3.3.1. Raw and fully oxidized surfaces

We start by a description and a comparison of the theoretical and experimental spectra of pure copper and pure cuprous oxide.

Theoretical absorbance spectra for pure copper samples of thickness 10, 30 and 50 nm and for the fully oxidized counterparts assuming a uniaxial dense growth of cuprous oxide (17, 50 and 84 nm respectively) and using the relative permittivities from Mc Peak [141] and Sopra [12] respectively, are represented on Figure III-12 (solid lines). One observes a general increase of the absorbance for increasing thicknesses of copper and cuprous oxide. However,

the profile of the spectra changes for thin layers due to multi-reflection on the thin layers and concomitant interferences. The absorbance spectra of copper are marked by a minimum around λ ~580 nm, assigned to the onset of interband transitions [143] which is more pronounced for thicker layers, and is responsible for the characteristic bright pink-salmon color of metallic copper. On the other hand, the absorbance spectra of cuprous oxide is strong for λ < 500 nm and drops rapidly above this threshold: cuprous oxide is essentially transparent for wavelengths larger than 600 nm, leading to a pale red color.

The experimental UV-visible absorbance of initial and fully-oxidized samples, as measured in transmission mode, are compared in Figure III-12 (dashed lines) The profiles of the calculated and experimental spectra of copper are very close, even though the experimental absorbances are systematically larger suggesting that the actual thicknesses are larger than the targeted ones, in agreement with the AFM results (11, 30 and 55 nm). Logically, the experimental absorbances are larger for oxide copper samples as well, with in addition slight differences in the profile suggesting that the permittivities used for the calculations are not perfectly matching those of the samples.

The model of pure copper fully transformed into cuprous oxide is supported and seems to be appropriate for the description of the samples.

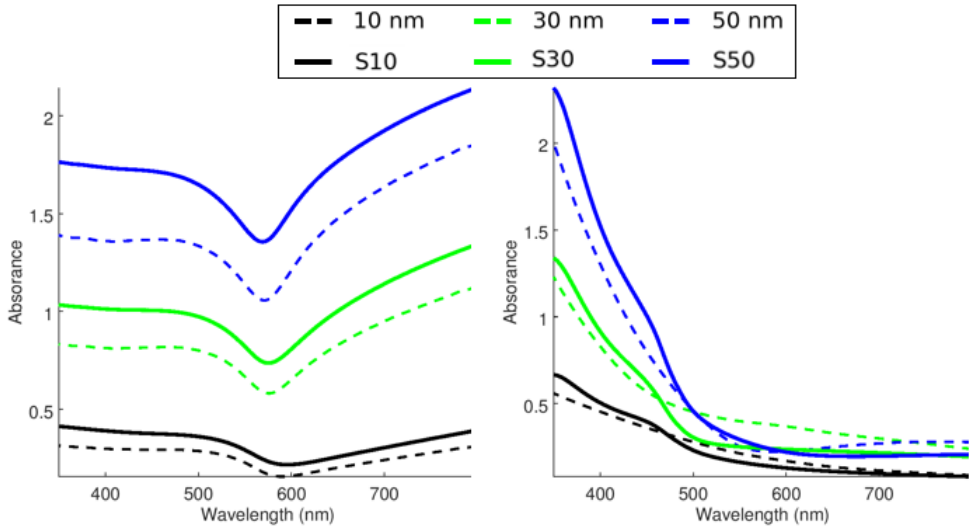

Figure III-12: Comparison of calculated (dashed lines) with experimental (solid lines) absorbances for copper (left) and cuprous oxide (right) thin films. Calculation of pure copper 10, 30 and 50 nm and their fully-oxidized Cu_2O counterpart of 17, 50 and 84 nm assuming a coefficient of $\alpha_{the} = 1.68$, and refractive indices from [141, 12]. Experiments are for raw and fully-oxidized samples of the series S10, S30 and S50

3.3.2. Partially oxidized samples

Figure III-13 shows the evolution of the absorbance spectra during thermal oxidation for the S10, S30 and S50 series. For each series, the absorbance of the raw samples is close to that of pure copper. Then, the growth of copper oxide is featured by rising and dropping absorbances at small and large wavelengths, respectively. For long oxidation treatments, the characteristic transmission peak of copper around 580 nm damps and the spectra are dominated by the signature of copper oxide.

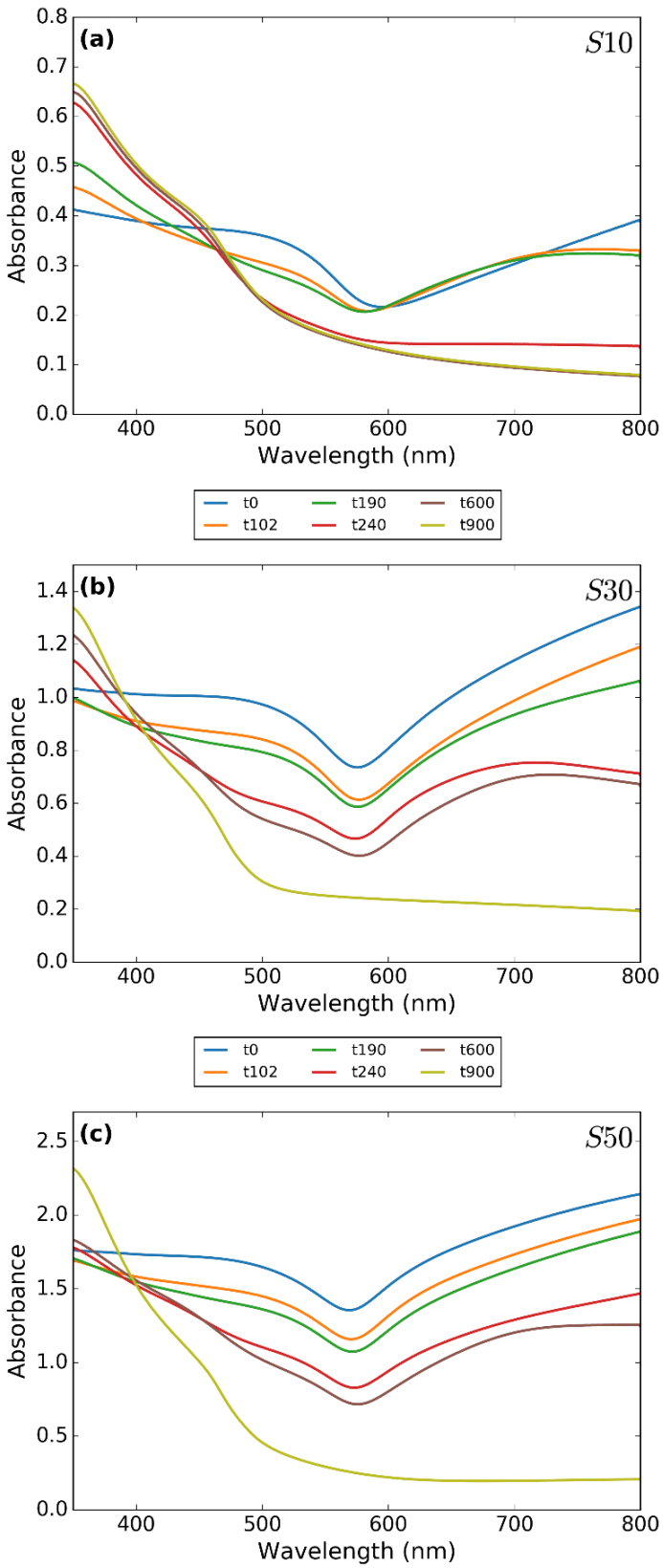

Figure III-13: Absorbance evolution with oxidation time, for S10 (a), S30 (b) and S50 (c) series.

3.3.3. Fitting procedure description.

Fresnel equations are used to model the absorbance data assuming a homogeneous cuprous oxide/copper bilayers with parallel faces, without roughness on visible light scale, deposited on a fused silica substrate, as sketched in Figure III-14 according to [144, 145]. The goal is to determine the effective thicknesses of copper and cuprous oxide (e_{Cu} , e_{Cu_2O}), and discuss their effective dielectric permittivities ($\epsilon_{Cu}(\lambda)$, $\epsilon_{Cu_2O}(\lambda)$). Note that the experimental absorbance of the bare silica substrate was measured and successfully fitted with dielectric permittivities of reference [142]

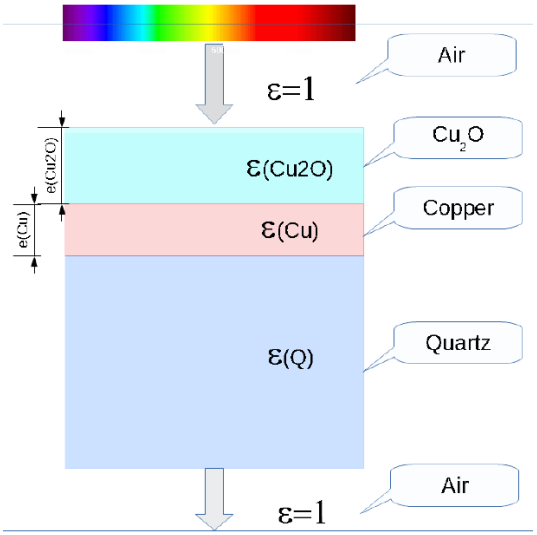

Figure III-14: Sketch of light transmission by a bilayer sample, with normal incident light coming from the Cu_2O side.

In the first method, the dielectric permittivities of copper, cuprous oxide and fused silica are fixed to values of the literature (from references [141, 12, 142], respectively), and the thicknesses of Cu and Cu_2O are fitted for each wavelength. The fit results are presented in Figure III-15 for the raw and fully oxidized samples of the S50 series. No unique solution is found but the ranges of fitted thickness is fairly narrow over the spectral range 400-800 nm, lying between 52 and 65 nm for copper and below 4 nm for cuprous oxide. By contrast, the results are surprisingly very different within the spectral range 350-400 nm, suggesting that the permittivities are not matching those of the samples.

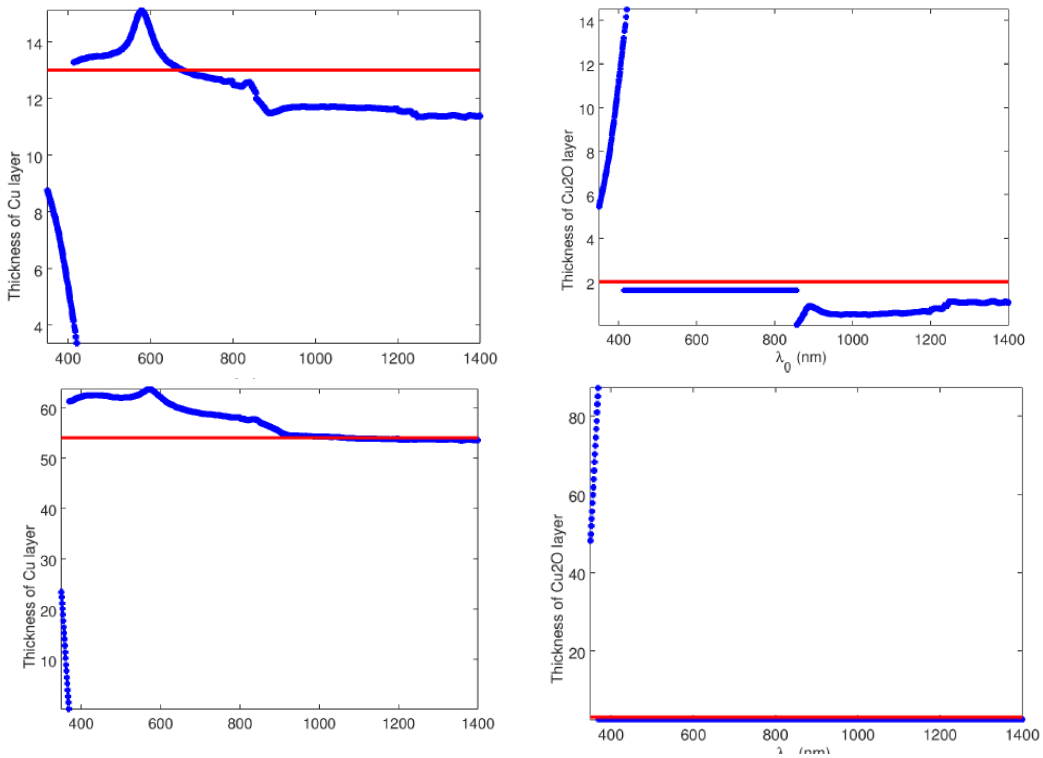

Figure III-15: Fitted thickness of Cu (left) and Cu_2O (right) for S10-t0 (top) and S50-t0 (bottom) for each wavelength in the range 350-1400 nm (blue symbols). The red line corresponds to the fitted thickness.

In the second method, the whole set of data is fitted simultaneously with unique values of the e_{Cu} and e_{Cu_2O}, and the following constraints:

- $e_{Cu} \in [0\,; e_{Cu}(AFM) + 10]$
- $e_{Cu_2O} \in [0\,; 5 * e_{Cu}(AFM)]$

This fitting method is first used to determine the approximate thicknesses of copper and cuprous oxide using the dielectric permittivities ($\epsilon_{Cu}(\lambda)$, $\epsilon_{Cu_2O}(\lambda)$, $\epsilon_{fused\ silica}(\lambda)$) still from the literature.

The best results for e_{Cu} and e_{Cu_2O}, are used as input values for the third method, where the effective permittivities $\epsilon_{Cu}(\lambda)$, $\epsilon_{Cu_2O}(\lambda)$ together with the effective copper and cuprous thicknesses (e_{Cu} , e_{Cu_2O}) are used. The effective permittivities are complex, so both the real and imaginary part are fitted, so that there are 6 fitting parameters (e_{Cu} , e_{Cu_2O}, $\Re(\epsilon_{Cu}(\lambda)), \Im(\epsilon_{Cu}(\lambda))$, $\Re(\epsilon_{Cu_2O}(\lambda)), \Im(\epsilon_{Cu_2O}(\lambda))$) with the following constraints:

- limited variations of the thicknesses (± 20% away from the input values)
- limited variations of the permittivities (a) ± 10% and b) ± 20% away from the input values from references [141] and [12])

Here, to limit the calculation time, the fit was achieved over a selection of 6, 15 and 25 equivalently spaced wavelengths. The strong constraints on the fit parameters, plus the good agreement between the fit results for these three selections, in addition to the local monotony of the permittivities, allow to state that the solutions are unique.

A comparison of fits achieved with this first method is proposed in Figure III-16 for S50-t0, S50-t102 and S50-t900, as example of raw partially and fully oxidized fits. The fits are unable to match them at any place. Therefore the second and the last method are considered, with typical results for the same samples S50-t0 -t102 and -t900 at the right of Figure III-16. The fit with the dielectric permittivities from the literature gives a result quite close to the experimental data but is unable to perfectly match them. On the other hand, fitting the permittivities leads to an excellent agreement with the experimental data.

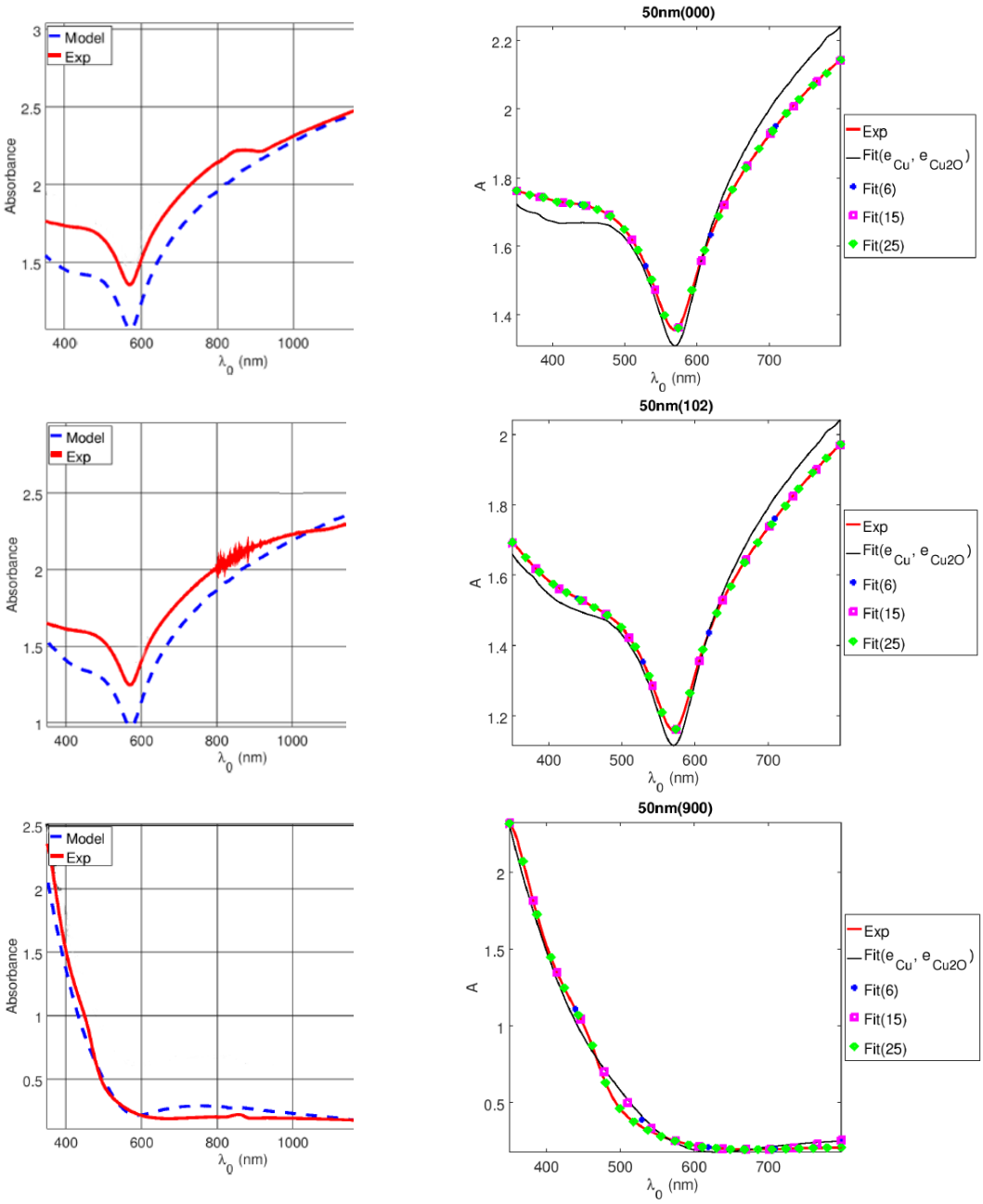

Figure III-16: Comparison of the experimental absorbance spectra for a raw S50-0 (upper) a partially oxidized S50-102 (center) and a fully oxidized S50-900 (lower) for fitting method 1 (left) and method 2 and 3 (right). The fits for the second method (black line) and the last method for a section of 6, 15 and 25 wavelengths selected.

Method 3a was used to fit the whole three series of spectra S10, S30 and S50 (Figure III-17). Very good results are achieved for raw and partly-oxidized samples, for the t102 and t190 for S10, S30 and S50. (S10-t0, S30-t0, S50-t0, S10-t102, S30-t102, S50-t102, S10-t190, S30-t190, S50-t190) On the other hand, the fits do not perfectly match the experimental data for further oxidation steps t240 and t600. This suggests that the refractive index of copper changes for small thicknesses, as already reported for thin gold films [146, 147]. For t900 the fit is also not perfect. These discrepancies are assigned to the increasing roughness (AFM data of Figure III-5 and Table III-2), porous and heterogeneous microstructure (see SEM pictures of sample S180-900 on Figure III-4), and presence of a significant cupric oxide layer for fully-oxidized samples (see XPS data of Figure III-9Figure III-8).

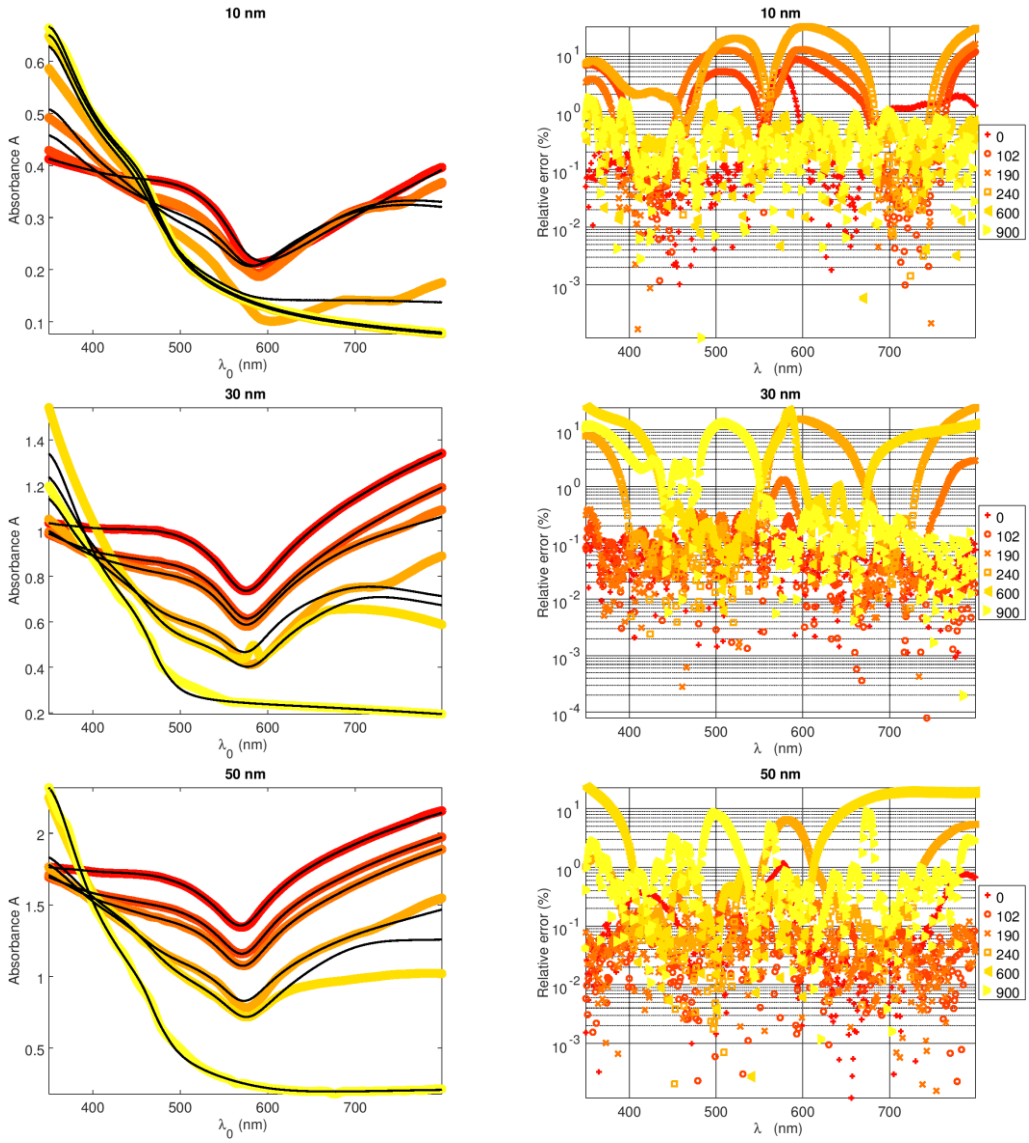

Figure III-17: Best fits (color lines, from red to yellow for increasing oxidation) of the absorbance spectra (black lines) for the three series of samples S10 (top) S30 (middle) and S50 (bottom) series with (right) the corresponding relative errors.

An alternative fit, with larger allowed variation of the refractive indices (Method 3b) gives perfect fits for the all samples, except for the fully-oxidized one (t900). Figure III-18, Figure

III-19 and Figure III-20 show these fits for a selection of 5, 15 and 25 fitted wavelengths and for the second method along.

Compared to the Method 3a, the relative error remains in the same range (0-0.01%). Even if the fit are better for Method 3b, we chose to rely on the fitted thicknesses determined in 3a, since the refractive indices are closer to the one from the literature.

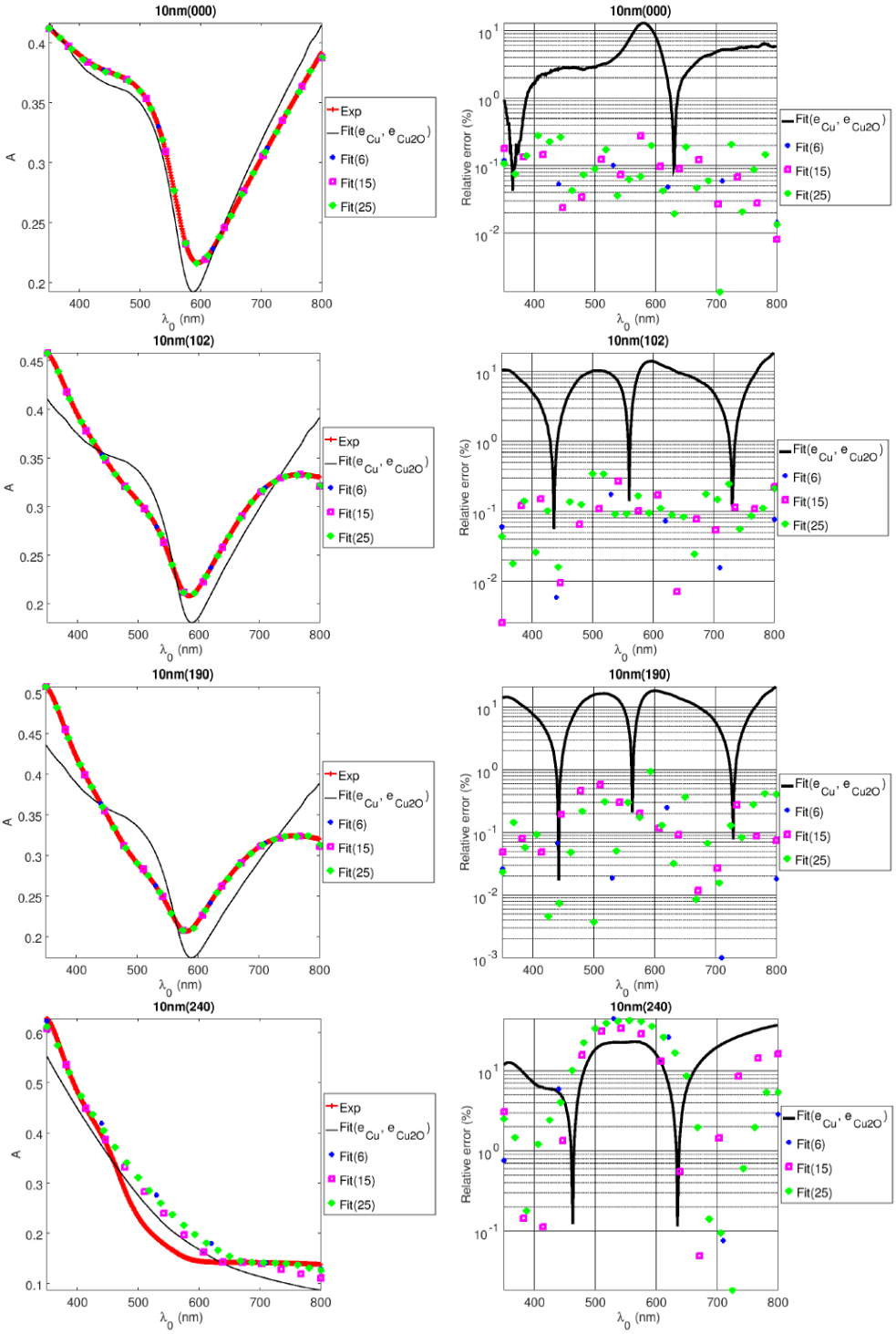

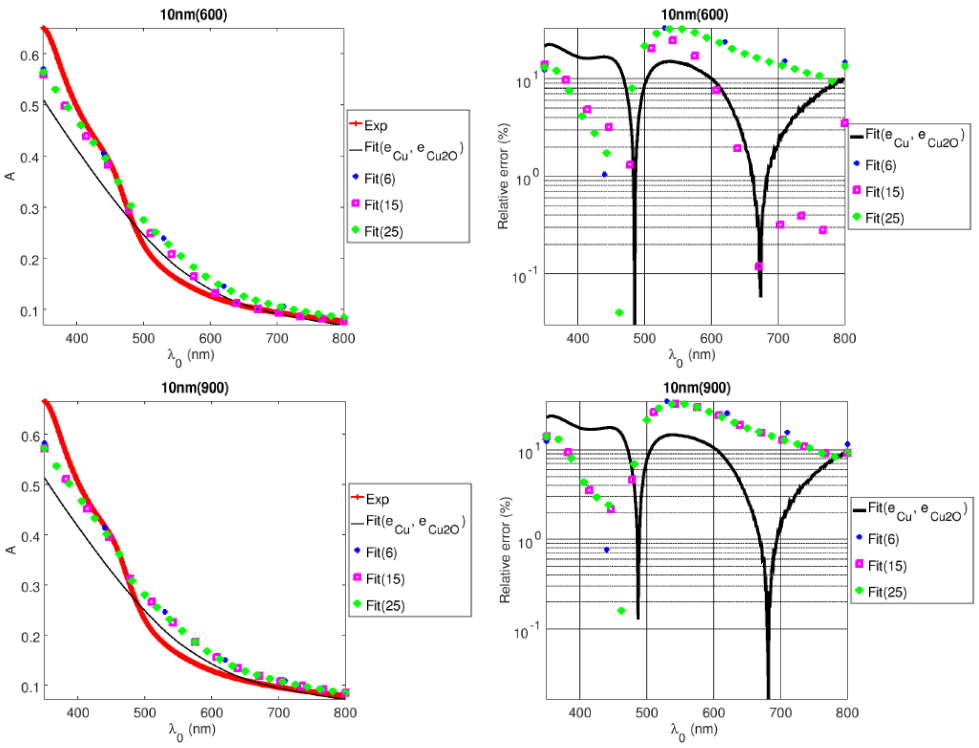

Figure III-18: Best fits (color lines) of the absorbance spectra (black lines) for the three series of samples S10-t0 to S10-t900 (top to bottom)

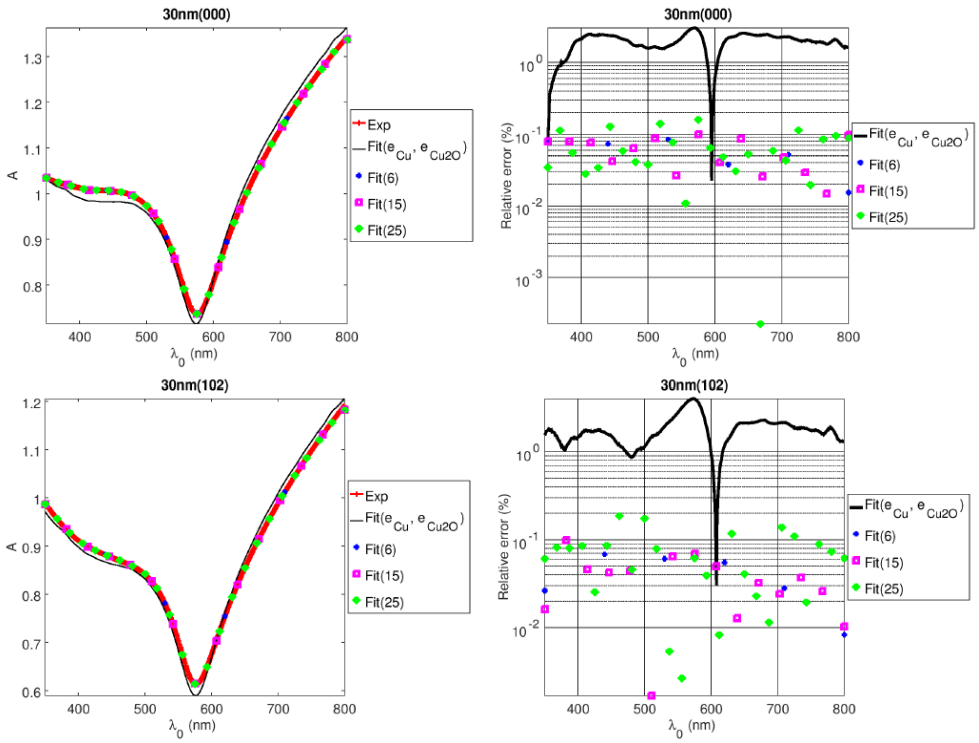

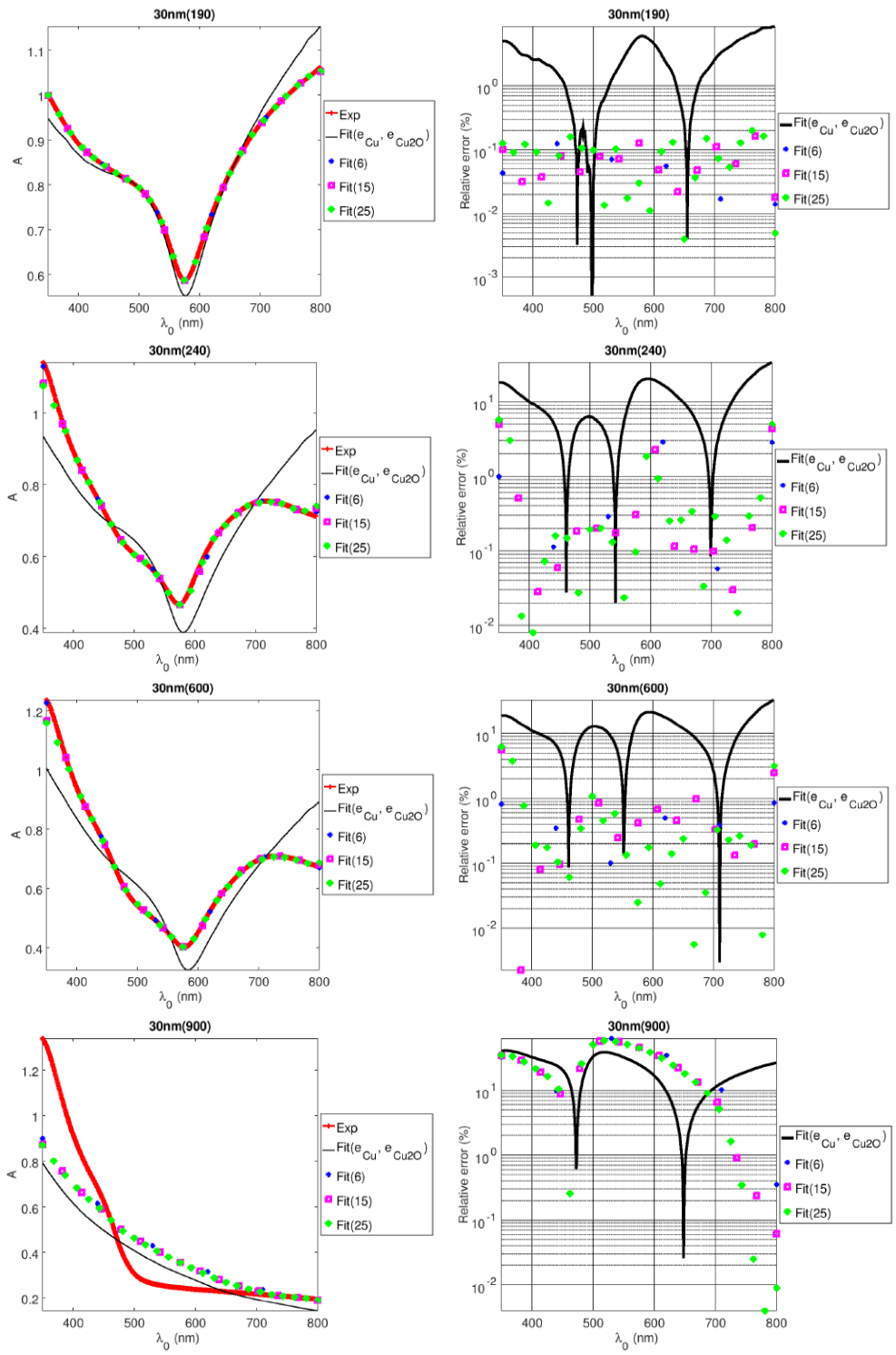

Figure III-19: Best fits (color lines) of the absorbance spectra (black lines) for the three series of samples S30-t0 to S30-t900 (top to bottom)

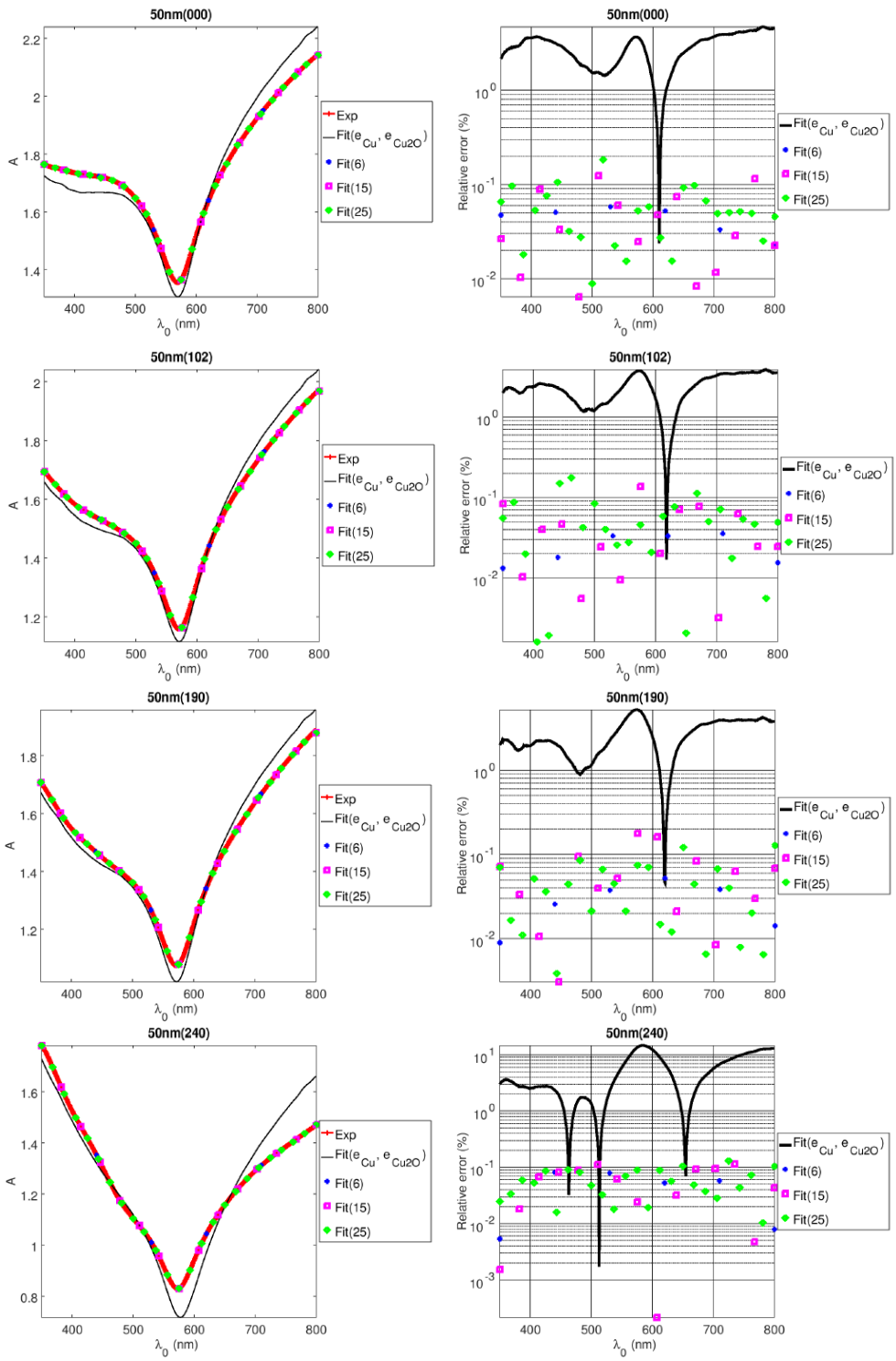
50nm(000)
50nm(102)
50nm(190)
50nm(240)
A
Relative error (%)
λ0 (nm)
Exp
Fit(eCu, eCu2O)
Fit(6)
Fit(15)
Fit(25)

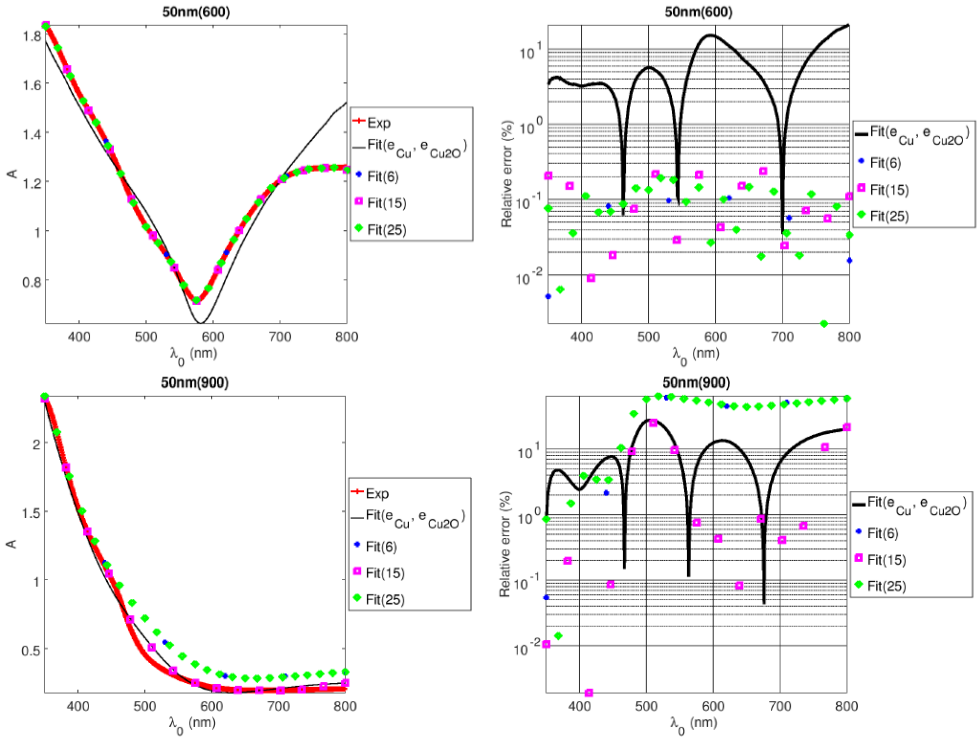

Figure III-20: Best fits (color lines) of the absorbance spectra (black lines) for the three series of samples S50-t0 to S50-t900 (top to bottom)

3.3.1. Refractive indices

Figure III-21 compares the fitted refractive indices with those from the literature. The fitted values for metallic copper are very close to the bibliographic values from Mc Peak [141]. By contrast, the fitted values for cuprous oxide Cu_2O systematically from those of Sopra [12], with a typical upshift of +0.2 over the whole spectral range for the real part $n(Cu_2O)$ and an increasing upshift up to 0.2 at 800 nm for the imaginary part $\kappa(Cu_2O)$

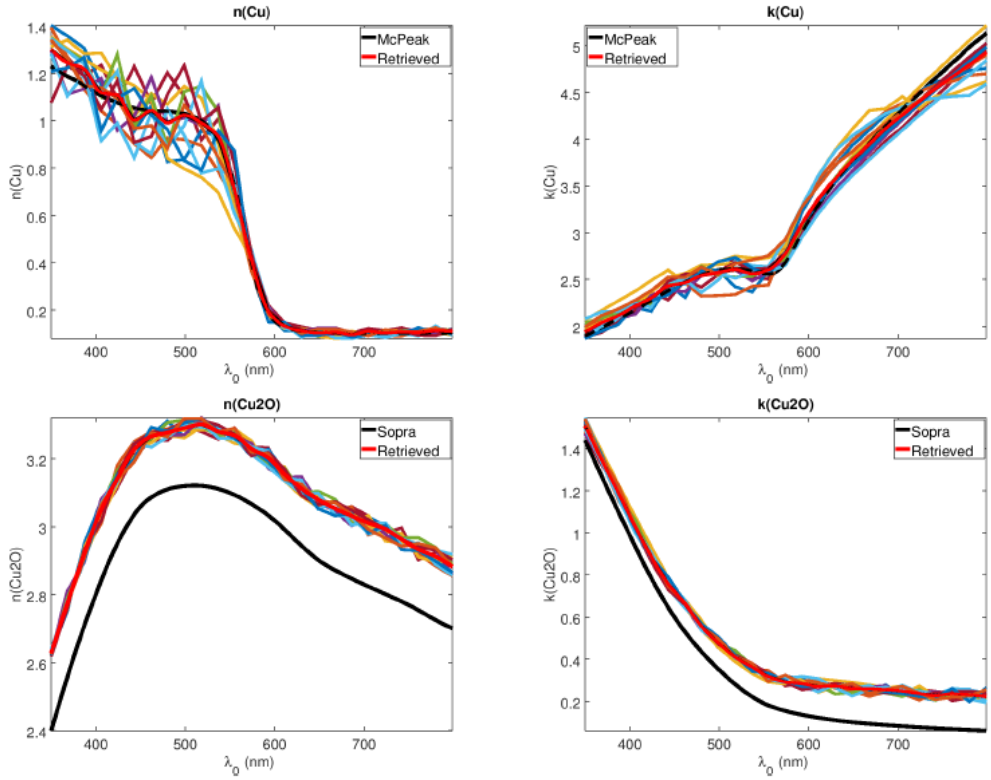

Figure III-21: Comparison of the real part (left) and imaginary part (right) of the fitted refractive indices (color lines for all oxidation step for S30 and S50 series) and those from Sopra ([12], black line), for Cu (top), and Cu_2O (bottom)

3.3.2. Summary of UVS fit

Table III-10 summarizes the best fit results for the effective copper and cuprous layers, corresponding to the effective refractive indices of Figure III-21.

The fitting results are coherent with the AFM/SEM measurements for all samples but the fully-oxidized samples S50-t900, for which the fitted oxide thickness is equal to ~90 nm, *ie* much smaller than the 120 nm measured by SEM. This is assigned to a weaker accuracy for absorbances larger than 2.

For the S10 series, the copper thickness decreases as the cuprous layer grows. We can remark the last value incoherence of total thickness, increasing up to 16 nm for S10-t240, and then decreasing down to 10 nm and 12 nm for S10-t600 and S10-t900 respectively.

Sample	Thickness (nm) from UV-vis fit		
	e_{Cu}	e_{Cu_2O}	e_{tot}
S10-t0	12.8 ± 0.6	0 ± 0.1	12.8 ± 0.7
S10-t102	12.3 ± 0.6	1.5 ± 0.1	13.8 ± 0.7
S10-t190	12.8 ± 0.6	3.3 ± 0.2	16.1 ± 0.8
S10-t240*	8.3 ± 0.4*	8.5 ± 0.4*	16.8 ± 0.8*
S10-t600*	0 ± 0.1*	10.5 ± 0.5*	10.5 ± 0.6*
S10-t900*	0 ± 0.1*	12.5 ± 0.5*	12.5 ± 0.6*
S30-t0	35.0 ± 1.8	0.5 ±0.1	35.5 ± 1.9
S30-t102	33.5 ± 1.7	2.8 ± 0.1	36.3 ± 1.8
S30-t190	31.0± 1.6	2.5 ± 0.1	33.5 ± 1.7
S30-t240*	28.0 ± 1.4*	9.8 ± 0.5*	37.8 ± 1.9*
S30-t600*	8.8 ± 0.4*	62.8 ± 3.1*	71.6 ± 3.5*
S30-t900*	0 ± 0.9*	89.5 ± 4.5*	89.5 ± 5.4*
S50-t0	63.0 ± 3.2	0.5 ± 0.1	63.5 ± 3.3
S50-t102	56.8 ± 2.8	6.3 ± 0.3	63.1 ± 3.1
S50-t190	55.3 ± 2.8	7.5 ± 0.4	62.8 ± 3.2
S50-t240*	47.0 ± 2.4*	14.3 ± 0.7*	61.3 ± 3.1*
S50-t600*	17.5 ± 0.9*	87.5 ± 4.3*	105.0 ± 5.2*
S50-t900*	0 ± 1.1*	88 ± 4.5*	88 ± 5.6*

*Table III-10: Copper and cuprous thickness from UV-vis fitting for S10, S30 and S50. *poor fit for method 3a*

4. Discussion

Different techniques are used to estimate the thickness of copper and its oxide layer. AFM and SEM give a direct estimation of the thickness but only on local selected areas (~1 µm), which may not necessarily be representative of the whole sample. On the other hand, spectroscopic techniques (ellipsometry and UVS) are probing larger areas (~1 mm), but the model used to fit the data relies on some hypothesis, *i.e.* homogeneous thin layers with parallel faces (no roughness), and requires the knowledge of the dielectric permittivities to determine accurately the thicknesses of Cu and Cu_2O. Below, we compare the thicknesses measured on the same samples by different techniques and discuss which technique(s) is (are) more relevant as a function of the nature of the samples and their thicknesses. Finally we discuss the kinetics of oxidation as a function of the thickness of the raw samples, and propose an extrapolation for ‘‘infinite’’ (bulk) samples.

4.1. Raw samples

The raw samples series S10, S30 and S50 were probed by AFM, MAI, SE, and UVS. The resulting total thickness (e_{Cu}+e_{Cu_2O}) are compared in the left part of Figure III-22. The error bars corresponds to the roughness for AFM and to the fitting accuracy for ellipsometry and UVS.

The results from different techniques are quite dispersed. Thicknesses measured with MAI and SE are systematically smaller and larger, respectively than those measured by UVS, but considering the error bars, SE and UVS are consistent. Here we remind that UVS model is

using optimized refractive indices, whereas the MAI uses literature values from Mc Peak (Cu) and Sopra (Cu_2O) and SE uses only Sopra's refractive indices [141, 12], so that the dispersion of results may be explained by these different sets of refractive indices. We remind that UV-vis spectra cannot be correctly fitted using Sopra's indices for cuprous oxide. We consider that the UVS results, using optimized refractive indices, are the most accurate spectroscopic results, and that providing the difference of refractive indices, the agreement with MAI and SE is fair. On the other hand, the thickness measured by AFM are systematically smaller than those measured by UVS, but the results are consistent within the error bars.

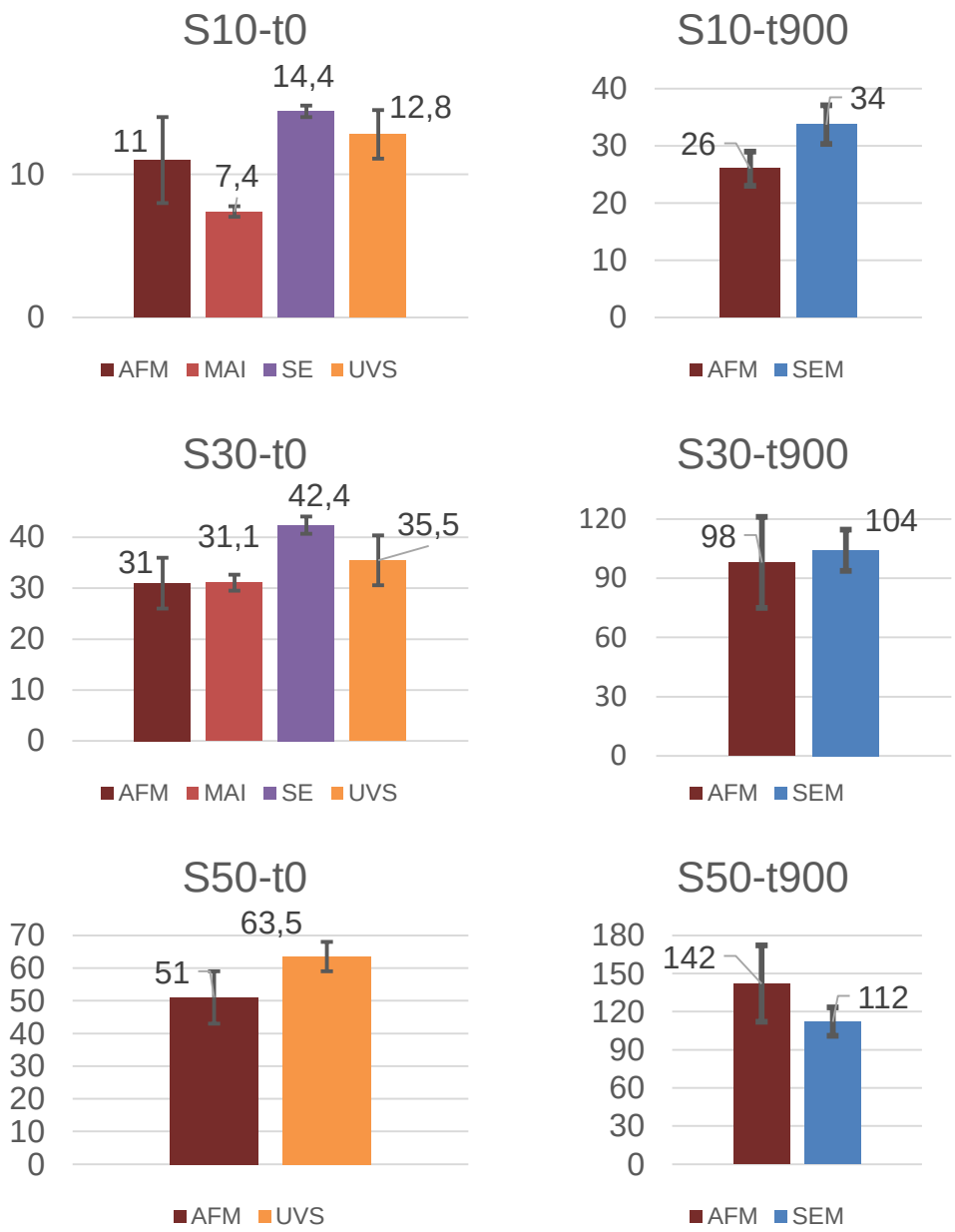

Figure III-22: Comparison of raw (left) and fully oxidized (right) samples of S10, S30 and S50 measured by AFM, angle dependent and spectroscopic ellipsometry, UVS and SEM.

4.2. Partly and fully oxidized surfaces

Due to the swiftness and convenience of the measurements, the thickness of partly oxidized was characterized by UVS only (the samples are also thoroughly investigated in Raman, as discussed in Chapter IV).

Moreover, good fits of the data are achieved for oxidation steps t102 to t600. Therefore, thicknesses measured by UVS will be considered for corresponding samples of series S10, S30 and S50.

However, no good fits of the UV-vis spectra could be achieved for fully-oxidized samples, likely because of the heterogeneous structure of the layers (see SEM cross-section of sample S180-t900) and/or the unneglectable optical contribution of the superficial layer of CuO (see XPS spectra of fully oxidized samples). Therefore, SEM and AFM measurements are privileged to determine the total thickness. Moreover, fully oxidized samples are considered as made of copper oxide only, since no underlying layer of copper could be detected neither from the UV-vis fits, nor from the SEM observations. Thicknesses measured by SEM and AFM are in fair agreement with each other (Figure III-22), and are the retained data for t900.

All the results are summarized in Table III-11:

Sample	Thickness (nm) from techniques comparison		
	e_{Cu}	e_{Cu_2O}	e_{tot}
S10-t0	12.8 ± 0.6	0 ± 0.1	12.8 ± 0.7
S10-t102	12.3 ± 0.6	1.5 ± 0.1	13.8 ± 0.7
S10-t190	12.8 ± 0.6	3.3 ± 0.2	16.1 ± 0.8
S10-t240	8.3 ± 0.4	8.5 ± 0.4	16.8 ± 0.8
S10-t600	0 ± 0.1	10.5 ± 0.5	10.5 ± 0.6
S10-t900*	0*	30 ± 7*	30 ± 7*
S30-t0	35.0 ± 1.8	0.5 ±0.1	35.5 ± 1.9
S30-t102	33.5 ± 1.7	2.8 ± 0.1	36.3 ± 1.8
S30-t190	31.0± 1.6	2.5 ± 0.1	33.5 ± 1.7
S30-t240	28.0 ± 1.4	9.8 ± 0.5	37.8 ± 1.9
S30-t600	8.8 ± 0.4	62.8 ± 3.1	71.6 ± 3.5
S30-t900*	0*	104 ± 20*	104 ± 20*
S50-t0	63.0 ± 3.2	0.5 ± 0.1	63.5 ± 3.3
S50-t102	56.8 ± 2.8	6.3 ± 0.3	63.1 ± 3.1
S50-t190	55.3 ± 2.8	7.5 ± 0.4	62.8 ± 3.2
S50-t240	47.0 ± 2.4	14.3 ± 0.7	61.3 ± 3.1
S50-t600	17.5 ± 0.9	87.5 ± 4.3	105.0 ± 5.2
S50-t900*	0*	136 ± 40*	136 ± 40*

*Table III-11: Thicknesses of Cu and Cu_2O for S10, S30 and S50 retained for future discussions, from UV-S. *values from AFM and SEM-cross section*

4.3. Estimation of the thickness of a cuprous oxide layer on a ‘‘bulk’’ copper substrate

In order to estimate the thickness of the copper oxide layer grown on a ‘‘bulk’’ copper substrate, a comparison of the kinetic oxidation is achieved on series S10, S30 and S50, and extrapolated to series S180, and to other series of bulk samples in chapter IV. The raw sample of series S180 is considered as a bulk copper substrate, since even at the last oxidation step (sample S180-t900), the copper thickness remains larger than 100 nm (see cross-section SEM picture in Figure III-4).

We first compare the evolution of copper and cuprous oxide thicknesses up to the oxidation step t600 for S10, S30 and S50 series (Figure III-23 fully oxidized samples are not considered since their microstructure and/or composition is different from the other samples of the series). The corresponding ratio of uniaxial transformation of Cu to Cu_2O (α_{t600}) are calculated from these data, and presented in Table III-12. Within the error bar, the coefficient is quite close to the theoretical value of $\alpha_{th} = 1.68$ for the S50.

By contrast, the coefficient is much smaller for the series S10, likely due to inaccuracies on the thickness or optical properties of such ultrathin layers, and much larger for the series S30, essentially because of the results for sample S30-t600, which may also present a heterogeneous / porous structure (no microstructural data available for this sample). For these two latter series, the ratio of uniaxial transformation is much closer to the theoretical value is one considers only the four first samples of the series (see the guidelines in Figure III-23).

Finally, as expected, the copper oxide thickness for fully oxidized α_{t900} samples is much larger than α_{th} for all series, which is attributed to the porous / inhomogeneous microstructure of these samples.

We now compare the kinetic of growth for the partly-oxidized samples of the three series (Figure III-24). In the first steps of oxidation (until the 4th, *ie* t240), the growth of the oxide layer is close for all series, but still slightly faster for series S50. At the 5th step, the kinetics is slowing down for series S10 as most of the copper layer is oxidized, and the kinetics of oxidation of series S30 remains slightly slower than that of series S50. In the following, we will assume that the kinetics of growth, and therefore the thickness of the cuprous oxide layer, is the same for the series S50 and S180 (‘‘bulk’’ samples) until the 5th oxidation step (t600).

As far as the 6th oxidation step is concerned, the bilayer structure and corresponding total thickness of oxide of sample S180-t900 is completely described by the SEM cross-section. The value of Cu_2O thickness evolution is summarized in Figure III-24 and Table III-13:

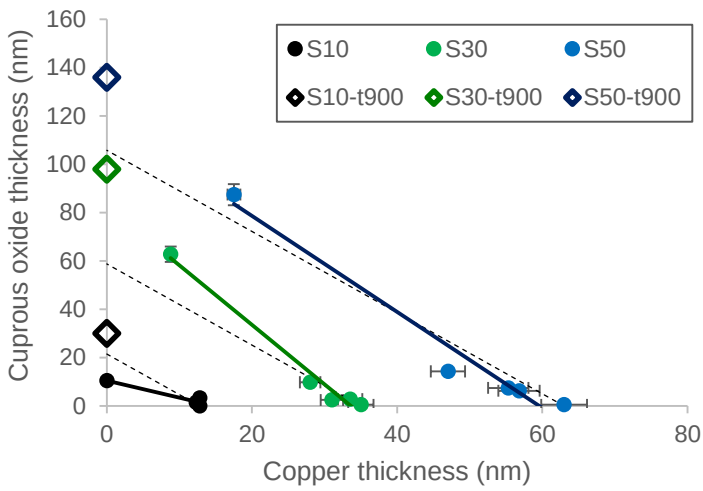

Figure III-23: Compared evolution of the thicknesses of copper and copper oxide layers for S10, S30 and S50

Series	α_{t600}	α_{t900}
S10	0.70 ± 0.12	2.36 ± 0.35
S30	2.47 ± 0.39	2.69 ± 0.45
S50	1.75 ± 0.87	2.17 ± 0.21

Table III-12: The values of the coefficient of transformation α_{t600} and α_{t900} are given for the oxidation step t600

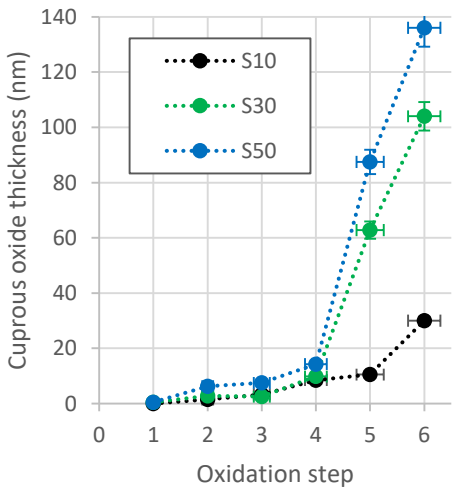

Figure III-24: Comparison of the thickness of Cu_2O for the oxidation steps (1: t0, 2: t102, 3: t190, 4: t240, 5:t600, 6: t900)

Oxidation step	e_{Cu_2O}
S180-t0	1 ± 1
S180-t102	4 ± 1
S180-t190	6 ± 1
S180-t240	13 ± 2
S180-t600	88 ± 5
S180-t900*	133 ± 20*

Table III-13: Values of Cu_2O for the sample S180, estimated from the average on S10, S30 and S50 series for t0 to t240. S180-t600 is the value of S50-t600. S180-t900 is the value estimated by SEM cross section

In conclusion UVS was shown to be a powerful technique to measure the thicknesses of Cu and Cu_2O layers in the range 1-50 nm. The probed surface is much larger (1-20 mm²) than those probed by AFM or SEM, and both Cu and Cu_2O thicknesses can be determined, by contrast with AFM which measures the total thickness of the samples. SEM is also eligible for measuring the thicknesses of the two layers but only when they are larger than ~30 nm and after a destructive and not straightforward preparation of the cross section.

On the other hand, UVS allows a determination of thicknesses in a larger range than ellipsometry. Indeed in UVS the transmitted light is measured directly while ellipsometry measures the intensity of (polarized) light after reflection on the bottom of the layer. Therefore on ellipsometry twice the thickness of the UVS layer will roughly give a twice absorbance. No reliable result are obtained with absorbance above 3 (0.1% of transmitted light), which corresponds to 90 nm in the visible range for UVS and thus leads to eligible copper thicknesses below 45 nm for ellipsometry.

In addition to the thickness determination, the proposed (third method) fitting process in UVS allows to get some knowledge on the optical properties as well. Note that this could have been done with ellipsometry as well, which is actually an interesting perspective of this work to interpret the UVS and ellipsometry results using the same sets of refractive indices. Table III-14 summarizes the advantages of the different techniques used in this study.

	Probed surface	Thickness range	Identification e_{Cu} / e_{Cu_2O}
AFM	Local (~1 µm²)	1 nm - 1 µm	no
SEM	Local (~1 µm²)	30 nm - 1 µm	If e > 30 nm
MAI SE	Global (~1 mm²)	Cu: 1 - 45 nm Cu_2O: 1 - 90 nm	Yes, if the refractive index are known
UVS	Global (1-20 mm²)	1 - 90 nm	Yes, if the refractive index are known or fitted

Table III-14: Compared probed surface area, and ranges of determinable thicknesses for copper and copper oxide layers, for the different techniques used in this study, for $\lambda \in (350 - 800)\ nm$

Chapter IV: Raman signature enhancement

In this chapter we will discuss the Raman enhancement on copper substrates, and discuss in particular Interference enhanced Raman spectroscopy (IERS) and Surface Enhanced Raman Spectroscopy (SERS) phenomena. We will study the Raman signal evolution as a function of the cuprous thickness. Then we will discuss the Raman signal of graphene deposited on flat or nanostructured samples.

1. Raman signatures of copper oxide

All spectra are normalized by the silicon peak at 521 cm^{-1}, acquired in the same conditions (120 s, ~200 µW) to take into account the spectrometer's response. The signatures are compared at 488, 532, 633 and 785 nm.

1.1. Pure powders

We first study the Raman signatures of CuO and Cu_2O pure powders, at different wavelengths. The Raman spectra of CuO are presented in Figure IV-1 with the main peaks at 300, 350 and 630 cm^{-1}, marked by the vertical dashed lines, corresponding to first-order Raman-active mode of A_g, B_g and A_g symmetries Their relative intensities with respect to that of the TO peak of silicon are larger at 488 and 532 nm and particularly a more prominent peak at 350 and 630 cm^{-1}.

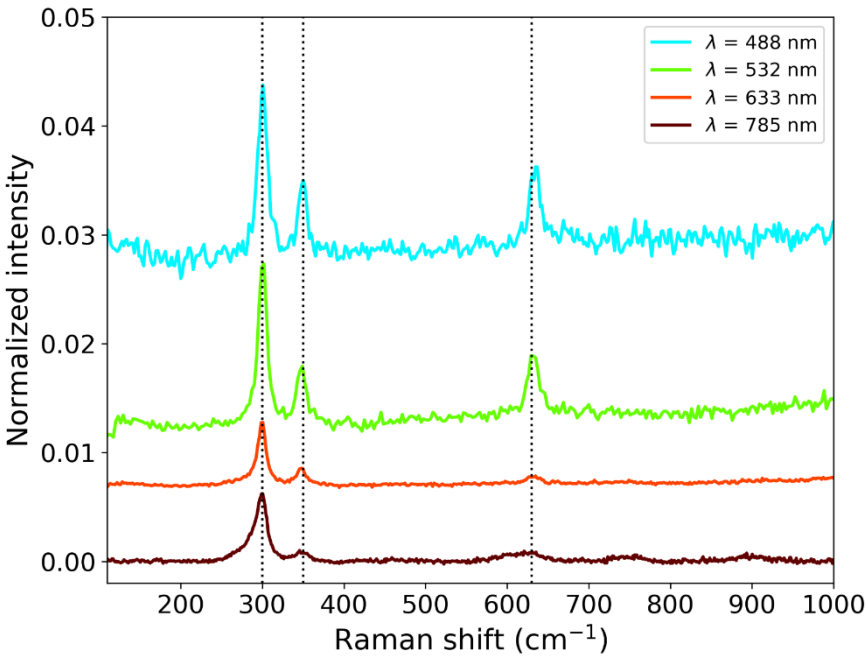

Figure IV-1: CuO powder spectra with main peaks at 300, 350, and 630 cm^{-1} (dashed vertical lines) excited at 488, 532, 633 and 785 nm. All spectra but the bottom one are vertically shifted for clarity.

Contrarily to CuO, the Cu_2O powder present a strong luminescence (PL) background at 488, 532, 633 nm and in a lesser extent at 785 nm. The PL spectrum can be appreciated in Figure IV-2, The main peak around 630 nm corresponds to the yellow 1s (Y1s) band (see chapter I, and the onset of a secondary peak at high wavelength is as-signed to single charged oxygen vacancies (V_O^+) [148, 149]. and Figure IV-3, for the same excitations wavelengths. The PL is represented in Figure IV-2 as a function of the wavelength, with its maximum yellow 1s (Y1s) band position between 570 and 700 nm (see chapter 1).

Photon excitation at 2.54 and 2.33 eV (488 and 532 nm) are largely above the PL gap (~2 eV). Resulting in the observation of the very intense Y1S PL signature, in particular at 532 nm. On the other hand for a laser excitation at 1.96 eV (633 nm) no PL should be observed, since the energy is lower than, the gap. However on those samples, the PL band is measured around 1.94 eV, which explains the weak observation of PL at 633 nm as well. Finally the photon energy at 1.56 eV (785 nm) is much smaller than the energy of the Y1s excitation series, and the weak PL is assigned to single charged oxygen vacancies

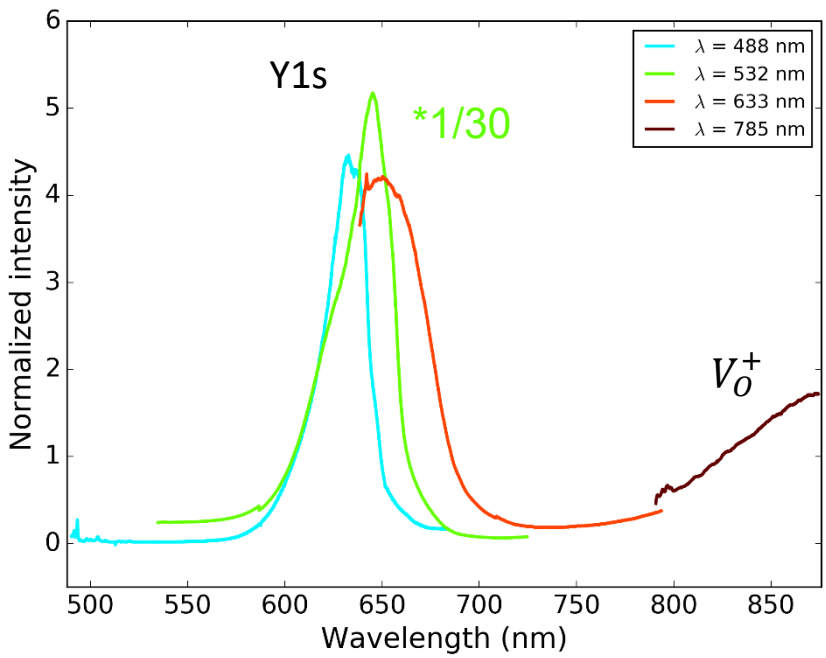

Figure IV-2: Cu_2O luminescence measured with 488, 532, 633 and 785 nm excitations.

Beside the strong PL which dominates the Raman spectra, characteristic Cu_2O Raman peaks are observed at 150, 220, 420, 500 and 630 cm^{-1} (Figure IV-3). For clarity, the normalized spectra are represented superimposed on the PL background (top) and after a manual subtraction of the PL using a 6th order polynomial background (bottom).

The peak at 220 cm^{-1}, a second order mode of E_u symmetry, dominates the Raman spectra for all exciting wavelengths. The peaks at 150 and ~640 cm^{-1}, are both of T_{1u} symmetry, and activated by defects (see chapter I for details). The motions corresponding of the copper and oxygen atoms are represented in chapter I (Figure I-29). The modes at 150 and 220 cm^{-1} correspond to rotations of the Cu tetrahedron around its center. The T_{1u} at ~640 cm^{-1}

corresponds to an out-of-phase motion of the Cu- and O- sublattices. For a laser excitation at 785 nm, an additional ill-defined peak is observed at 180 cm^{-1}.

Note that local heating of powder leads to an oxidation of Cu_2O into CuO, which explains the observation of a weak CuO peak at 300 cm^{-1} for a laser excitation at λ = 488 nm.

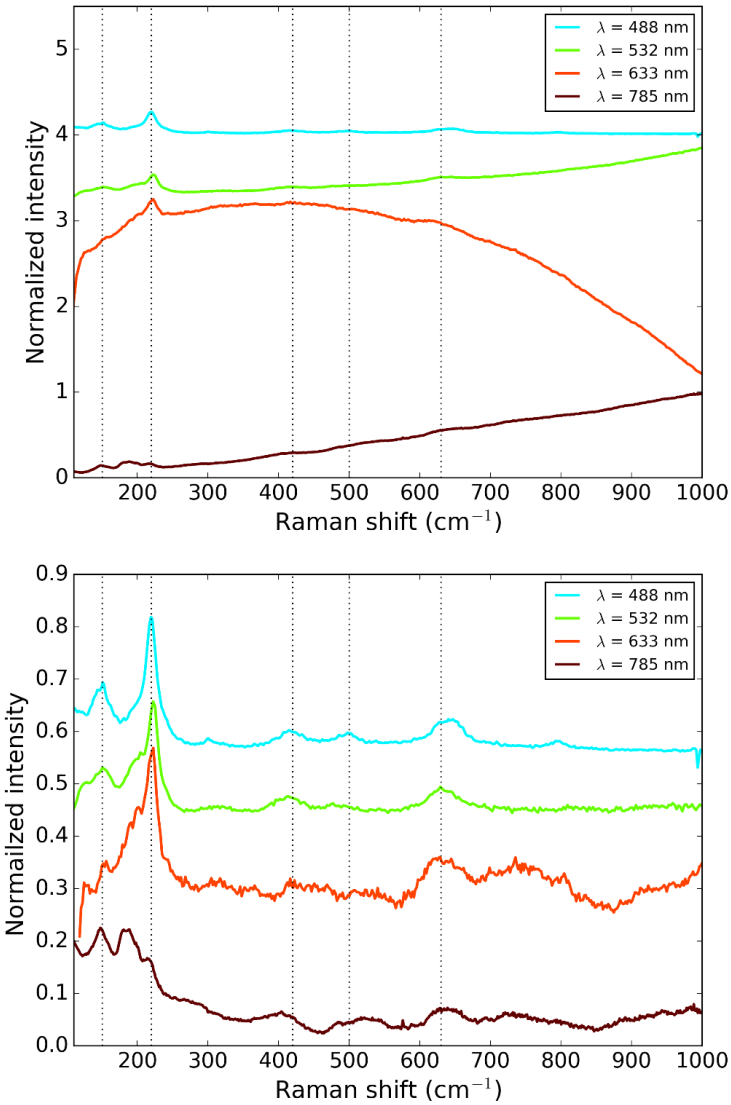

Figure IV-3: Cu_2O spectra excited at 488, 532, 633 and 785 nm before (top) and after (bottom) subtraction of the PL background. The main Raman peaks at 150, 220, 420, 500 and 630 cm^{-1} are marked by vertical dashed lines. All spectra but the bottom one are vertically shifted for clarity.

The most relevant wavelength to measure the cuprous oxide Raman signatures is 488 nm since the PL is significantly upshifted with respect to the Raman peaks. For all exciting wavelengths, the Raman intensities for Cu_2O are about 20 times larger than those for CuO.

1.2. Calibrated thin films

1.2.1. Series S50

The evolution of the Raman spectra as a function of oxidation for the S50 series are presented in Figure IV-4, Figure IV-5 and Figure IV-6. For a laser excitation at 488 nm, both Raman and PL signatures can be observed. The PL intensity is much larger than the Raman, which is surprisingly rarely discussed in the literature. The PL is already quite strong for the raw sample (S50-t0), its intensity increases continuously with oxidation until the 4th oxidation step (S50-t240) without any significant change of its spectral profile. Then, the PL intensity stops increasing and broadens after the 5th oxidation step (S50-t600), and finally drops for the fully oxidized sample. The evolution of the Raman signal with oxidation is quite similar to that of the PL. It increases continuously with oxidation until the 4th oxidation step, then saturates at the 5th oxidation step and finally drops for the fully oxidized sample. Note that the ratio I_{220}/I_{150} is about 1, significantly lower than for the powders (about 4), due to different grain sizes and defects density.

There are three possible origins for the drop of the PL / Raman signal observed for the fully oxidized sample:

i) the growth of a superficial layer of CuO (as revealed by XPS) provides possible non-radiative relaxation channels involving charge transfer from the excited states of cuprous oxide to those of cupric oxide. However, this mechanism is expected to be efficient only for the interfacial layer of Cu_2O and not for the whole thickness. Moreover, XPS results indicate that an ultrathin CuO layer is present on the raw sample as well, which makes this hypothesis unlikely

ii) for fully-oxidized sample changes of the cuprous oxide layer microstructure, revealed by SEM observations and changes of the fitted dielectric permittivities, may lead to a larger elastic scattering and/or a quenching by new electronic states. Such changes were observed only for fully oxidized samples, and therefore cannot explain the decrease of intensity after the 5th oxidation step

iii) the presence of an undercoating of copper with a strong reflectance leads to interference enhanced Raman scattering (IERS) of the Raman/PL intensities, as already reported by several groups [100, 102]. Maxima of IERS are expected to be observed when multiple reflections on the copper oxide interfaces are in phase, which depends on both the permittivities and the exciting/scattering wavelength. Then a drop of IERS is expected for larger copper oxide thicknesses corresponding to out-of-phase mutliple reflections. On the other hand, IERS depend on the reflectance of the copper undercoating so that a decrease of IERS is also expected as soon as the decrease of the thickness of the underlying copper layer leads to a drop of its reflectance, and a severe drop of IERS is expected for fully oxidized samples because of the complete transformation of the copper undercoating

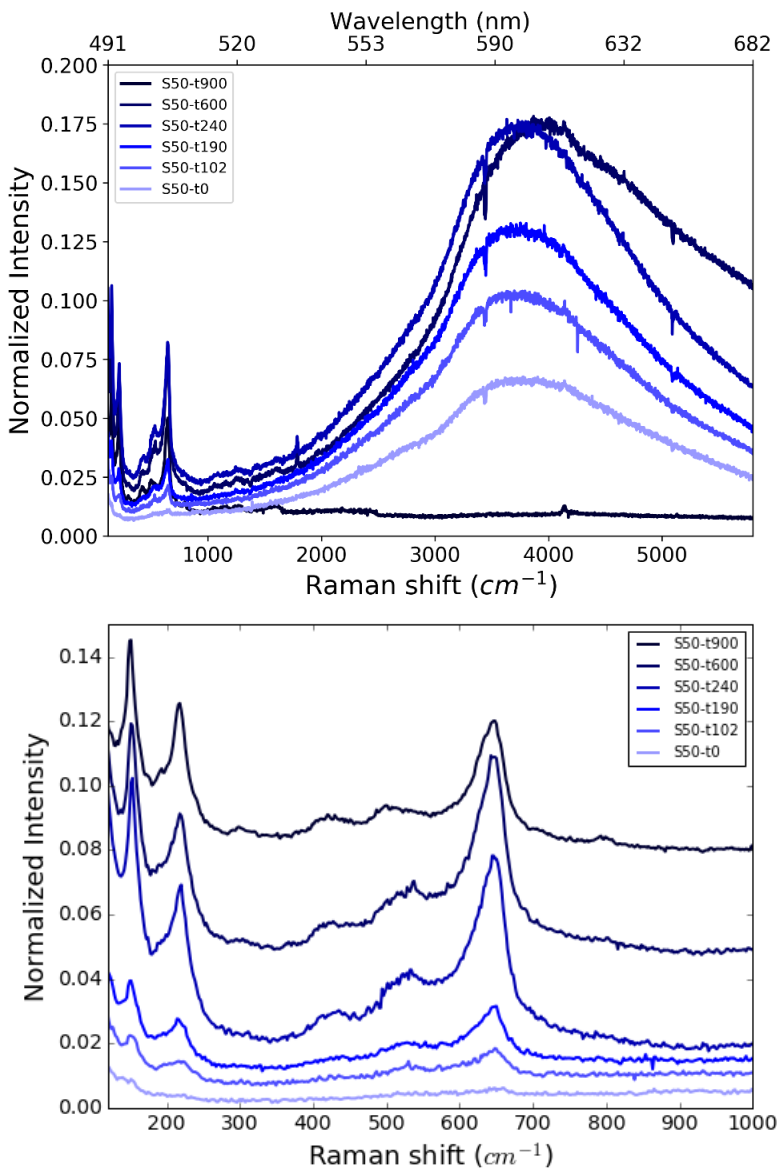

Figure IV-4: Evolution of PL/Raman (top) and Raman (bottom) spectra of S50 series during oxidation (488 nm excitation). All spectra but the bottom one are vertically shifted for clarity.

To confirm the trends observed at 488 nm the Raman/PL spectra of the S50 series are studied using other excitation wavelengths. Results at 532 nm are presented in Figure IV-5. The PL intensity follows a similar evolution than that observed at 488 nm, with an initial increasing intensity in the first steps of oxidation followed by a drop for the fully oxidized sample. As already mentioned, the Raman signatures at 532 nm are difficult to measure due to the superimposed large PL. The most intense Raman peak is the one at 220 cm^{-1} and can only be observed after the 4th oxidation step (S50-t240).

The evolution of the Raman spectra for the S50 series with excitation at 633 and 785 nm are presented in Figure IV-6. Once again, the Raman intensities of Cu_2O are increasing up to the the 5th oxidation step t600 (5th at 633 nm, and t240, the 4th oxidation step at 785 nm for which no data are available for the 5th step), and then drop for the fully oxidized sample. By contrast with the results at 488 and 532 nm, the Raman signal completely vanishes for the

fully oxidized sample excited at 633 and 785 nm, and the remaining Raman signatures observed for this sample (a broad band centered at 400 cm^{-1}) are those of the fused silica substrate.

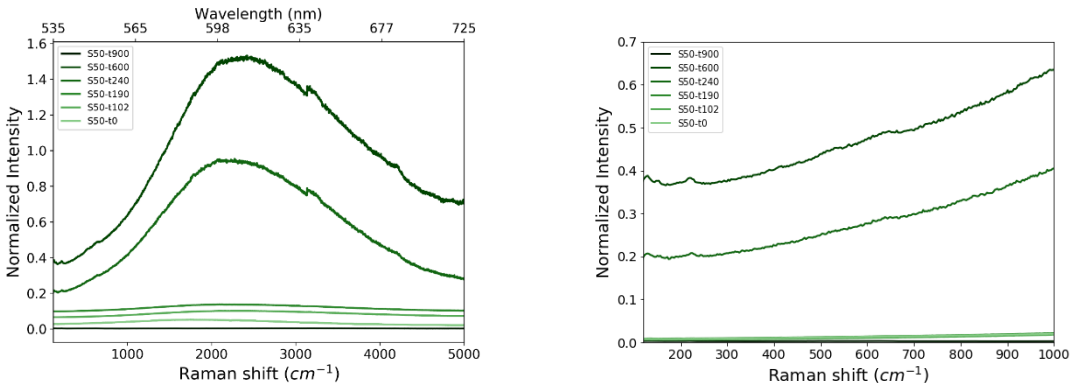

Figure IV-5: Evolution of PL/ Raman (left) and Raman (right) signatures for S50 series excited at 532 nm.

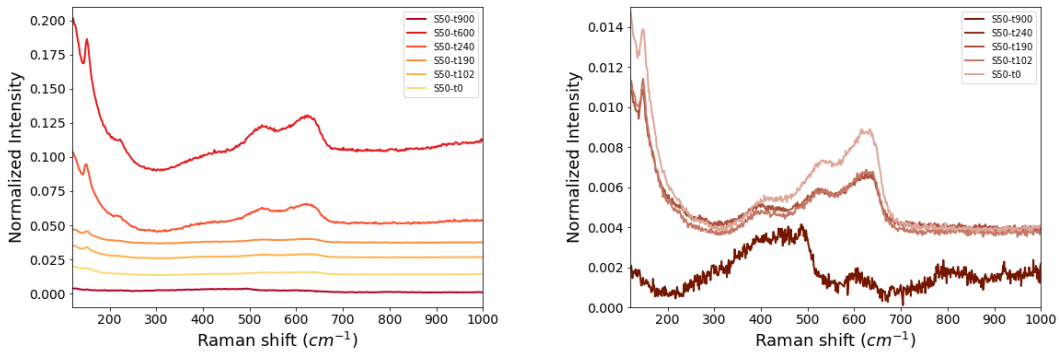

Figure IV-6: Evolution of the Raman signatures for S50 series during oxidation, excited at 633 (left) and 785 nm (right). At 633 nm, all spectra but the bottom one are shifted for clarity. Note that due to a temporal laser deficiency, no spectrum could be measured at 785 nm for sample S50-t600

To conclude for the S50 series, oxidation leads to a continuous increase of the PL and Raman signals up to the 4th oxidation step (S50-t240) at 488 nm and to the 5th for the other exciting wavelengths. For the fully oxidized sample (S50-t900), the Raman signatures of Cu_2O drop and even vanish at 633 and 785 nm, and the PL vanishes as well (at 488 and 532 nm). This drop is assigned to the complete oxidation of the underlying copper layer, associated to a drop of its reflectance and the corresponding IERS. The increase of the surface roughness and heterogeneity of the copper oxide layer for fully oxidized samples may also contribute to the drop of the IERS.

1.2.2. Influence of the initial thickness of the undercoating of copper

Series S10, S30 and S180 show general similar trends than the S50 series, with a few differences which are underlined below.

Figure IV-7 compares the evolution during oxidation of the Raman/PL spectra excited at 488 nm for the four series of samples. For all series, the PL intensity reaches a maximum after the 4th step (t240), except for the S10 series where the maximum occurs after the 3rd step (t190). Then, the PL intensity decreases and broadens, and finally vanishes for the fully oxidized sample of series S10, S30 and S50, *i.e.* for all samples where the copper is fully transformed into Cu_2O (there is a remaining layer of copper of ~160 nm for the S180-t900 sample). The PL broadening on the red side is attributed to a larger concentration of defects in the Cu_2O layer (V_O^{2+} at 740 nm).

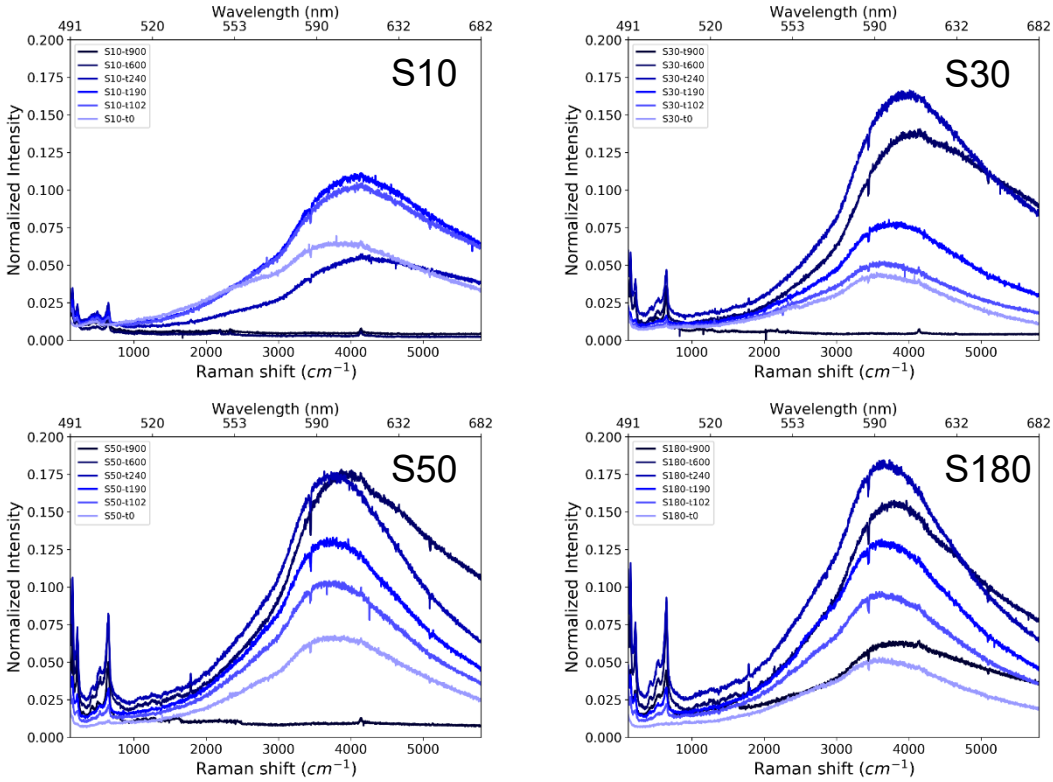

Figure IV-7: Evolution of the Raman/PL spectra excited at 488 nm for S10 (upper left), S30 (upper right), S50 (lower left) and S180 (lower right) series

Figure IV-8 to Figure IV-10 show the spectral evolution with oxidation for the S10, S30 and S180 series at the other wavelengths.

The spectra of the S10 series display signatures of the underneath silica substrate at all oxidation time and wavelengths, because of the very small thickness of the initial copper layer, and its concomitant significant transmittance in the visible range. Accordingly, at 633 and 785 nm the spectra of samples S10-t600 and S10-t900 show only the silica signatures, which are more intense that for the raw samples since the absorption of cuprous oxide is very weak at these wavelengths.

For the S30 series, the only noticeable difference is for the sample S30-t240, which displays very intense spectra for excitation lines at 633 and 785 nm.

Finally, the S180 series is interesting since a quite thick under-coating copper layer remains after the last oxidation step (S180-t900). However, the Raman signatures of cuprous oxide drop as well for this sample, which may be assigned to significant increase of roughness and heterogeneity as revealed by the SEM observation of this sample.

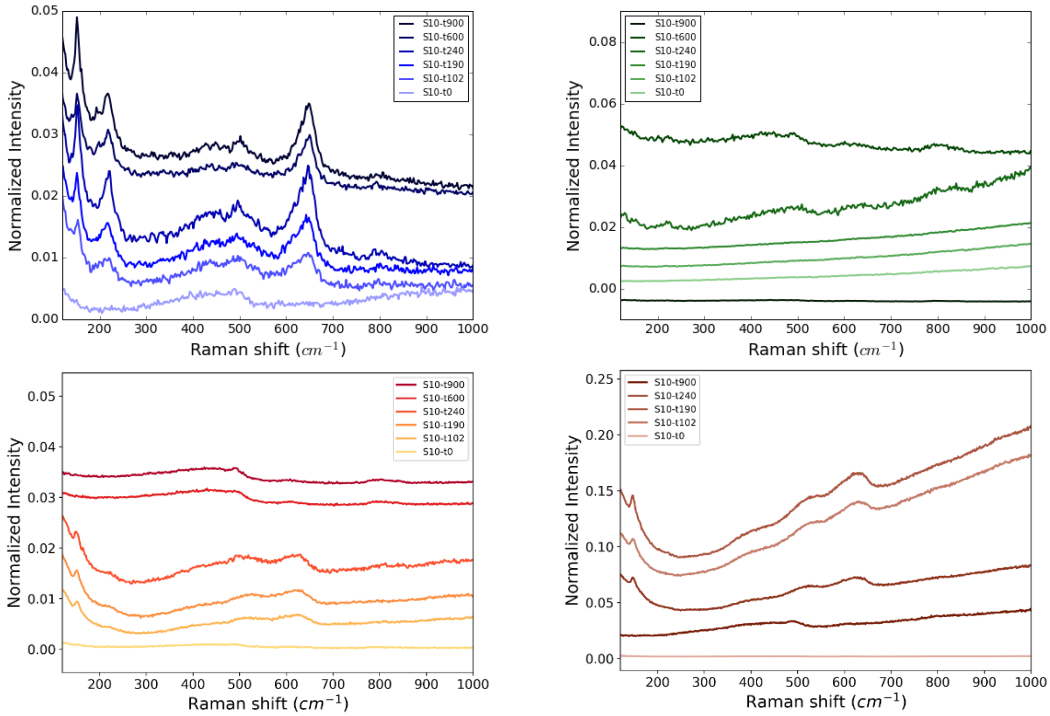

Figure IV-8: Evolution of Raman spectra during oxidation for S10 series for excitations at 488 nm (upper left), 532 nm (upper right), 633 nm (lower left) and 785 nm (lower right). All spectra but the bottom one are vertically shifted for clarity.

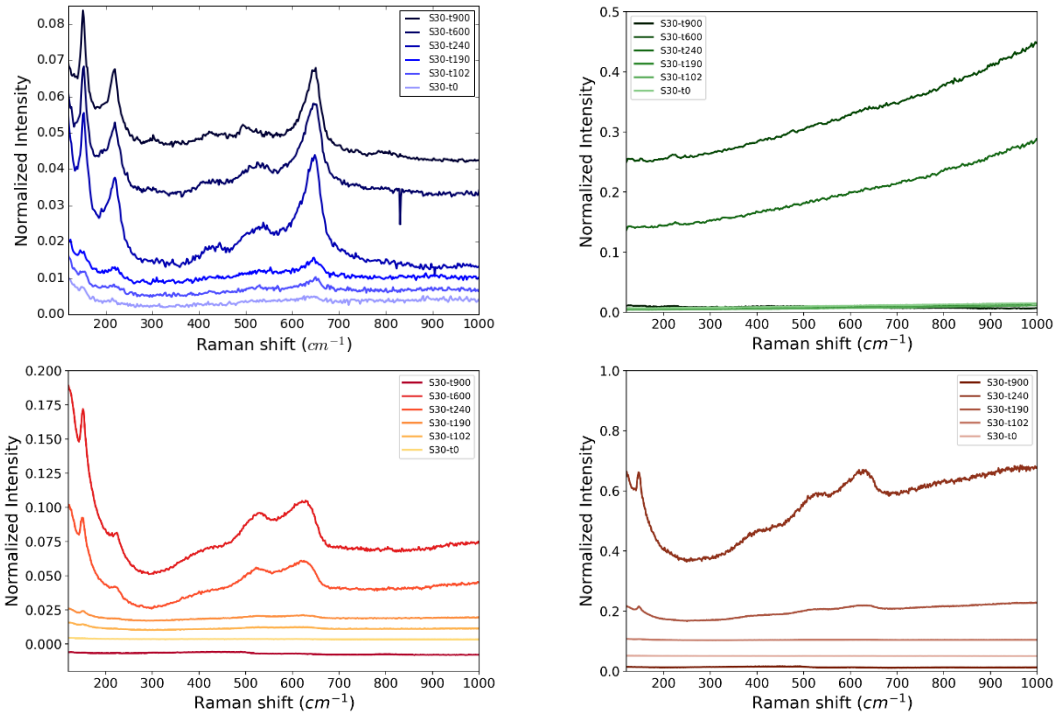

Figure IV-9: Evolution of Raman spectra during oxidation for S30 series for excitations at 488 nm (upper left), 532 nm (upper right), 633 nm (lower left) and 785 nm (lower right). All spectra but the bottom one are vertically shifted for clarity.

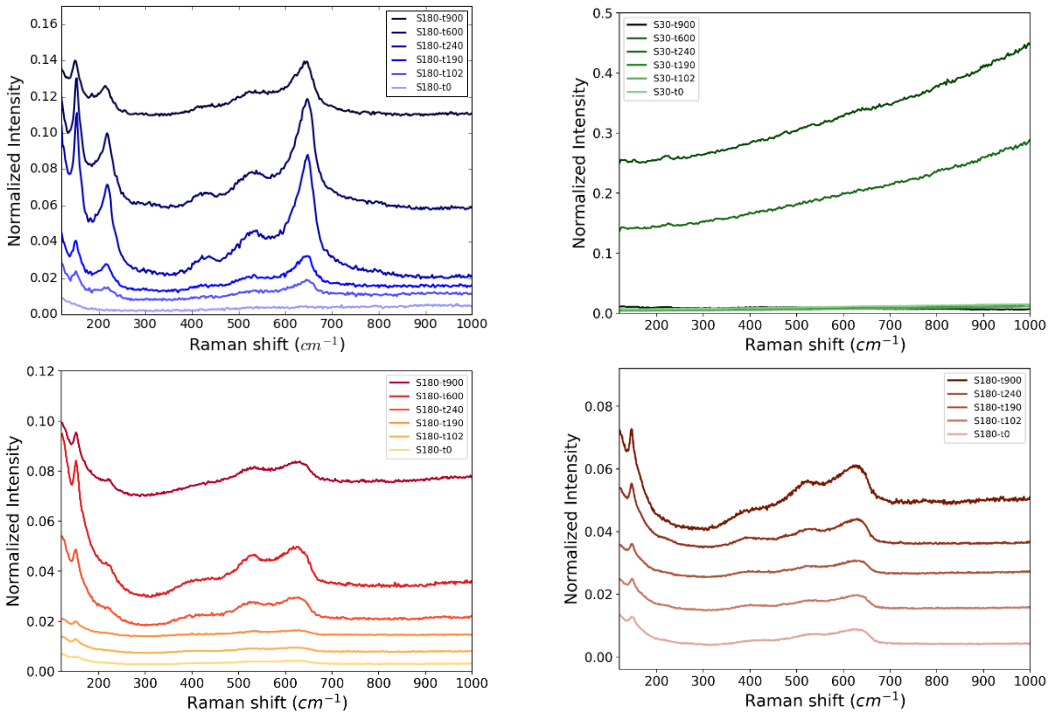

Figure IV-10: Evolution of Raman spectra during oxidation for S180 samples for excitations at 488 nm (upper left), 532 nm (upper right), 633 nm (lower left) and 785 nm (lower right). All spectra but the bottom one are vertically shifted for clarity.

Figure IV-11 compares the evolution of the fitted PL intensities excited at 488 and 532 nm as a function of the thickness of the cuprous oxide layer. Figure IV-12 displays a similar representation for the fitted Raman intensities at 150 cm^{-1} or 220 cm^{-1} (for 532 nm excitation only).

In general, the largest enhancements are measured for the 4th (at 488 and 785 nm) or 5th (at 532 and 633 nm) oxidation step of the S50 and S180 series, which display quite close results. Indeed, the thickness of the copper under-coatings is quite thick for these series, except for the fully oxidized sample of series S50, so that their reflectance is almost constant and close to that of bulk copper, leading to the largest expected IERS enhancements. Accordingly, the thickness-dependence of the IERS enhancement are very close for all series until the 4th oxidation step, *ie* until the thickness of the undercoating copper downs to 8.3 and 47, for S10 to S50 respectively. Then, the IERS enhancements are weaker for the last steps with respect to those of S50 and S180 series, because of the smaller thickness of the copper undercoating. Finally, the IERS enhancement drops for each series after the last oxidation step. This is assigned to the complete transformation of the undercoating layer for series S10, S30 and S50, and to the heterogeneous structure of the cuprous layer for series S180.

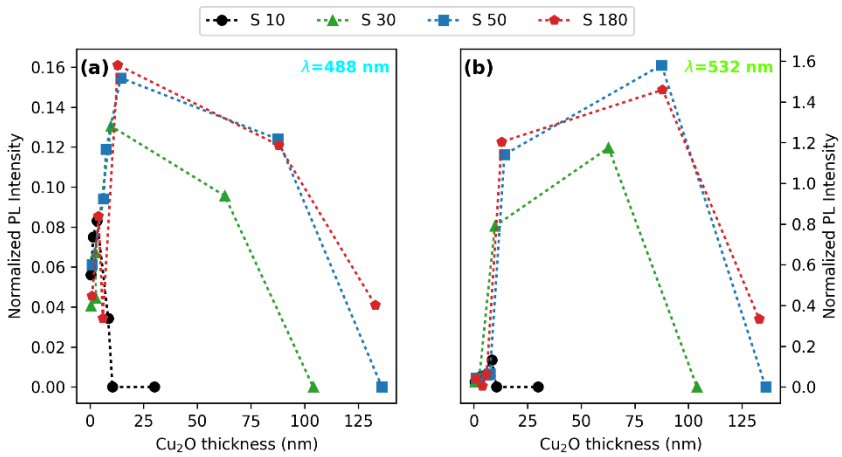

Figure IV-11: PL intensity as a function of Cu_2O thickness for excitation at 488 nm (a) and 532 nm (b)

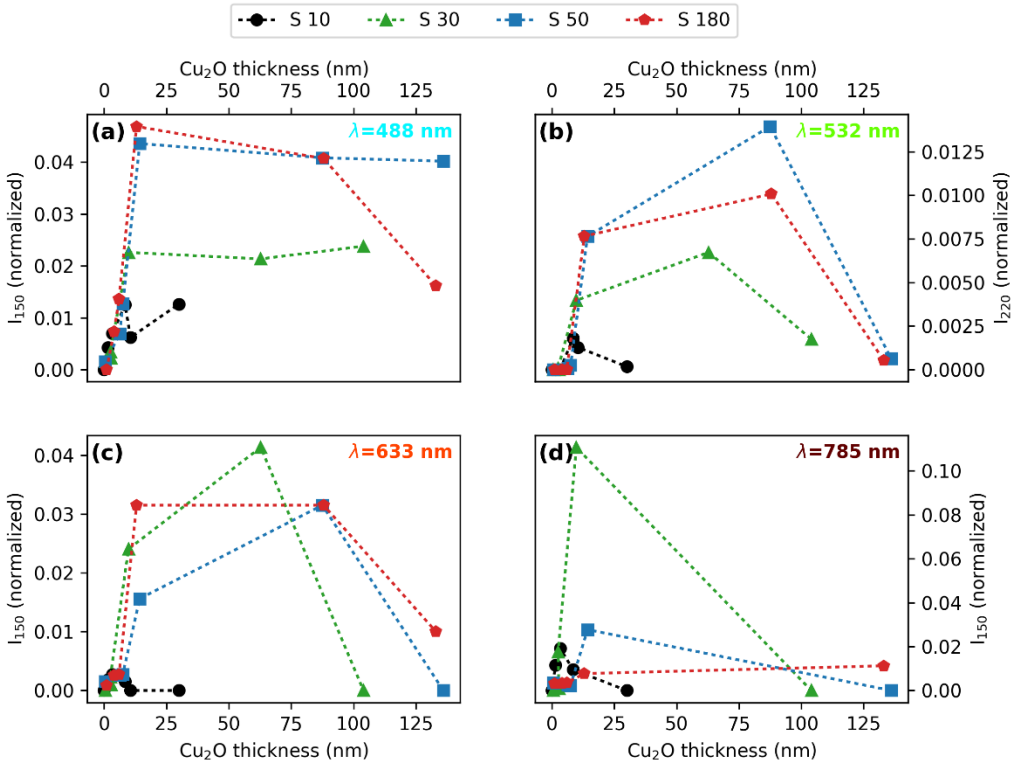

Figure IV-12: Raman peak intensity of Cu_2O as a function of Cu_2O thickness for excitation at 488 nm (a), 532 nm (b), 633 nm (c) and 785 nm (d)

In summary, the Raman / PL intensities increase continuously during the first steps of oxidation, independently of the decreasing thickness of the copper undercoating until the main part of this layer is transformed. Maxima of Raman intensity are measured for all samples after the 4th or 5th oxidation step, which corresponds to different copper oxide thicknesses for the different series. These maxima are assigned to maxima of IERS enhancement. The drops of Raman intensities following the maxima may be due to out-of-phase interference conditions, or to the drop of reflectance of the copper undercoating, or to significant changes in the roughness or microstructure of the layers.

In the next subsections, we will consider the multi-reflection model to calculate enhancements expected from IERS [102, 98, 150] and compare quantitatively with these data.

1.2.3. Discussion on the IERS enhancement

1.2.3.1. Calculated SMEF profiles through the samples

In order to explain the results above, calculations of single molecule enhancement factor (SMEF) and integrated SMEF (ISMEF) are performed according to the general equation (1) [151] pp 217, as a function of the wavelength, Cu_2O and the copper thicknesses.

$$SMEF \cong \frac{|E_{loc}(\omega_L)|^2}{|E_{inc}|^2} * \frac{|E_{loc}(\omega_R)|^2}{|E_{inc}|^2} \tag{67}$$

$$ISMEF \cong \int \frac{|E_{loc}(\omega_L)|^2}{|E_{inc}|^2} * \frac{|E_{loc}(\omega_R)|^2}{|E_{inc}|^2} \, d(e_{Cu_2O}) \tag{68}$$

The variation of the SMEF at 150 cm^{-1} along the axis perpendicular to the surface is compared for different samples (raw, t190, t240 and fully oxidized) of series S10, S30 and S50 in Figure IV-13, Figure IV-14 and Figure IV-15, respectively. For all samples the SMEF is constant in the silica, but its value depends on the thicknesses of the copper and copper oxide layers. For raw and partly oxidized samples, the SMEF increases in the copper layer, continues to increase albeit with a smaller slope in the copper oxide layer and in air, until it reaches a maximum at a distance of the interface which depends on the copper oxide thickness and on the wavelength. By contrast, for fully oxidized samples with no residual copper layer, the SMEF decreases in the copper oxide layer, goes through a minimum which depends on the wavelength, and then increases again. The location of the extrema shifts at larger distances for increasing wavelength.

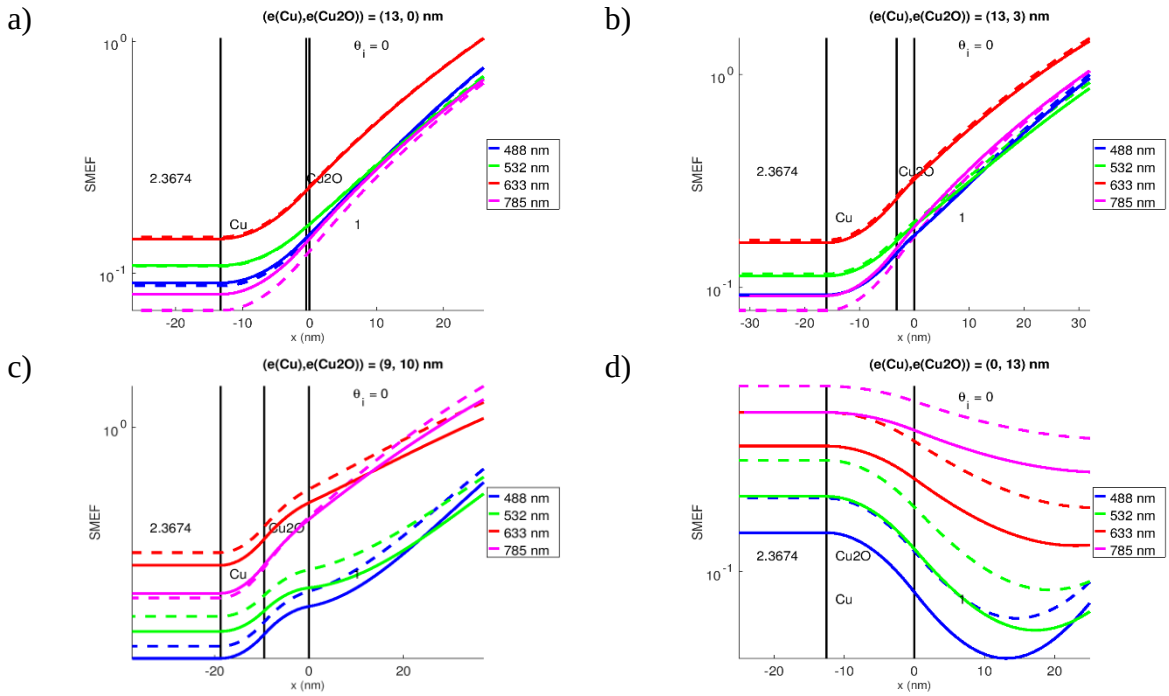

Figure IV-13: Calculated SMEF at 150 cm^{-1} for samples S10-t0 (a), S10-t190 (b), S10-t240 (c) and S10-t900 (d) for 4 different laser lines using permittivities from the literature (Cu: [139] and Cu_2O: [12] (dashed lines) and the fitted permittivities (full lines).

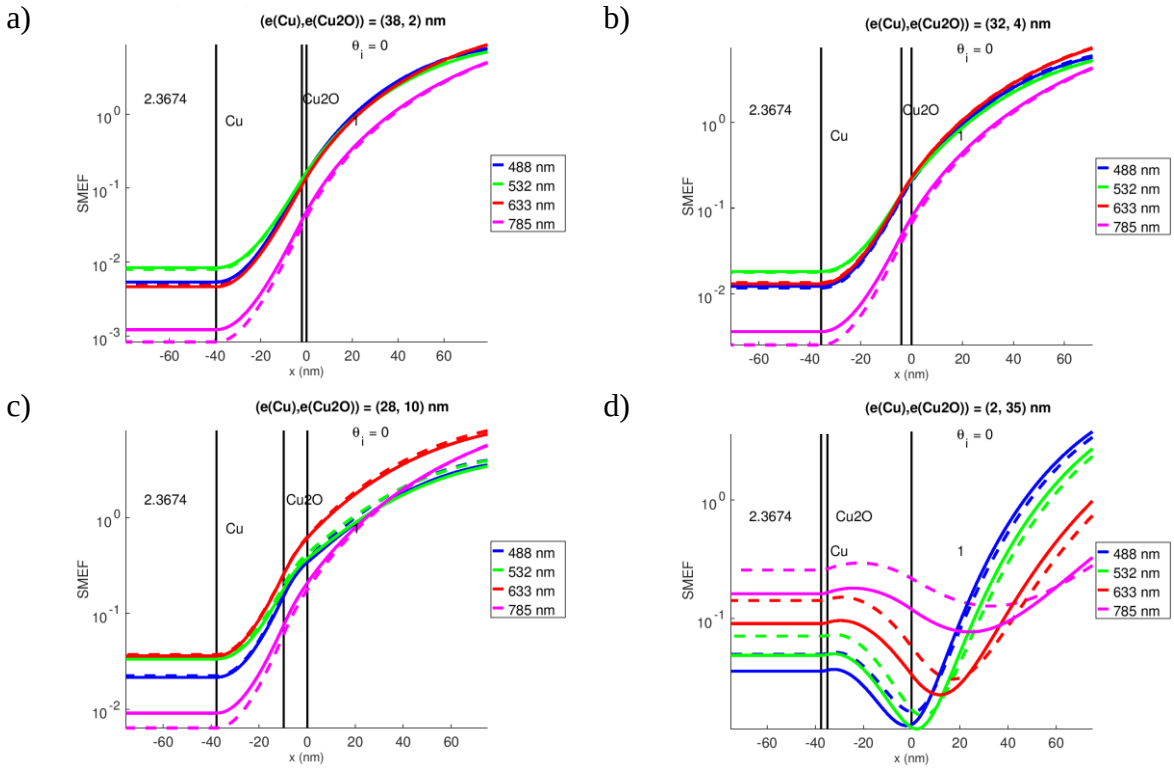

Figure IV-14: Calculated SMEF at 150 cm^{-1} for samples S30-t0 (a), S30-t190 (b), S30-t240 (c) and S30-t900 (d) for 4 different laser lines using permittivities from the literature (Cu: [139] and Cu_2O: [12] (dashed lines) and the fitted permittivities (full lines).

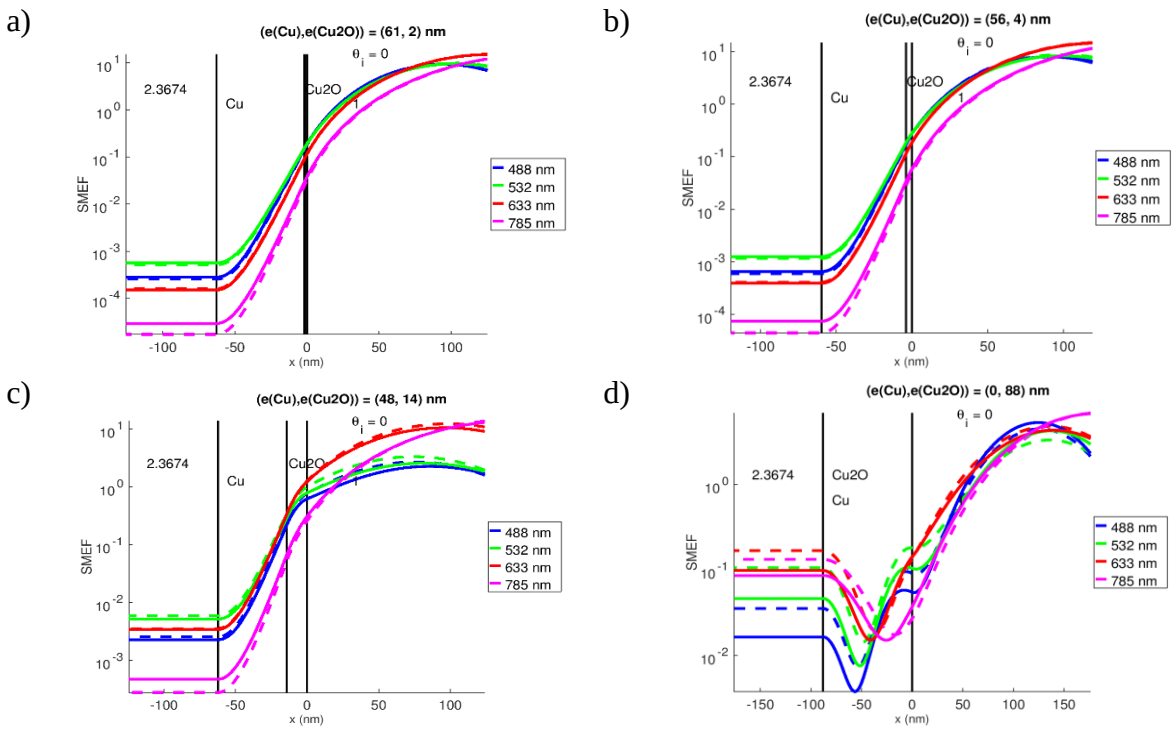

Figure IV-15: Calculated SMEF at 150 cm^{-1} for samples S50-t0 (a), S50-t190 (b), S50-t240 (c) and S50-t900 (d) for 4 different laser lines using permittivities from the literature (Cu: [139] and Cu_2O: [12] (dashed lines) and the fitted permittivities (full lines).

1.2.3.2. Calculated ISMEF as a function of copper and copper oxide thicknesses

The integrated SMEF can be directly compared with the experimental data as long as the thickness remains small with respect to the experimental depth of field (which is about 1 micron for a numerical aperture of 0.5). It is plotted in Figure IV-16 as a function of Cu and Cu_2O thicknesses. . For copper thicknesses larger than ~50 nm ISMEF maxima (yellow areas) are observed periodically as a function of cuprous oxide thickness. The position of the maxima position is independent of the copper thickness but it increases for increasing wavelength. Using the fitted permittivities, the maxima are reached for cuprous thickness around 15, 17, 28 and 50 nm for laser lines 488, 532, 633 and 785 nm, respectively. If now one considers the permittivities from the literature, this leads to a slight upshift of the Cu_2O thickness at maxima. For decreasing copper thicknesses below 50 nm, the maxima progressively shift to smaller copper oxide thicknesses. The largest enhancement are expected at 633 and 785 nm with respectively a SMEF of 125, 140, 420 and 450.

Solid symbols on Figure IV-16 locate the thicknesses of copper and copper oxide for S10, S30 and S50 series. According to the calculation, one expects the highest enhancements at 488 and 532 nm for the 4th samples of series S50 and S30 which match the first order of interferences. The fully oxidized sample of series S50 matches also quite well with the maximum expected for the 2nd interference order, but without undercoating copper, not interference is expected. On the other hand, larger ISMEF are theoretically expected at 633 and 785 nm but the thicknesses of the samples does not match those of the first maxima. The interference effect for S10 is not evident, the only evidence of its presence of an increased Raman signal of Cu_2O, as its thickness grows. The fact that the underneath copper layer is rather thin and thus is not a good reflector explains why the Raman signal is not greatly enhanced for this series.

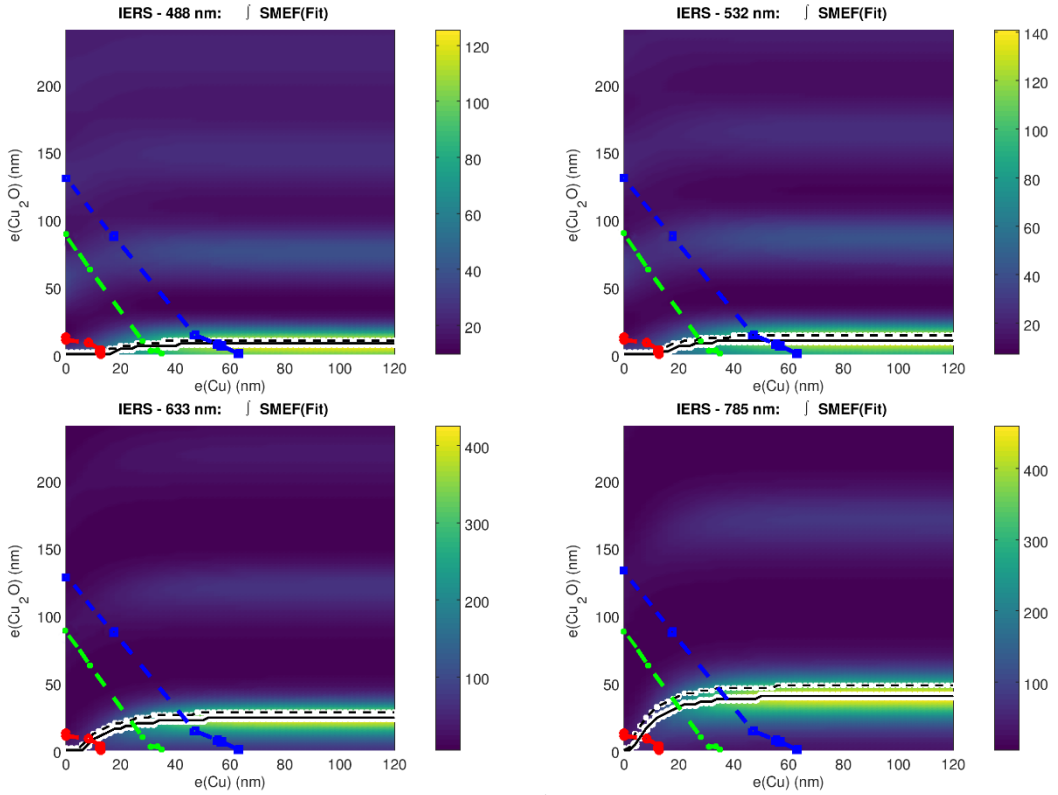

Figure IV-16: Calculated ISMEF at 150 cm^{-1} of the Cu_2O layer as a function of Cu_2O and Cu thicknesses at 488 nm (upper left), 532 nm (upper right), 633 nm (lower left) and 785 nm (lower right). The ISMEF maxima calculated using the permittivities from the literature (Cu: [139] and Cu_2O: [12]) (dashed lines) and the fitted permittivities (full lines). Red, green and blue symbols locate the thicknesses for series S10, S30 and S50, respectively

Globally, the calculations supports the experimental observations. In particular the initial increase of the Raman signature for growing Cu_2O layers for all wavelengths follows the trend of the calculation. The weaker enhancement for S10 is explained by the smaller Cu and Cu_2O thicknesses. According to the calculations, the higher enhancements should be measured at 633 or 785 nm for 35 or 50 nm of Cu_2O, respectively, but none of the samples are in these ranges. By contrast, no strong enhancement is expected for sample S30-t240 at 785 nm, so that the intense experimental Raman signature cannot be interpreted by IERS.

1.3. Expected IERS on copper substrates

We now focus on the IERS properties of copper ‘‘bulk’’ substrates (corresponding to copper undercoating thicker than 100 nm). First, we will discuss the experimental results for the series S180, and then we will compare with calculations for the different wavelengths.

1.3.1. Series S180

The last sample of the S180 series (S180-t900) is not fully oxidized, a quite thick underlying copper layer is present for all the samples of the series. Figure IV-17 corresponds to a section of Figure IV-16 for a copper thickness of 100 nm, a range where the copper thickness has no influence on the calculated IERS. As expected, the position of the maxima

increase for increasing wavelengths. The first maxima of interferences are always the most intense and the corresponding ISMEF increases for increasing wavelengths, and is maximum at 785 nm. The cuprous oxide thicknesses for the samples of the S180 series are marked by dashed vertical lines in figure IV-17. At 488 nm, the maximum of IERS is expected for the 4th sample (14 nm of copper oxide), with a slight decrease for the 5th, and a drop for the most oxidized. At 532 nm, the ISMEF are expected to be close for the 4th and 5th samples. These expectations match well with the experimental observations. By contrast, maxima of IERS are expected for the last sample at 633 and 785 nm, but they are not observed in the experiments. This is assigned to the large roughness and heterogeneities of this sample, leading to a strong damping of the interferences.

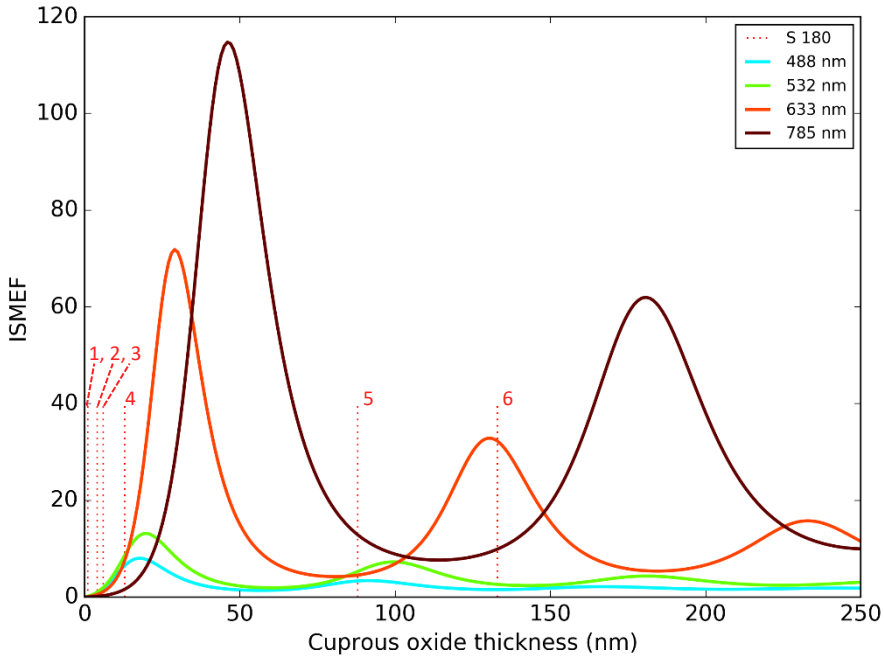

Figure IV-17: Calculated ISMEF at 150 cm^{-1} as a function of cuprous oxide thickness for an underlying copper thickness of 100 nm, for four different exciting lines. The vertical dotted lines mark the Cu_2O thicknesses for the S180 series

We now discuss the IERS enhancement when Raman measurements of copper oxide are achieved on copper rather than on a silica substrate. For this, we normalize the ISMEF of copper oxide calculated for an undercoating copper thickness of 100 nm by that calculated on fused silica.

Results are presented in Figure IV-18 for both permittivities from the literature (dashed lines) and from fitted values (solid lines). The increase of the real part of the permittivity for the fitted values (10%, see Figure III-21) leads to a downshift of the maxima (of about 15 %) and to a significant decrease of ISMEF (by a factor of about 2.5). On the other hand, the ISMEF at maxima still decreases at higher orders, and increases with increasing wavelengths. The largest normalized enhancements are reported in Table IV-1, they remain quite small (<10) for exciting lines at 488 and 532 nm, but increase up to about 35 at 633 and 785 nm. The maxima position are shifted toward larger Cu_2O thicknesses as the excitation wavelength increases.

Fitted permittivity	Ef, IERS (normalized ISMEF)	1st maxima position
488 nm	7	21
532 nm	9	22
633 nm	34	30
785 nm	36	35

Table IV-1 Maximum interference enhancement factor using fitted permittivities for the SiO_2/100 nm Cu/Cu_2O system, normalized by the calculated value on the SiO_2/Cu_2O system.

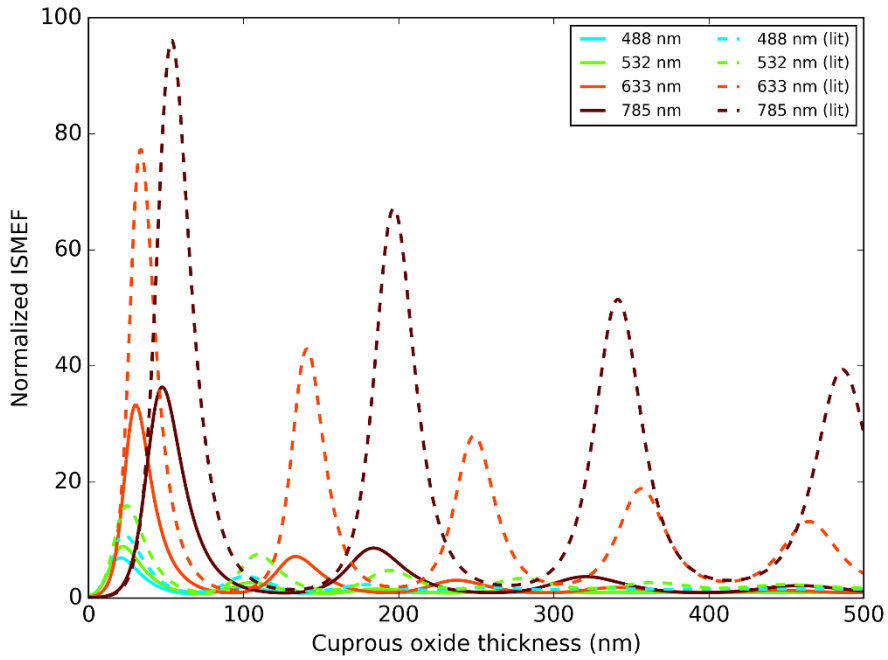

Figure IV-18: Normalized ISMEF for copper oxide Raman peak at 150 cm^{-1} on copper substrates, with respect to silica substrates, as a function of cuprous thickness, for four different exciting lines, for both fitted permittivities (solid lines) and permittivities from the literature Cu: [139] and Cu_2O: [12] (dashed lines).

The experimental evolution of the Raman intensities for thin films (S30, S50 and S180 series) are matching quite well the calculated enhancements: on (Figure IV-19), the calculated IERS were divided by an *adhoc* factor to match the experimental data. Additional reference samples, with cuprous oxide thicknesses in the range 14 to 90 nm, would be helpful to validate definitely the calculations, and especially the values of the refraction index. However, we will use the results presented in Figure IV-19 as reference curves to estimate the cuprous oxide thickness on other series of samples.

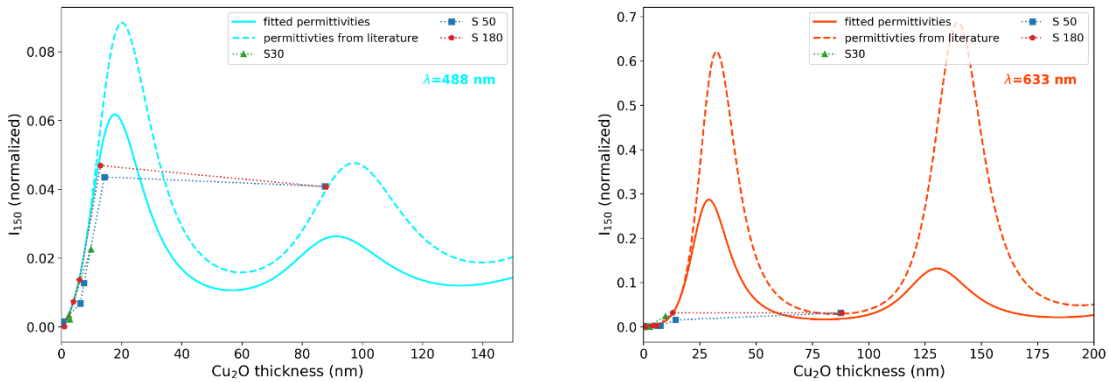

Figure IV-19: Evolution of the intensity of the copper oxide Raman peak at 150 cm^{-1} for all samples of series S30, S50 and S180 but the most oxidized ones (symbols), for λ=488 and 633 nm (left and right, respectively), compared to IERS enhancements calculated for fitted and literature permittivities (solid and dashed lines). The IERS enhancements were divided by an adhoc factor to match the experimental data.

1.3.2. Correlated Raman / PL signatures of various series of samples

1.3.2.1. General case

During this thesis various copper-based samples have been studied: commercial oxide powder, copper single crystals and copper foils, used as received. But also copper thin layers deposited on silicon wafer by electroless deposition. Single layer graphene was transferred on these different copper materials. Additionally we studied SLG grown by CVD on copper foils.

Lots of single spectra and maps were measured on all those samples. Before discussing the relation between the Raman intensities of copper oxide and graphene, we discuss the correlations between the Raman/PL signatures of copper oxide for spectra where both cuprous oxide and SLG are observed, *ie*:

- intensity of the Raman peak of Cu_2O at 150 cm^{-1} at least three times larger than the noise)
- intensity of the G band of SLG at least three times larger than the noise

The Raman peaks at 150, 220 and 640 cm^{-1} were well-fitted by lorentzian peaks. By contrast, the PL band of Cu_2O cannot be fitted by any simple analytical function. Therefore we used a data smoothing followed by a numerical integration to determine its position and intensity (technical details are given in the appendix 2).

For all samples, the Raman peaks at about 150 and 220 cm^{-1} are actually measured in the ranges 148-154 and 214-220 cm^{-1}, respectively, and their intensity ratio is constant for all samples I_{220}/I_{150} ~0.6 except the powder sample for which I_{220}/I_{150} ~2 (Figure IV-20 a and b). On the other hand, the bunch at 640 cm^{-1} has several contributions, and we found different intensity ratio for the samples where the maximum peak is centered at 645 cm^{-1} (I_{645}/I_{150} ~0.7, but I_{645}/I_{150} ~0.4 for the powder, (Figure IV-20c) and for those where the peak is

centered at 635 cm^{-1} (I_{635} /I_{150} ~1.1, Figure IV-20d). The intensity ratio I_{640} /I_{150} is also essentially constant for all samples but the powder (Figure IV-20c)

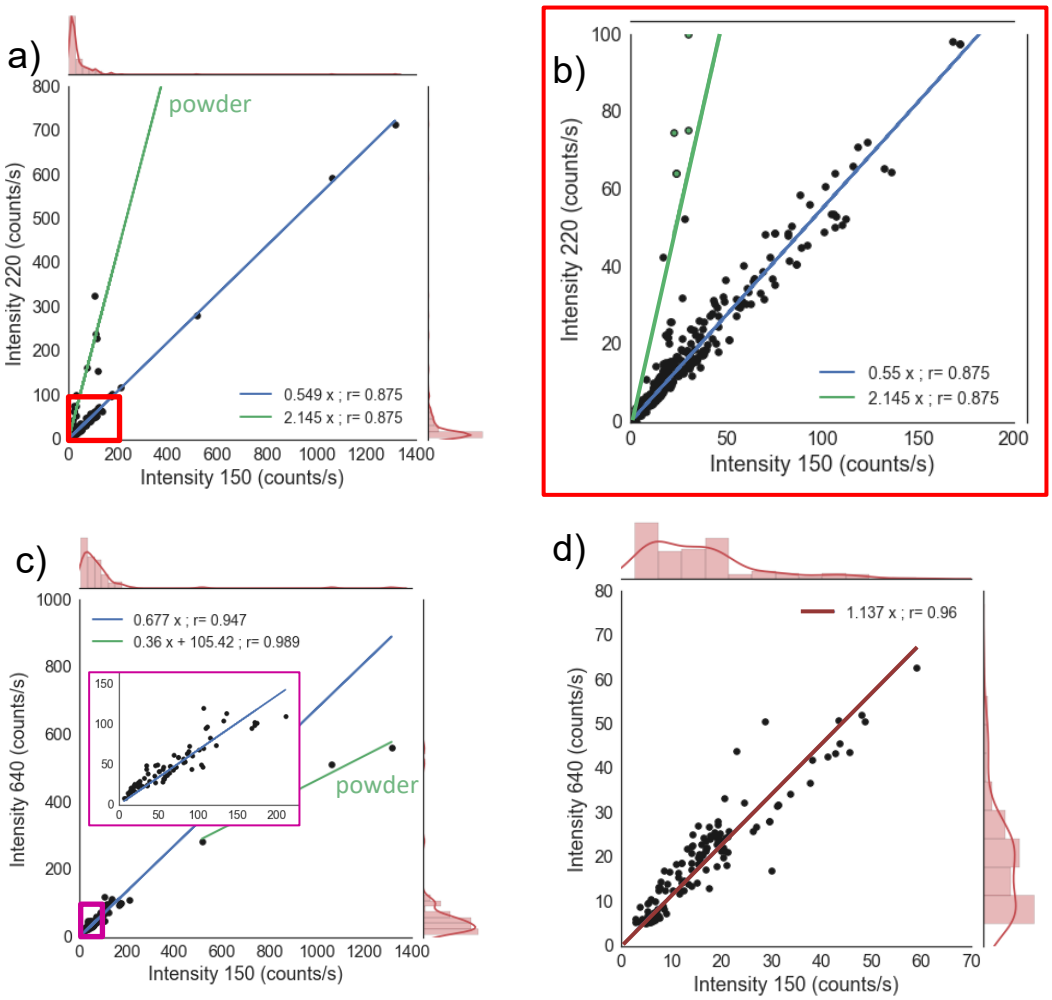

Figure IV-20: Correlation between the intensities of Raman modes of cuprous oxide at 150 and 220 cm^{-1} (a and b), 150 and 645 cm^{-1} (c) 150 and 635 cm^{-1} (d)

On the other hand, the PL area and intensity are well-correlated, with a ratio A_{PL}/I_{PL} ~3000 for all samples but the powders (A_{PL}/I_{PL} ~800). As mentioned above, the PL band is found to redshift for long oxidation times/high oxidation temperatures. However, no clear correlation can be observed between the PL position and its intensity, even though the analysis of the whole data confirms the tendency of a red shift for increasing intensities (Figure IV-21).

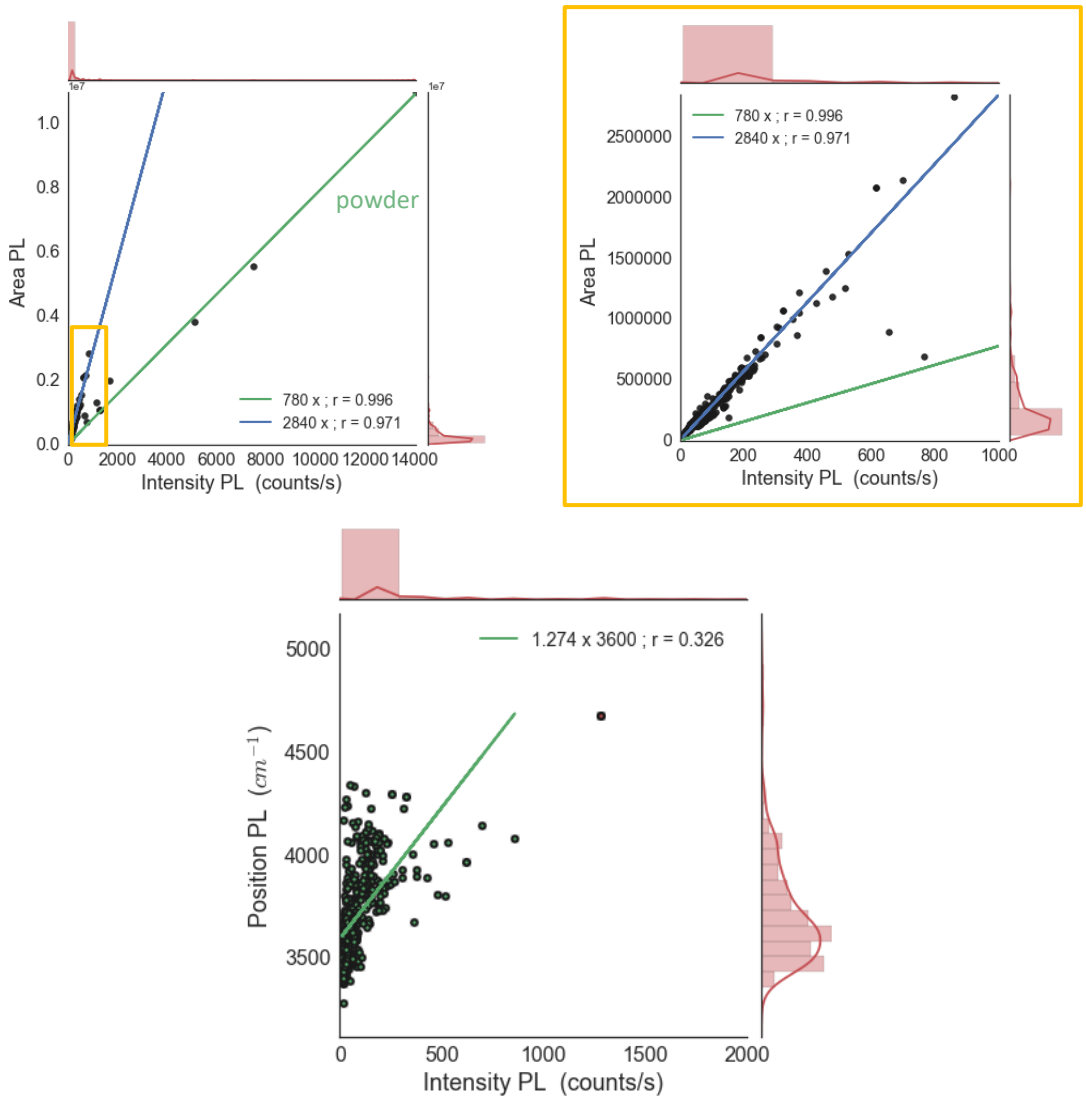

Figure IV-21: Correlation between the PL intensity at maximum and PL area (top) or PL position (bottom)

Finally, no universal correlation could be found between the intensity of the Raman peak at 150 cm^{-1} and the PL intensity (Figure IV-21) but one observes that I_{PL}/I_{150} is constant for a given series of samples such as electroless samples (to be discussed below).

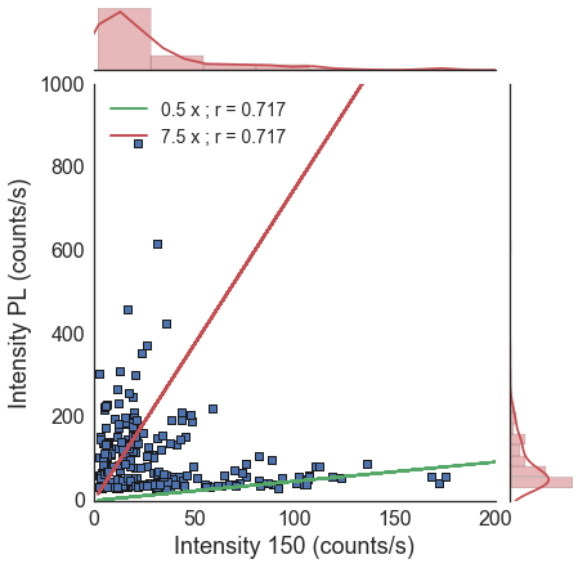

Figure IV-22: Correlation of the PL intensity with that of Raman peak of Cu_2O at 150 cm^{-1}.

1.3.2.2. *In situ* monitoring during oxidation

In-situ Raman/PL monitoring of the thermal oxidation/reduction in controlled atmosphere was achieved for different samples. We present the results for a copper electroless thin film (thickness ~300 nm). The copper electroless deposition leads to a grain size ~100 nm and a R_{ms} around 15 nm, as measured on a 10x10 µm² area, close to the one of the calibration samples surfaces.

Figure IV-23 shows the evolution of the PL/Raman signatures from a same spot on the sample during three successive oxidation/reduction cycles: i) a first oxidation of about 10 min at 150°C under 400 sccm of O_2, ii) a reduction at 400°C under 360 sccm of H_2 for 10 min, followed by a second oxidation under O_2 up to 250°C for less than 10 min, iii) another reduction (same conditions than the first one) followed by a third, more gentle, oxidation cycle up to 130°C.

The qualitative evolution of the spectra is comparable to those presented above, but three new features can be underlined. Firstly, no PL intensity can be measured after a reduction cycle. Which confirms that the PL observed on all copper samples is due to the thin Cu_2O layer. Note that this is not clearly stated in the literature, and the PL background is often subtracted and not referred as an intrinsic signature of cuprous oxide. Secondly, after an oxidation-reduction cycle, the PL intensity never reaches again its intensity in the first cycle, *ie* ~10-15 times larger than that of the Raman signal at 150 cm^{-1}). This supports that the PL intensity is very sensitive to the microstructure and the level of impurities/doping which may change during the oxidation/reduction cycles. On the other hand, the PL evolution during the second oxidation cycle is particularly interesting: the red-shift of the PL maximum is followed by a drop of the PL intensity, correlated to the apparition of the Raman signature of CuO at 300 cm^{-1}. This is an experimental evidence that the growth of a superficial layer of CuO offers non radiative dexcitation channels which quench the PL of Cu_2O. Note that after the second reduction cycle, this effect is not observed anymore during the third ‘‘gentle’’ oxidation cycle.

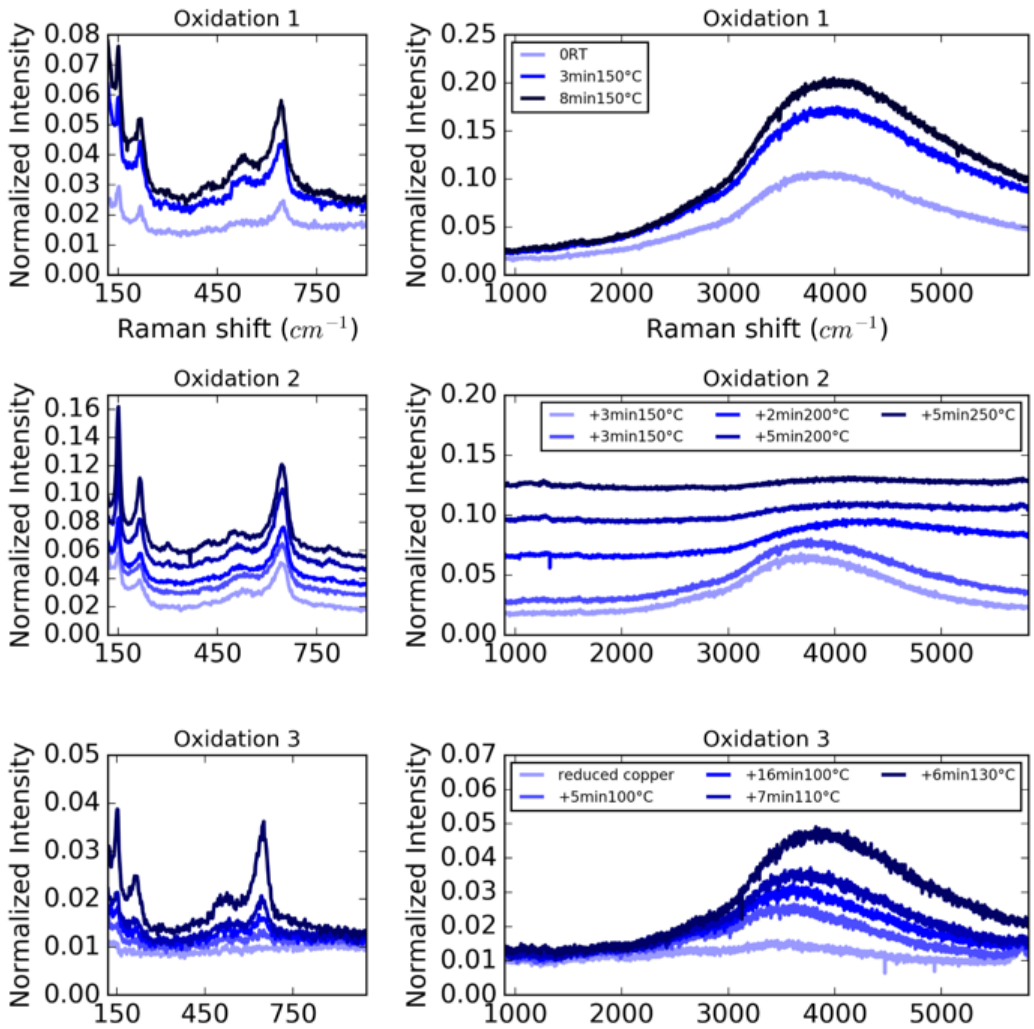

Figure IV-23: Normalized Raman spectra evolution on the same spot during oxidation/reduction cycles from top to bottom, oxidation cycle 1, 2 and 3. For clarity all spectra but the bottom one are vertically shifted for oxidation 2.

Correlations between PL and Raman positions and intensities are reported in Figure IV-24. As expected, PL intensity and PL area are proportional to each other, *ie* A_{PL} / I_{PL} ~3000, independently of the thermal history of the sample (Figure IV-24a). Furthermore, the position of the PL maximum increases linearly with its intensity for low temperature/short times of oxidation (Figure IV-24b) and, for each oxidation cycle, the PL intensity is proportional to that of the peak at 150 cm^{-1} (Figure IV-24c). This suggests that the position and intensity of the PL can be used for monitoring the oxidation of cuprous oxide as long as the microstructure/purity of the samples are comparable.

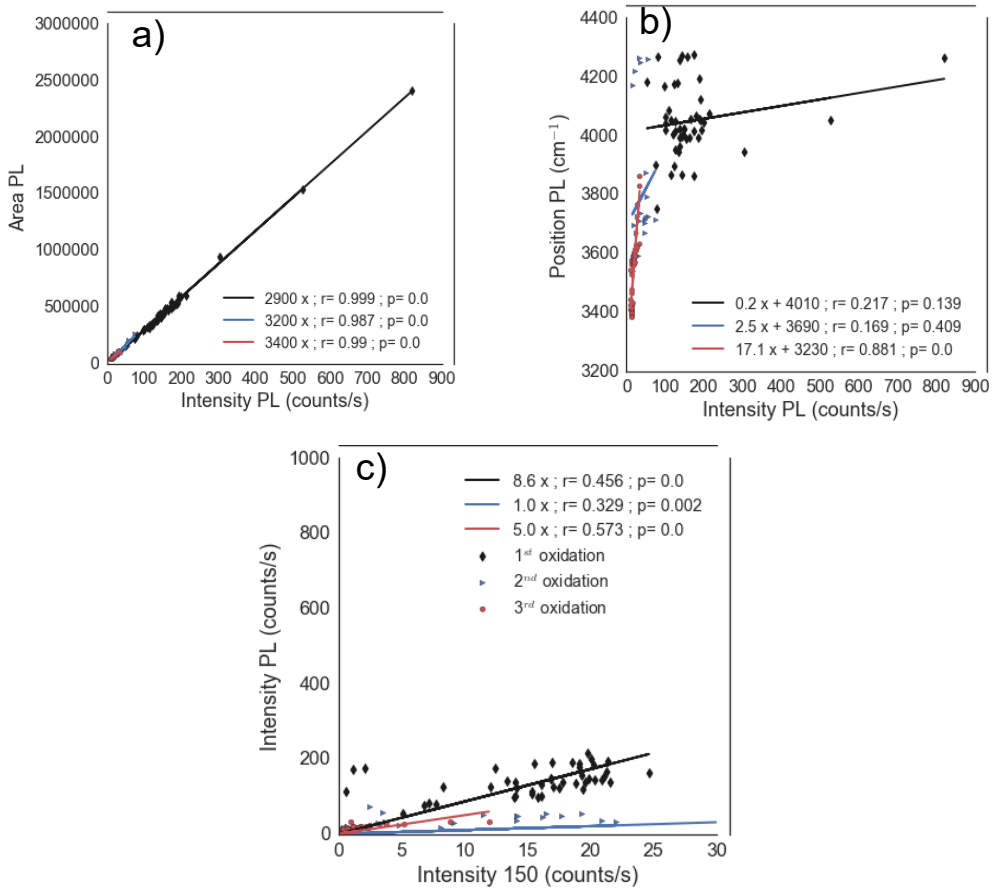

Figure IV-24: Correlation between the PL intensity with its area (a) and position (b) and the peak at 150 cm^{-1} (c). Black, blue and red symbols correspond to data for the 1st, 2nd and 3rd oxidation cycles, respectively

On the other hand, the intensity of the Raman peaks at 150 and 220 cm^{-1} appear to be not sensitive to the details of the microstructure/purity, so that they can be used to monitor the thickness of the superficial layer of cuprous oxide on copper.

The evolution of the Raman intensity of the Cu_2O peak at 150 cm^{-1} during the three oxidation cycles of the electroless sample is presented in Figure IV-25 by horizontal dotted lines. For each oxidation cycle, the Raman intensity of Cu_2O is increasing, from 0.009 to 0.023 (1st oxidation), 0.019 to 0.082 (2nd oxidation) and 0 to 0.016 (3rd oxidation).

The smallest intensities are logically measured during the 3rd oxidation cycle, performed under oxygen at low temperature (T < 130°C) and short oxidation time (t < 20min) after a complete reduction of the sample. Such small intensities can only be assigned to thicknesses in in the range 0-5 nm.

As far as the 1st oxidation cycle is concerned, the Raman intensity for the initial sample is too low to be assigned to any other thickness than 4 nm. Then for such low oxidation time and temperature (< 10 min at 150°C) thicknesses are likely corresponding to the left side of the first IERS peak as well (about 5 and 6 nm of Cu_2O).

Finally, the Raman intensities increase much more during the second oxidation cycle Since the intensities are increasing continuously, the thicknesses for the first oxidation steps of the cycle are likely corresponding to the left side of the first IERS peak as well (*ie* to the range 5-9 nm). For the most oxidized sample of this cycle two thicknesses are possible: 13.5 and

22.5 nm, corresponding to the left and right sides of the first IERS peak, respectively, but again due to the oxidation time and temperature (5 min at 250°C at maximum) this last thickness is unlikely.

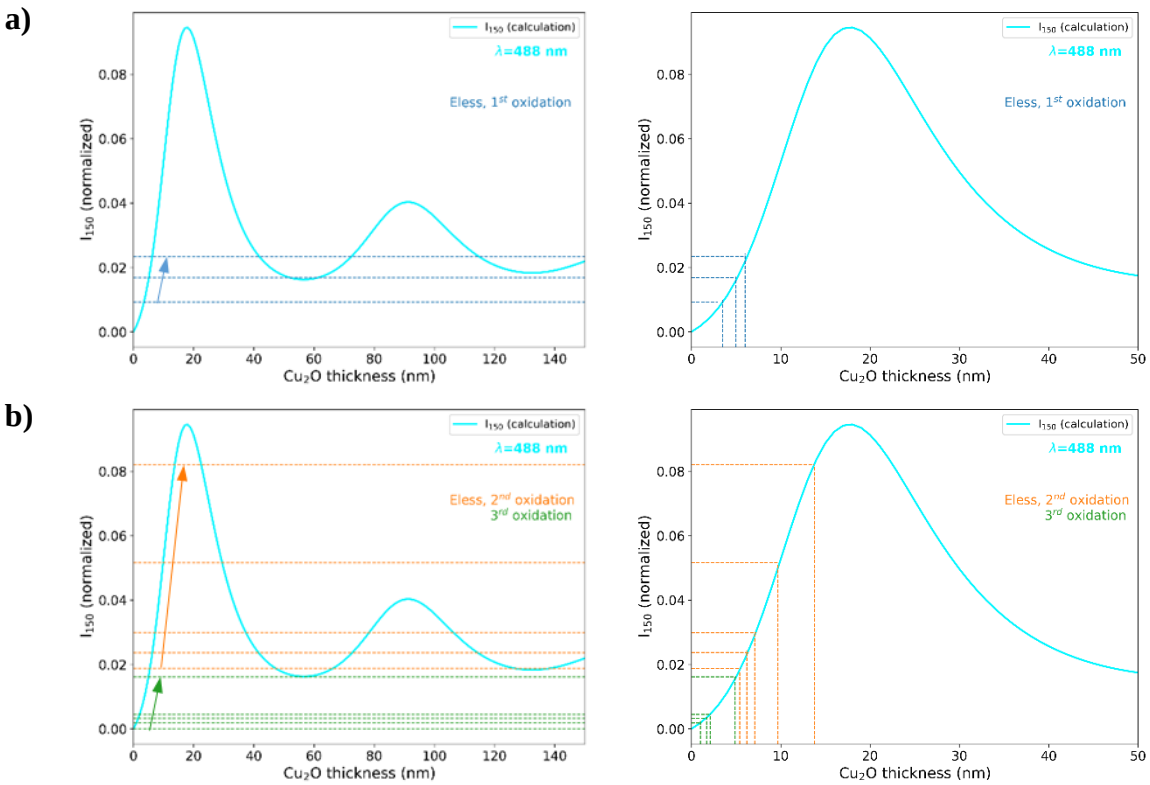

Figure IV-25: Determination of the Cu_2O thickness during three successive oxidation/reduction cycles of an electroless sample by comparison of the intensity of its Raman peak at 150 cm^{-1} (exciting line at 488 nm), with IERS best matches for thin films (Figure IV-19) for the 1st (a) 2nd and 3rd (b) in-situ oxidation series for electroless sample. The horizontal dotted lines correspond to the measured Raman intensities, and the vertical dotted lines show the most likely copper oxide thickness for each sample.

To conclude on this part, the intrinsic spectral signature of copper was measured in a controlled reducing environment, which allows to state that the PL measured on copper samples in air arises from its superficial cuprous oxide layer. This PL signal is even more tangible than the Raman one, but is very sensitive to the microstructure / impurities, and therefore strongly varies as a function of the deposition process and/or the thermal history of the samples. The most relevant excitation line for monitoring ultrathin copper layers is 488 nm, since both Raman and PL can be measured easily, even though a much larger IERS enhancement factor is achieved in the red / near infrared for larger thicknesses. Taking advantage of sensitivity of the PL signal and of the IERS enhancement, and providing a thorough calibration is achieved with appropriate samples, Raman/PL spectroscopy appears as a powerful technique to detect and quantify the thickness of superficial Cu_2O on copper.

2. Expected IERS enhancement for molecules deposited on the copper / copper oxide surface

2.1. IERS study on a copper single crystal

Optimal IERS enhancements are expected for perfectly parallel and flat thin layers. Therefore the ideal sample to investigate IERS is a copper single crystal. In order to study IERS enhancement, we chose single layer graphene (SLG) as an ideal probe, due to its large surface coverage and passivation properties, as well as high sensitivity to its environment. Figure IV-27 shows a typical optical microscopy picture of a single crystal of copper covered by a SLG (transferred using the PMMA method). Lines of different colors and typical width of 1 µm can be observed: white, orange, red, and black lines corresponding to crescent oxidation. The darker colors are linked to a larger oxide thickness, as we could measure with the transparent calibration sample substrate. The periodicity of the pattern recalls the microstructure of the copper foils on which SLG are CVD grown, due to the lamination by drum. We assign the differences in oxidation on the different lines to amount of water trapped under the SLG during the transfer.

Raman maps showing the spatial variation of the intensities of the Cu_2O mode at 150 cm^{-1} and of the G band of SLG are compared to the optical microscopy picture in Figure IV-27. The color lines are clearly correlated with the intensity of both the Cu_2O and G modes.

It is worth noting that the typical position of the G band for this sample, and for most of the SLG transferred on copper-based materials, is about 1595 cm^{-1}, *i.e.* significantly blue shifted with respect to the value of suspended SLG (about 1580 cm^{-1} [152]). This is in agreement with previous studies on Cu (111) single crystal [96], where the shift was assigned to electronic and mechanical interactions with the copper / copper oxide substrate. The ranges of positions for the G and 2D bands for our sample is compared to Lee *et al.* [93] representation (Figure IV-26). According to this representation SLG transferred on a (111) copper single crystal is p-doped and under compressive stress.

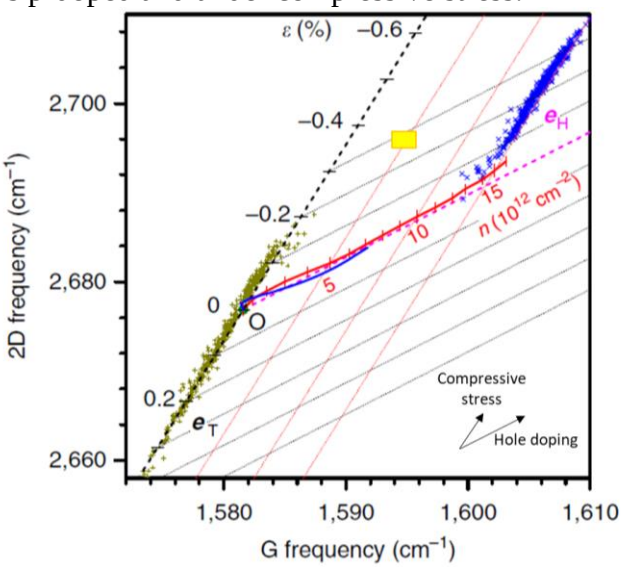

Figure IV-26: Evolution of the G and 2D band positions for SLG under stress and doping (symbols and dotted lines, from [93]). By comparison, the upshifts of G and 2D measured on copper samples (yellow square) can be interpreted as due to compressive stress and p doping

Two spectra, typical of the measurements on white and red lines (areas marked by stars on (Figure IV-27) are compared in Figure IV-28, The intensity ratio of the Cu_2O and G band are about 6 and 3, respectively. This can be well interpreted in terms of IERS.

Using the best match between calculations and data measured for thin films at 633 nm (Figure IV-19) the oxide thickness is likely about 7 nm on the white line On the other hand, the Raman intensity on the red line corresponds to about 10 nm on the left side of the first IERS peak. Note that the color difference makes it tempting to assign a much thicker thickness to the red line *ie* to the interference minima at ~75 nm, but therefore one would expect to find some areas around with intermediate thicknesses and therefore much larger intensities, which was actually not observed.

On the other hand, the enhancement of the G band corresponds to the SMEF enhancement at the surface of copper oxide, and must be calculated at a significantly different scattered energy. The relative Raman intensities for copper oxide and graphene could confirm the thickness assignments.

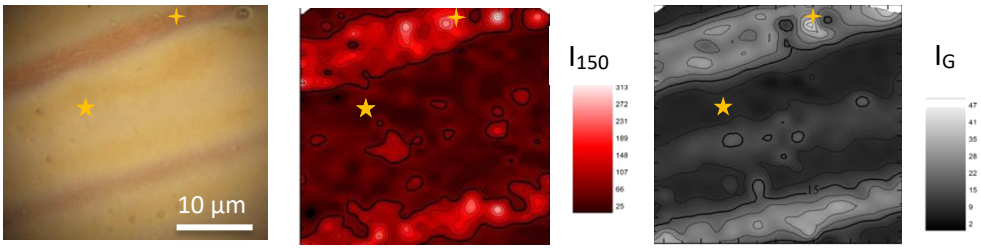

Figure IV-27: Optical image (left) and Raman maps, measured with an excitation line at 633 nm and a step of 1 micrometer, showing the intensities of the Cu_2O peak at 150 cm^{-1} (middle) and that of the G peak of SLG (right).

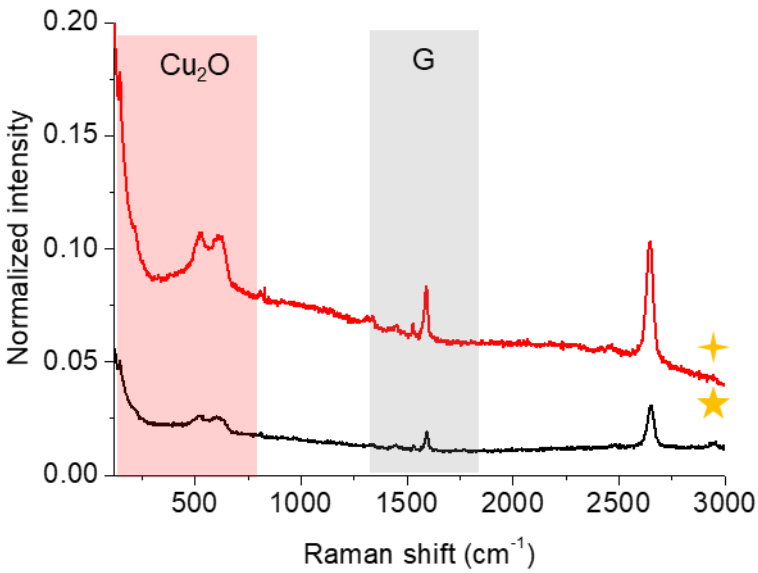

Figure IV-28: Typical Raman spectra excited at 633 nm on white and red lines (areas marked by 5 and 4 branches stars in Figure IV-27)

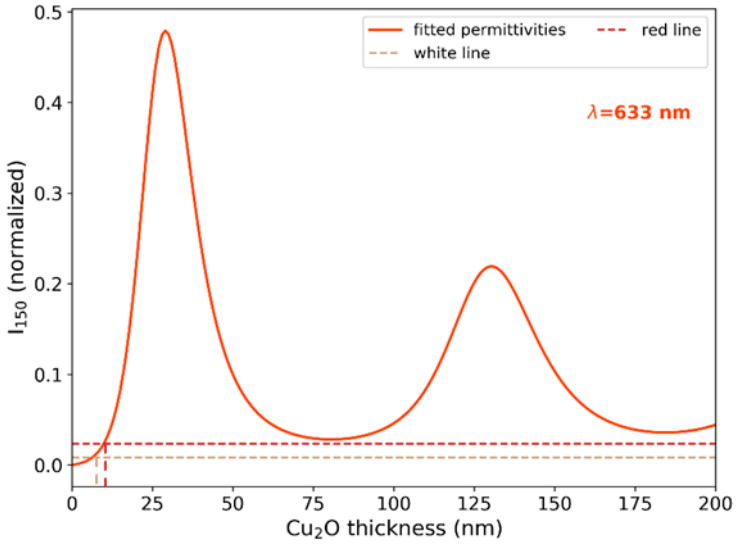

Figure IV-29: Determination of the Cu_2O thickness during on white and red lines of a copper single crystal covered by SLG by comparison of the intensity of its Raman peak at 150 cm^{-1} (exciting line at 488 nm), with IERS best matches for thin films (Figure IV-19) The horizontal dotted lines correspond to the measured Raman intensities, and the vertical dotted lines show the most likely copper oxide thickness for each sample

2.2. Influence of the nanostructuration on IERS of SLG

Various nano- and micro- structuration techniques, and in particular process used in Atotech GmbH, have been used in the framework of this thesis.

Below, we present a selection of results on two kinds of samples, covered by transferred SLG: the first one was prepared by electroless copper deposition on a silicon wafer, and the second one by etching of a bare copper foil.

2.2.1. Electroless copper samples

Figure IV-30 shows a typical optical microscopy picture of the sample, at the edge of a SLG layer (the top part of the picture, covered with SLG, shows color lines close to those observed on the single crystal, while the bottom part, free of SLG, does not), as well as four Raman spectra corresponding to four different colored lines. For white and orange lines, intensities are weak for Cu_2O while the signal of SLG is quite strong. By contrast, for red and black areas, the Raman and PL signatures of Cu_2O is much larger while that of SLG is significantly weaker. To better understand these differences, the sample was oxidized at 150°C for 3, 8, and 17 min in pure O_2 (400 sccm). The corresponding evolutions of the spectra for the orange and red areas are compared in Figure IV-31. For the red series, the graphene and Cu_2O Raman signatures remains almost constant during the oxidation process, while for the orange series, the graphene decreases rapidly, as the copper oxide increase. These observations are not in good agreement with the proposed interference model from the literature, where the maxima of Cu_2O and G should occur for the same Cu_2O thickness [102]. As for the copper single crystal it is difficult to estimate the thicknesses, and further oxidation / reduction cycles should be applied to get more quantitative data. The intensity changes between the samples can be all interpreted by IERS. In order to quantify theses evolutions,

calculation of the graphene signal should be calculated for the vibration at 1595 cm^{-1}, and compared to additional data acquired during gentle oxidation /reduction cycles.

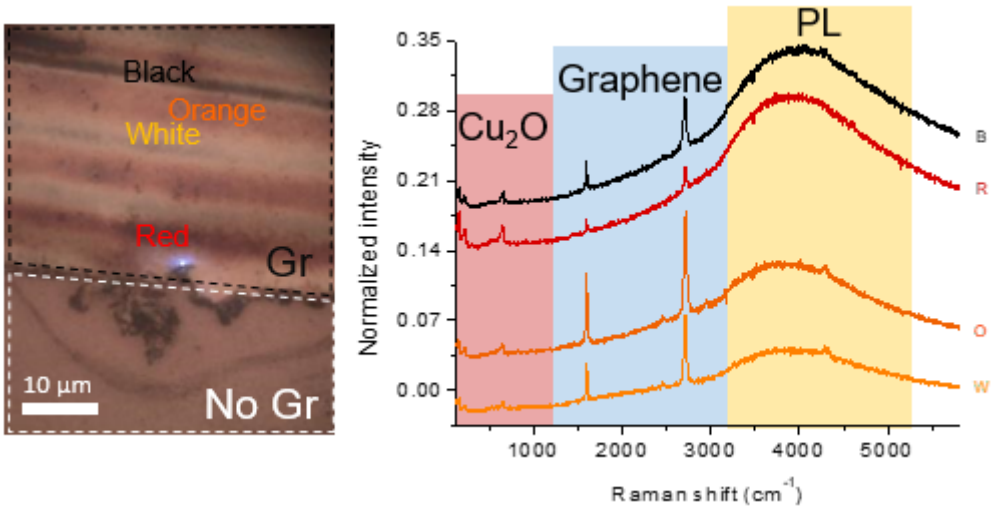

Figure IV-30: Left: optical microscopy picture of an electroless sample, with characteristic colored lines below the SLG (top), and an homogeneous color outside the SLG area (bottom). Right: Raman spectra, excited at 488 nm, on Black (B), Red (R), Orange (O) and White (W) lines.

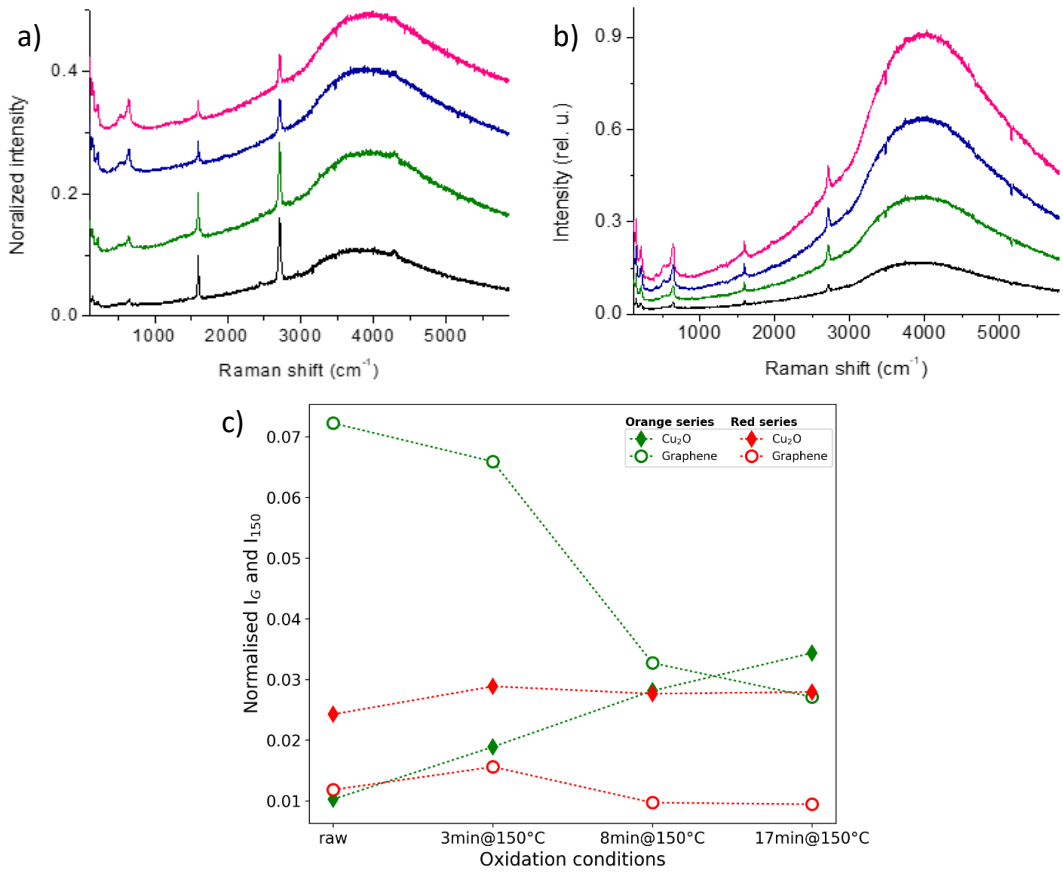

Figure IV-31: Evolution of the Raman spectra during oxidation at 150°C (during 0, 3, 8 and 17' from bottom to top) on an orange line (a) and on a red line (b) and representation of the fitted I_{150} and I_G (c)

2.2.2. Copper etching sample

A Raman map of the G peak of SLG transferred on an etched copper foil is presented in Figure IV-32(left), along with two Raman spectra (right), one being a typical spectrum, and the other one corresponding to the highest intensity measured, on a so-called ‘‘hot spot’’. The Raman spectra on the hotspot shows both Cu_2O and G intense signature. The enhancement on Cu_2O is large, with Raman peaks below the detection limit for a regular spectrum and of intensity comparable to that of graphene G band on the hot spot.

As for the electroless sample, the G peak position is around 1595 cm^{-1} and its FWHM ~ 14 cm^{-1}. The enhancement factor for the G band on the ‘‘hot spot’’ is ~ 30 with respect to the typical spectra. Such enhancement factor about 30 have been observed on bubble trapped between graphene and the copper substrate [102]. However, the graphene G band position is at a typical position of Cu / Gr, far from that of suspended graphene ~1580 cm^{-1}. This enhancement is larger than that measured at 488 nm for the electroless sample, but according to the calculations of Figure IV-18, this could still be assigned to IERS, since IERS enhancements are expected to be larger for excitations in the red. This assumption should however be confirmed by the IERS calculation of the G mode at 1600 cm^{-1} for an excitation at 638 nm, using the fitted refractive index.

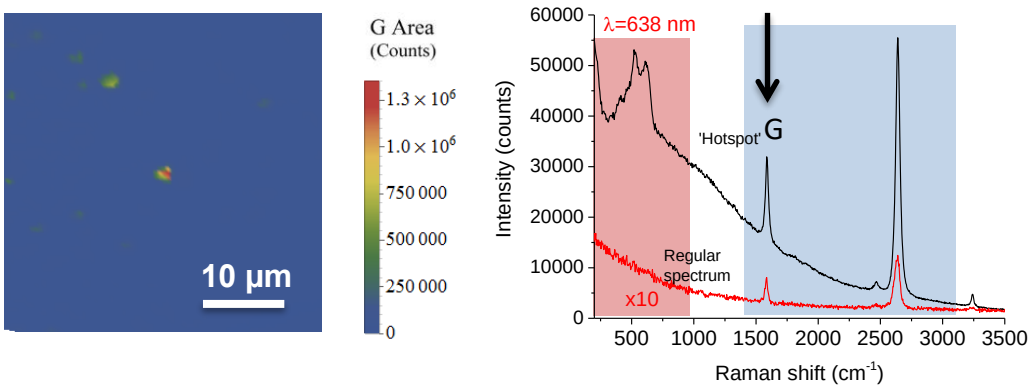

Figure IV-32: Raman map showing the spatial evolution of the G band intensity, excited at 638 nm with a step of 0.5 µm, on a copper etched sample

In conclusion, rough/nanostructured samples prepared using Atotech processes show quite small SMEF enhancements, not lager than 5 and 30 for exciting lines at 488 and 633 nm, respectively. These enhancements can be fully explained by IERS considering homogeneous superficial layers of copper oxide, whose thickness can be estimated from the Raman intensities of the cuprous oxide mode at 150 cm^{-1}.

Such small enhancements make these nanostructured copper-based samples unfit for the detection of small amounts of non-resonant molecules on their surface, even though detecting SLG is quite easy because of its resonant signal and complete coverage of the surface.

Chapter V: Comparative SERS studies of gold and copper

In this chapter, we use a commercial product, made of gold nanostructured pillars and named SERStrate, to compare the performances of gold and copper as supporting metal for SERS. We define the optimal measurement conditions, and estimate the enhancement factors for the gold SERStrate. Then, we deposit a thin layer of copper on the SERStrate and compare the SERS enhancements. BPE, is used as a -model dye. Finally, we discuss the possibility to monitor *in situ* adsorption followed by a chemical reaction of organic additives of interest for Atotech.

1. Optimization of the SERS measurements on raw Au-SERStrate

1.1. Raman spectra of bare substrate

Typical Raman spectra of the bare Au-SERStrate are presented in Figure V-1a. Intense peaks are observed in the range 120 to 1700 cm^{-1} with very different spectral features on different areas, and a lack of reproducibility when several spectra are measured successively on the same area. This is assigned to dynamic adsorption / reorientation / desorption of various molecular species on the gold surface. The signal of these parasite molecules is not observed anymore after dipping the SERStrate in a dye solution, which we assign to a better affinity of dye molecules with respect to these organic impurities. On the other hand, a weak peak is systematically measured around 2120-2130 cm^{-1} not attributed.

On the other hand, no more parasite signals are observed after the deposition of a thin layer (~50 nm) of copper on the SERStrate (Figure V-1b). The spectra present rather intense peaks at 150, 400, 530 and 620 cm^{-1}, characteristic of Cu_2O. For comparison, deposition in the same conditions on a fused silica substrate gives the same spectrum profile but with an intensity about 40 times weaker, the larger signal on Cu-plated SERStrate being assigned to SERS enhancement.

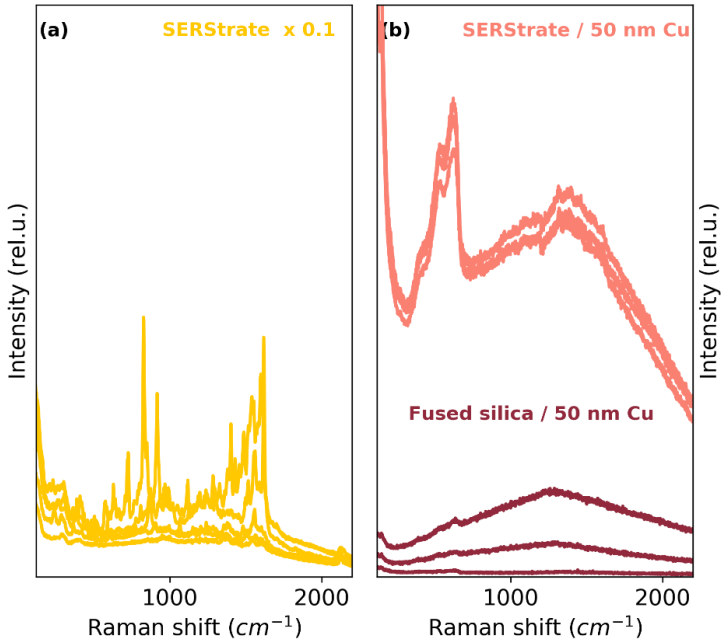

Figure V-1: Raman spectra, excited at 785 nm, measured on different areas on a bare Au-SERStrate (left), and after deposition of 50 nm of Cu on the SERStrate (right, with comparison with the spectrum of a similar copper layer deposited fused silica).

1.2. Wavelength dependence of the SERS enhancement

Before studying the wavelength dependence, we give the extinction spectra of the raw SERStrate, considering the pillar structure before and after 'leaning' (agglomeration of pillars, due to the capillarity force during drying after immersion). The microstructure of the bare Au-SERStrate, as revealed by SEM, is shown in Figure V-2 left, silicon pillars of ~1 µm height are covered by gold and reach a diameter ~100 nm. After leaning the pillars (by dipping the substrate in a liquid and drying it in air), one observes agglomerated bunches (Figure V-2-right)

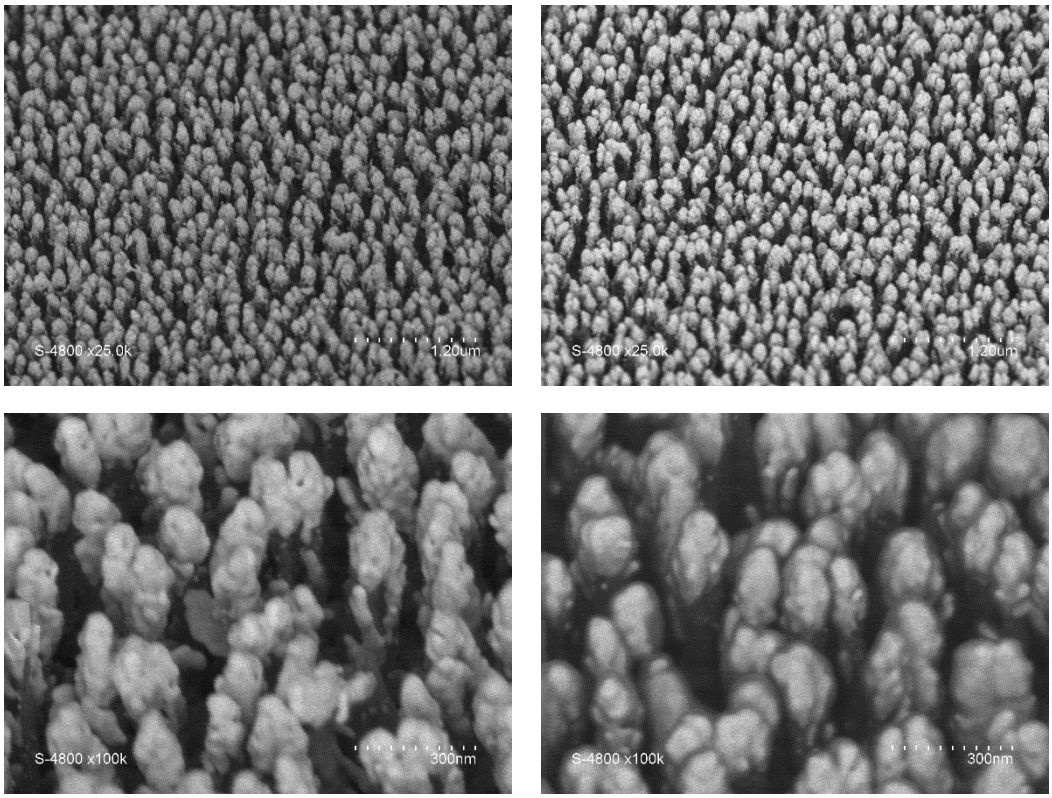

Figure V-2: SEM pictures of the bare Au-SERStrate before (left) and after dipping in a liquid and drying in air (right), with magnifications 25 k (top) and 100 k (bottom).

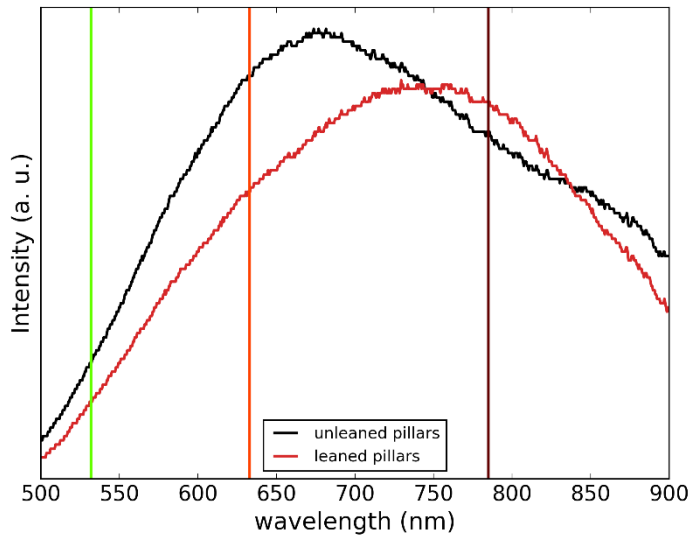

Figure V-3: Extinction spectra in the visible range for a raw SERStrate with un-leaned pillar and after immersion and rinsing with lead to a pillar leaning.

Note that the diffuse reflectance spectra of the raw SERStrate changes after dipping (Figure V-3). The redshift of the maximum from ~680 to ~745 nm is likely related to a redshift of the LSPR and therefore an expected larger SERS enhancement for larger excitation wavelengths [103].

Accordingly, we find that the largest enhancement factor for BPE on Au-SERStrate is 785 nm (Figure V-4), with respect to excitations at 633 nm (typically one order of magnitude below) and at 532 nm (typically three orders of magnitude below). Here, the Au-SERStrate was dipped in an ethanol solution of BPE at 10^{-6} M, and then rinsed with the solvent (ethanol) and dried in air.

The main characteristic peaks of BPE are observed at ~1200, 1600 and 1638 cm^{-1}. Note that the Raman signal of BPE is very homogeneous on the Au-SERStrate, the general intensity only varying by a maximum factor of 2 between different areas (the spectra in Figure V-4). However, the intensity ratio of the different peaks vary between the different areas, which likely reveals different orientation with respect to the laser polarization. The shown spectra correspond to the averaged spectrum of 36 different areas). To compare the enhancement factors at different wavelengths, we used the intensity of the peak at 1200 cm^{-1}, assigned to C-C stretching ($\nu(C-C)$) and C-N bending ($\delta(C-N)$), which is about 2.10^3 and 30 times more intense at 785 nm than at 532 and 633 nm, respectively.

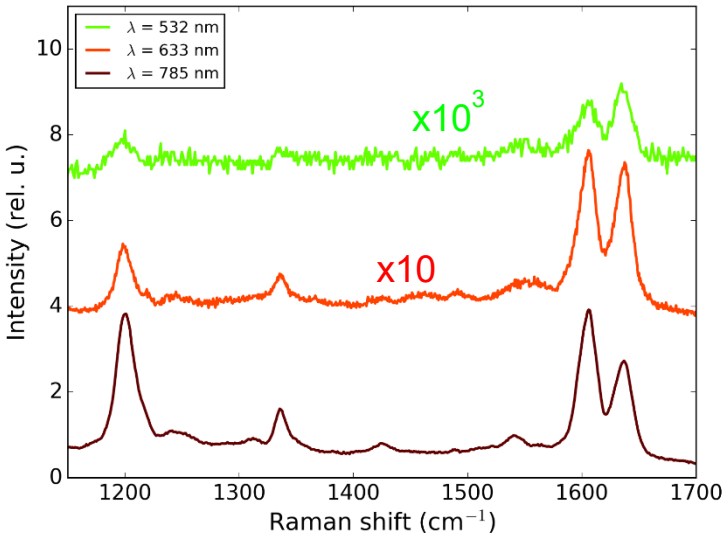

Figure V-4: Comparison of Raman spectra measured on a Au-SERStrate after dipping in a BPE solution (c=10^{-6}M), rinsing and drying, for three excitation lines at 532, 633 and 785 nm. The intensities are normalized by HOPG (acquired in the same conditions: 1 s, power ~200 µW). For clarity all spectra but the bottom one are vertically shifted.

1.3. Effect of the pillar leaning

In order to check the effect of pillar leaning two samples are studied, one raw Au-SERStrate, and one Au-SERStrate which is pre-leaned in water and dried in air before dipping in the BPE solution. Figure V-5 compares the spectrum for BPE (c = 10^{-6} M) deposited on these two samples. The pre-leaned SERStrate shows the same characteristic peaks of BPE but they are significantly less intense (by a factor of about 7). The apparition of an additional band located at 1380 cm^{-1} is assigned to C-H bending mode ($\delta(C-H)$). The large intensity compared to other vibrations modes of BPE is assigned to a preferred bonding of the vinyl group [87].

The larger enhancement factor for raw samples is explained by molecules trapped in hotspots between the pillars:

- The molecules adsorb on the pillars when the SERStrate is dipped in the solution
- As the sample dries, the pillars agglomerate because of capillarity effects, and the molecules are eventually trapped in between. The local fields are expected to be maximum in between the pillars due to coupling effect of combined metallic tips [86]. By contrast, no molecule can be trapped on the hot spots between the pillars for pre-leaned SERStrate.

In summary, the largest signal over noise ratio is obtained for 785 nm as expected from the extinction spectra. The pre-leaning of the SERStrate leads to an intensity drop by a factor of 7 compared to the raw SERStrate sample. In order to detect a molecule at a low concentration, the selected wavelength should be 785 nm, and the SERStrate should not be pre-leaned (note that this is incompatible with *in-situ* monitoring of molecular adsorption.

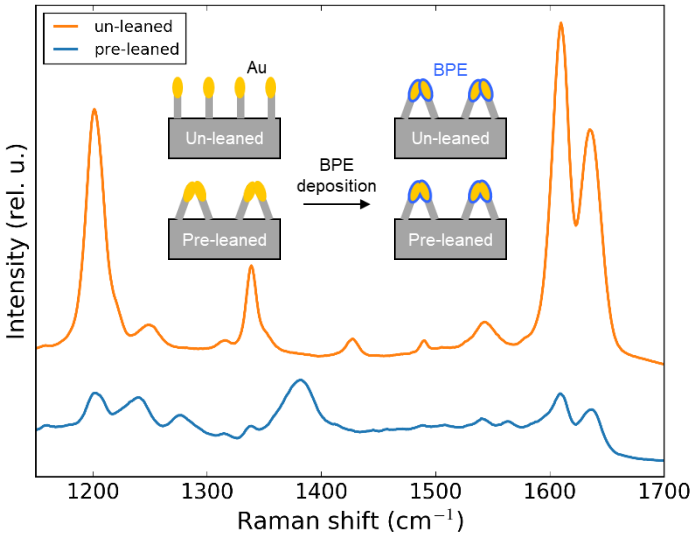

Figure V-5: Comparison of pre-leaned and un-leaned SERStrate for the detection of BPE (c= 10^{-6} M), at 785 nm. The un-leaned spectrum is vertically shifted for clarity.

1.4. Estimation of the enhancement factor in optimal conditions

The enhancement factor of the SERStrate sample is estimated below.

When a gold surface with a very small roughness (R_{ms} < 7 nm) is dipped in the BPE solution, only the Raman signatures of ethanol can be measured, but no Raman signature of BPE can be detected (Figure V-6).

Therefore, the enhancement factor is estimated by comparing the Raman intensities for the concentrated solution of BPE (10^{-1} M) and the SERStrate dipped in a diluted solution of BPE (10^{-6} M). The calculated enhancement factor for the Raman peak intensities at 1200 cm^{-1} is

$Ef = \frac{I_{SERStrate}}{C_{SERStrate}} * \frac{C_{sol\,BPE\,10^{-1}M}}{I_{sol\,BPE\,10^{-1}M}}$ ~10^7. The difference of ratio between the Raman peaks at 1600 and 1638 cm^{-1} fir the different samples is assigned to the preferred orientation of BPE on the SERStrate, leading to a favored vertical orientation with a bond by the amino group. This explains the larger intensity of the 1600 cm^{-1}, assigned to the symmetric pyridyl ring breathing, coupled with C-C stretching and C-H in plan bending, compared to the concentrated BPE solution.

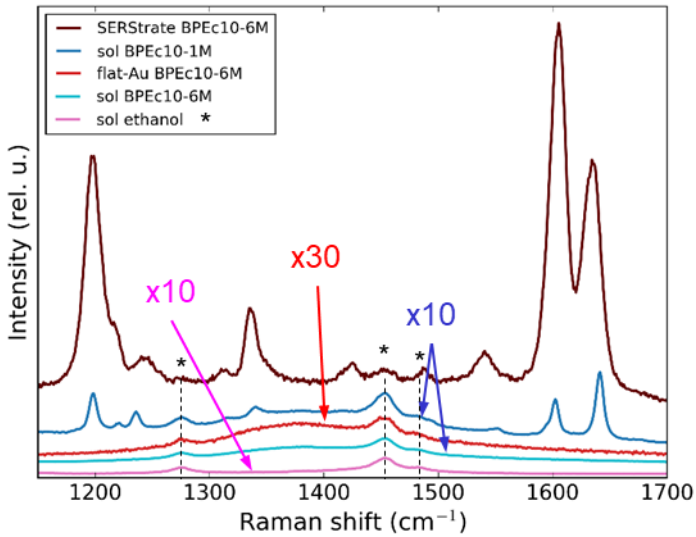

Figure V-6: Comparison of BPE spectra on reference 'flat' gold surface and a SERStrate after dipping in BPE (c = 10^{-6} M), rinsing and drying, and on two solutions (c = 10^{-1} ; 10^{-6} M) in ethanol. Spectra are multiplied by ad hoc factors for sake of comparison and vertically shifted for clarity

2. Comparison of Au- and Cu- plated SERStrates

In order to compare the SERS performances of Au and Cu for comparable nanostructured substrates, and to study the effect of oxidation of copper, measurements on an original Au SERStrate are compared to measurements on a Cu-plated (~50 nm of thermally evaporated Cu) SERStrate, in the optimal conditions described above.

The measurements are performed at different steps:

- raw SERStrate vs Cu-plated SERStrate (~50 nm) in air (step 0)
- during dipping the samples in an aqueous solution of BPE (10^{-6} M) (step 1)
- after thorough rinsing and drying in air (step 2)
- during short dipping in an acidic solution of BPE (10^{-6} M) containing sulfuric acid (0.1 M) to remove the copper oxide superficial layer (step 3)
- after another rinsing and drying in air (step 4)
- after 2 hours of final dipping in the acidic solution to remove the whole copper layer, and therefore retrieve the original Au-SERStrate (step 5)
- after a final rinsing and drying in air (step 6)

2.1. Microstructure evolution on a copper covered SERStrate

The microstructure evolution on the gold and copper surfaces are compared in Figure V-7. For raw surfaces (step 0) the additional evaporated copper leads to larger diameter of the pillars. After dipping in water and drying in air (step 2), the pillars of the Au-SERStrate are leaned while those of the Cu-plated sample remain similar. In step 4 the shape is different for the golden surface leading to smoother surface, while the step 6 leads to similar smooth structure, with a decrease of the diameter.

	Au-SERStrate	Au-SERStrate + ~50 nm Cu
step 0	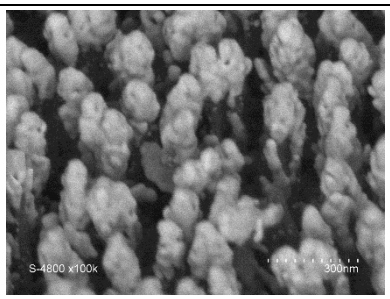	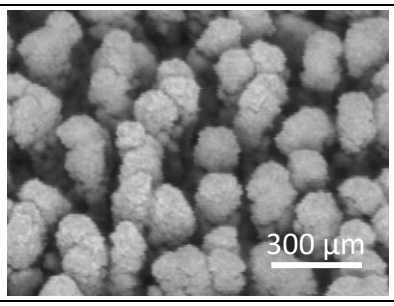
step 2	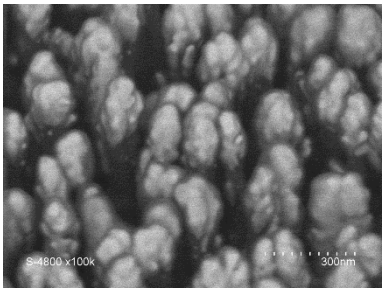	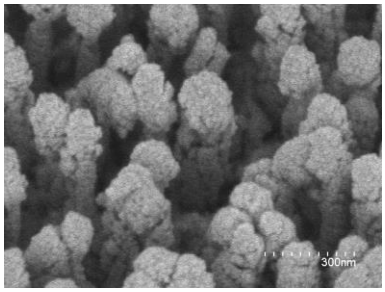
step 4: Au-SERStrate 6: Cu-SERStrate	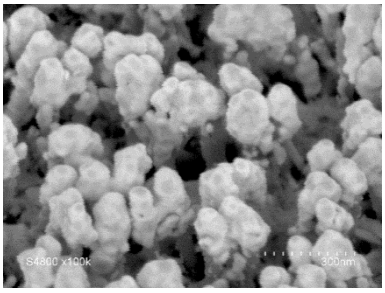	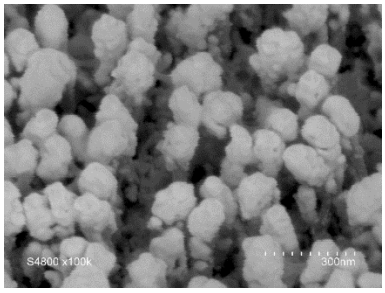

Figure V-7: SEM pictures of the pillar nanostructures for raw Au-SERStrate (left) and for a Cu plated SERStrate (right), after immersion in water, and the acidic solution (step 2, 4 and 6).

For clarity, sketches of the pillar nanostructures at different steps are compared in Figure V-8. We assume a cuprous oxide layer in air and water solution, while superficial copper and gold are expected in acidic solution, for short and long time exposures to acid, respectively.

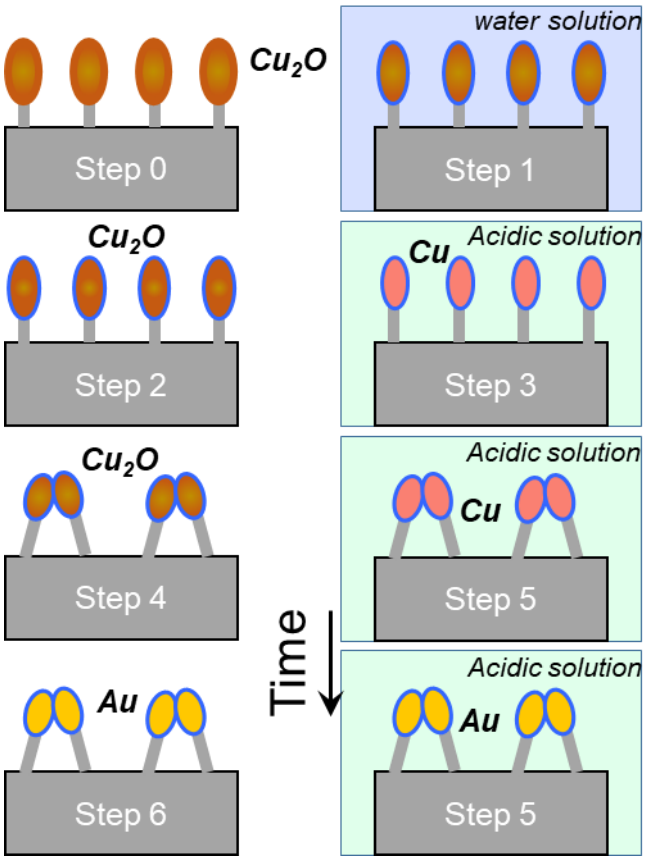

Figure V-8: Sketch of the pillar nanostructures at different steps (cf §2) for Cu-plated SERStrate The blue and green background represent aqueous and acidic solutions, respectively. The absence of background represents a measurement in air. The blue coating of the pillars represent the attached BPE molecules. The pink, brown and gold pillar colors are for copper, cuprous oxide and gold, respectively.

2.2. In situ Raman monitoring of the surface of the SERStrate

Figure V-9 represents the Raman spectrum for the first 4 steps. Copper oxide signatures are observed in steps 0, 1, 2 and 4. Steps 0, 1 and 2 show the characteristic Cu_2O oxide peaks (150, 400, 530 and 620 cm^{-1}) and no extra peak. Those characteristics intensities increase from step 0 to step 2. An additional signature of the oxide in step 2 is the intense luminescence background. In step 4, when rinsing and drying the sample again in air, the peak at 150 cm^{-1} cannot be not observe but weak characteristic features at 530 and 620 cm^{-1} suggest that a very thin layer of Cu_2O is formed.

The oxide signatures augmentation from step 0 to step 2 is assigned to the growth of Cu_2O in the water based BPE solution. The weaker Raman intensity of cuprous oxide in step 1 (aqueous BPE solution) is assigned to the difference in the dielectric properties of the environment, changing the LSPR.

As expected, immediately after introduction in acidic solution the copper oxide signatures disappear, and are never observed in acidic conditions (step 3, and step 5).

On the other hand the main BPE signatures (1202, 1610 and 1638 cm^{-1}) are easily detected directly after immersion in BPE water solution even if the peaks have a low signal over noise

ratio (step 1). In air (step 2), the oxide luminescence background is strong and hinders the observation of the BPE signal. Then, in acidic conditions the BPE signature raise strongly, with signatures in the same intensity range after rinsing and drying (step 3 and 4).

During step 3 in acidic conditions, an additional band apparition between 200 and 300 cm^{-1} is attributed to M-N or M-S stretch (M= Cu or Au) [153]. During this step the peak at 1610 cm^{-1} assigned to C-C stretch or C-N bending is much less intense than the C=C stretch at 1638 cm^{-1}. These peaks are the proof of the adsorption of molecules adsorption on the metallic surfaces.

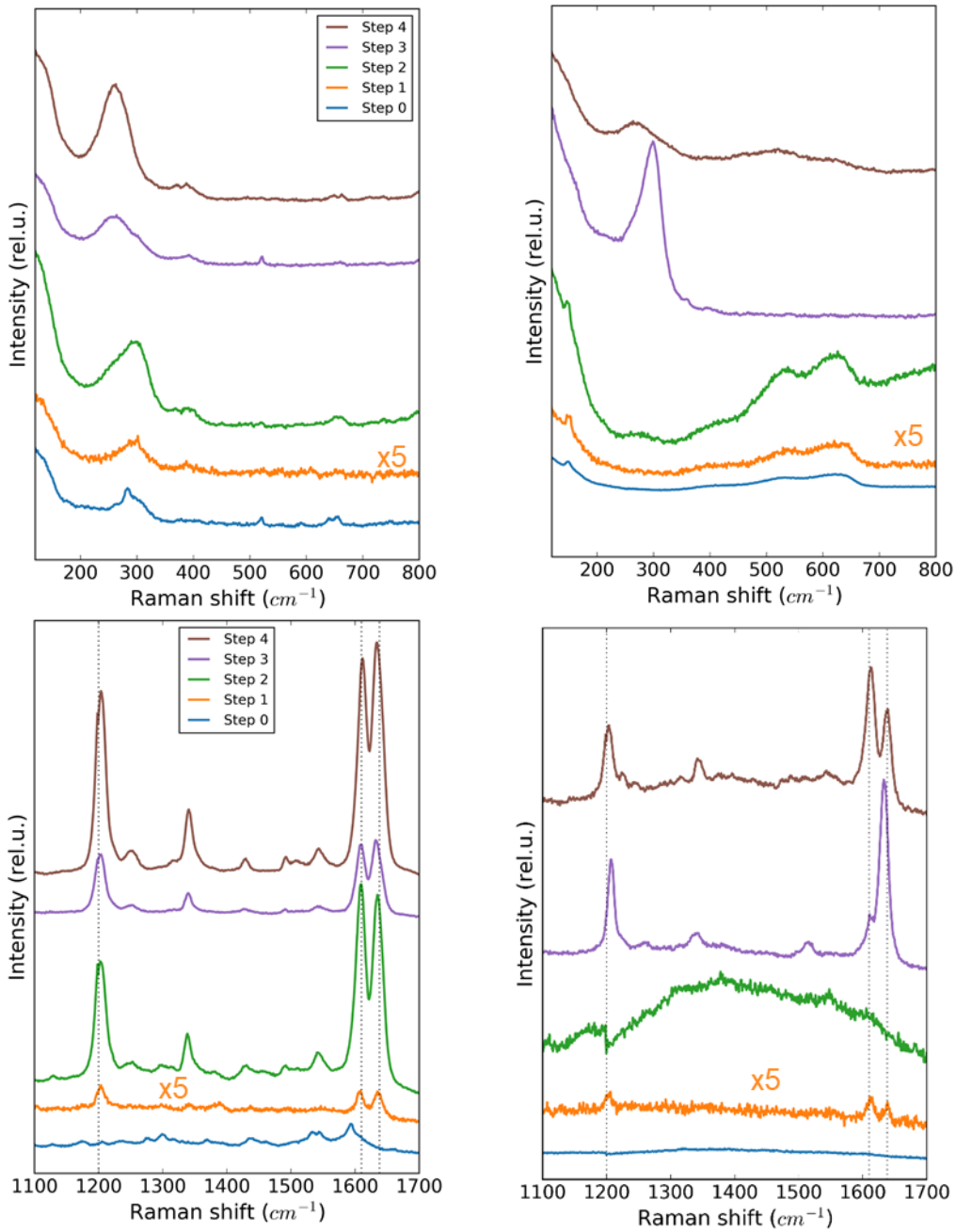

Figure V-9: Comparison of the Raman spectra of BPE on Au- (left) and Cu-plated (right) SERStrates at different steps (see Figure V-8). The dashed lines mark the most intense BPE signatures (1200, 1610, 1638 cm^{-1}).

In order to further compare the signal on copper to that on gold, we carried out an *in situ* monitoring of the Raman spectra in acidic solution as a function of time (step 5). As recalled above, the kinetics of etching is very fast for copper oxide. On the other hand, the time for etching 50 nm of copper in these conditions was estimated to ~2h. The intensity of the peak at 1200 cm^{-1} is plotted as a function of time in Figure V-10.

Due to a focus loss, the 'raw data' are corrected, removing the fitted intensity of the focus loss.

On the corrected data, the intensity of the BPE characteristic peak at 1200 cm^{-1} first remains almost constant during the first 1000 s. Then the intensity increases continuously with time up to 3400 s, where it reaches a second plateau.

The first plateau is assigned to a sufficiently thick layer of copper covering the gold surface. Then, between~15-60 min, the LSPR and associated local fields are sensitive to decrease of the copper thickness leading to a more intense Raman signature. After ~ 60 minutes, the copper layer is completely etched and the Raman intensity does not evolve anymore on the gold surface.

The focus loss was corrected by assuming that data evolved with a quadratic shape in and out the best focused position. The collected Raman intensity was then corrected using this quadratic dependence. On the 'corrected data', BPE characteristic peak at 1200 cm^{-1} intensity first remains almost constant during the time 0-1000 s. Then, the intensity raises with time in the acidic BPE solution up to 3400 s, where it reaches a second plateau, with constant intensity of 1200 cm^{-1} Raman peak.

This can be explained by the etching of copper surface giving place to golden surface: during the first ~15 min a homogeneous copper layer covers the pillar structure, and starts to be etched away between~15-60 min, revealing the underlying gold, leading to a more intense Raman signature, that remains constant. After a time ~ 60 minutes, the Raman signature of BPE does stop evolving in acidic solution. This is interpreted as a stable surface, which occurs when the copper is entirely consumed, and only the gold remains. At the end of step 5, only gold is present, no trace of copper remains.

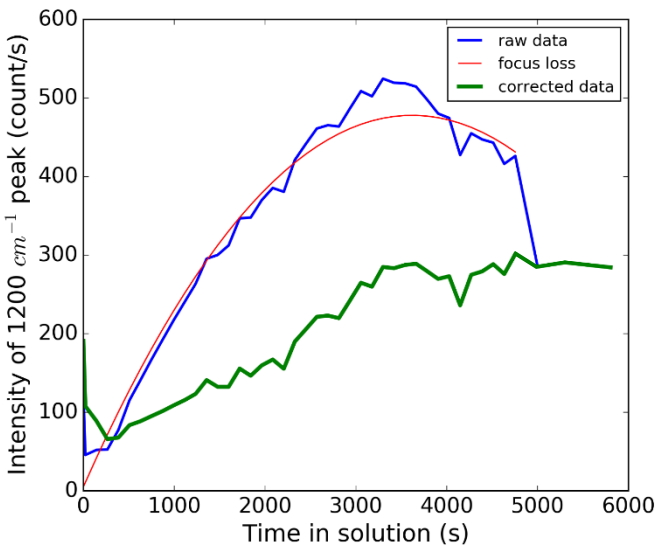

Figure V-10: Kinetic monitoring of the BPE peak intensity at 1200 cm^{-1} in the acidic solution (10^{-6} M) during step 5, before (top) and after (bottom) correction of the focus loss.

The last Raman spectrum, measured after rinsing and drying (step 6), does not present any copper oxide signatures which confirms that the copper layer is completely etched in step 5.

Another way to confirm that only gold is present at the final surface is to compare its Raman spectrum to that of a raw SERStrate (Au-SERStrate (step 4)) following the same steps. The spectra of Au SERStrate and Cu-plated SERStrate after step 6 are compared in Figure V-11. The profiles and intensities of the Raman signatures of BPE are very close, which supports the hypothesis that the copper layer of the Cu-plated SERStrate was completely etched in the acidic solution. We also remark the peak position centered at 1634 cm^{-1} for both samples, red shifted on copper (1634 cm^{-1}).

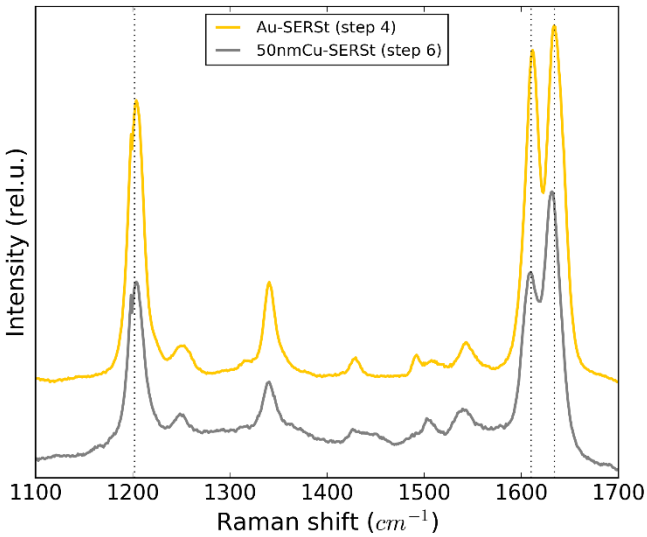

Figure V-11: Comparison of the BPE spectra on Au-SERStrate (step 4) and Cu-plated -SERStrate (step 6). The dashed lines represents the peak positions at 1200, 1610 and 1634 cm^{-1}.The spectrum on the Au-SERStrate is vertically shifted for clarity.

Finally, spectra of BPE on the Cu-plated SERStrate are compared after steps 4 and 6 on Figure V-12. The two spectra present the characteristic BPE signature. A first difference is the position of the peak at ~1635 cm^{-1} assigned to the stretching between 2 pyridyl rings. On cuprous oxide its position is 1638 cm^{-1} blue shifted on gold at 1634 cm^{-1}. This difference is assigned to a mix bond of BPE in horizontal and vertical configuration, according to Chen *et al*. [87].

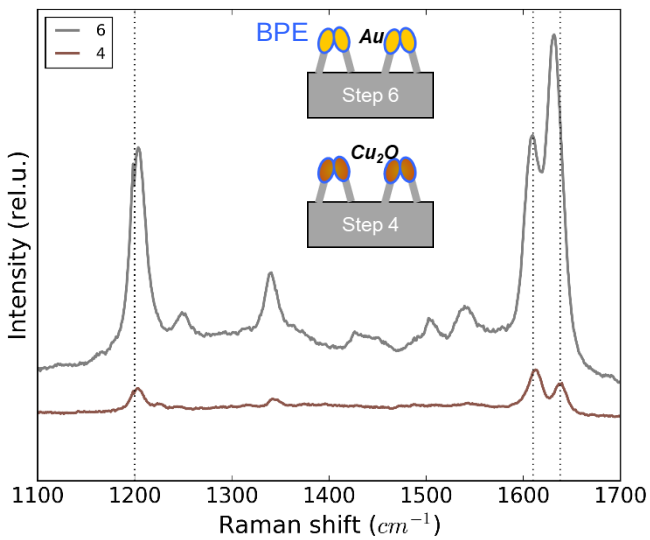

Figure V-12: Comparison of Raman spectra acquired in air at step 4 (after rinsing and drying on cuprous oxide) and step 6 (after rinsing and drying on gold). The dashed lines represents peak positions at 1200, 1610 and 1638 cm^{-1}. The intensity of spectrum at step 6 is vertically shifted for clarity.

The second difference is that the SERS signal on gold is about 10 times larger than on copper. This is tempting to conclude that the enhancement factor for gold is larger than that for copper. However, the two cross-sections are not directly comparable for several reasons:

- the copper surface is recovered by a superficial oxide layer, as probed by the low frequency signal (Figure V-9) and even if this layer if likely ultrathin, the distance from the BPE molecule to the metallic surface is larger than on gold, thus decreasing the local field intensity at the surface
- the plasmon resonance of gold and copper are not the same even though they are expected to be close, plus the copper layer likely shifts and broaden the resonance [154, 155]. The spectra are excited at 785 nm close to the maximum of the experimental extinction spectrum of Au SERStrate, but this may be shifted for Cu-plated SERStrate. Experimental measurements of the extinction spectrum of Cu SERStrate will be required to conclude.

In summary, the most intense signature of BPE (c = 10^{-6} M) are detected with 785 nm excitation on Au-SERStrate. The signature of BPE was detected in aqueous solution on a copper / cuprous oxide sample. In acidic conditions no copper oxide presence is detected, and the BPE signature on copper increases by a factor of 50 with respect to copper oxide.

The acid etching allows a complete copper consumption after ~ 60 min (~50 nm of Cu). The spectra measured on gold are only about 7 times larger than those on copper.

2.3. Influence of BPE concentration

In order to probe the detection limit on copper, similar experiments are carried out using a diluted BPE concentration of (10^{-8} M). The results are presented in Figure V-13. As for the study at larger concentration, Cu_2O characteristic signatures are observed at steps 0, 1 and 4. No luminescent background is observed, which allows the observation of BPE signatures as well at steps 1 to 4. Step 3 in acidic solution and step 6 in air are free of Raman copper oxide contributions, and present only the Raman signatures of BPE. At this lower concentration, the detection on BPE was still possible on both copper and copper/copper oxide. On gold, the BPE Raman signal of BPE are very intense (step 6).

As for the study at larger concentration, we study the signal evolution in the acidic solution. Results are shown in Figure V-14. Compared to the study in a larger concentrated solution the intensities are higher, however, the kinetics profiles are similar, featured by a first plateau, followed by a continuously increasing signal and finally a second plateau.

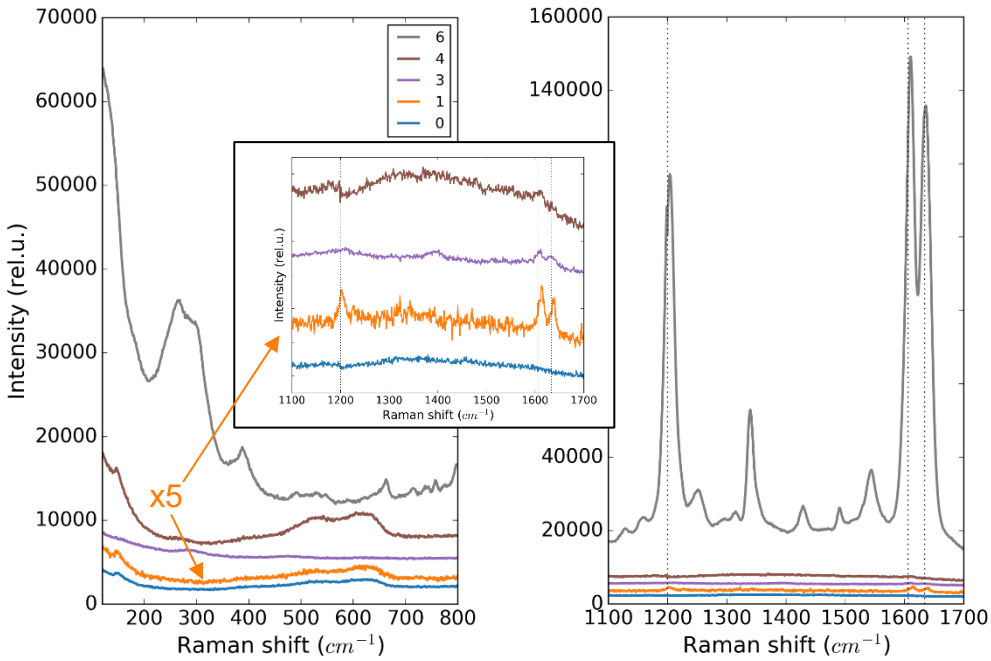

Figure V-13: Comparison of the Raman spectra of BPE (10^{-8} M) on Cu-plated SERStrates at different steps (see Figure V-8). The dashed lines mark the most intense BPE signatures (1200, 1610, 1634 cm^{-1}. The inset is a zoom of the BPE signatures on steps 0, 1, 3 and 4.

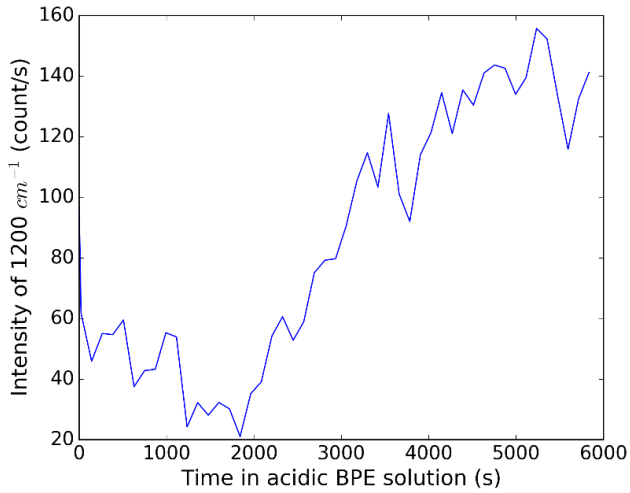

Figure V-14: Kinetic monitoring of the BPE peak intensity at 1200 cm^{-1} in the acidic solution (10^{-8} M) during step 5.

To summarize, very small concentrations of BPE (10^{-6} M - 10^{-8} M) can be detected on copper (in acidic solution), and on thin copper oxide (in air and water). However the signal on gold is larger (factor 7), which is explained partially by the sample resonance optimized for gold, but could also be assigned to the microstructure, with the copper coverage (~50 nm) hindering the pillar leaning. The pillar leaning is permitted by the etching of a part of copper. To check this particular point, the overall time in acidic solution (step 3 and 5) should be carefully control and the microstructure should be checked for different times.

2.4. Detection of another organic molecule: MBT

To check the feasibility of an *in situ* monitoring of organic additives of interest for Atotech, we probed the signature of MBT on the Au-SERStrate at 785 nm. The concentration of MBT at 10^{-8} M was fixed to be comparable at the concentration in industrial baths. Only the measurement in air and in water solution are performed, giving the characteristic MBT signatures at 998, 1020 and 1200 cm^{-1}, assigned to ring breathing, $\nu(C = S)$ and $\nu(C - N)$ respectively, according to Rai *et al* [156].

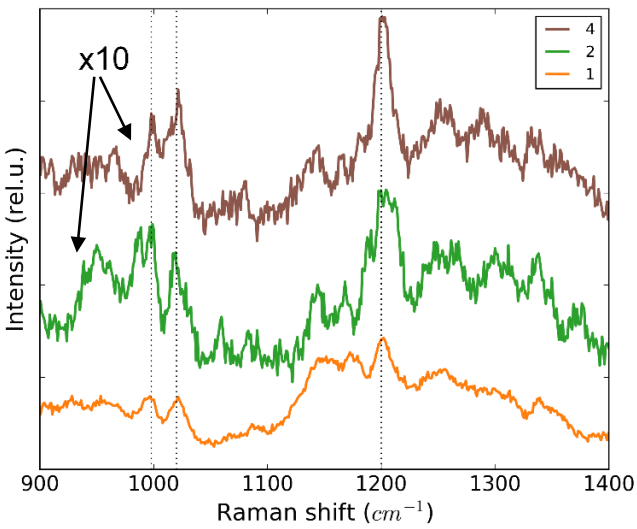

Figure V-15: Comparison of the Raman spectra of MBT solution (10^{-8} M) on Au-SERStrate. Step 1: just after immersion, step 2 and 4: in air (after rinsing and drying from previous step). The dashed lines mark the most intense MBT signatures (998, 1020, 1200 cm^{-1}).

The much smaller Raman intensity of MBT compared to BPE on gold should be explained by different adsorption properties of this molecule at the surface of the SERStrate, or simply by smaller Raman scattering cross-section. We tried to compare the Raman cross-sections by measuring the Raman signal of the MBT solution in water or in ethanol, or at the surface of a regular gold substrate, but no signal could be measured even at the maximal concentrations (1 g/L ~10^{-2} M in ethanol and 10^{-3} M in water). Therefore we conclude that the Raman cross section of MBT is much smaller than that of BPE.

At 10^{-8} M, the Raman signatures of MBT on Cu-plated SERStrate are not measurable. For BPE, the signal on copper is expected to be about 7 times smaller than on gold. Since the signal over noise ratio on Au-SERStrate is close to the detection threshold, one can expect to detect MBT on Cu-plated SERStrate for concentrations about ten times larger, *ie* 10^{-7} M.

In summary, low concentrations (down to 10^{-8} M) of a model dye molecule (BPE) can be detected on a gold commercial SERStrates, as well as on copper covered ones, in acidic conditions. Other molecules, *e.g.* organic additives of possible interest for Atotech, can be detected as well at concentrations of (10^{-8} M) on a gold substrate.

Conclusion and perspectives

During this PhD thesis, various copper-based materials were prepared by various processes. The thickness of thin and ultrathin films of copper/copper oxide was measured by coupling microscopic and spectroscopic techniques. A special focus was made on the fit of UV-visible absorption spectra, as a powerful tool to determine the thickness and refractive index. The refractive index of copper was found to be in good agreement with the literature, while that for cuprous oxide is slightly larger (about 10 %).

Raman spectroscopy was also used as a powerful technique for the study of copper oxide. The technique allows an unambiguous identification of Cu_2O and CuO, the two main forms of copper oxides. Thanks to IERS enhancement, ultrathin layers of Cu_2O on copper can be detected down to 1 nm. The PL of Cu_2O is even more sensitive. I*n situ* measurements in reducing atmosphere, showed the complete absence of PL for non-oxidized copper. However, the quantification of copper oxide from PL measurements is not straightforward since many parameters such as the microstructure, the presence of defects or that of CuO, can influence the PL profile and intensity.

The largest IERS enhancements are expected for laser excitations in the red and near infrared, with theoretical enhancement factors of 75 and 120 for a Cu_2O thickness on copper of 30 and 50 nm at 633 and 785 nm, respectively. The variations of Raman intensities for both cuprous oxide and SLG transferred on nanostructured samples using Atotech processes are of this order of magnitude and can be fully described by IERS, without any further SERS enhancement. IERS alone is not enhancing the Raman signal enough for detecting molecules on electroless/etched samples. Such substrates are therefore not eligible for *in situ* Raman monitoring of the adsorption and decomposition of additives during copper plating.

On the other hand, BPE can be easily detected at concentration down to ~10^{-6} M on gold commercial SERStrate, and on Cu-plated SERStrates as well. BPE can even be detected on superficial thin copper oxide layers. Preliminary experiments with organic molecules of interest for Atotech (MBT) show that the detection threshold is as low as ~10^{-6} M.

As short term perspectives of this work, it would be interesting to use the refractive index determined from the modelling of the UV-visible absorption spectra as inputs for the fits of the ellipsometry data to check that the thickness determined by these two techniques are matching well. On the other hand, it would be interesting to take into account the presence of a superficial layer CuO to try to optimize the modelling of the UVS, especially when oxidation is achieved above 150°C for times over 2h.

As far as IERS studies are concerned, some experimental data in the range of 20-40 nm of Cu_2O are missing to confirm the maximum enhancements for the different wavelengths. Note that these results could be helpful to better characterize the oxidation of copper or other metallic substrates during CVD growth.

Raman spectroscopy appears as a powerful tool to detect and quantify superficial copper oxide layers on copper, and could be used as an industrial analytical technique, *e.g.* in the microelectronics field where the control of surface state of printed circuit boards is crucial.

Finally, different perspectives can be proposed regarding the initial goal of this thesis, *i.e.* the *in situ* detection of organic molecules on copper in electroless or electrolytic bath: i) developing a nanostructured substrate eligible for strong SERS enhancements, ii) running static measurements in solutions of composition closer to that of an industrial bath, iii) finding the optimal conditions for kinetic studies.

Appendix

Appendix 1: Ratio of transformation

The transformation of a mole of metallic copper to cuprous and cupric oxide is leading to a certain volume increase determined as follow:

First we remind the equation of transformation of copper to copper oxide. To form a mole of Cu_2O, 2 moles of Cu are required (69), so $n_{Cu_2O} = \frac{n_{Cu}}{2}$, while for CuO (70): $n_{CuO} = n_{Cu}$

$$2Cu + \frac{1}{2}\ O_2 \rightarrow Cu_2O \tag{69}$$

$$Cu + \frac{1}{2}\ O_2 \rightarrow CuO \tag{70}$$

The volume of Cu-ox (Cu_2O or CuO) is given as:

$$V_{Cu-ox} = \frac{n_{Cu-ox} * M_{Cu-ox}}{\rho_{Cu-ox}} \tag{71}$$

Our sample are cuboid, considering an uniaxial growth, with fixed section, the transformations law can be written as:

Transformation laws		
Cu_2O	$e_{Cu_2O} = \left(\frac{1}{2} \cdot \frac{\rho_{Cu}}{\rho_{Cu_2O}} \cdot \frac{M_{Cu_2O}}{M_{Cu}}\right) e_{Cu}$	$e_{Cu_2O} \cong 1.68\ e_{Cu}$
CuO	$e_{CuO} = \left(\frac{\rho_{Cu}}{\rho_{CuO}} \cdot \frac{M_{CuO}}{M_{Cu}}\right) e_{Cu}$	$e_{CuO} \cong 1.77\ e_{Cu}$

Data:

	Cu	Cu_2O	CuO
Density (ρ)	8.96	6.00	6.32
Molar masse (M)	63.55 g/mol	143.09 g/mol	79.54 g/ mol

Appendix 2: Fitting procedure

In order to get quantitative information on the different spectra a fitting procedure was developed to extract the important parameter from a Raman spectra.

A typical Raman spectrum with its fit result is given in Figure 16. Cu_2O and graphene Raman signature in red and blue colors, the PL background in yellow. Raman spectra are fitted by lorentzian function with a linear background. The fit is not done with any constraints on the positions, or FWHM, the only imposed parameter is a positive peak intensity, and the fitted range (Table 2). The peak at 640 cm^{-1} has multiples contribution, with the main contributions at 420, 530 and 640 cm^{-1}, fitted by 3 lorentzian and a common linear background. Often a presence of contamination carbon is detected along with the G peak of graphene. Therefore this G band is fitted in a large range, by a lorentzian function and a second voigt contribution related to C-contamination,

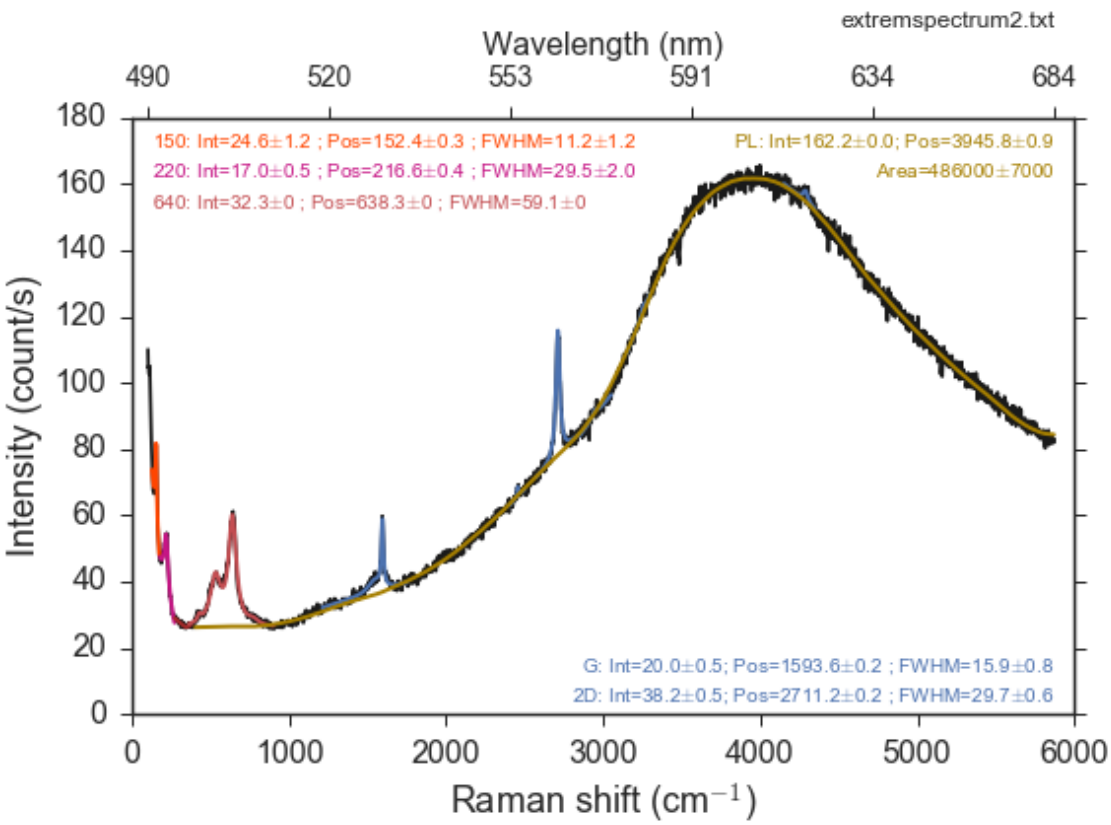

Figure 16: Raman spectra with fitted copper oxide and graphene Raman signatures as well as PL signature.

	Peak	Fitted range (cm^{-1})	Peak position range in case of multiples peak contribution (cm^{-1})
Cu_2O	150 cm^{-1}	135- 165	
	220 cm^{-1}	200-230	
	640 cm^{-1}	400-655	420: 400- 450 530: 500-560 640: 625-655
CuO	300 cm^{-1}	285-315	
Graphene	G	1210-1750	C-contamination: 1250-1570 G: 1575-1625
	2D	2570-2850	

Table 2: Raman fitted positon ranges for Cu_2O, CuO and graphene

The PL background could not be easily fitted, and therefore to get it maximal intensity and the position at maxima, we used a smoothing procedure. A classical method for data smoothing is the Savitsky-Golay method [1]. This method has two parameters to be optimized: the window size, and the polynomial order by which the approximation will be done.

Here we present the influence of the windows size for a first order polynomial and second order polynomial in Figure 17 and Figure 18 respectively, for two typical Raman spectra with a low and a large PL signature. According to Figure 17, for the first polynomial, the local variations are larger on the 'low PL' spectrum, due to small intensity, local maxima are found. The window size has little effect until it reaches 6000-8000 points (Raman spectra are ~12 kpoints), where the position of the PL reaches the upper limit at 5800 cm^{-1}. For the second order polynomial, the maxima are in an acceptable position range for all window size. Looking in detail to the suitability of the smoothed function and the PL peak, it appear that the best ranges are between 500 and 1000 points for the first polynomial order, and 500 and 2000 points for the second order polynomial.

We retain the position and intensity of the PL from the average of acceptable range of the between 500 and 2000 points for the second order polynomial.

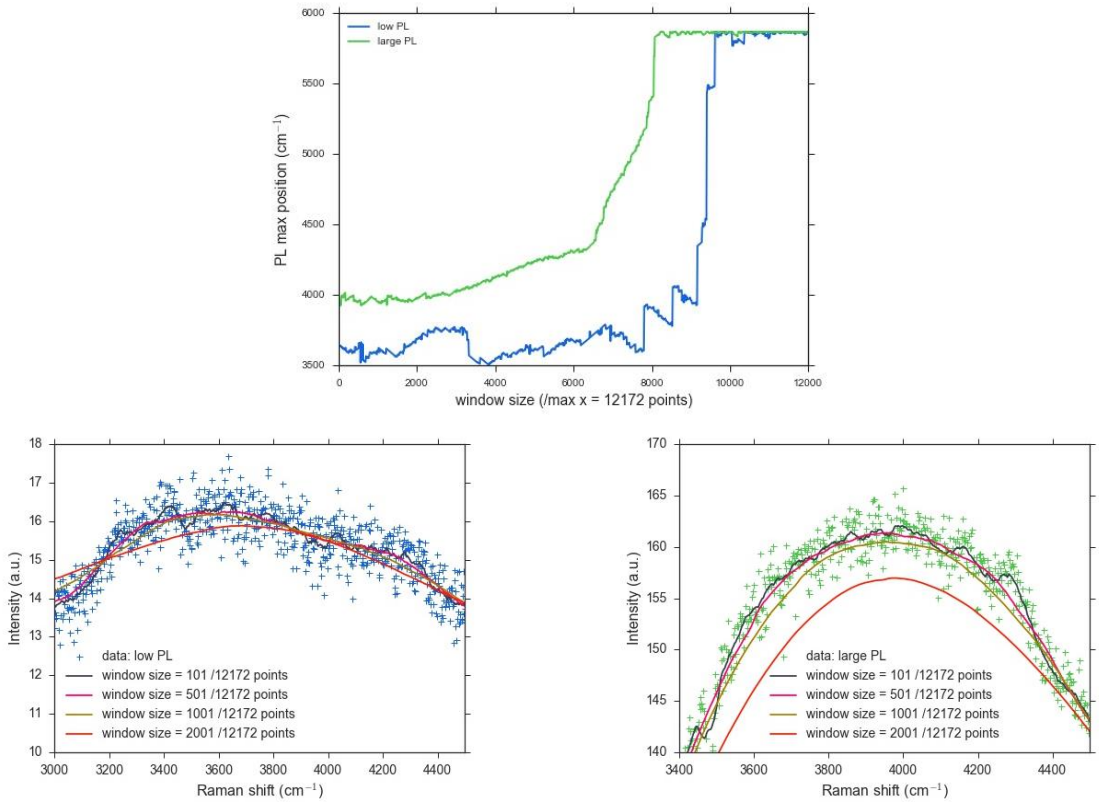

Figure 17: Fitting plot and returned PL maximum position for various smoothing window size, and a savitzky-golay smooth with a first order polynomial

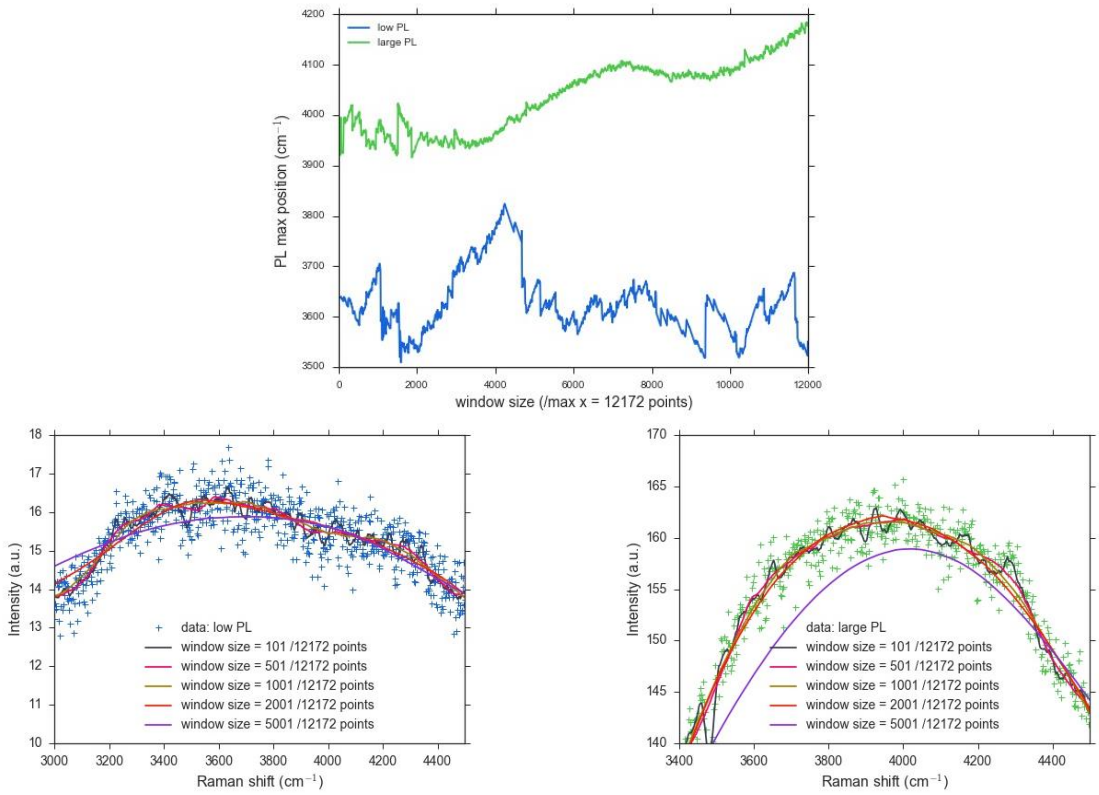

Figure 18: Fitting plot and returned PL maximum position for various smoothing window size, and a savitzky-golay smooth with a second order polynomial

In order to compare the different samples, we used only the spectra with detectable Cu_2O Raman signature (peak at 150 cm^{-1} above the noise) and another filter for the samples with graphene G band. The peak presence is ascertain when the intensity is larger than 3 times the noise, determined on a flat area of the silicon (1100-2000 cm^{-1}), as shown in Figure 19. In general, the noise value is ~0.7 counts/s, so a peak presence is retained for statistics, when its intensity is above 2 counts/s.

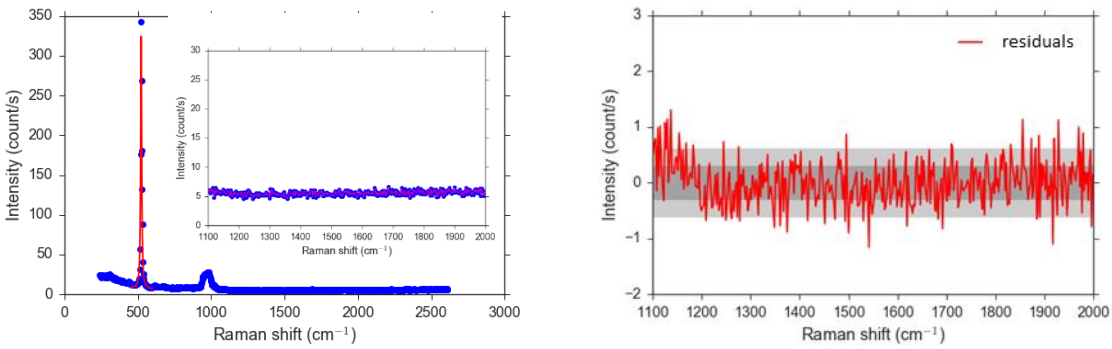

Figure 19: Fit of silicon peak at 521 cm-1 and on a flat range (1100-2000 cm^{-1}) (left) with residuals (right)

Using this rejection parameters, we compare the different Raman peaks, with position and FWHM reported in Table 3:

	Peak	Position (cm^{-1})	FWHM (cm^{-1})
Cu_2O	150 cm^{-1}	151 ± 1	15 ± 3
	220 cm^{-1}	218 ± 2	20 ± 3
	640 cm^{-1}	640 ± 6	40 ± 4
CuO	300 cm^{-1}	300 ±1.5	13 ± 3
Graphene	G	1591± 3	15 ± 2
	2D	2079 ± 4	31 ± 3

Table 3: Positon and FWHM for Cu_2O, CuO and graphene Raman signatures.

To compare two different parameters, they are represented in a xy map, as in Figure 20, with additional density of the points represented first by the colored area in the map and by the distribution of points on the sides.

The two parameter used to evaluate whether the parameters x and y are linked together by a linear representation are the pearson's r and the p. The Pearson coefficient ("Pearson's r") varies between -1 and 1. A value close to 0 means no linear correlation, while a value close to ±1 shows a linear correlation. The sign + means that when x increase y increase proportionally, while a negative sign (-) means that when x increases the y decreases [2].

$$r = \frac{cov(x,y)}{\sigma_x \sigma_y}$$

$$\text{with } \left| \begin{array}{l} cov(\quad) \text{ the covariance} \\ \sigma \quad \text{the standard deviation} \end{array} \right. \tag{72}$$

The p value is view as a significance of the empirical analysis. The p value is the probability that a random dataset distribution will give the same dataset distribution, the

actual measurement. The lower the p the better the confidence that the linear correlation is real and not due to a random distribution. For instance a p value of 0.01 correspond to a probability of 1% that a random distribution will exhibit the same behavior (a linear correlation) as the dataset measurement. In practice, the use of p value to conclude on a correlation is reliable for p values as low as 0.05, which show a high significance. In other words this means that the data is significant at the 0.05 level'.

For instance here the position are not linearly correlated, since the pearson's r is around 0.5 and 0.23 for Raman peak at 150 cm^{-1} and the peak at 220 cm^{-1} and with the 2D band positions respectively. The significance is however high, with the p value lower than 0.05.

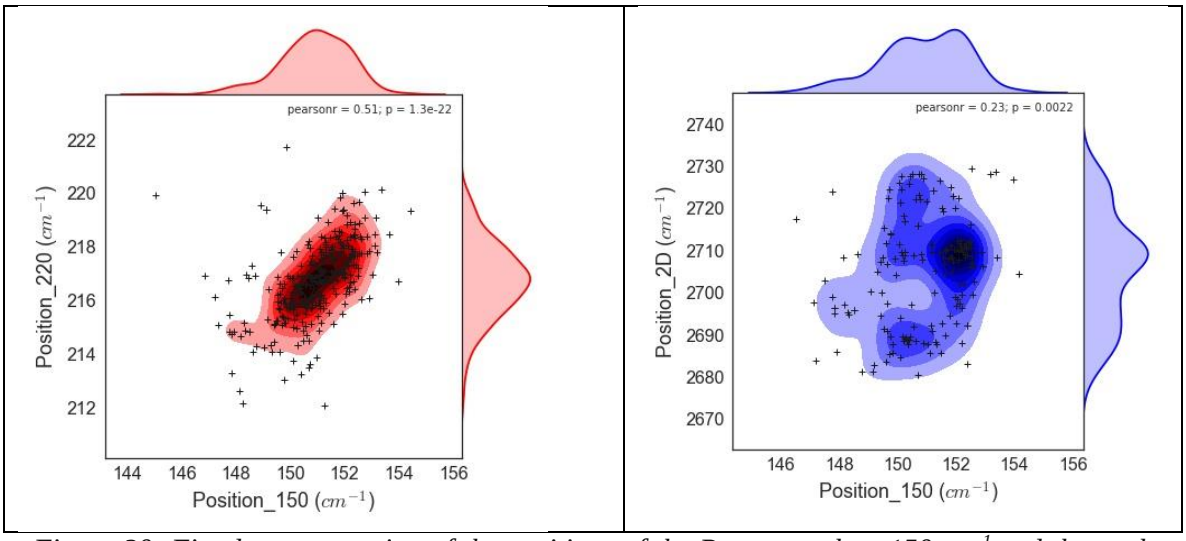

Figure 20: Fitted representation of the positions of the Raman peak at 150 cm^{-1} and the peak at 220 cm^{-1} (left) or with the 2D band positions (right)

Appendix 3: Quantification of the copper species by XPS

In addition to the identification of the element chemical state, a semi-quantitative analysis of Cu, Cu_2O and CuO can be performed from the deconvolution of the Cu $2p_{3/2}$, O1s and C1s XPS peaks. As the Cu $2p_{3/2}$ peaks for Cu and Cu_2O are not separated, the O1s peak is analyzed. Additionally the C1s peak deconvolution is used to conclude about the oxygen concentration due to contamination layer. Cano *et al* [138] suggested a deconvolution for the and O1s peaks of a copper tubes after corrosion in humid environment (100%) at temperature lower than 40°C for 50 to 330 days (Figure 21). The C1s peak is assumed to be due to the contribution of the C-C, C-O-C, C=O and HO-C=O bindings. The corresponding O1s spectrum confirms the C=O and HO-C=O bindings and shows additional contributions of Cu-OH and H_2O ones. Skinner *et al* [139] studied the surface of copper platted zinc sulfide particles. Using deconvolution of the O1s and the C1s spectra they identified mixed Cu_2O and CuO contributions. The different peak positions are summarized in Table 4.

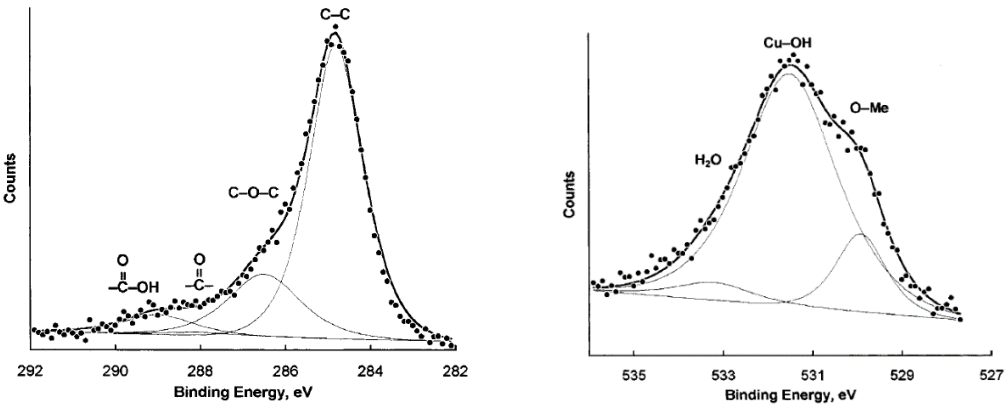

Figure 21:C1s (left) and O1s (right) deconvolution from [138]

Bond	Peak position	
	O1s	C1s
Cu-O	529.5-530.0	
Cu-O-Cu	530.0-530.5	
Cu-OH	531.2-531.9	
H-O-H	532.2-533.5	
>C=O	530.0-530.8	288.0
>C-OH	531.6	289.0
C-O-C		286.5
C-C		284.8

Table 4: Peak position for decovoluted C1s and O1s spectra from [138] [4] [140]

In the present study this methodology will be used to determine the Cu_2O and CuO contents of the thickness calibration samples.

The deconvolution of the C1s and O1s, on the raw and fully oxidized samples are shown on Figure 22 and Figure 23 respectively. C1s spectra are dominated by the C-C peak, with additional peaks at higher binging energy, related to carbon binding to oxygen. O1s spectra is indeed dominated by the broad peak of oxygen bounded to carbon. The additional contribution of oxygen bound to copper (O-Cu and Cu-O-Cu) is decovoluted from this major peak, its importance raise with oxidation. On the raw samples the peak is hidden by the major C-O contribution and corresponds to ~15 % of the major peak. The fully oxidized samples have a larger content of oxygen bound to copper (~22 %). Table 5summarizes the atomic percentage (%at) associated to each decovoluted peak area.

For C-O, C-C-O and C=O bindings, there is one oxygen for one carbon, therefore the atomic percentage of the deconvolution on C1s and O1s should match. There is however a difference from 15 to 49 % depending on the sample. This difference is assigned to a poor deconvolution of O1s peaks, with the broad C-O or C=O contribution overlapping with the Cu-O contribution. We trust the deconvolution on the C1s, and assign the additional oxygen to the bound with copper.

The comparison of the atomic percentage of copper and oxygen is given in Table 6. For CuO compound, the percentage of copper Cu(II) is correlated to the fitted Cu-O peak on the O1s spectra. The Cu(I) atomic percentage can partially explain the mismatch between carbon and oxygen. One oxygen is bound to two copper (Cu(I)).

Due to the excess of unassigned oxygen, we suppose the absence of metallic copper on the surface probed by XPS.

As stated in Chapter 3, the percentage of CuO is large (~50 % for raw samples and increases up to ~70 % for fully oxidized samples) on the probed thickness. The probed thickness assuming 3 atomic copper layers should be ~10 nm, which can convert to ~5 nm of CuO for the raw samples and ~7 nm for the fully oxidized samples.

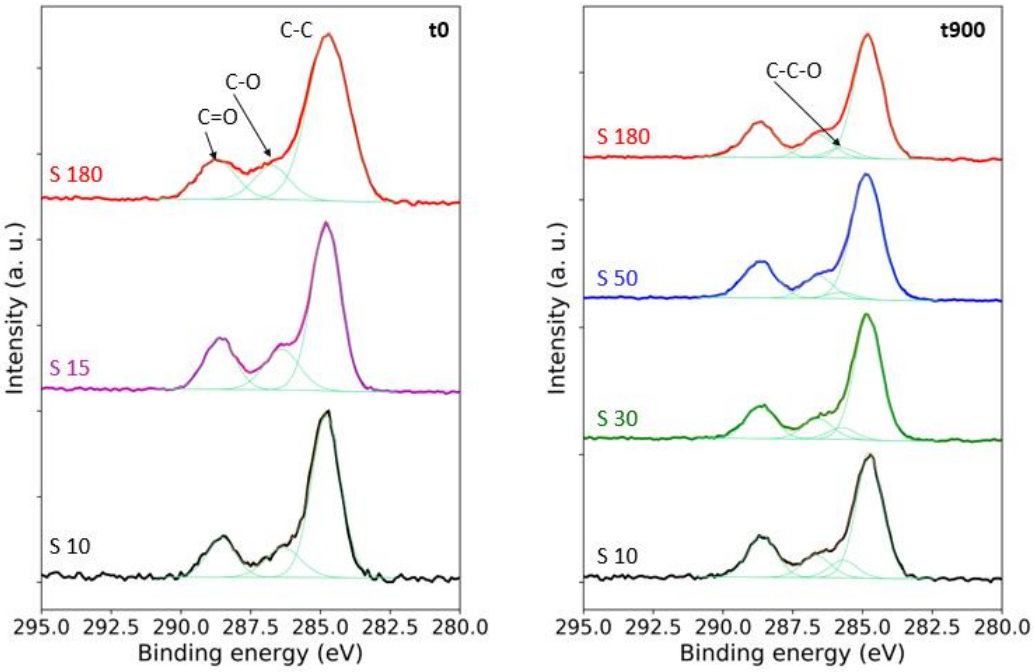

Figure 22: C1s deconvolution for raw (left) and oxidized (right) samples

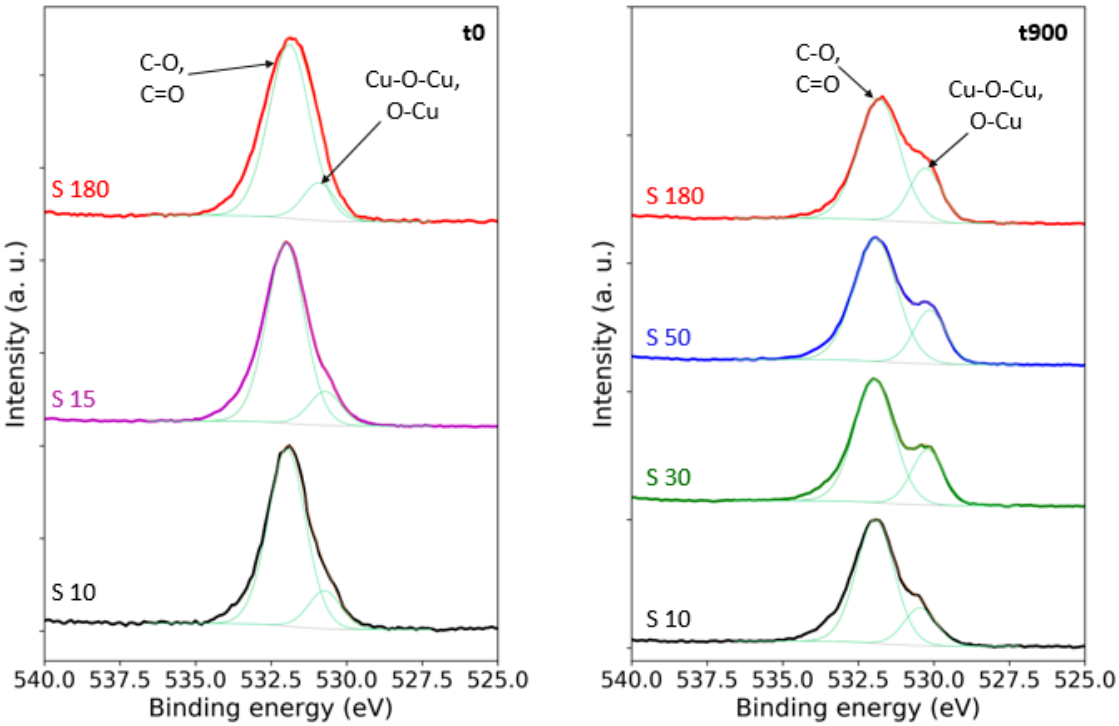

Figure 23: O1s deconvolution for raw (left) and oxidized (right) samples

%at	C-O, C-C-O and C=O		Δ = O (at%) - C (at%)
	Carbon	Oxygen	
Raw samples			
S10	20.3	23.8	*3.6 (15%)*
S15	22.0	27.9	*5.8 (21%)*
S180	19.2	24.8	*5.5 (22%)*
Fully oxidized samples			
S10	19.9	29.1	*9.2 (31%)*
S30	16.9	27.3	*10.5 (38%)*
S50	15.3	30	*14.8 (49%)*
S180	19.2	24.8	*5.5 (22%)*

Table 5: Atomic percentage of carbon and oxygen from C-O, C-C-O and C=O bindings

%at	Cu-O (CuO)		Δ = Cu (at%) - O (at%)	Cu-O-Cu (Cu_2O)		
	Oxygen	Cu(II)		Oxygen (mismatch)	Cu(I)	%CuO
Raw samples						
S10	4.4	4.8	*0.4*	*3.6*	6.4	43
S15	4.5	6.8	*2.3*	*5.8*	4.5	60
S180	4.3	4.6	*0.4*	*5.5*	4.7	50
Fully oxidized samples						
S10	7.7	10.2	*2.6*	*9.2*	4.7	68
S30	10.1	12.0	*1.9*	*10.5*	3.6	73
S50	9.9	13.7	*3.8*	*14.8*	2.7	84
S180	4.3	4.6	*0.4*	*5.5*	4.7	43

Table 6: Atomic percentage of Cu and O for Cu-O and O-Cu-O bonds

Bibliography

[1] M. Lenglet, K. Kartouni, J. Machefert, J. M. Claude, P. Steinmetz, E. Beauprez, J. Heinrich and N. Celati, "Low temperature oxidation of copper: The formation of CuO," *Materials research bulletin,* vol. 30, no. 4, pp. 393-403, 1995.

[2] D. L. Cocke, R. Schennach, M. A. Hossain, D. E. Mencer, H. McWhinney, J. R. Parga, M. Kesmez, J. A. G. Gomes and M. Y. A. Mollah, "The low-temperature thermal oxidation of copper, Cu3O2, and its influence on past and future studies," *Vacuum,* vol. 29, no. 1, pp. 71-83, 2005.

[3] M. Heinemann, B. Eifert and C. Heiliger, "Band structure and phase stability of the copper oxides Cu2O, CuO, and Cu4O3," *Physical Review B,* vol. 87, no. 11, p. 115111, 2013.

[4] F. A. Kröger, "The thermodynamics of imperfections in AgBr," *Journal of Physics and Chemistry of Solids,* vol. 26, no. 5, pp. 901-909, 1965.

[5] D. O. Scanlon, B. J. Morgan, G. W. Watson and A. Walsh, "Acceptor levels in p-type Cu2O: rationalizing theory and experiment," *Physical Review Letters,* vol. 103, no. 9, p. 096405, 2009.

[6] M. Nolan and S. D. Elliott, "The p-type conduction mechanism in Cu2O: a first principles study," *Physical Chemistry Chemical Physics,* vol. 8, no. 45, pp. 5350-5358, 2006.

[7] J. Bloem, "Discussion of some optical and electrical properties of Cu2O," *Philips Research Reports,* vol. 13, pp. 167-193, 1958.

[8] R. Dieckmann, "Point defects and transport in non-stoichiometric oxides: solved and unsolved problems," *Journal of Physics and Chemistry of Solids,* vol. 59, no. 4, pp. 507-525, 1998.

[9] N. L. Peterson and C. L. Wiley, "Diffusion and point defects in Cu2O," *Journal of Physics and Chemistry of Solids,* vol. 45, no. 3, pp. 281-294, 1984.

[10] J.-H. Park and K. Natesan, "Oxidation of copper and electronic transport in copper oxides," *Oxidation of Metals,* vol. 39, no. 5, pp. 411-435, 1993.

[11] O. Porat and I. Riess, "Defect chemistry of Cu2O at elevated temperatures," *Solid State Ionics,* vol. 74, p. 229, 1994.

[12] Sopra, "The Sopra S.A. company," [Online]. Available: http://www.sopra-sa.com/indices.htm. [Accessed june 2015].

[13] B. K. Meyer, A. Polity, D. Reppin, M. Becker, P. Hering, P. J. Klar, T. Sander, T. Reindl, C. Benz, J. Eickhoff and C. M. Heiliger, "Binary copper oxide semiconductors: From materials towards devices," *Physica status solidi (b),* vol. 249, no. 8, pp. 1487-1509, 2012.

[14] J. Li, Z. Mei, D. Ye, H. Liang, L. Liu, Y. Liu, A. Galeckas, A. Y. Kuznetsov and X. Du, "Engineering of optically defect free Cu2O enabling exciton luminescence at room temperature," *Optical Materials Express,* vol. 3, no. 12, pp. 2072-2077, 2013.

[15] İ. Y. Erdoğan and Ö. Güllü, "Optical and structural properties of CuO nanofilm: its diode application," *Journal of Alloys and Compounds,* vol. 492, no. 1, pp. 378-383, 2010.

[16] D. I. Son, C. H. You and T. W. Kim, "Structural, optical, and electronic properties of colloidal CuO nanoparticles formed by using a colloid-thermal synthesis process," *Applied surface science,* vol. 255, no. 21, pp. 8794-8797, 2009.

[17] C. Gattinoni and A. Michaelides, "Atomistic details of oxide surfaces and surface oxidation: the example of copper and its oxides," *Surface Science Reports,* vol. 70, no. 3, pp. 424-447, 2015.

[18] A. E. Rakhshani, "Preparation, characteristics and photovoltaic properties of cuprous oxide—a review," *Solid-State Electronics,* vol. 29, no. 1, pp. 7-17, 1986.

[19] M. R. Wright, Ph.D thesis, Dept. Chemistry, Wayne State Univ., Detroit, MI, 1962.

[20] J. R. Coughlin, *U.S. Eur. Mines Bull.,* vol. 542, no. 20, 1954.

[21] M. O'Keeffe and J. O. Bovin, "The crystal structure of paramelaconite Cu4O3," *American Mineralogist,* vol. 63, no. 12, p. 180–185, January–February 1978.

[22] A. Dubois-Salomon, Chimie de l'état solide, Paris: Ed. Masson, 1978.

[23] C. Wagner, "Contribution to the Theory of Formation of Oxidation Films," *Z. Physik. Chem. B,* vol. 21, p. 25, 1933.

[24] K. Mimura, J.-W. Lim, M. Isshiki, Y. Zhu and Q. Jiang, "Brief review of oxidation kinetics of copper at 350 C to 1050 C," *Metallurgical and materials transactions A,* vol. 37, no. 4, pp. 1231-1237, 2006.

[25] R.-M. Liang, Y.-M. Chang, P.-W. Wu and P. Lin, "Effect of annealing on the electrodeposited Cu2O films for photoelectrochemical hydrogen generation," *Thin Solid Films,* vol. 518, no. 24, pp. 7191-7195, 2010.

[26] N. F. M. N. Cabrera and N. F. Mott, "Theory of the oxidation of metals," *Reports on progress in physics,* vol. 12, no. 1, p. 163, 1949.

[27] K. Fujita, D. Ando, M. Uchikoshi, K. Mimura and M. Isshiki, "New model for low-temperature oxidation of copper single crystal," *Applied Surface Science,* vol. 276, pp. 347-358, 2013.

[28] J. T. N. Rhodin, "Low temperature oxidation of copper. I. Physical mechanism," *Journal of the American Chemical Society,* vol. 72, pp. 5102-5106, 1950.

[29] M. Raugh and P. Wibmann, "The oxidation kinetics of thin copper films studied by ellipsometry," *hin Solid Films,* vol. 228, pp. 121-124, 1993.

[30] H. Derin and K. Kantarli, "Optical characterization of thin thermal oxide films on copper by ellipsometry," *Applied Physics A: Materials Science and Processing,* vol. 75, pp. 391-395, 2002.

[31] U. R. Evans, "The mechanism of oxidation and tarnishing," *Transactions of the Electrochemical Society,* vol. 91, no. 1, pp. 547-572, 1947.

[32] F. Bouillon, "Sur I'oxydation sèche du cuivre et de ses alliages II.-Etude de I'oxydation isotherme du cuivre pur," *Bulletin des Sociétés Chimiques Belges,* vol. 60, no. 9-10, pp. 451-458., 1951.

[33] M. O'Reilly, X. Jiang, J. T. Beechinor, S. Lynch, C. NiDheasuna, J. C. Patterson and G. Crean, "Investigation of the oxidation behaviour of thin film and bulk copper," *Applied Surface Science,* vol. 91, pp. 152-156, 1995.

[34] W. Gao, H. Hong, J. He, A. Thomas, L. Chan and S. Li, "Oxidation behaviour of Cu thin films on Si wafer at 175–400 °C," *Materials Letters,* vol. 51, pp. 78-84, 2001.

[35] J. Iijima, J.-. W. Lim, S.-H. Hong, S. Suzuki, K. Mimura and M. Isshiki, "Native oxidation of ultra high purity Cu bulk and thin films," *Applied surface science,* vol. 253, no. 5, pp. 2825-2829, 2006.

[36] J. E. Boggio and R. C. Plumb, "Theory of formation of very thin oxide films on metals," *The Journal of Chemical Physics,* vol. 44, no. 3, pp. 1081-1086, 1966.

[37] T. Homma, T. Yoneoka and S. Matsunaga, "Nucleation and growth behavior of oxide on copper single crystals: their roles in kinetics," *Japanese Journal of Applied Physics,* vol. 13, no. S2, p. 101, 1974.

[38] K. R. Lawless and A. T. Gwathmey, "The structure of oxide films on different faces of a single crystal of copper," *Acta metallurgica,* vol. 4, no. 2, pp. 153-163, 1956.

[39] J. F. W. Young, "Spirals Developed on Single Crystals of Copper by Heating to High Temperatures in High Vacuums," *Journal of Applied Physics,* vol. 27, no. 5, pp. 545-552, 1956.

[40] R. Haugsrud and P. Kofstad, "On the oxygen pressure dependence of high temperature oxidation of copper," *Materials science,* vol. 251, pp. 65-71, 1997.

[41] A. Yabuki and S. Tanaka, "Oxidation behavior of copper nanoparticles at low temperature," *Materials Research Bulletin,* vol. 46, no. 12, pp. 2323-2327, 2011.

[42] S. K. Roy, S. K. Bose and S. C. Sircar, "Pressure dependencies of copper oxidation for low-and high-temperature parabolic laws," *Oxidation of metals,* vol. 35, no. 1, pp. 1-18, 1991.

[43] Y. Zhu, K. Mimura and M. Isshiki, "Oxidation mechanism of copper at 623–1073 K," *Materials Transactions,* vol. 43, pp. 2173-2176, 2002.

[44] P. Kofstad, High temperature oxidation of metals, New York: JOHN WILEY & SONS, 1966.

[45] M. Mansour, L. Favergeon and M. Pijolat, "Kinetic modeling of low temperature oxidation of copper nanoparticles by O2," *Thermochimica acta ,* vol. 570, pp. 41-50, 2013.

[46] L. Bouzidi and A. J. Slavin, "Ultrathin films of lead oxide on gold: dependence of stoichiometry, stability and thickness on O2 pressure and annealing temperature," *Surface science,* vol. 580, no. 1, pp. 195-206, 2005.

[47] A. Njeh, T. Wieder and H. Fuess, "Reflectometry studies of the oxidation kinetics of thin copper films," *Surface and Interface Analysis,* vol. 33, pp. 626-628, 2002.

[48] P. K. Krishnamoorthy and S. C. Sircar, "Formation of very thin oxide films on copper: kinetics and mechanism," *Oxidation of Metals,* vol. 2, pp. 349-359, 1970.

[49] Y. Z. Hu, R. Sharangpani and S. P. Tay, "Kinetic investigation of copper film oxidation by spectroscopic ellipsometry and reflectometry," *Journal of Vacuum Science and Technology A,* vol. 18, pp. 2527-2532, 2000.

[50] A. Manara, V. Sirtori and L. Mammarella, "Optical ellipsometry and electron spectroscopy studies of copper oxidation related to copper on printed circuit boards," *Surface and Interface Analysis,* Vols. 18,, pp. 32-38, 1992.

[51] S. K. Roy and S. C. Sircar, "A critical appraisal of the logarithmic rate law in thin-film formation during oxidation of copper and its alloys," *Oxidation of Metals,* vol. 15, pp. 9-20, 1981.

[52] M. G. Hapase, M. K. Gharpurey and A. B. Biswas, "The oxidation of vacuum deposited films of copper," *Surface Science,* vol. 9, pp. 87-99, 1968.

[53] J. Iijima, Doctoral thesis, Tohoku University, 2005.

[54] W. E. Garner, T. J. Gray, F. S. Stone, S. D. Savage and P. F. Tiley, "Reactions on the surface of copper oxide," *Discussions of the Faraday Society,* vol. 8, pp. 246-258, 1950.

[55] J. Benard, L'oxydation des métaux, Gauthier-Villars and Cie, 1963.

[56] M. Shanid, A. ,. M. Khadar and V. G. Sathe, "Frohlich interaction and associated resonance enhancement in nanostructured copper oxide films," *Journal of Raman Spectroscopy,* vol. 42, no. 9, pp. 1769-1773, 2011.

[57] V. Figueiredo, E. Elangovan, G. Goncalves, P. Barquinha, L. Pereira, N. Franco, M. E. R. Alves and E. Fortunato, "Effect of post-annealing on the properties of copper oxide thin films obtained from the oxidation of evaporated metallic copper," *Applied Surface Science,* vol. 254, no. 13, pp. 3949-3954, 2008.

[58] M. Ramirez, L. Henneken and S. Virtanen, "Oxidation kinetics of thin copper films and wetting behaviour of copper and Organic Solderability Preservatives (OSP) with lead-free solder," *Applied Surface Science,* vol. 257, no. 15, pp. 6481-64, 2011.

[59] R. Poilblanc and F. Crasnier, Spectroscopies infrarouge et Raman, Grenoble sciences: EDP sciences, 2006.

[60] N. B. Colthup, L. H. Daly and S. W. E. Wiberley, Introduction to Infrared ans Raman spectroscopy, London academic press, 1990.

[61] G. P. Srivastava, The physics of phonons, CRC press, 1990, pp. 226-230.

[62] A. Compaan and H. J. Trodahl, "Resonance Raman scattering in Si at elevated temperatures," *Physical Review B,* vol. 29, no. 2, p. 793, 1984.

[63] R. M. Martin and L. M. Falicov, Resonant raman scattering, vol. In Light scattering in Solids I, Springer Berlin Heidelberg, 1983, pp. 79-145.

[64] L. Debbichi, M. C. Marco de Lucas, J. F. Pierson and P. Kruger, "Vibrational properties of CuO and Cu4O3 from first-principles calculations, and Raman and infrared spectroscopy," *The Journal of Physical Chemistry C,* vol. 116, no. 18, pp. 10232-10237, 2012.

[65] Y. W. P. H. Petroff, P. Y. Yu and Y. R. Shen, "Study of photoluminescence in Cu2O," *Physical Review B,* vol. 12, no. 6, p. 2488, 1975.

[66] J. C. Irwin, J. Chrzanowski, T. Wei, D. J. Lockwood and A. Wold, "Raman scattering from single crystals of cupric oxide," *Physica C: Superconductivity,* vol. 166, no. 5-6, pp. 456-464, 1990.

[67] A. P. Litvinchuk, A. Möller, L. Debbichi, P. Krüger, M. N. Iliev and M. M. Gospodinov, "Second-order Raman scattering in CuO," *Journal of Physics: Condensed Matter,* vol. 25, no. 10, p. 105402, 2013.

[68] T. Sanders, "Monitoring defect-induced perturbations of the ideal crystal structure of ZnO and Cu2O by Raman spectroscopy," Univeresität Giessen, 2015.

[69] P. Y. Yu and Y. R. Shen, "Study of dispersive raman modes in Cu2O by resonant raman scattering," *Physical Review Letters,* vol. 32, pp. 939-942, 1974.

[70] P. Y. Yu and Y. R. Shen, "Multiple resonance effects on raman scattering at the yellow-exciton series of Cu2O," *Physical Review Letters,* vol. 32, pp. 373-376, 1974.

[71] R. M. Martin, "Theory of the one-phonon resonance Raman effect," *Physical Review B,* vol. 4, no. 10, p. 3676, 1971.

[72] A. Pinczuk and E. Burstein, "Raman Scattering from InSb surfaces at photon energies near the E1 energy gap," *Physical Review Letters,* vol. 21, no. 15, p. 1073, 1968.

[73] M. V. Klein, "Equivalence of resonance Raman scattering in solids with absorption followed by luminescence," *Physical Review B,* vol. 8, no. 2, p. 919, 1973.

[74] N. A. M. Shanid and M. A. Khadar, "Evolution of nanostructure, phase transition and band gap tailoring in oxidized Cu thin films," *Thin Solid Films,* vol. 516, no. 18, pp. 6245-6252, 2008.

[75] M. N. A. Shanid, M. Abdul Khadar and V. G. Sathe, "Frohlich interaction and associated resonance enhancement in nanostructured copper oxide films," *Journal of Raman Spectroscopy ,* vol. 42, no. 9, pp. 1769-1773, 2011.

[76] A. Z. Genack, H. Z. Cummins, M. A. Washington and A. Compaan, "Quadrupole-dipole Raman scattering at the 1 S yellow exciton in Cu2O," *Physical Review B,* vol. 12, no. 6, p. 2478, 1975.

[77] P. F. Williams and S. P. S. Porto, "Symmetry-forbidden resonant Raman scattering in Cu2O," *Physical Review B,* vol. 8, no. 4, p. 1782, 1973.

[78] A. Compaan, "Surface damage effects on allowed and forbidden phonon raman scattering in cuprous oxide," *Solid State Communications,* vol. 16, no. 3, pp. 293-296, 1975.

[79] A. Compaan and H. Z. Cummins, "Resonant Quadrupole-Dipole Raman Scattering at the 1 S Yellow Exciton in Cu2O," *Physical Review Letters,* vol. 31, no. 1, p. 41, 1973.

[80] P. Y. Yu, Y. R. Shen, Y. Petroff and L. M. Falicov, "Resonance Raman Scattering at the Forbidden Yellow Exciton in Cu2O," *Physical Review Letters,* vol. 30, no. 7, p. 283, 1973.

[81] P. Y. Yu, Y. R. Shen and Y. Petroff, "Resonance Raman scattering in Cu2O at the blue and indigo excitons," *Solid State Communications,* vol. 12, no. 10, pp. 973-975, 1973.

[82] C.-H. Wu and J. L. Birman, "Theory of resonant Raman enhancement of a forbidden phonon in Cu2O," *Solid State Communications,* vol. 14, no. 6, pp. 465-467, 1974.

[83] M. A. Washington, A. Z. Genack, H. Z. Cummins, R. H. Bruce, A. Compaan and R. A. Forman, "Spectroscopy of excited yellow exciton states in Cu2O by forbidden resonant Raman scattering," *Physical Review B,* vol. 15, no. 4, p. 2145, 1977.

[84] P. Y. Yu and Y. R. Shen, "Resonance Raman studies in Cu2O. II. The yellow and green excitonic series," *Phys. Rev., B,* vol. 17, no. 10, pp. 2145-2153, 1978.

[85] J. S. Weiner and P. Y. Yu, "Time-resolved hot luminescence and resonant Raman scattering: Cu2O revisited," *Solid state communications,* vol. 50, no. 6, pp. 493-496, 1984.

[86] A. Kim, F. S. Ou, D. A. Ohlberg, M. Hu, R. S. Williams and Z. Li, "Study of molecular trapping inside gold nanofinger arrays on surface-enhanced Raman substrates," *Journal of the American Chemical Society,* vol. 133, no. 21, p. 823, 2011.

[87] T. Chen, A. Pal, J. Gao, Y. Han, H. Chen, S. Sukhishvili, H. Du and S. G. Podkolzin, "Identification of vertical and horizontal configurations for BPE adsorption on silver surfaces," *The Journal of Physical Chemistry C,* vol. 119, no. 43, pp. 24475-24488, 2015.

[88] A. H. Castro Neto, F. Guinea, N. M. R. Peres, K. S. Novoselov and A. K. Geim, "The electronic properties of graphene," *Rev. Mod. Phys.,* vol. 81, no. 1, pp. 109-162, 2009.

[89] A. C. Ferrari and D. M. Basko, "Raman spectroscopy as a versatile tool for studying the properties of graphene," *Nature nanotechnology,* vol. 8, no. 4, pp. 235-246, 2013.

[90] M. Bayle, N. Reckinger, J. Huntzinger, A. Felten, A. Bakaraki, P. Landois, J. Colomer and e. al., "Dependence of the Raman spectrum characteristics on the number of layers and stacking orientation in few-layer graphene," *physica status solidi (b),* vol. 252, no. 11, pp. 2375-2379, 2015.

[91] A. Tiberj, M. Rubio-Roy, M. Paillet, J.-R. Huntzinger, P. Landois, M. Mikolasek, S. Contreras, J.-L. Sauvajol, E. Dujardin and A.-A. Zahab, "Reversible optical doping of graphene," *Scientific reports,* vol. 3, 2013.

[92] F. Otakar, J. Vejpravova, V. Holy, L. Kavan and M. Kalbac, "Interaction between graphene and copper substrate: The role of lattice orientation," *Carbon,* vol. 68, pp. 440-451, 2014.

[93] J. E. Lee, G. Ahn, J. Shim, Y. S. Lee and S. Ryu, "Optical separation of mechanical strain from charge doping in graphene," *Nature Communications,* vol. 3, p. 1024, 2012.

[94] M. Lazzeri and F. Mauri, "Nonadiabatic Kohn anomaly in a doped graphene monolayer," *Physical review letters,* vol. 97, no. 26, p. 266407, 2006.

[95] S. Berciaud, S. Ryu, L. E. Brus and T. F. Heinz, "Probing the intrinsic properties of exfoliated graphene: Raman spectroscopy of free-standing monolayers," *Nano Letters,* vol. 9, no. 1, pp. 346-352, 2009.

[96] O. Frank, J. Vejpravova, V. Holy, L. Kavan and M. Kalbac, "Interaction between graphene and copper substrate: The role of lattice orientation," *Carbon,* vol. 68, pp. 440-451, 2014.

[97] M. Ramsteiner, C. Wild and J. Wagner, "Interference effects in the Raman scattering intensity from thin films," *Appl. Opt.,* vol. 28, pp. 4017-4023, 1989.

[98] D. Yoon, H. Moon, Y.-W. Son, J. S. Choi, B. H. Park, Y. H. Cha, D. Kim Young and H. Cheong, "Interference effect on Raman spectrum of graphene on SiO2/Si," *Phys. Rev. B,* vol. 80, p. 125422, 2009.

[99] J.-R. Huntzinger, *Raman summer school,* Montpellier, June, 2017.

[100] X. Yin, Y. Li, F. Ke, C. Lin, H. Zhao, L. Gan, Z. Luo, R. Zhao, T. F. Heinz and Z. Hu, "Evolution of the Raman spectrum of graphene grown on copper upon oxidation of the substrate," *Nano Res.,* vol. 7, p. 1613–1622, 2014.

[101] Y. Cheng, Y. Song, D. Zhao, X. Zhang, S. Yin, P. Wang, M. Wang, Y. Xia, S. Maruyama, P. Zhao and H. Wang, "Direct Identification of Multilayer Graphene Stacks on Copper by Optical Microscopy," *Chem. Mater.,* vol. 28, p. 2165−2171, 2016.

[102] R. Ramírez-Jímenez, L. Alvarez-Fraga, F. J.-V. Jimenez-Villacorta, E. Climent-Pascual, C. Prieto and A. de Andrés, "Interference enhanced Raman effect in graphene bubbles," *Carbon,* vol. 105, pp. 556-565, 2016.

[103] E. Le Ru and P. Etchegoin, Principles of Surface-Enhanced Raman Spectroscopy: and related plasmonic effects, Elsevier, 2008.

[104] L. Tsang, J. ,. A. Kong and K.-H. Ding, Scattering of Electromagnetic Waves: Theories and Applications, John Wiley & Sons, Inc., 2000.

[105] A. Trügler, Optical Properties of Metallic Nanoparticles: Basic Principles and Simulation, vol. 232, Springer, 2016.

[106] G. Heimel, L. Romaner, J.-L. Brédas and E. Zojer, "Interface energetics and level alignment at covalent metal-molecule junctions: π-conjugated thiols on gold," *Physical review letters,* vol. 96, no. 19, p. 196806, 2006.

[107] A. H. Pakiari and Z. Jamshidi, "Interaction of amino acids with gold and silver clusters," *The Journal of Physical Chemistry A,* vol. 111, no. 20, pp. 4391-4396, 2007.

[108] M. H. Jazayeri, H. Amani, A. A. Pourfatollah, H. Pazoki-Toroudi and B. Sedighimoghaddam, "Various methods of gold nanoparticles (GNPs) conjugation to antibodies," *Sensing and Bio-Sensing Research,* vol. 9, pp. 17-22, 2016.

[109] B. Sharma, R. R. Frontiera, A.-I. Henry, E. Ringe and R. P. Van Duyne, "SERS: materials, applications, and the future," *Materials today,* vol. 15, no. 1, pp. 16-25, 2012.

[110] K. Kneipp, M. Moskovits and H. Kneipp, Surface-Enhanced Raman Scattering, Verlag Berlin Heidelberg: Springer, 2006.

[111] G. H. Chan, J. Zhao, E. M. Hicks, G. C. Schatz and R. P. Van Duyne, "Plasmonic properties of copper nanoparticles fabricated by nanosphere lithography," *Nano Letters,* vol. 7, no. 7, pp. 1947-1952, 2007.

[112] T. Ghodselahi and M. A. Vesaghi, "Localized surface plasmon resonance of Cu@ Cu2O core–shell nanoparticles: absorption, scattering and luminescence," *Physica B: Condensed Matter,* vol. 406, no. 13, pp. 2678-2683, 2011.

[113] M. Dendisová-Vyškovská, V. Prokopec, M. Člupek and P. Matějka, "Comparison of SERS effectiveness of copper substrates prepared by different methods: what are the values of enhancement factors?," *Journal of Raman Spectroscopy,* vol. 43, no. 2, pp. 181-186, 2012.

[114] M. Muniz-Miranda, C. Gellini and E. Giorgetti, "Surface-enhanced Raman scattering from copper nanoparticles obtained by laser ablation," *The Journal of Physical Chemistry C,* vol. 115, no. 12, pp. 5021-5027, 2011.

[115] L. Chen, J. Yu, T. Fujita and M. Chen, "Nanoporous copper with tunable nanoporosity for SERS applications," *Advanced Functional Materials,* vol. 19, no. 8, pp. 1221-1226, 2009.

[116] J. Cejkova, V. Prokopec, S. Brazdova, A. Kokaislova, P. Matejka and F. Stepanek, "Characterization of copper SERS-active substrates prepared by electrochemical deposition," *Applied Surface Science,* vol. 255, no. 18, pp. 7864-7870, 2009.

[117] C. A. Deckert, "Electroless copper plating. A review. I," *Plating and surface finishing,* vol. 82, no. 2, pp. 48-55, 1995.

[118] M. Paunovic, Modern Electroplating, John Wiley & Sons, Inc., 2010, pp. 433-446.

[119] Y. Y. Shacham-Diamand, "Electroless copper deposition using glyoxylic acid as reducing agent for ultralarge scale integration metallization," *Electrochemical and Solid-State Letters,* vol. 3, no. 6, pp. 279-282, 2000.

[120] S. Jayalakshmi, P. Venkatesh and P. BalaRamesh, "Recent acvances in electroless copper deposition - A review," *International Journal of Advanced Research in Engineering and Applied Sciences,* vol. 5, no. 8, 2016.

[121] H. P. Hofmann, "Method of manufacturing a circuit carrier and the use of the method". Atotech Deutschland Gmbh Patent US 8927899 B2, 20 Jan 2005.

[122] M. Dammasch, M. HARYONO, S. KARASAHIN and H.-J. SCHREIER, "Method for depositing a copper seed layer onto a barrier layer and copper plating bath". ATOTECH Deutschland GmbH Patent EP 3049550 A1, 11 Sept 2011.

[123] M. Kalbac, O. Frank and L. Kavan, "The control of graphene double-layer formation in copper-catalyzed chemical vapor deposition," *Carbon 50,* vol. 50, no. 10, pp. 3682-3687, 2012.

[124] X. Li, W. Cai, J. An, S. Kim, J. Nah, D. Yang, R. Piner, A. Velamakanni, I. Jung and E. Tutuc, "Large-area synthesis of high-quality and uniform graphene films on copper foils," *Science,* vol. 324, no. 5932, pp. 1312-1314, 2009.

[125] A. Reina, H. Son, L. Jiao, B. Fan, M. S. Dresselhaus, Z. Liu and J. Kong, "Transferring and identification of single-and few-layer graphene on arbitrary substrates," *The Journal of Physical Chemistry C,* vol. 112, no. 46, pp. 17741-17744, 2008.

[126] C. Wang, W. Chen, C. Han, G. Wang, B. Tang, C. Tang and Y. Wang, "Growth of millimeter-size single crystal graphene on Cu foils by circumfluence chemical vapor deposition," *Scientific reports,* vol. 4, 2014.

[127] A. C. Ferrari and D. M. Basko, "Raman spectroscopy as a versatile tool for studying the properties of graphene," *Nature nanotechnology,* vol. 8, no. 4, pp. 235-246, 2013.

[128] D. Graf, F. Molitor, K. Ensslin, C. Stampfer, A. Jungen, C. Hierold and L. Wirtz, "Spatially resolved Raman spectroscopy of single-and few-layer graphene," *Nano Lett.,* vol. 7, no. 2, p. 238–242, 2007.

[129] Z. H. W. H. M. Ni, J. Kasim, H. M. Fan, T. Yu, Y. H. Wu, Y. P. Feng and Z. X. Shen, "Graphene thickness determination using reflection and contrast spectroscopy," *Nano letters,* vol. 7, no. 9, pp. 2758-2763, 2007.

[130] C. Song, Z. Wang, J. Yang, R. Zhang and Y. Cui, "Preparation of 2-mercaptobenzothiazole-labeled immuno-Au aggregates for SERS-based immunoassay," *Colloids and Surfaces B: Biointerfaces* , vol. 81, no. 1, pp. 285-288, 2010.

[131] R. Gavrila, A. Dinescu and D. Maradare Rom, "A power spectral density study of thin films morphology," *J. Inform. Sci. Technol.,* vol. 10, no. 3, pp. 291-300, 2007.

[132] M. Ramonda, Evolution dynamique de rugosité de surface lors de processus d'érosion et de croissance. Etude par microscopie en champ proche, Marseille, 1998.

[133] D. Briggs and J. T. Grant, Surface analysis by auger and X-ray photoelectron spectroscopy in IM Publications and SurfaceSpectra Limited, Chichester/Manchester UK, 2003.

[134] S. Hwang, "Proximity scanning transmission electron microscopy/spectroscopy," *arXiv preprint arXiv:1601.00786,* 2016.

[135] M. C. Biesinger, L. W. Lau, A. R. Gerson and R. S. C. Smart, "Resolving surface chemical states in XPS analysis of first row transition metals, oxides and hydroxides: Sc, Ti, V, Cu and Zn," *Applied Surface Science,* vol. 257, no. 3, pp. 887-898, 2010.

[136] J. F. Watts and J. Wolstenholme, "An introduction to surface analysis by XPS and AES," 2003.

[137] A. V. Naumkin, A. Kraut-Vass, S. W. Gaarenstroom and C. J. Powell, "NIST Standard Reference Database 20, Version 4.1," 2003. [Online]. Available: (http://physics.nist.gov/xps/Default.aspx), 2003.. [Accessed 4 June 2016].

[138] T. Wächter, "Thin Films of Copper Oxide and Copper Grown by Atomic Layer Deposition for Applications in Metallization Systems of Microelectronic Devices," Fakultät für Elektrotechnik und Informationstechnik Technischen Universität Chemnitz, 2010.

[139] K. M. McPeak, S. V. Jayanti, S. J. P. Kress, S. Meyer, S. Iotti, A. Rossinelli and D. J. Norris, "Plasmonic films can easily be better: Rules and recipes," *ACS Photonics,* vol. 2, pp. 326-333, 2015.

[140] M. C. Biesinger, L. W. Lau, A. R. Gerson and S. C. S. Roger, "Resolving surface chemical states in XPS analysis of first row transition metals, oxides and hydroxides: Sc, Ti, V, Cu and Zn," *Applied Surface Science,* vol. 257, no. 3, pp. 887-898, 2010.

[141] K. M. McPeak, S. V. Jayanti, S. J. P. Kress, S. Meyer, S. Iotti, A. Rossinelli and D. J. Norris, "Plasmonic films can easily be better: Rules and recipes," *ACS Photonics,* vol. 2, pp. 326-333, 2015.

[142] G. Ghosh, "Dispersion-equation coefficients for the refractive index and birefringence of calcite and quartz crystals," *Optics communications,* vol. 163, no. 1, pp. 95-102, 1999.

[143] H. R. P. H. Ehrenreich and H. R. Philipp, "Optical properties of Ag and Cu," *Physical Review,* vol. 128, no. 4, p. 1622, 1962.

[144] D. Barchiesi, N. Lidgi-Guigui and M. Lamy de la Chapelle, "Functionalization layer influence on the sensitivity of surface plasmon resonance (SPR) biosensor," *Optics Communications,* vol. 285, no. 6, pp. 1619-1623, 2012.

[145] D. Barchiesi, "A 3-D Multilayer Model of Scattering by Nanostructures. Application to the Optimisation of Thin Coated Nano-Sources," *Optics Communications,* vol. 126, no. 1-3, pp. 7-13, 1996.

[146] X. Wang, K.-p. Chen, M. Zhao and D. D. Nolte, "Refractive index and dielectric constant evolution of ultra-thin gold from clusters to films," *Optics express,* vol. 18, no. 24, pp. 24859-24867, 2010.

[147] S. Laref, J. Cao, A. Asaduzzaman, K. Runge, P. Deymier, R. W. Ziolkowski, M. Miyawaki and K. Muralidharan, "Size-dependent permittivity and intrinsic optical anisotropy of nanometric gold thin films: a density functional theory study," *Optics express,* vol. 21, no. 10, pp. 11827-11838, 2013.

[148] J. Z. M. D. Y. H. L. L. L. Y. L. A. G. A. Y. K. X. D. Li, "Engineering of optically defect free Cu 2 O enabling exciton luminescence at room temperature," *Optical Materials Express,* vol. 3, no. 12, pp. 2072-2077, 2013.

[149] B. K. A. P. D. R. M. B. P. H. P. J. K. T. S. T. R. C. B. J. E. M. H. C. Meyer, "Binary copper oxide semiconductors: From materials towards devices," *Physica status solidi (b) ,* vol. 249, no. 8, pp. 1487-1509, 2012.

[150] X. Yin, Y. Li, F. Ke, C. Lin, H. Zhao, L. Gan, Z. Luo, R. Zhao, T. F. Heinz and Z. Hu, "Evolution of the Raman spectrum of graphene grown on copper upon oxidation of the substrate," *Nano research,* vol. 7, no. 11, pp. 1613-1622, 2014.

[151] E. P. E. Le Ru, Principles of Surface-Enhanced Raman Spectroscopy: and related plasmonic effects, Elsevier, 2008.

[152] A. C. Ferrari, J. C. Meyer, V. Scardaci, C. Casiraghi, M. Lazzeri, F. Mauri and S. Piscanec, "Raman spectrum of graphene and graphene layers," *Physical review letters,* vol. 97, no. 18, p. 187401, 2006.

[153] T. J. Thamann, P. Frank, L. J. Willis and T. M. Loehr, "Normal coordinate analysis of the copper center of azurin and the assignment of its resonance raman spectrum," *Proceedings of the National Academy of Sciences,* vol. 79, no. 20, pp. 6396-6400, 1982.

[154] T. Ghodselahi and M. A. Vesaghi, "Localized surface plasmon resonance of Cu@ Cu2O core–shell nanoparticles: absorption, scattering and luminescence," *Physica B: Condensed Matter,* vol. 406, no. 13, pp. 2678-2683, 2011.

[155] G. H. Chan, J. Zhao, E. M. Hicks, G. C. Schatz, V. Duyne and P. Richard, "Plasmonic properties of copper nanoparticles fabricated by nanosphere lithography," *Nano Letters,* vol. 7, no. 7, pp. 1947-1952, 2007.

[156] A. K. Rai, R. Singh, K. N. Singh and V. B. Singh, "FTIR, Raman spectra and ab initio calculations of 2-mercaptobenzothiazole," *Spectrochimica Acta Part A: Molecular and Biomolecular Spectroscopy ,* vol. 63, no. 2, pp. 483-490, 2006.